NASA/CR—2003-212313

Supersonic Test of the 10-Inch Bifurcated Two-Stage Supersonic Inlet (BTSSI)

C.M. Carlin, I. Frisch, J.J. Kolden, J.L. Koncsek, K.J. Marrs, D.W. Mayer,
S.L. McMahon, K.H. Milligan, and D.M. Sommerfield
The Boeing Company, Seattle, Washington

July 2003

The NASA STI Program Office . . . in Profile

Since its founding, NASA has been dedicated to the advancement of aeronautics and space science. The NASA Scientific and Technical Information (STI) Program Office plays a key part in helping NASA maintain this important role.

The NASA STI Program Office is operated by Langley Research Center, the Lead Center for NASA's scientific and technical information. The NASA STI Program Office provides access to the NASA STI Database, the largest collection of aeronautical and space science STI in the world. The Program Office is also NASA's institutional mechanism for disseminating the results of its research and development activities. These results are published by NASA in the NASA STI Report Series, which includes the following report types:

- TECHNICAL PUBLICATION. Reports of completed research or a major significant phase of research that present the results of NASA programs and include extensive data or theoretical analysis. Includes compilations of significant scientific and technical data and information deemed to be of continuing reference value. NASA's counterpart of peer-reviewed formal professional papers but has less stringent limitations on manuscript length and extent of graphic presentations.

- TECHNICAL MEMORANDUM. Scientific and technical findings that are preliminary or of specialized interest, e.g., quick release reports, working papers, and bibliographies that contain minimal annotation. Does not contain extensive analysis.

- CONTRACTOR REPORT. Scientific and technical findings by NASA-sponsored contractors and grantees.

- CONFERENCE PUBLICATION. Collected papers from scientific and technical conferences, symposia, seminars, or other meetings sponsored or cosponsored by NASA.

- SPECIAL PUBLICATION. Scientific, technical, or historical information from NASA programs, projects, and missions, often concerned with subjects having substantial public interest.

- TECHNICAL TRANSLATION. English-language translations of foreign scientific and technical material pertinent to NASA's mission.

Specialized services that complement the STI Program Office's diverse offerings include creating custom thesauri, building customized databases, organizing and publishing research results . . . even providing videos.

For more information about the NASA STI Program Office, see the following:

- Access the NASA STI Program Home Page at ***http://www.sti.nasa.gov***

- E-mail your question via the Internet to help@sti.nasa.gov

- Fax your question to the NASA Access Help Desk at 301–621–0134

- Telephone the NASA Access Help Desk at 301–621–0390

- Write to:
  NASA Access Help Desk
  NASA Center for AeroSpace Information
  7121 Standard Drive
  Hanover, MD 21076

NASA/CR—2003-212313

Supersonic Test of the 10-Inch Bifurcated Two-Stage Supersonic Inlet (BTSSI)

C.M. Carlin, I. Frisch, J.J. Kolden, J.L. Koncsek, K.J. Marrs, D.W. Mayer,
S.L. McMahon, K.H. Milligan, and D.M. Sommerfield
The Boeing Company, Seattle, Washington

Prepared under Contract NAS3–25963

National Aeronautics and
Space Administration

Glenn Research Center

July 2003

Note that at the time of research, the NASA Lewis Research Center was undergoing a name change to the NASA John H. Glenn Research Center at Lewis Field. Both names may appear in this report.

Available from

NASA Center for Aerospace Information
7121 Standard Drive
Hanover, MD 21076

National Technical Information Service
5285 Port Royal Road
Springfield, VA 22100

Available electronically at http://gltrs.grc.nasa.gov

SUMMARY

Experimental results from testing the supersonic diffuser of a novel supersonic inlet model are presented. The patented inlet concept, called Two–Stage Supersonic Inlet (TSSI) incorporates a large cavity, or throat slot, in the supersonic diffuser to enhance the stability of the normal shock. The design flight Mach number of the inlet is 2.35, while the throat Mach number remains 1.30 during started operation.

The inlet model was mounted to a facility cold pipe which in turn was mounted to an existing facility sting. A facility gust generator plate was mounted above and forward of the model from the tunnel ceiling to reduce the inlet freestream Mach number for operation below Mach 2.0, which is the minimum test section Mach number of the tunnel. The test was conducted in NASA Lewis Research Center's 10– by 10–ft supersonic wind tunnel during the second quarter of 1994.

The model is a modification of an existing bifurcated inlet. A new supersonic section was built to represent the configuration evaluated analytically as a candidate concept for a High Speed Civil Transport. The subsonic section of the model consists of the original hardware. At the outset of the program it was known that the subsonic diffuser would introduce unrealistically high total pressure losses and would generate excessive distortion. It was felt that the supersonic section operating characteristics could be demonstrated adequately in spite of these shortcomings. The subsonic diffuser ducts were equipped with vortex generators to mitigate flow separation.

Three different vortex generator patterns were studied. Due to the poor subsonic diffuser, achieving an acceptable level of distortion was not possible with any of the vortex generator configurations. The lowest level of distortion was over 18% whereas a level on the order of 10% is considered acceptable. The measured total pressure losses in the subsonic diffuser were between 4% and 6%.

During the course of the testing an unusual "semi–started" mode of operation was encountered. The inlet was able to spill up to 30% of the captured airstream without fully expelling the normal shock. In this mode the total pressure recovery dropped approximately 6% without increasing distortion. Fully started inlet stability did not improve as the shock trap plenum doors were opened. This result was unexpected.

Dynamic instrumentation at the cowl lip station indicates the semi–start mode may in fact be a series of unstart/re–start cycles with frequency ranging from 0.2 to 20 Hz at an amplitude of 3 to 4 psi. The frequency of the unstart event could be controlled. It is unclear how this mode would effect an engine, however, since the effect depends on performance of the subsonic diffuser. It is reasonable to assume some effect would be realized. Total pressure measurements taken during the current test indicate an impact due to semi–start at about the same amplitude as the aerodynamic noise resulting from a poor subsonic diffuser design. Further investigation of this phenomenon is required before it is fully understood.

The supersonic and throat regions of the model incorporate boundary layer bleed to prevent flow separation in the extreme adverse pressure gradients typical of supersonic inlets. Excess bleed capacity is provided to compensate for possible inaccuracies in the analytical predictions. The porosity of the bleed plates was reduced in the test by filling rows of holes in order to determine the optimum bleed rates. The aim of the bleed optimization is high recovery with minimum bleed. A total of nine bleed configurations were tested.

CFD predictions using the PARC code compare well with experimentally measured surface static pressures and throat station and engine face recoveries. The PARC calculations use a constant mass flux across a smooth surface to model the bleed without taking into account roughness effects produced by the bleed. Thus the theoretical model requires less bleed to achieve a given recovery level.

The aft ramp leading edge is located in a region where several flow phenomena interact. A parametric study was conducted to optimize the geometry of this key component. The baseline leading edge was a 2:1 ellipse with the highlight located at the focus of the cowl compression waves. Alternate #1 was thicker than the baseline, #2 was located downstream of the baseline location, while #3 was designed with the highlight moved toward the plenum. Alternate #3 provides slightly better performance showing good recovery at the throat. Test results indicate that the shape of the aft ramp leading edge is less important than its location.

The Boeing supplied inlet control system was installed in a facility rack in the 10– by 10–foot supersonic wind tunnel control room. Two Brush recorders displayed control system dynamic data. A Motorola 68040 processor was used to implement the real time control laws. The compression ramps were remotely adjustable via hydraulic actuation. The ramp control scheme was found to be acceptable in that it was relatively straightforward to implement a control law which would maintain the ramps in a configuration appropriate to the prevailing inlet angle of sideslip and Mach number.

The bypass door loop never achieved satisfactory operation. Signal noise was found to be a severe limiting factor in all control loops evaluated. Rapid analysis of control system results was impeded by lack of supporting software.

Although the stability benefits propounded for the BTSSI inlet were not confirmed, the inlet proved to have the following potentially attractive features: it is virtually buzz free; unstart is much less violent than that of a conventional mixed compression inlet; and thus the external effects of unstart are much less significant than that of a conventional mixed compression inlet.

TABLE OF CONTENTS

LIST OF FIGURES

LIST OF TABLES

1. INTRODUCTION

This report presents a description of and the findings from wind tunnel testing of a novel supersonic diffuser. Section 2 describes the test model and instrumentation. Model variations to optimize diffuser performance are discussed in section 3. Measured steady state performance is presented in section 4. The model control system is described in section 5. In section 6 computational fluid dynamics (CFD) simulations of the model internal flowfield, including comparisons with experimental results are shown.

The project was a cooperative effort between the Boeing Commercial Airplane Group and NASA Lewis Research Center. Funding was provided by NASA under Phase I of the High Speed Research project via the Propulsion Airframe Integration Technology (PAIT) contract (NAS3–25963). The model was designed and fabricated by NASA with technical support from Boeing (Task 11). The test was conducted in Lewis's 10– by 10–ft supersonic wind tunnel by NASA personnel. On–site engineering support was provided by Boeing (Task 22).

The overall objective of the HSR inlet development effort is to develop supersonic inlet technology required for an economically viable and environmentally acceptable High Speed Civil Transport (HSCT). The specific objectives of Tasks 11 and 22 of the PAIT contract were to explore the performance potential of a novel supersonic diffuser.

Early in this effort a decision was made to modify an existing inlet model, using as much of the existing hardware as possible, to minimize costs. The net effect of this decision was an evaluation of the supersonic diffuser only. The resulting subsonic diffuser would not be suitable for evaluation.

The supersonic diffuser aerodynamic lines and bleed system were generated by Boeing using procedures and methods developed during the Supersonic Transport (SST) and Supersonic Cruise Research (SCR) programs. CFD analyses of the design were performed using the PARC Navier–Stokes code.

Preliminary design of the wind tunnel test model was performed at Boeing. Digital solid representations of the model components were generated with the CATIA CAD system used at Boeing. The drawing files were transferred to NASA electronically and were converted to the CADAM system used at Lewis. Detail design and fabrication of the model were accomplished by NASA.

Preparation of the test plan, instrumentation plan, and data processing requirements were joint efforts between Boeing and NASA. All of the facilities and operations duties were performed by NASA personnel. Engineering support of the wind tunnel experiments were shared between NASA and Boeing.

Joseph Wasserbauer and David Saunders were the NASA Technical Monitors for this project. In addition to reviewing the work performed by Boeing they made significant contributions to the design and testing phases.

2. APPARATUS

This section presents a description of the model and its installation, the control system and instrumentation for the BTSSI inlet.

2.1. MODEL DESCRIPTION

The model was a modification of the NASA 10 inch bifurcated inlet (8.961 in. wide by 6.923 in. high). An isometric cutaway view of the model with modified parts identified is shown in Figure 2–1. The modified parts are (1) the leading edge, (2) two cowl lip sections, one for each duct, (3) sidewalls, and (4) forward and aft ramps. The aft ramps translate and pivot while the forward ramps are flexed to provide isentropic compression on these ramps. Each ramp was remotely adjustable via hydraulic actuation, thus requiring 4 hydraulic cylinders and associated controls. The existing set of cowl aft bypass doors were used during the testing.

2.1.1. Supersonic Section

The supersonic section of the inlet was modified to the BTSSI configuration evaluated analytically in PAIT Tasks 1 and 2 of the PAIT contract. Modifications were made to the supersonic compression system and the boundary layer bleed system. A plenum/bypass system was added under the ramps.

2.1.1.1. Compression System

The supersonic compression system at Mach 2.35 (design Mach number) consists of a 5 degree oblique shock from the leading edge of the forward ramp followed by 7.3 degrees of isentropic compression focused on the cowl lip, a 7 degree oblique shock from the leading edge of the cowl lip followed by 9.9 degrees of isentropic compression focused on the aft ramp. This compression system results in a throat Mach number of 1.30. At off–design Mach numbers the amount of isentropic compression on the forward ramp and the strength of the cowl lip shock are decreased to maintain a throat Mach number of 1.30. Table 2–1 shows the design values for the compression system. The model was instrumented with three total pressure rakes (Fig. 2–8) at the throat of the inlet on the starboard side. The rakes were installed for all of the test.

2.1.1.2. Boundary Layer Bleed

The boundary layer bleed system was divided into three parts: (1) cowl bleed, (2) sidewall bleed, and (3) plenum bleed. The cowl and sidewall boundary layer was removed through a 26% porous plate (0.025 dia. holes at 90 degrees to the surface, see Fig. 2–3 for hole pattern) at the locations shown on Fig. 2–4. Boundary layer bleed analysis of the supersonic section of the inlet shows that a 26% porous plate will remove more than the required amount of the boundary layer to maintain attached flow through the normal shock, assuming choked flow through the bleed plate. Excess bleed capacity was provided to compensate for possible inaccuracies in the analytical predictions, and to accommodate possibly higher bleed requirements during angle of incidence operation. The porosity of the bleed plates was reduced by filling rows of holes during the performance optimization test series to determine the optimum bleed rates. The design bleed pattern developed from CFD analysis is shown in Fig. 2–5.

2.1.1.3. Shock Trap Plenum/Bypass System

The shock trap plenum/bypass system has three functions: (1) remove the boundary layer developed on the forward ramp, (2) stabilize the normal shock during subcritical operation, and (3) allow the inlet to be started/restarted without moving the ramp system. The boundary layer de-

veloped on the forward ramp was removed by bleeding nominally 2% of the inlet captured flow through the plenum/bypass doors at all supersonic Mach numbers. The inlet stability system controls the opening of the plenum/bypass doors to maintain the inlet in a started mode (normal shock inside lip) when the upstream or downstream throat conditions (throat Mach or corrected airflow) are changed a small amount. When the control system senses that the normal shock is moving forward, the plenum/bypass doors are opened to decrease the corrected airflow through the throat causing the normal shock to move aft (this feature requires an active inlet controller). The inlet can be started/restarted at all Mach number from 1.80 to 2.35 by cycling the plenum/bypass doors (the engine airflow plus subsonic bypass airflow needs to be near the design value). The port and starboard shock trap systems share a common plenum containing a partial splitter. The splitter reduces interaction between the port and starboard airflows in the plenum.

2.1.1.4. Sidewall Leading Edge

The baseline leading edge of the inlet sidewall starts at the beginning of the forward ramp and ends at the cowl lip of the inlet. An alternate leading edge was to be evaluated as part of the test; however the alternate leading edge was not tested. The alternate leading edge was to extend forward 0.40 inches and parallel to the baseline leading edge.

2.1.2. Subsonic Section

The subsonic section of the model, made up of the subsonic diffuser and bypass system was not modified from the original NASA 10 inch model.[1] The subsonic section of the model is not the configuration developed during the PAIT Tasks 1 & 2, however the existing parts were felt to be adequate to demonstrate the BTSSI supersonic section operating characteristics. The existing subsonic section is described below.

2.1.2.1. Subsonic Diffuser

The subsonic diffuser was formed by the sidewalls, cowl, and aft ramp between the supersonic section throat and the engine face. The sidewalls and cowl internal flow contours were not modified. The aft ramp was remade to fit the BTSSI supersonic section at the throat. The external surfaces of the sidewalls and cowl were modified to accommodate the shock trap plenum/bypass system.

2.1.2.2. Vortex Generators

The entrance to the port and starboard subsonic diffusers were equipped with vortex generators. The vortex generators were installed just down stream of the cowl and sidewall bleed plates (about one inch downstream of the inlet throat). The baseline configuration is shown in Fig. 3–36. There were eight pairs of vortex generators, two pairs on the cowl surface, two pairs on the aft ramp surface and one pair in each of the four corners.

2.1.2.3. Bypass System

The bypass system was an existing part of the original model. The system was not changed or modified for this configuration of the model. The bypass system has six openings in the outer cowling of the model. The openings end just forward of the engine face. The flow through the openings was controlled by fixed louvers. Four louver settings were available (closed, 5°, 10°, and 15°). Only the closed bypass system was used during the test.

2.1.2.4. Aft Ramp Leading Edge

The baseline leading edge of the aft ramp is a 2:1 ellipse, minor diameter 0.15 inches (ramp thickness). Three alternate leading edge shapes were fabricated for evaluation during the test. The aft ramp leading edge configurations are shown in Fig. 3–29.

2.1.3. Model Installation

The inlet model was mounted to a facility cold pipe which in turn was mounted to an existing facility sting. A facility gust generator plate was mounted above and forward of the model from the tunnel ceiling. The entire model installation is shown in Fig. 2–6.

2.1.4. Engine Simulation (Cold Pipe)

The facility cold pipe simulates the engine effects on the inlet airflow. The effects simulated are the engine face spinner and changes in engine corrected airflow. The change in engine corrected airflow are achieved by opening and closing the variable area exit plug at the end of the cold pipe. The cold pipe contains instrumentation to measure the airflow exhausting through the exit plug.

2.1.5. Inlet Mounting

The model was mounted to the existing cold pipe/sting adapter shown in Fig. 2–6. The sting adapter was mounted to the 10– by 10–ft. SWT sting support. During the test the model and sting adapter were rolled 90 degrees to obtain yaw data.

2.1.6. Wing Simulation

The 10– by 10–ft. SWT facility gust generator plate, see Fig. 2–6, was installed in the test section and used to reduce the inlet freestream Mach number from 2.0 to approximately 1.6. A determination of the local flow conditions under the gust generator plate at the various gust plate angles of attack was made using gust plate static and total pressure instrumentation.

2.2. INLET CONTROL SYSTEM

The BTSSI control system consists of a 19" rack mounted VME chassis installed in a facility rack in the 10– by 10–ft. SWT control room, a Sun workstation in the control room, and an IBM PC clone in the "wire room". Two brush recorders display control system dynamic data. The VME chassis contains a Motorola 68040 processor used to implement the real time control laws and appropriate analog I/O hardware. It also outputs analog voltages to the brush recorders for display. The 10– by 10–ft. SWT facility presents feedback data to the VME chassis in high level analog format and accepts high level analog outputs as commands to inlet surface servos and some facility controls. The Sun computer serves as the display and digital recording system for the VME chassis, and as the software development facility for the 68040. The Sun and the VME chassis are interconnected through Ethernet and RS 232 links. The IBM compatible PC serves as the interface between the optical shock sensor and the VME chassis and also serves to display shock sensor data. The system is described in detail in the BTSSI Interface Control Document (ICD).[2]

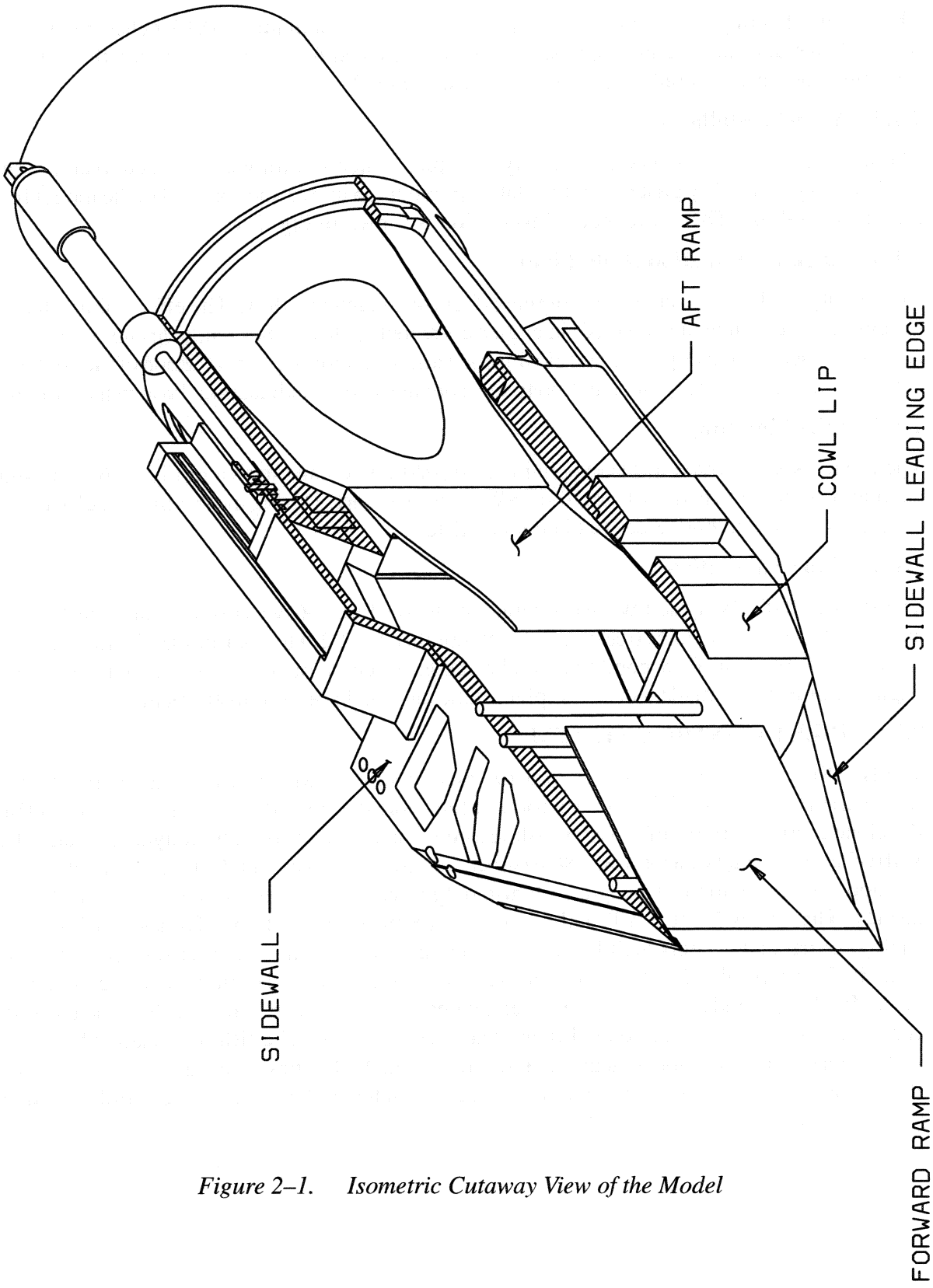

Figure 2–1. Isometric Cutaway View of the Model

Table 2–1. Compression System Schedule

Mach No.	Forward Ramp				Cowl		
	Fixed Ramp	Isen-tropic Ramp	Angle at end	Distance from Cowl Lip to Ramp*	Cowl Lip Shock	Isen-tropic Turning	Distance from Cowl to Aft Ramp**
2.35	5.00°	7.30°	12.32°	3.006	7.00°	9.90°	2.083
2.20	5.00°	5.40°	10.40°	3.201	5.10°	9.90°	2.314
2.00	5.00°	2.75°	7.75°	3.479	2.50°	9.90°	2.703
1.8	5.00°	0.00°	5.00°	3.761	–0.26°	9.90°	3.157
1.6	5.00°	0.00°	5.00°	3.761	–0.26°	9.90°	3.157

* normal to end of forward ramp

** normal to cowl to P_{SAR} 1,9,12,15,23,26

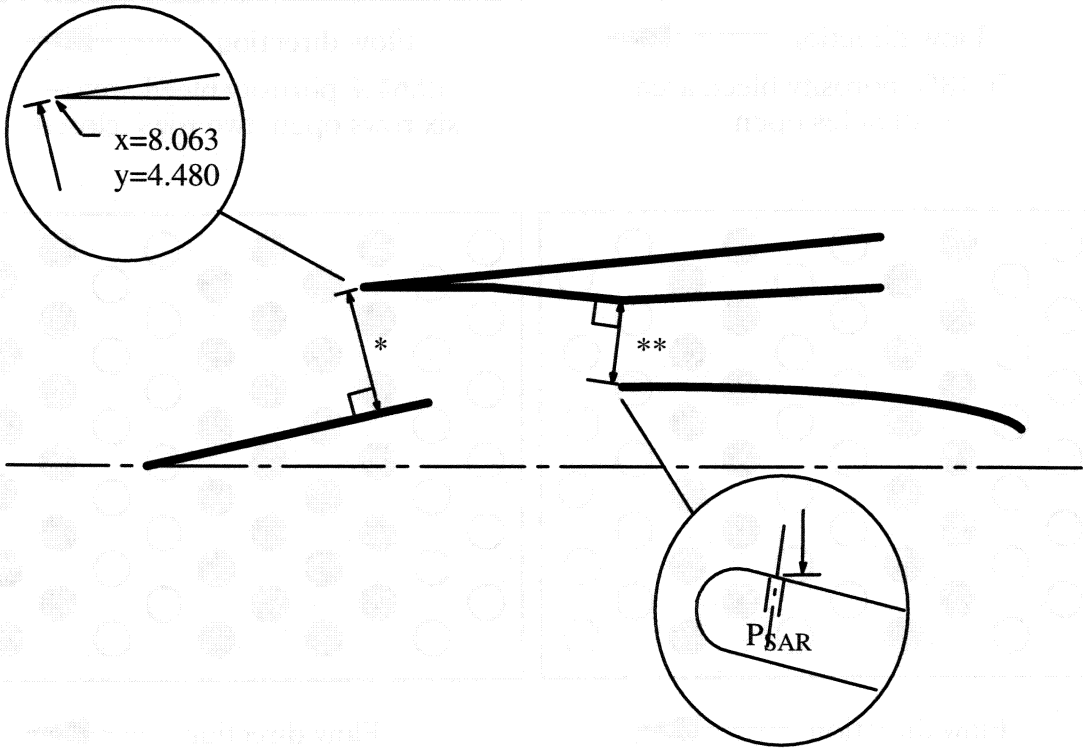

Figure 2–2. Schematic of Ramp Positioning Distances given in Table 2–1.

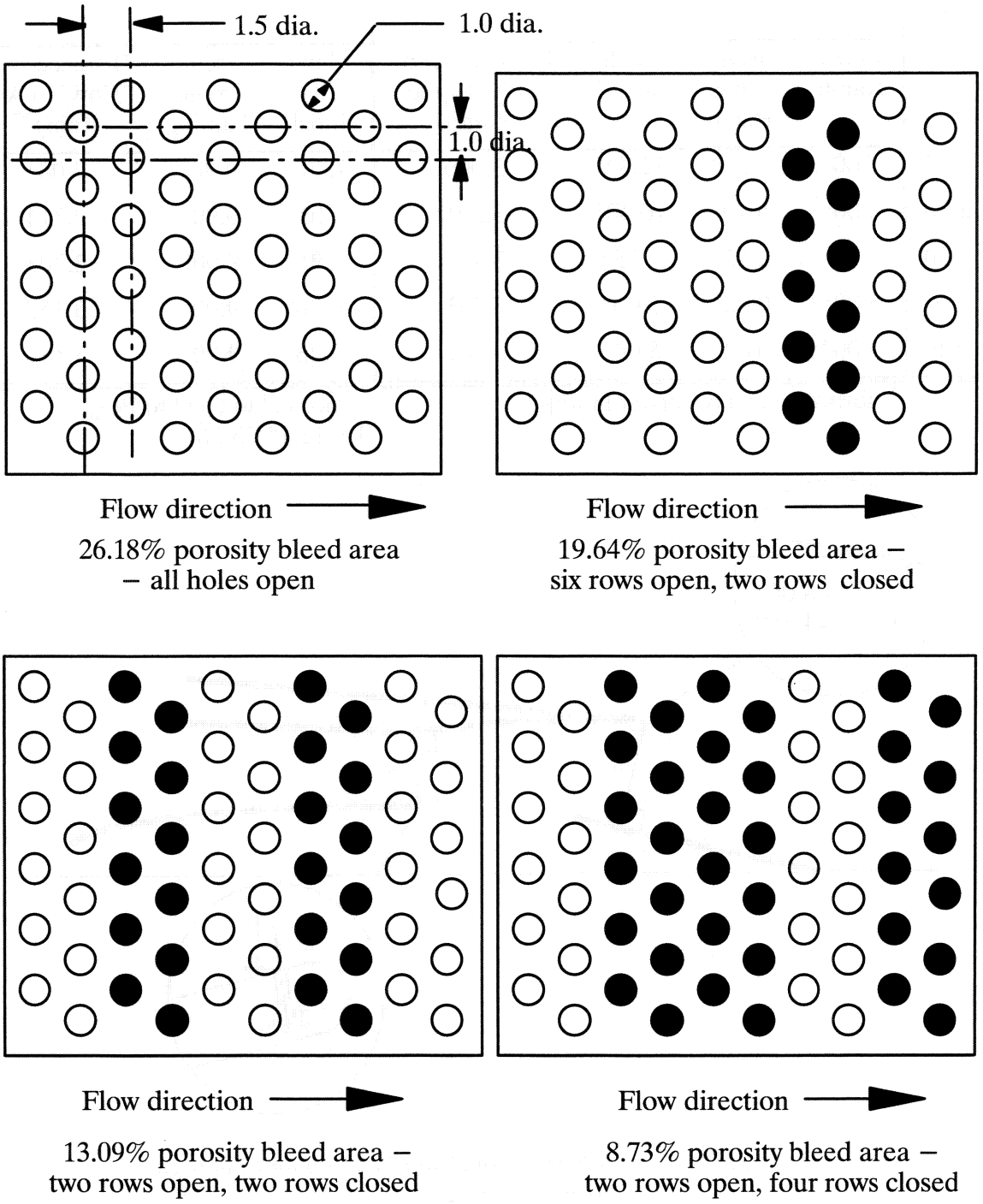

Figure 2–3. Bleed Hole Patterns

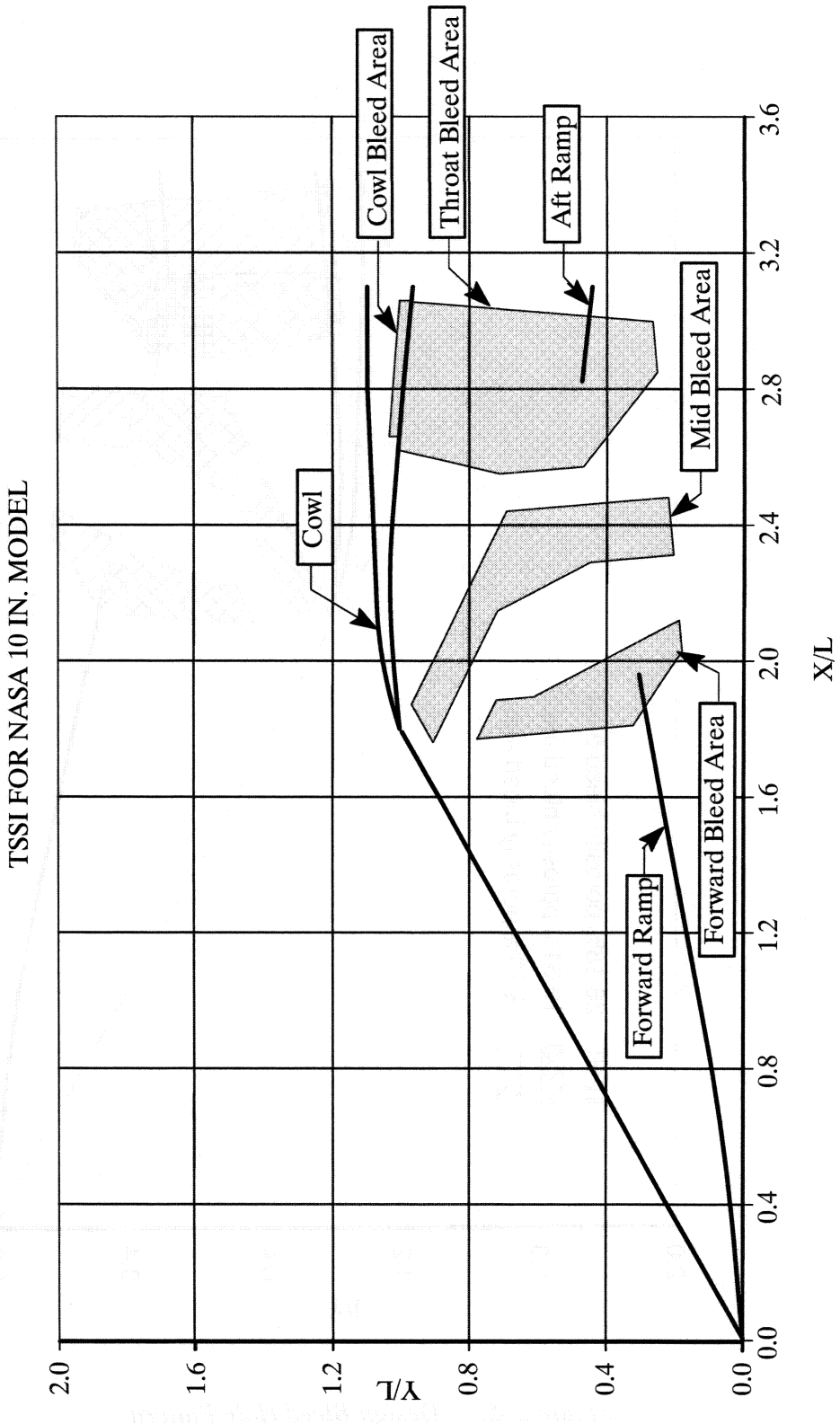

Figure 2–4. Boundary Layer Bleed Hole Locations

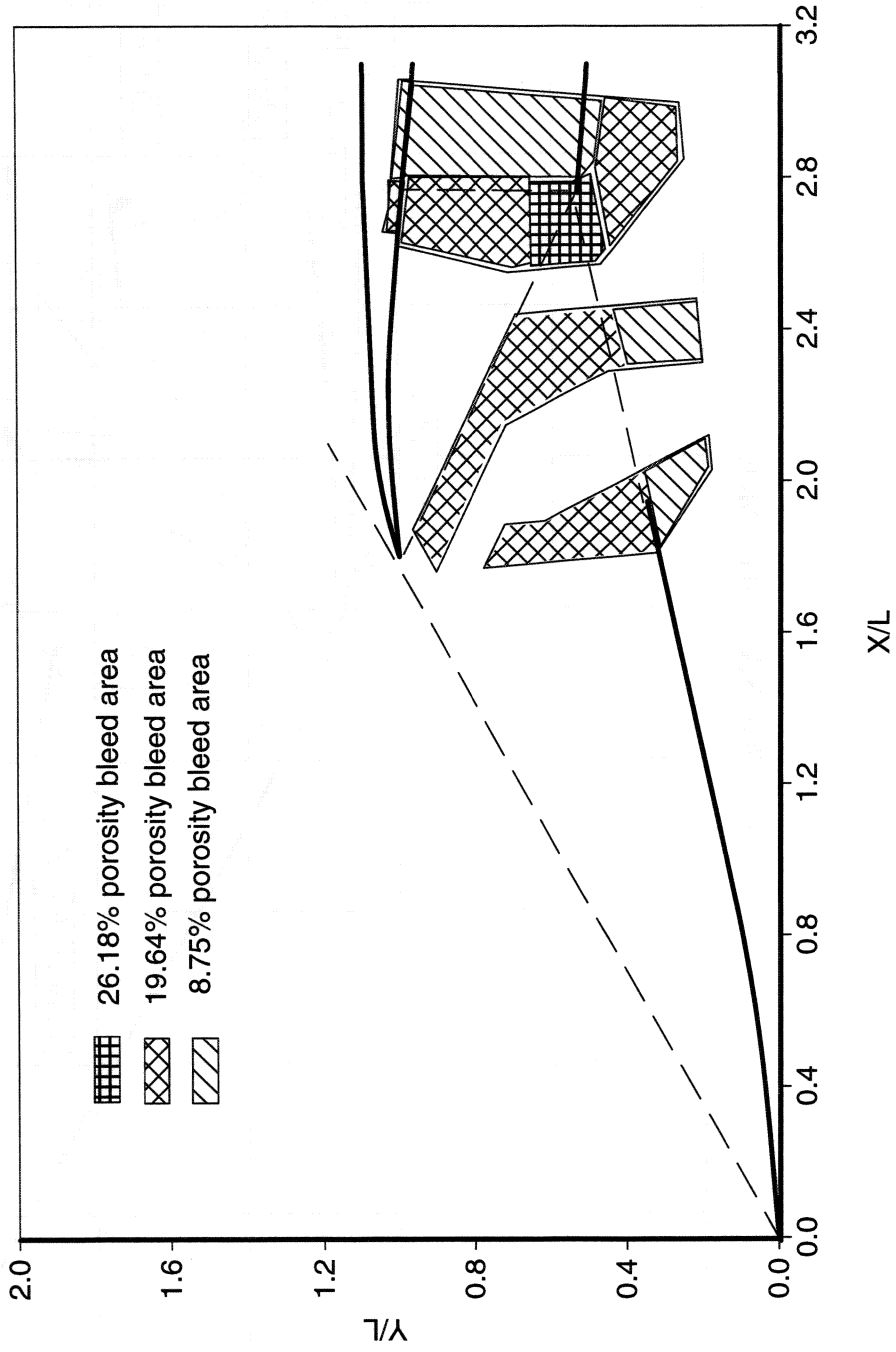

Figure 2–5. Design Bleed Hole Pattern

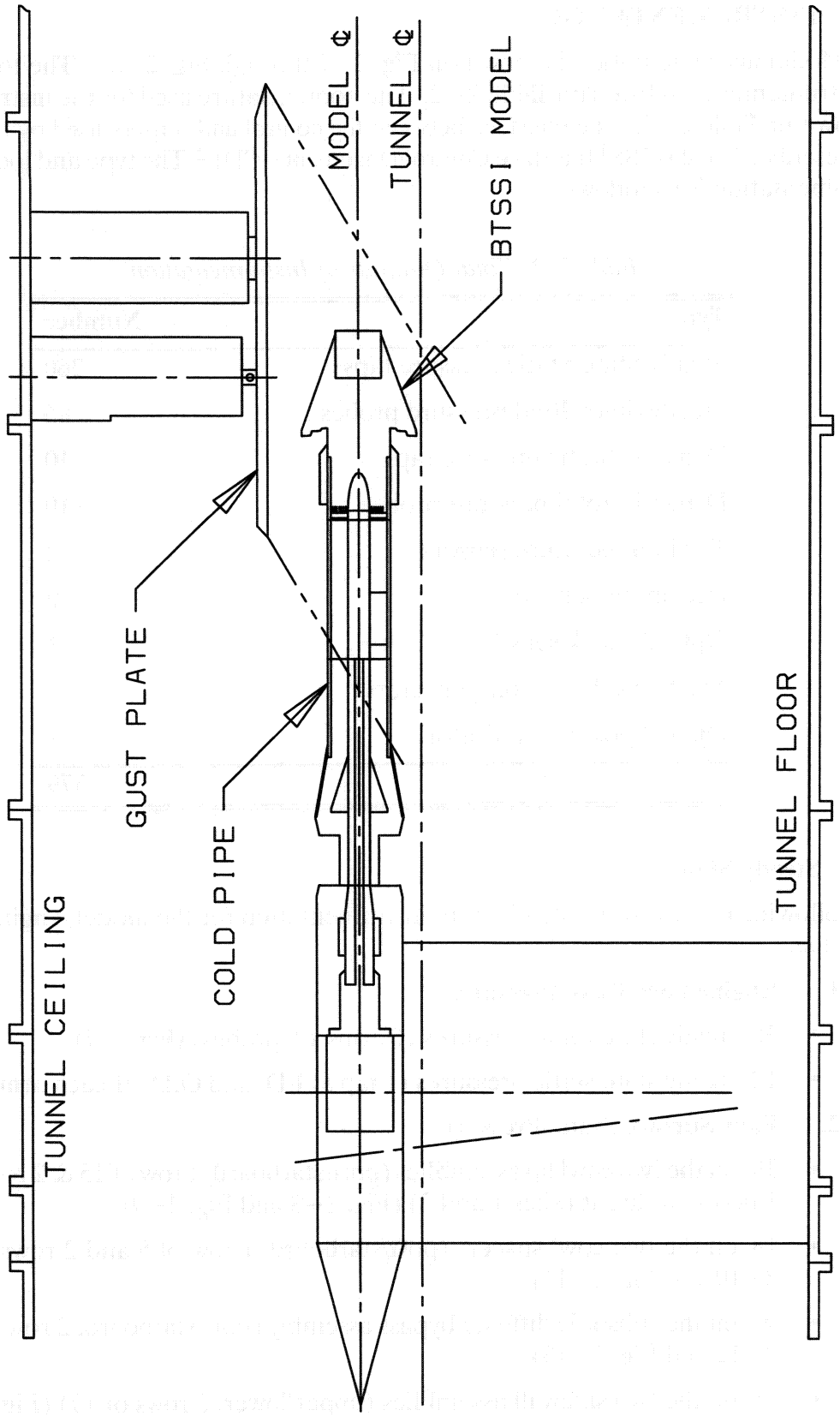

Figure 2–6. Model Installation

2.3. INSTRUMENTATION

The Model instrumentation is shown on Fig. 2−7 through Fig. 2−27. The total quantity of instrumentation is listed on Table 2−2. The nomenclature used for the instrumentation is shown in Table 2−3. The interface between the control and sensors used by the control is also described in the BTSSI Interface Control Document (ICD).[2] The type and location of the instrumentation is as follows:

Table 2–2. Total Quantity of Instrumentation

Type	Number
Steady State Static pressure taps	260
Steady State Total pressure probes	86
Dynamic Static pressure taps	10
Dynamic Total pressure probes	10
Total temperature sensors	2
Pneumatic sensors	2
Optical shock sensor	1
Mechanical position indicators	7
Optical position indicator	1
Total	379

2.3.1. Steady State

The following is a list of the steady state instrumentation for the model, engine face, and cold pipe.

2.3.1.1. Engine Face Rake Pressures

- 36 steady state total pressures (6 arms x 6 probes) (Fig. 2–7)
- 12 steady state static pressures (1 tap at I.D. and O.D. of each arm) (Fig. 2–7)

2.3.1.2. Flow Surface Static Pressures

- 39 on the two cowl lip assemblies (port/starboard, 1 row of 15 & 2 rows of 2 plus 1 between throat rakes 1 and 2) (Fig. 2−8 and Fig. 2−9)
- 18 on the two cowl spacers (port/starboard, 1 row of 5 and 2 rows of 2) (Fig. 2−10 and Fig. 2−11)
- 8 on the subsonic diffuser bypass assembly (port/starboard, 2 rows of 2) (Fig. 2−12 and Fig. 2−13)
- 68 on the two sidewall assemblies (upper/lower, 2 rows of 17) (Fig. 2−15 and Fig. 2−16)

- 18 on the forward ramp assembly (port/starboard, 3 rows of 3 on each ramp) (Fig. 2−17 and Fig. 2−18)
- 28 on the two aft ramp assemblies (port/starboard, 1 row of 8 & 2 rows of 3) (Fig. 2−19 and Fig. 2−20)
- 10 on the spinner/wedge (port/starboard, 1 rows of 1 and 2 rows of 2) (Fig. 2−21 and Fig. 2−22)

2.3.1.3. Boundary Layer Bleed Plenum Pressures

- 2 on the two cowl lip assemblies (Fig. 2−8 and Fig. 2−9)
- 12 on the two sidewall assemblies (1 static in each plenum (6)) (Fig. 2−15 and Fig. 2−16)

2.3.1.4. Throat Slot Bypass Plenum Pressures

- 4 static pressures in the plenum (1 on the sidewall and 1 in the forward frame of the (2) throat slot bypass systems) (Fig. 2−15, Fig. 2−16, Fig. 2−23 and Fig. 2−24)
- 2 total pressures in the plenum (1 in the forward frame of the (2) throat slot bypass systems) (Fig. 2−23 and Fig. 2−24)

2.3.1.5. Subsonic Diffuser Bypass Doors Pressures

- 4 total pressures in one bypass door section (Fig. 2−14)
- 23 static pressures in one bypass door plenum and on the four doors in that plenum (Fig. 2−14).

2.3.1.6. Exit Cover Pressures

- 8 static pressures (4 on sidewall covers, 2 on cowl covers, and 2 on throat slot bypass covers) (Fig. 2−25 and 2−26)
- 8 total pressures (4 on sidewall covers, 2 on cowl covers, and 2 on throat slot bypass covers) (Fig. 2−25 and 2−26)

2.3.1.7. Cold Pipe Flow Measurement Pressures

- 3 total pressures (Fig. 2−27)
- 6 static pressures (Fig. 2−27)
- 4 base static pressures (Fig. 2−27)

2.3.1.8. Flow Quality Pressure Rakes

- 7 one 7 probe total pressure boundary layer rake on cowl lip assembly (port) (Fig. 2−9)
- 7 one 7 probe total pressure boundary layer rake on sidewall assembly (upper/port) (Fig. 2−15)
- 18 Three 6 probe throat rakes on cowl lip assembly (starboard) (Fig. 2−8)
- 1 Static pressure between throat rakes 1 and 2 (Fig. 2−8)

- 1 A single total pressure probe will be installed if the three 6 probe rakes are removed from the cowl. The single probe will be at the same location as P_{TTC-1} (Fig. 2–8)

2.3.1.9. Temperature sensors

- 2 total temperature sensors (1 in each pneumatic shock sensor) (See note on Fig. 2–8 and Fig. 2–9)

2.3.1.10. Mechanical Position Indicators

- 1 engine airflow control plug (See note on Fig. 2–27)
- 2 throat slot bypass door (1 on each actuator) (Fig. 2–23 and Fig. 2–24)
- 2 forward ramp (1 on each actuator) (See note on Fig. 2–17 and Fig. 2–18)
- 2 aft ramp (1 on each actuator) (See note on Fig. 2–19 and Fig. 2–20)

2.3.2. Dynamic Pressures

The following is a list of the dynamic instrumentation for the model and engine face.

2.3.2.1. Engine Face Rake

- 8 dynamic total pressures (8 arms x 1 probe) mounted from O.D. (frequency response 1 to 2000 Hz. (see Fig. 2–7)
- 2 Dynamic static pressures mounted on the tip diameter. (frequency response 0 to 200 Hz) (Fig. 2–7)

2.3.2.2. Flow Surface Static Pressures

- 2 dynamic pressures on forward end of lip (one on each lip) (frequency response 0 to 200 Hz) (Fig. 2–8 and Fig. 2–9)
- 2 dynamic pressures at aft end forward ramp (one on each ramp) (frequency response 0 to 200 Hz) (Fig. 2–17 and Fig. 2–18)

2.3.2.3. Flow Quality Pressure Rakes

- 1 A single dynamic total pressure probe will be installed if the three 6 probe rakes are removed from the cowl. The single probe will be at the same location as P_{TTC-1} and will be co–located with P_{TTC-19} (Fig. 2–8)
- 1 A single dynamic total pressure probe will be co–located with P_{TBC-7} (Fig. 2–9)

2.3.2.4. Throat Slot Bypass Plenum Pressure

- 2 dynamic pressures (frequency response 0 to 200 Hz) (Fig. 2–15 and Fig. 2–16)

2.3.2.5. Normal Shock Position Sensors

- 2 pneumatic sensors, 10 static pressure taps manifolded together with a single dynamic pressure transducer (1 on each cowl lip assembly) (Fig. 2–8 and Fig. 2–9)

2.3.3. Optical Sensors

2.3.3.1. Normal Shock Position Sensor

- 1 optical sensors (starboard side of the sidewall assemblies) (See note on Fig. 2−15 and Fig. 2−16)

2.3.3.2. Optical Position Indicator

- 1 optical indicator (on the upper throat slot bypass door actuator) (Fig. 2−23)

2.3.4. Schlieren

- Facility system to observe external flow field of model

Table 2–3. Instrumentation Nomenclature and List

Type	Symbol	No.	Ref. Fig.	Name
Mechanical	XM_{FP}	1	2–27	Engine airflow control plug position sensor
	XM_{PAR}	2	2–19, 2–20	Aft ramp position sensor
	XM_{PFR}	2	2–17, 2–18	Forward ramp position sensor
	XM_{PTD}	2	2–23, 2–24	Throat slot bypass door position sensor
Optical	O_{NSS}	1	2–15, 2–16	Optical normal shock sensor
	O_{PTD}	1	2–23	Throat slot bypass door optical position sensor
Dynamic Pressure	RP_{DCL}	2	2–8, 2–9	Cowl Lip dynamic static pressure
	RP_{DFR}	2	2–15, 2–16 2–17, 2–18	Forward ramp / throat slot plenum delta dynamic static pressure
	RP_{DNS}	2	2–8, 2–9	Pneumatic normal shock sensor dynamic static pressure
	RP_{DSEF}	2	2–7	Engine face dynamic static pressure
	RP_{DTEF}	8	2–7	Engine face dynamic total pressure
	RP_{DTP}	2	2–15, 2–16	Throat slot plenum dynamic static pressure
	RP_{SCL}	2	2–8, 2–9	Cowl Lip dynamic static pressure
	RP_{TBC}	1	2–9	Cowl boundary layer rake dynamic total pressure
	RP_{TTC}	1	2–8	Cowl throat rake dynamic total pressure
Steady State Pressure	P_{BCP}	4	2–27	Cold pipe base static pressure
	P_{SAR}	28	2–19, 2–20	Aft ramp static pressure
	P_{SBD}	8	2–12, 2–13	Subsonic diffuser bypass static pressure
	P_{SCE}	2	2–25, 2–26	Cowl boundary layer bleed exit cover static pressure
	P_{SCL}	39	2–8, 2–9	Cowl lip static pressure
	P_{SCP}	2	2–8, 2–9	Cowl boundary layer bleed plenum static pressure
	P_{SCS}	18	2–10, 2–11	Cowl spacer static pressure

Table 2–3 Instrumentation Nomenclature and List (cont'd)

Type	Symbol	No.	Ref. Fig.	Name
Steady State Pressure	P_{SD}	23	2–14	Subsonic diffuser bypass door static pressure
	P_{SEF}	12	2–7	Engine face static pressure
	P_{SFR}	18	2–17, 2–18	Forward ramp static pressure
	P_{SFS}	6	2–27	Cold pipe duct static pressure
	P_{SSE}	4	2–25, 2–26	Sidewall boundary layer bleed exit static pressure
	P_{SSP}	12	2–15, 2–16	Sidewall boundary layer bleed plenum static pressure
	P_{SSR}	10	2–21, 2–22	Spinner/Wedge static pressure
	P_{SSW}	68	2–15, 2–16	Sidewall static pressure
	P_{STE}	2	2–25, 2–26	Throat slot bypass exit static pressure
	P_{STP}	4	2–15, 2–16 2–23, 2–24	Throat slot plenum static pressure
	P_{TBC}	7	2–9	Cowl boundary layer rake total pressure
	P_{TBS}	7	2–15	Sidewall boundary layer rake total pressure
	P_{TCE}	2	2–25, 2–26	Cowl boundary layer bleed exit total pressure
	P_{TDL}	4	2–14	Bypass door total pressure
	P_{TEF}	36	2–7	Engine face total pressure
	P_{TFS}	3	2–27	Cold pipe duct total pressure
	P_{TSE}	4	2–25, 2–26	Sidewall boundary layer bleed exit total pressure
	P_{TTC}	19	2–8	Cowl throat rake total pressure
	P_{TTE}	2	2–25, 2–26	Throat slot bypass exit total pressure
	P_{TTP}	2	2–23, 2–24	Throat slot plenum total pressure
Temperature	T_{TPS}	2	2–8, 2–9	Pneumatic normal shock sensor total temperature

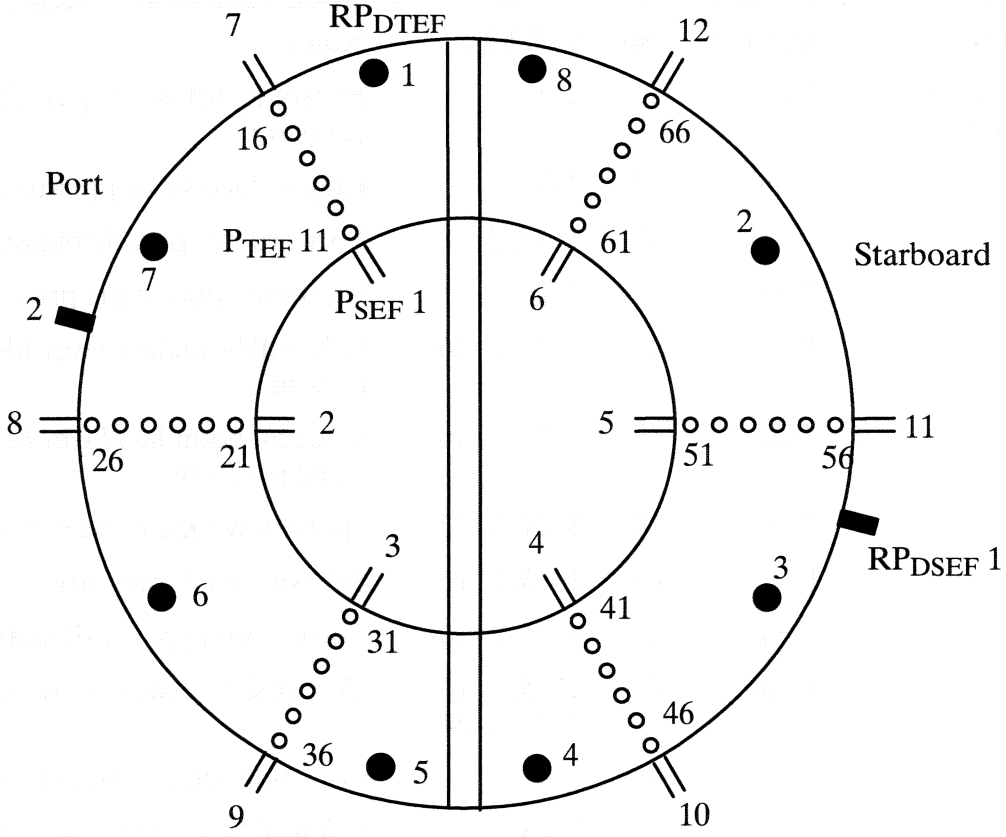

Instrumentation:			Priority
||	12	Static pressure tap	1
o	36	Steady State Total Pressure Probe	1
▮	2	Dynamic Static Pressure Tap	1
●	8	Dynamic Total Pressure Probe	1

Note:

XM_{FP}	1	Engine airflow control plug position	1

Figure 2–7. Engine Face Rake Instrumentation

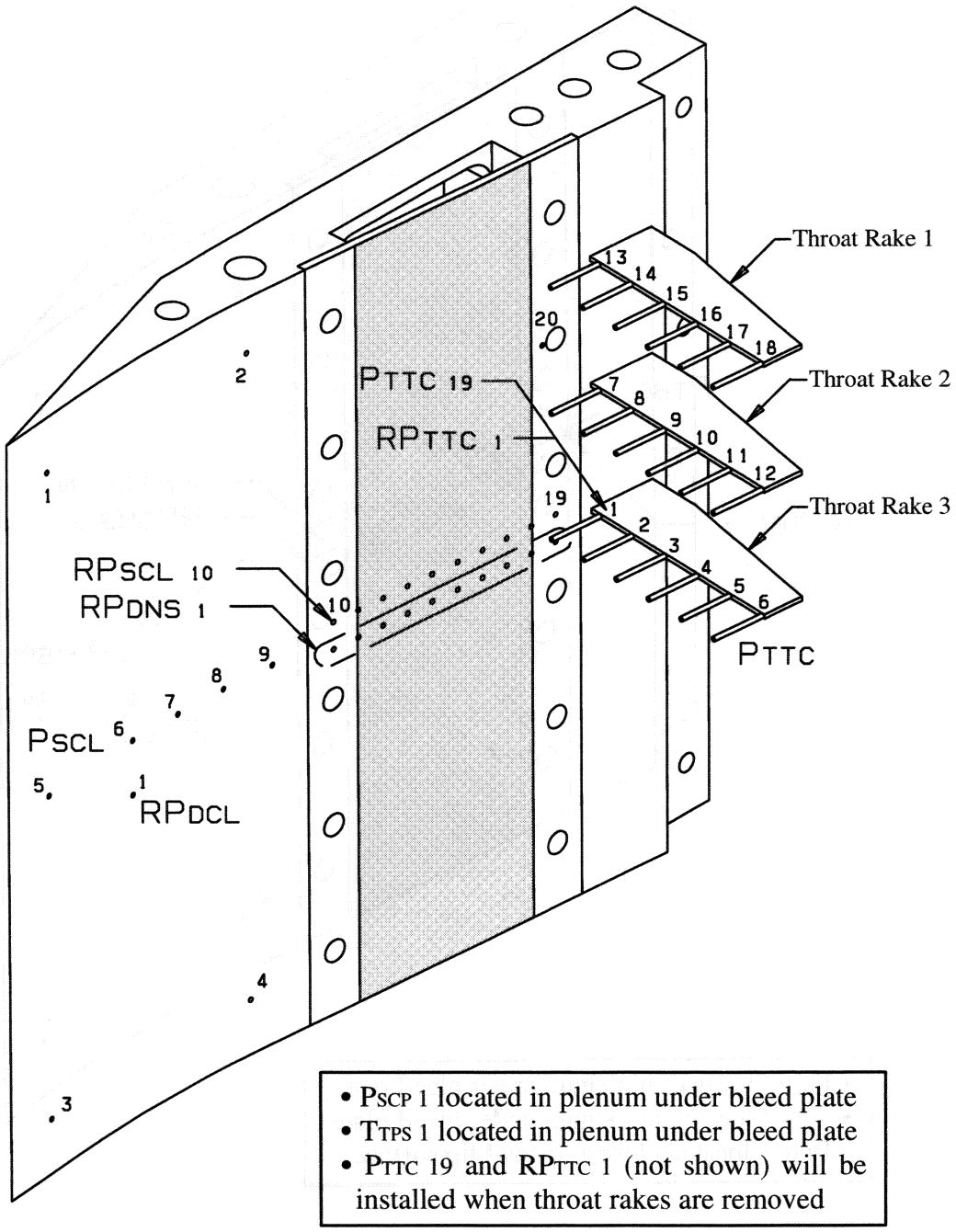

Figure 2–8. Cowl Lip Instrumentation (starboard)

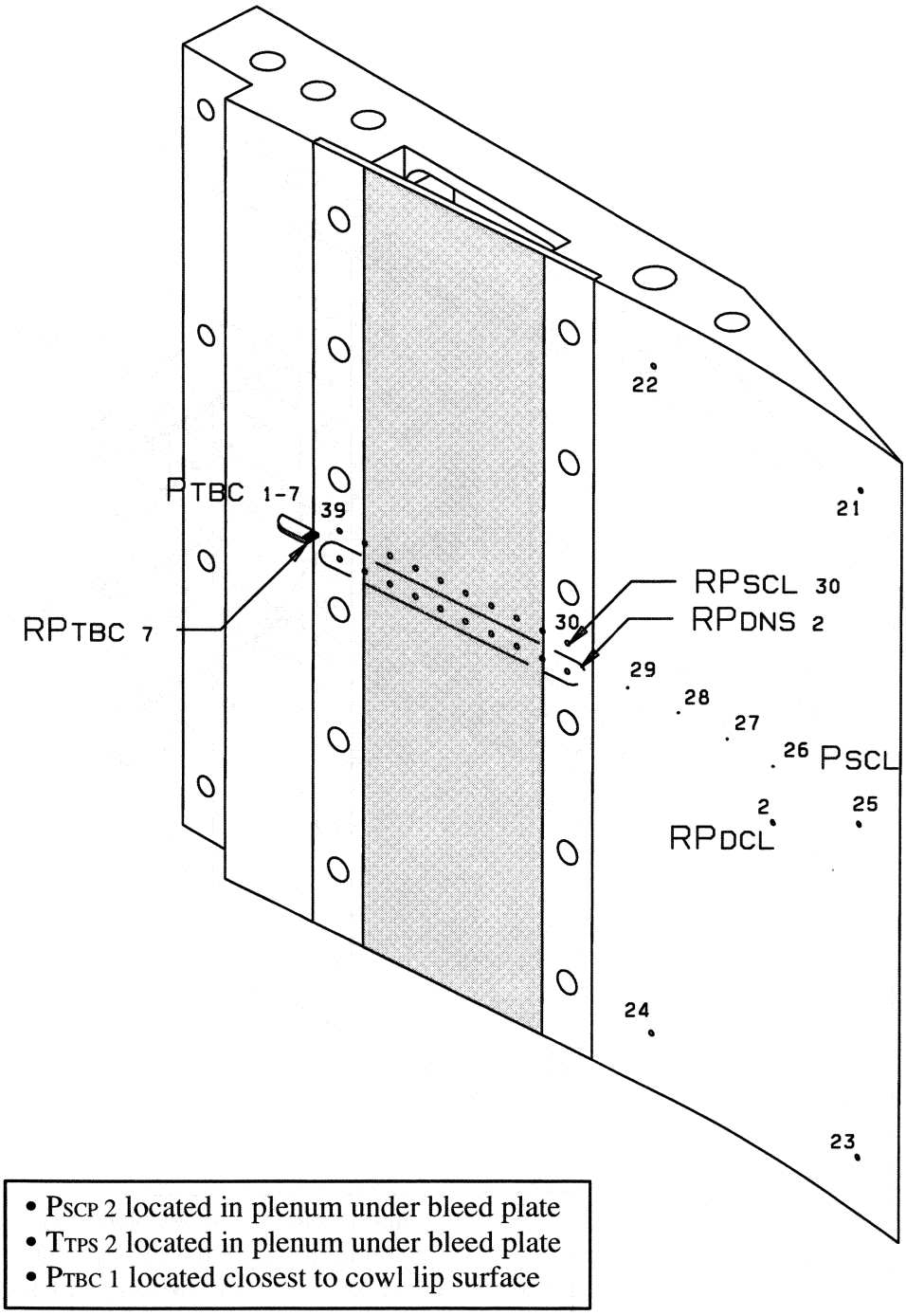

Figure 2–9. Cowl Lip Instrumentation (port)

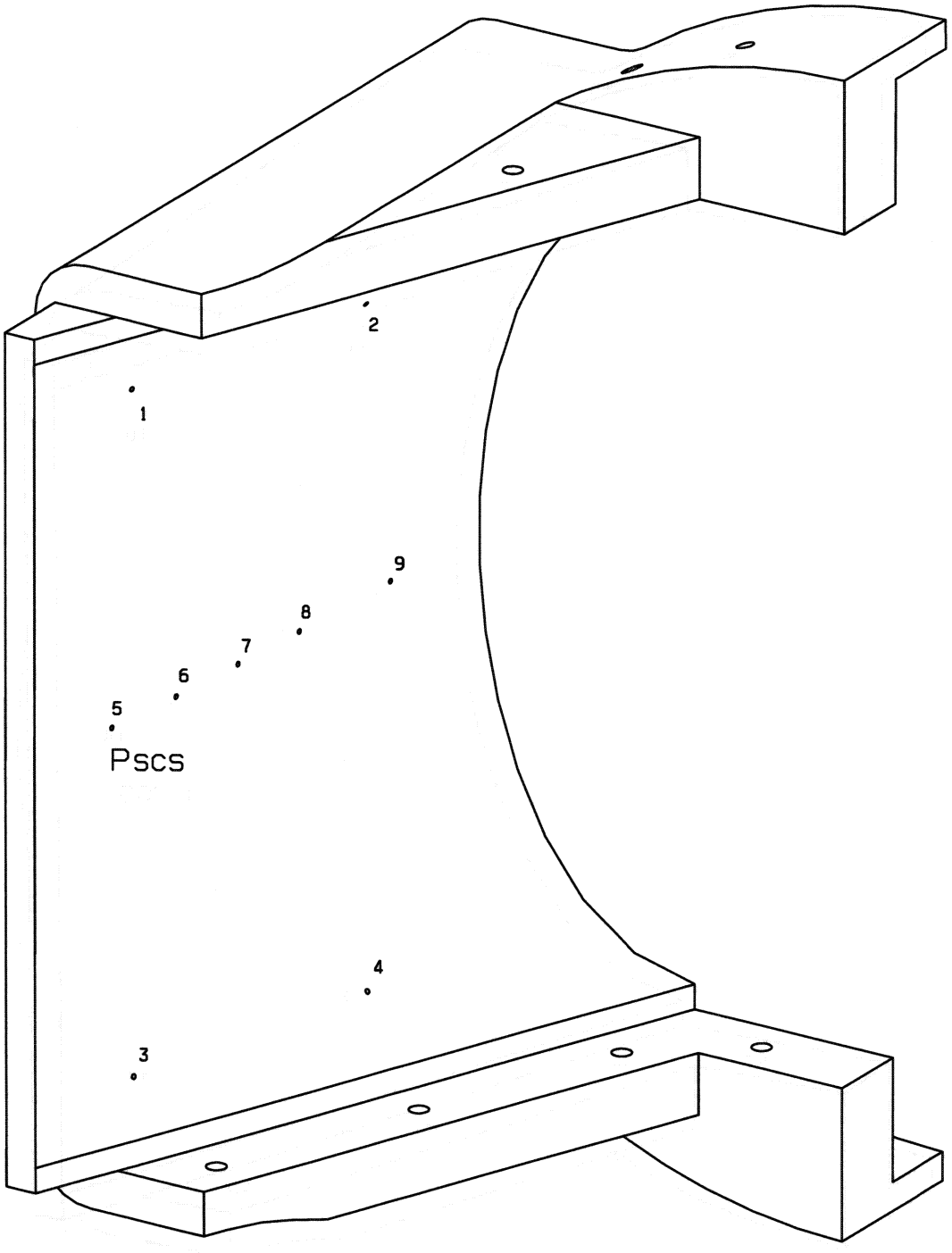

Figure 2–10. Cowl Spacer Instrumentation (starboard)

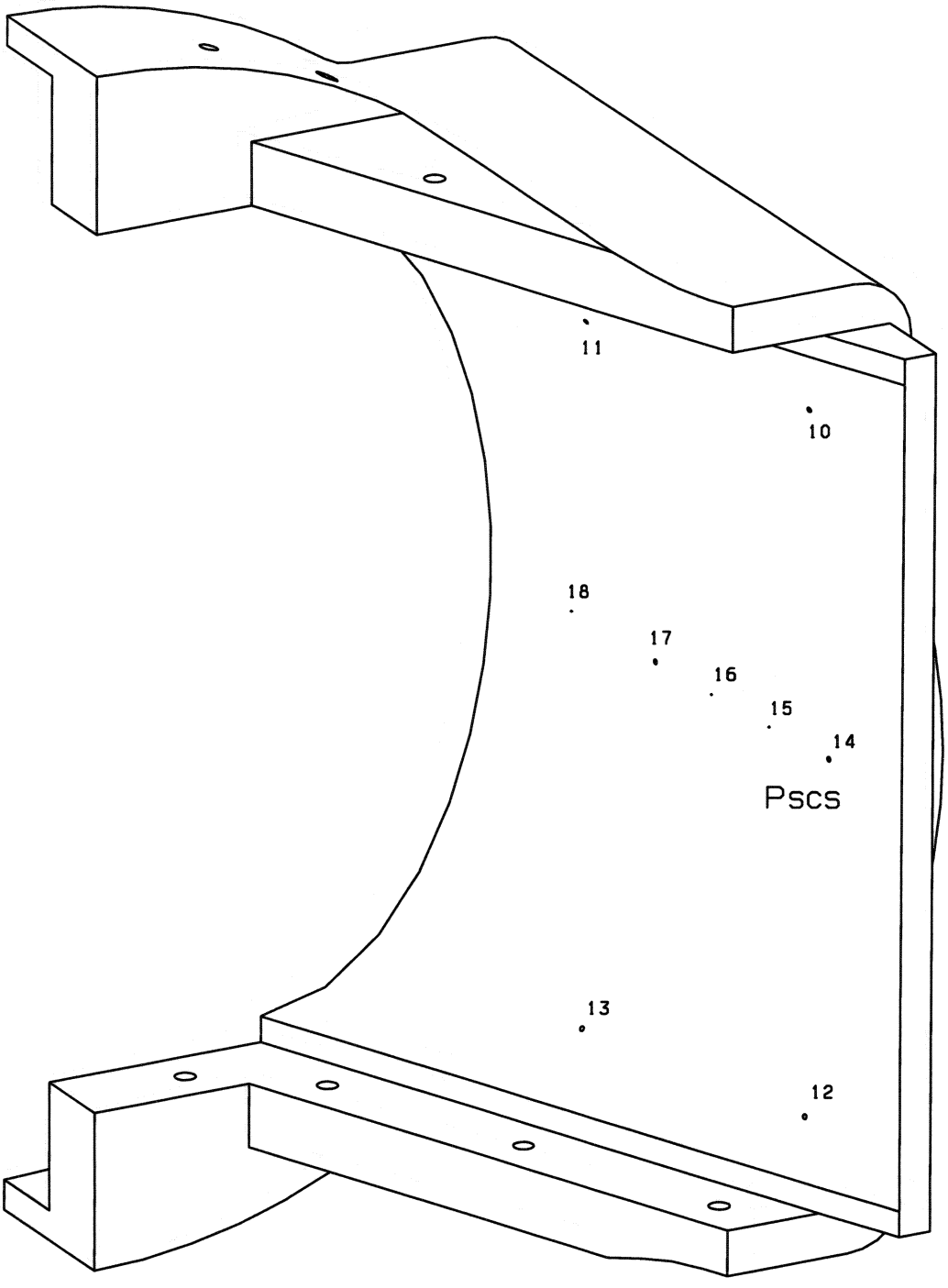

Figure 2–11. Cowl Spacer Instrumentation (port)

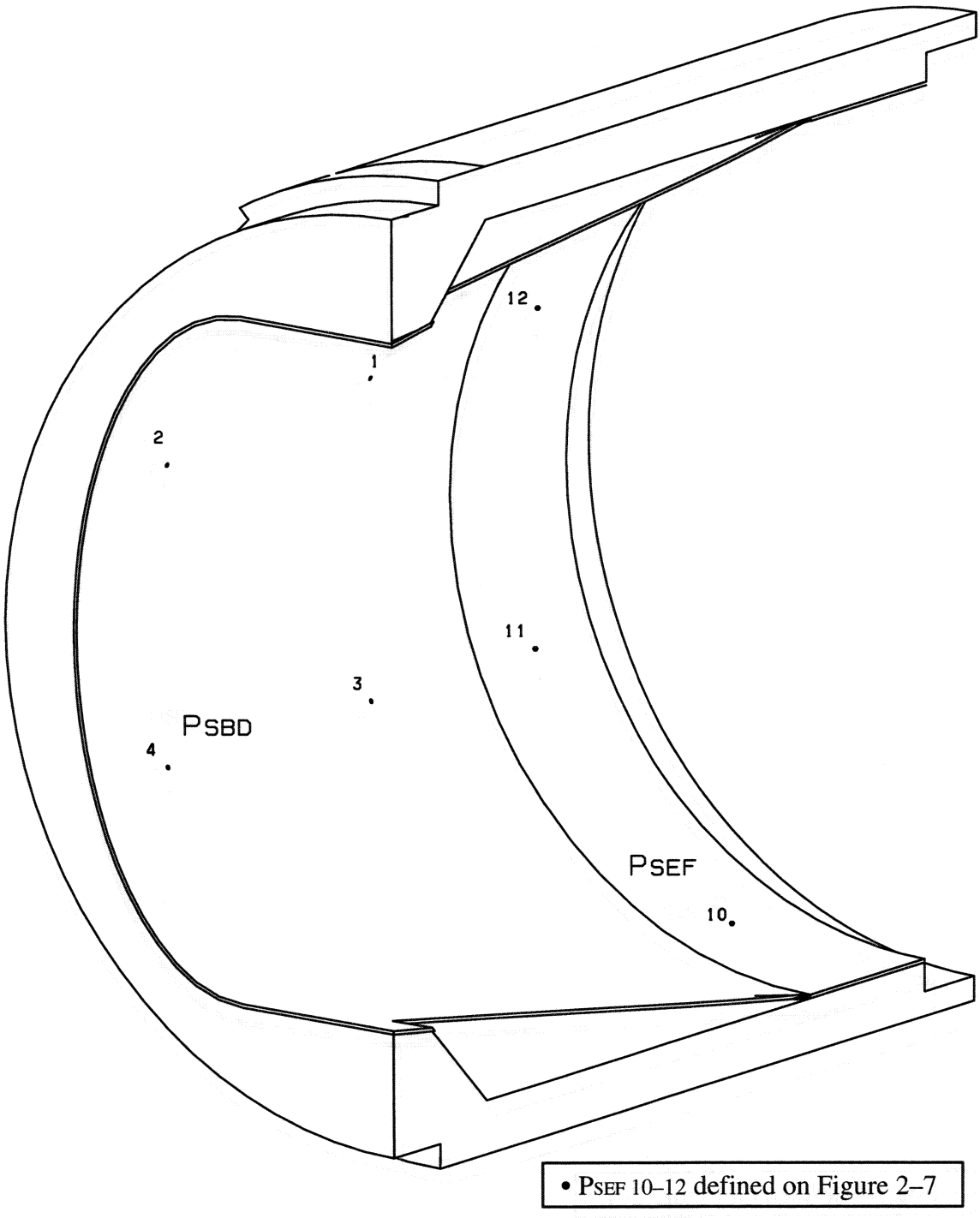

Figure 2–12. Main Bypass Instrumentation (starboard)

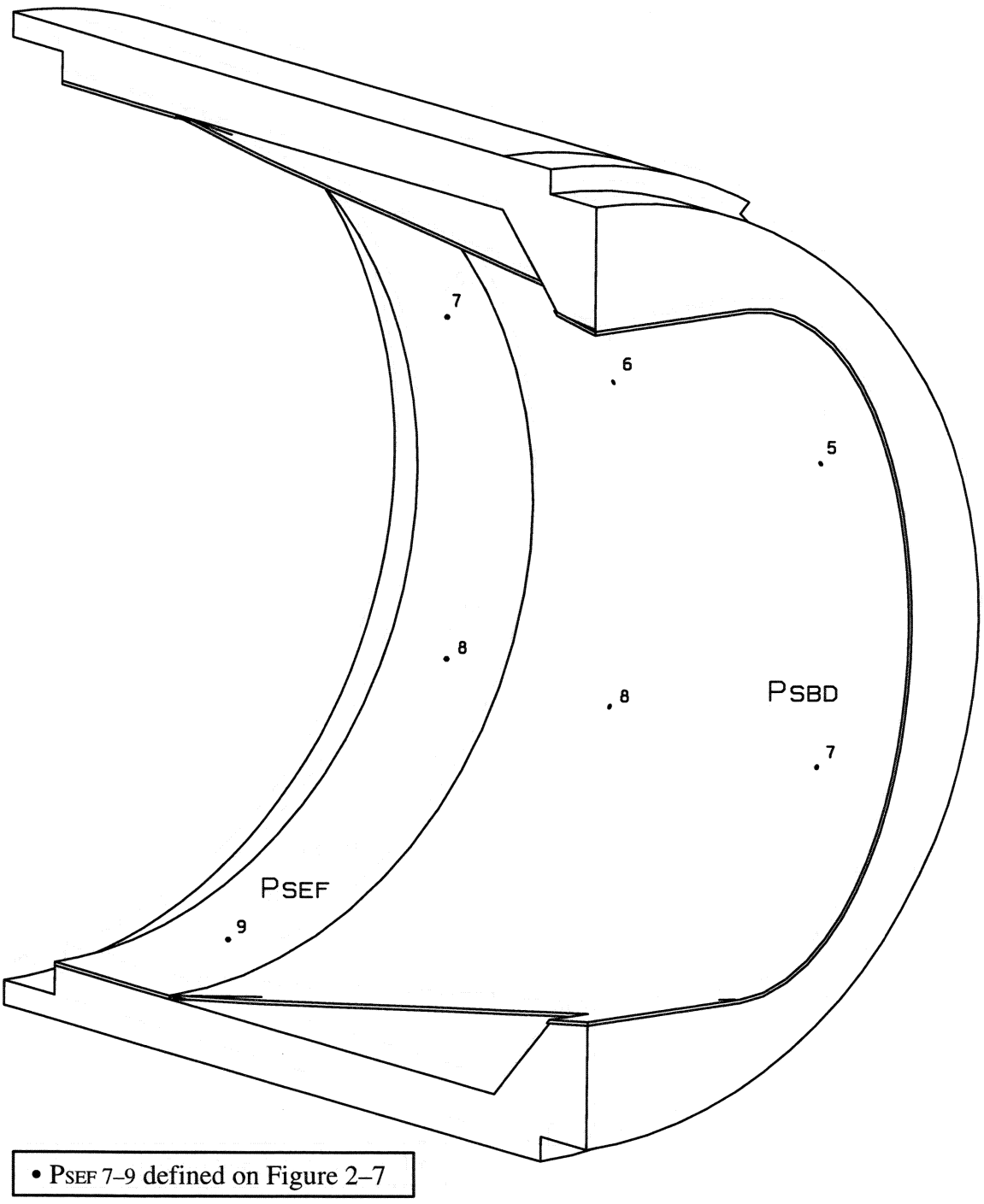

Figure 2–13. Main Bypass Instrumentation (port)

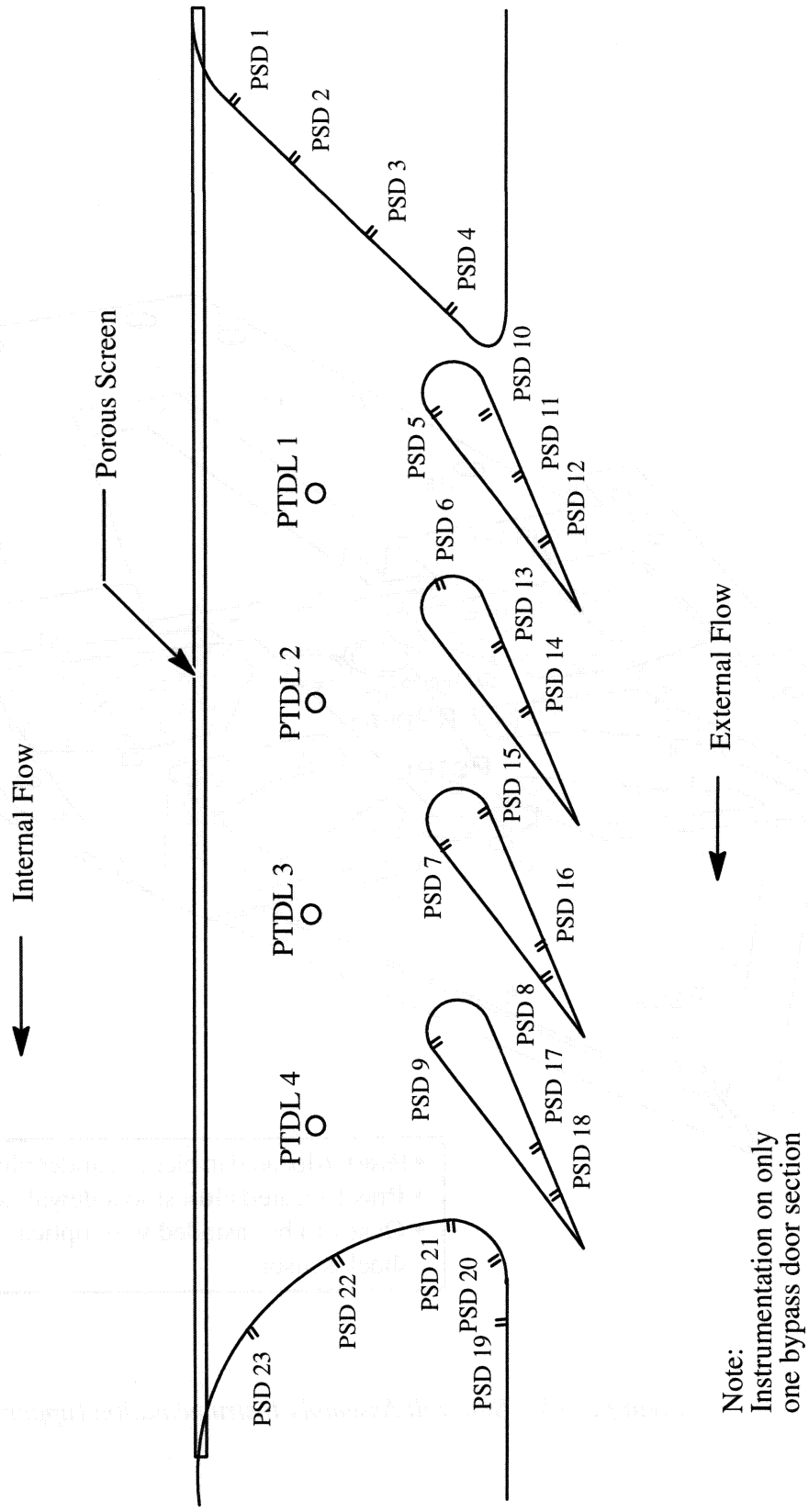

Figure 2–14. Bypass Door Instrumentation

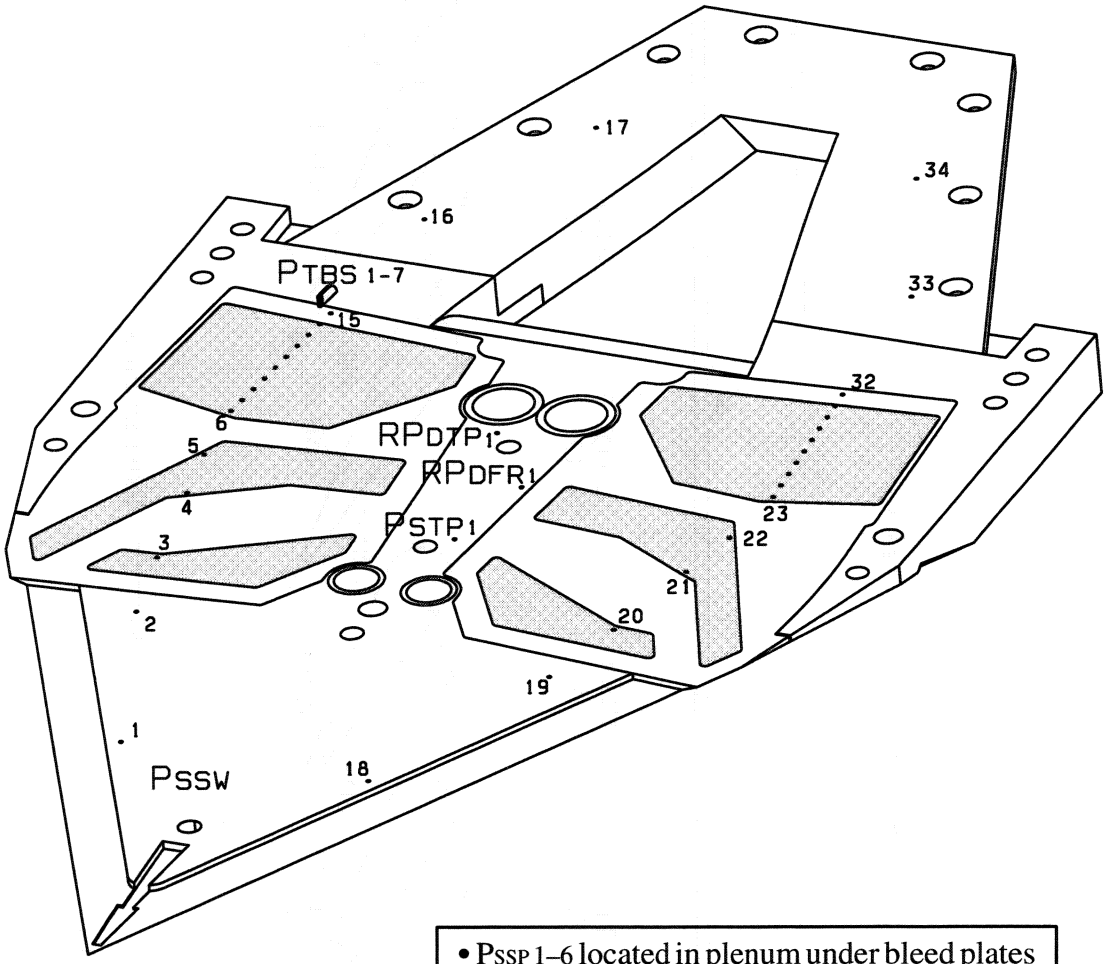

Figure 2–15. Sidewall Assembly Instrumentation (upper)

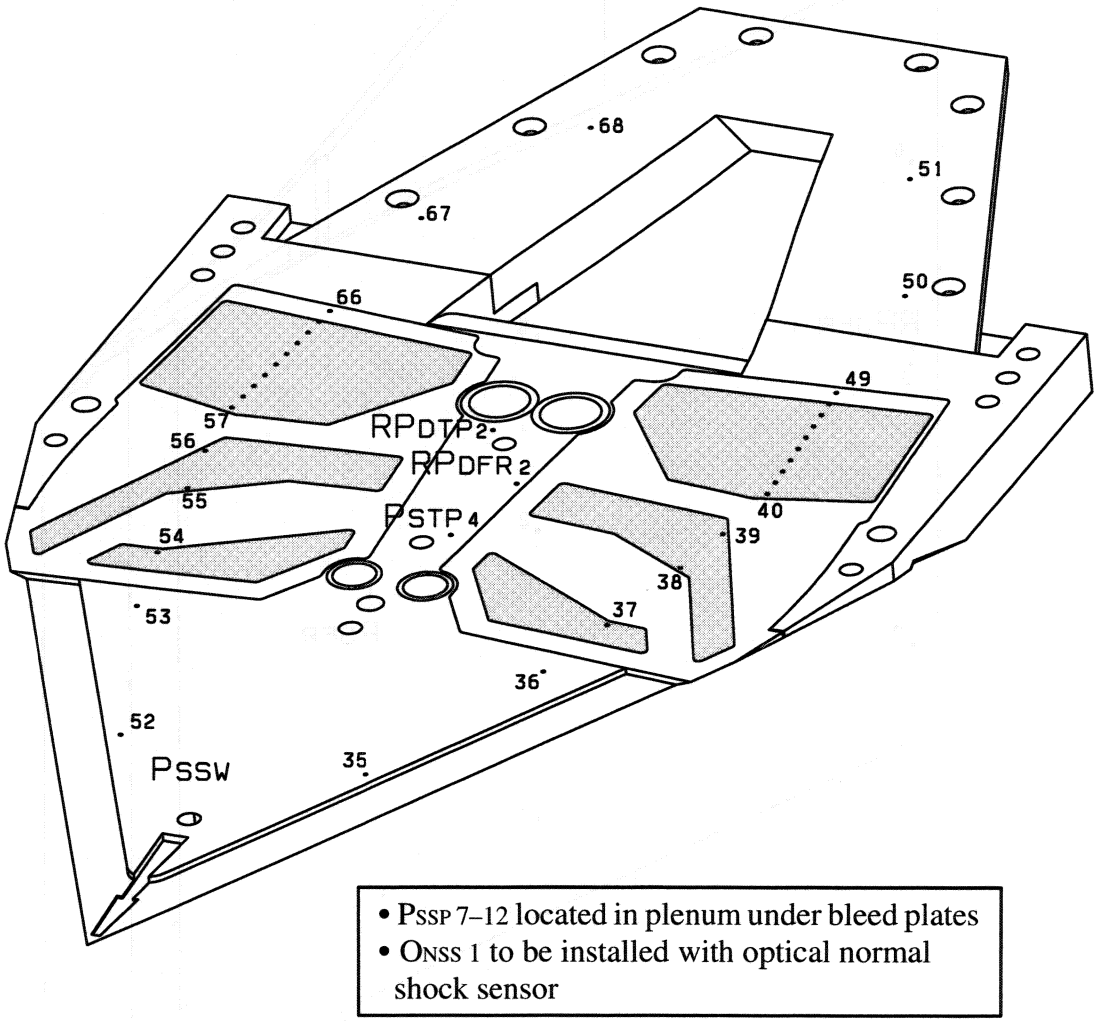

Figure 2–16. Sidewall Assembly Instrumentation (lower)

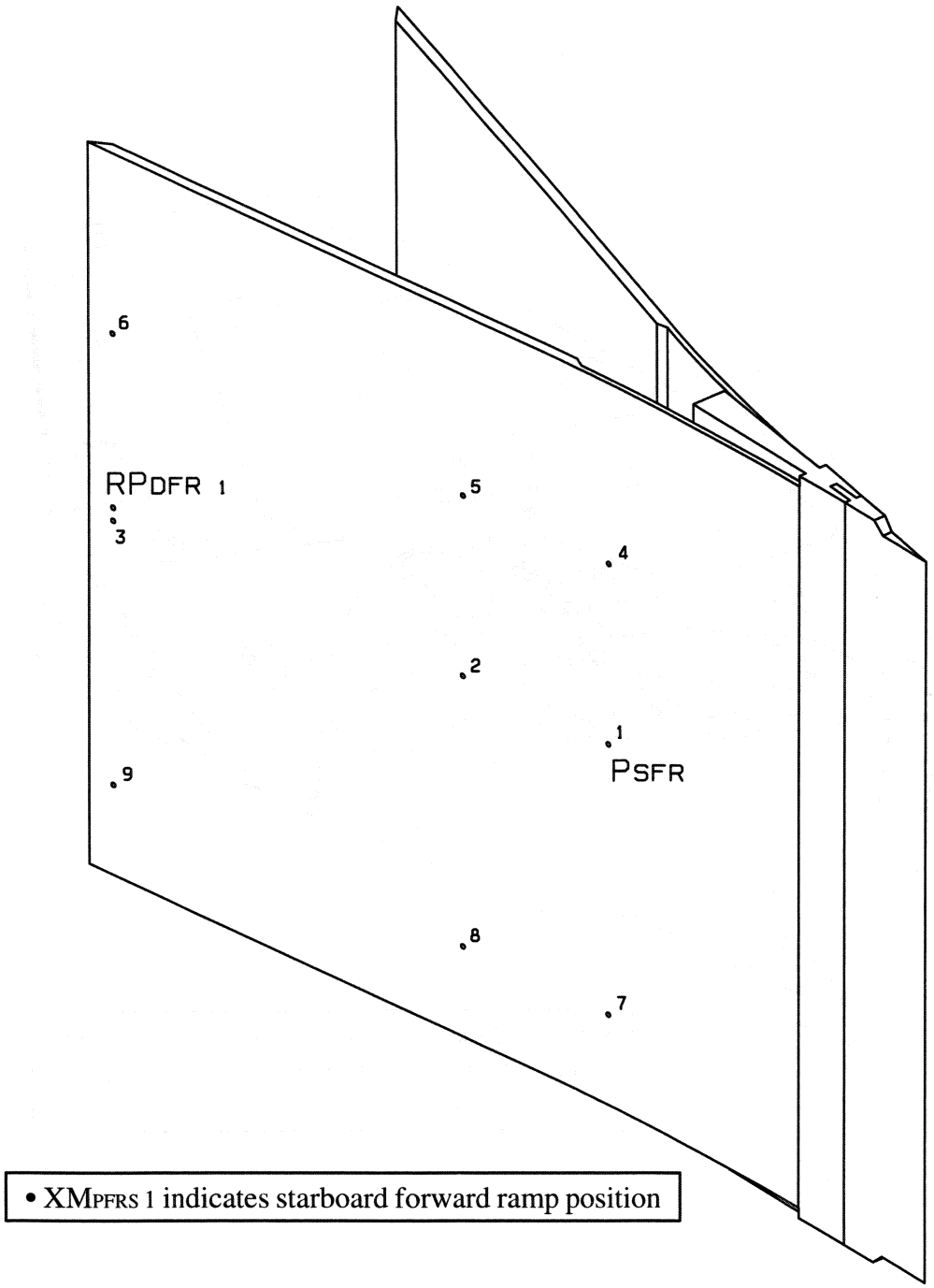

Figure 2–17. Forward Ramp Instrumentation (starboard)

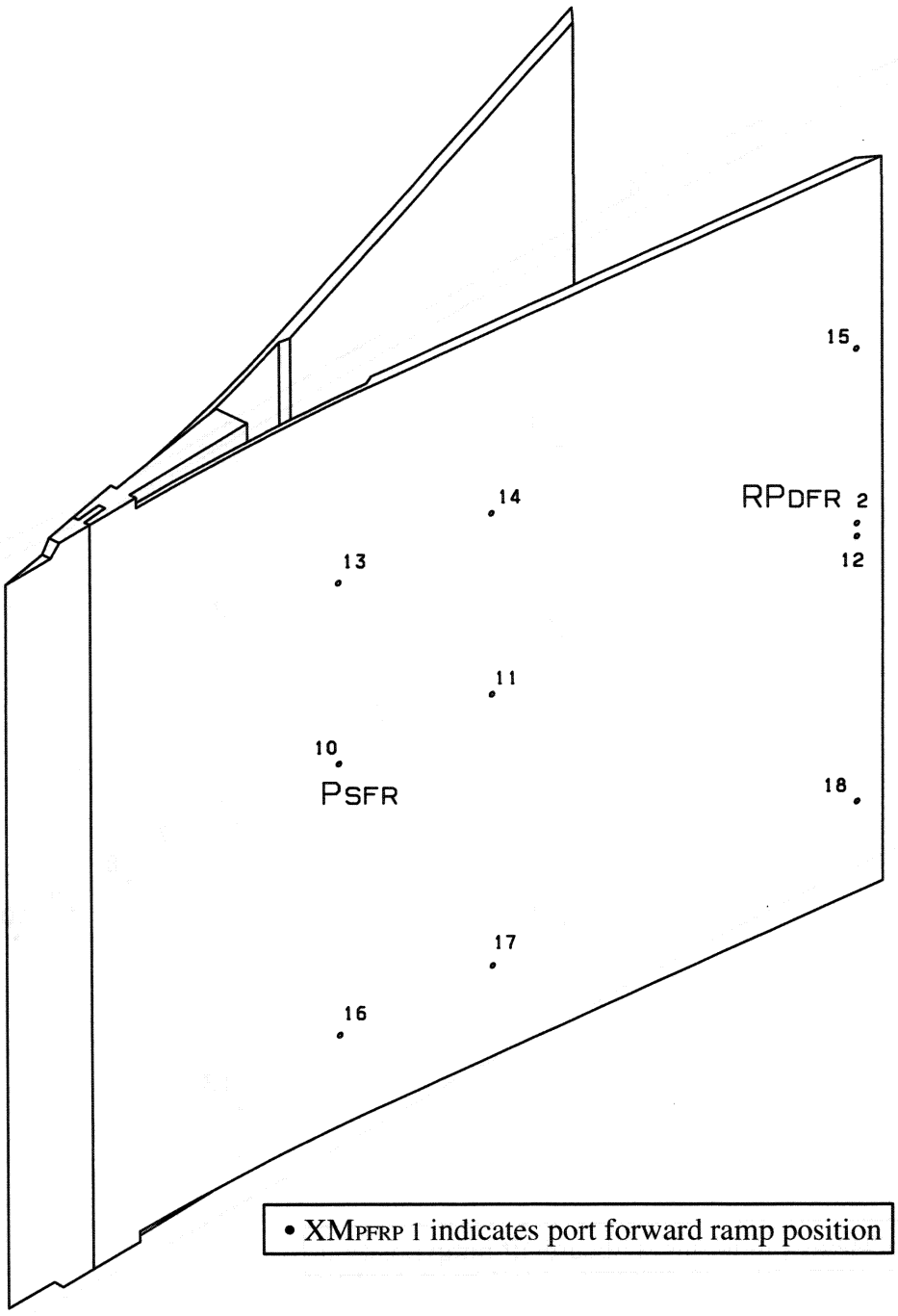

Figure 2–18. Forward Ramp Instrumentation (port)

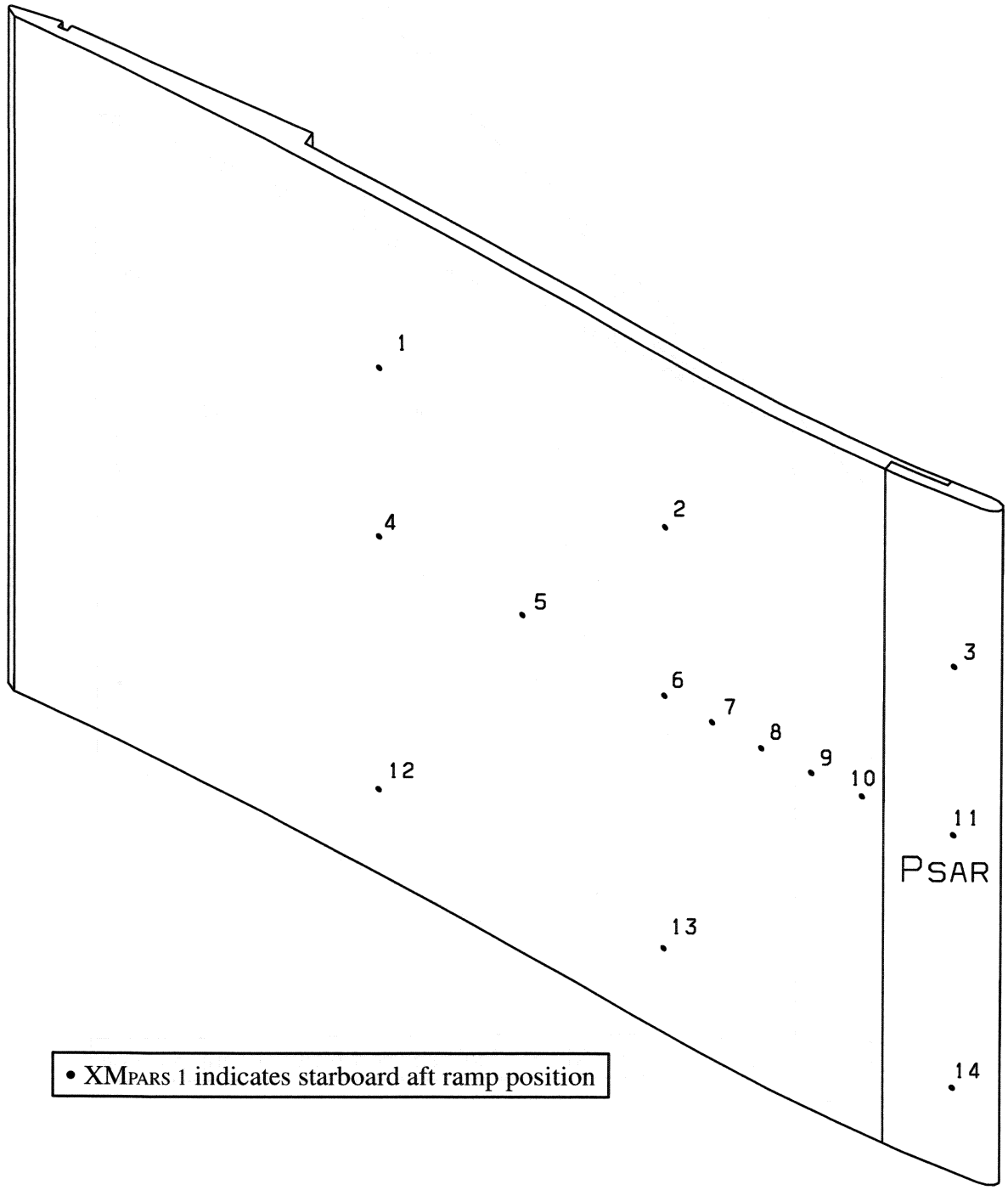

Figure 2–19. Aft Ramp Assembly Instrumentation (starboard)

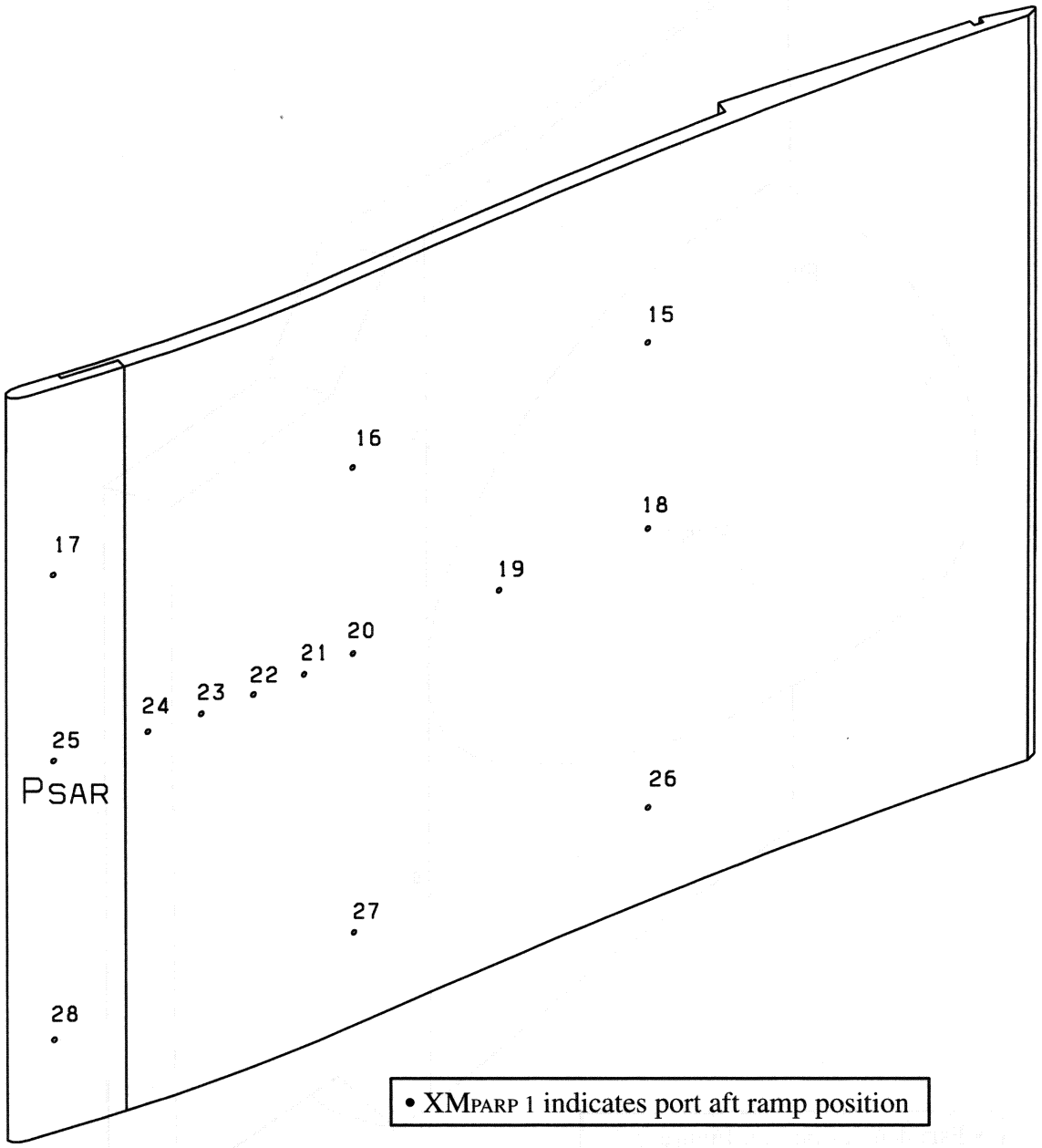

Figure 2–20. Aft Ramp Assembly Instrumentation (port)

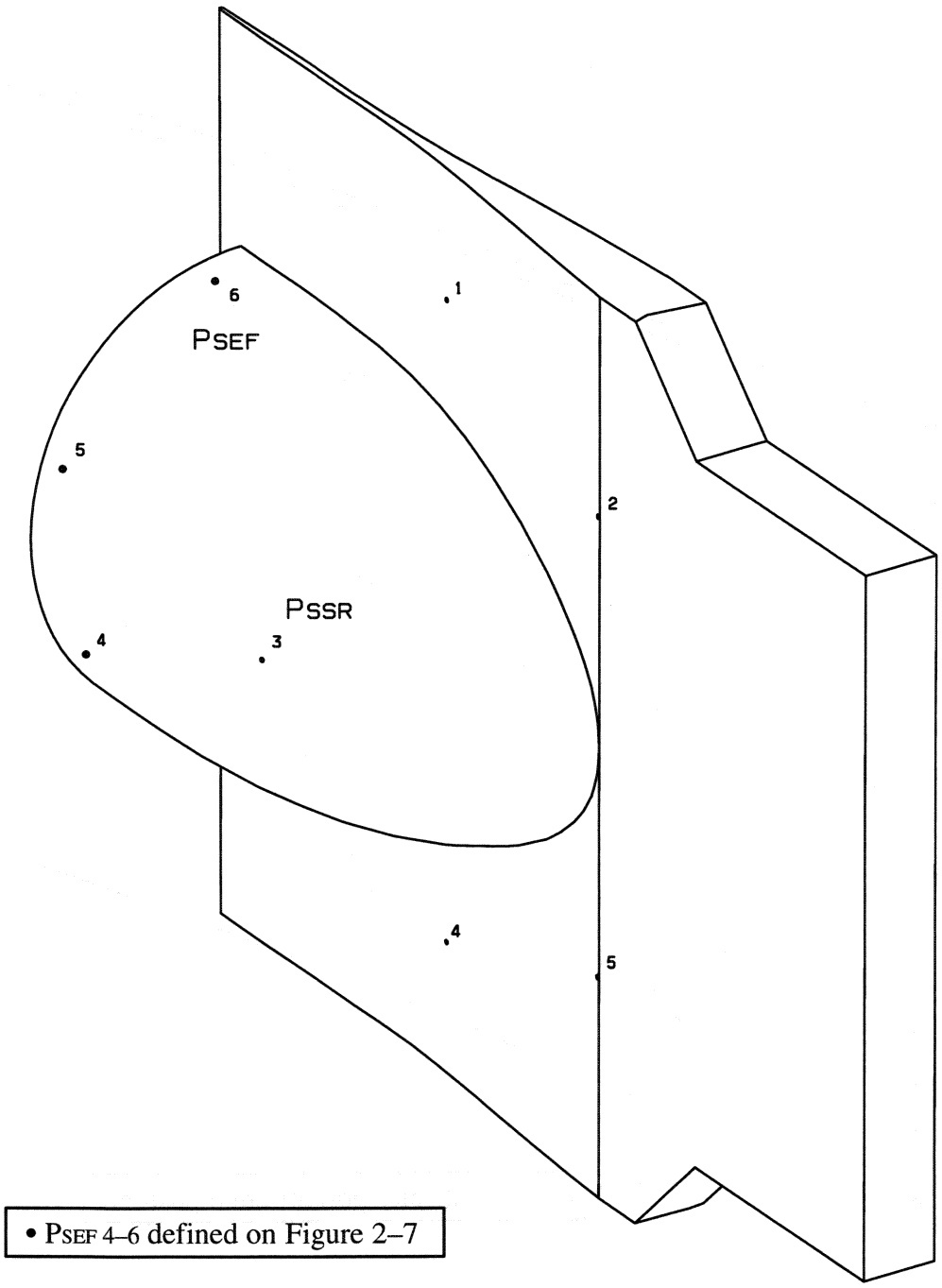

Figure 2–21. Spinner/Wedge Instrumentation (starboard)

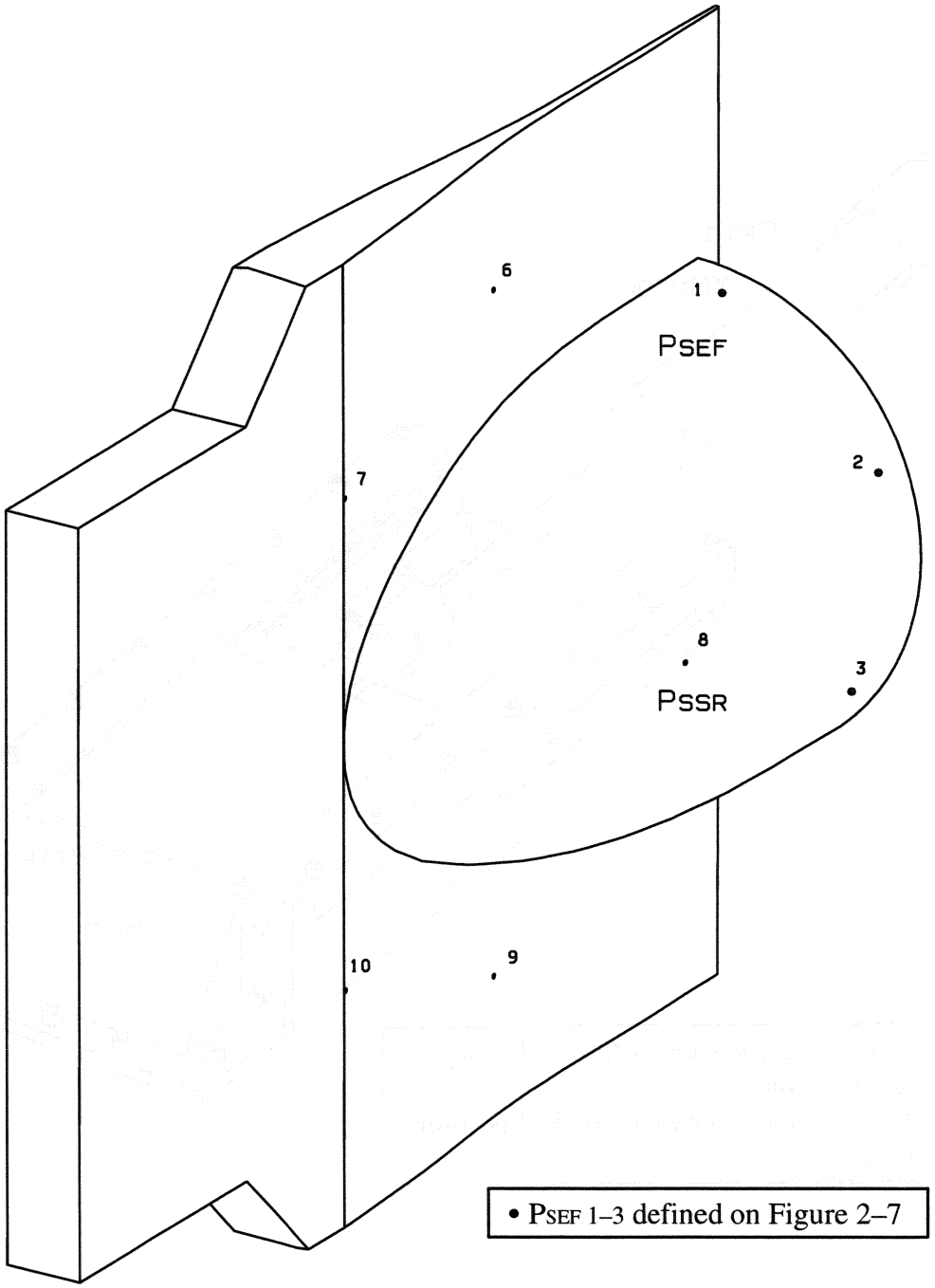

Figure 2–22. Spinner/Wedge Instrumentation (port)

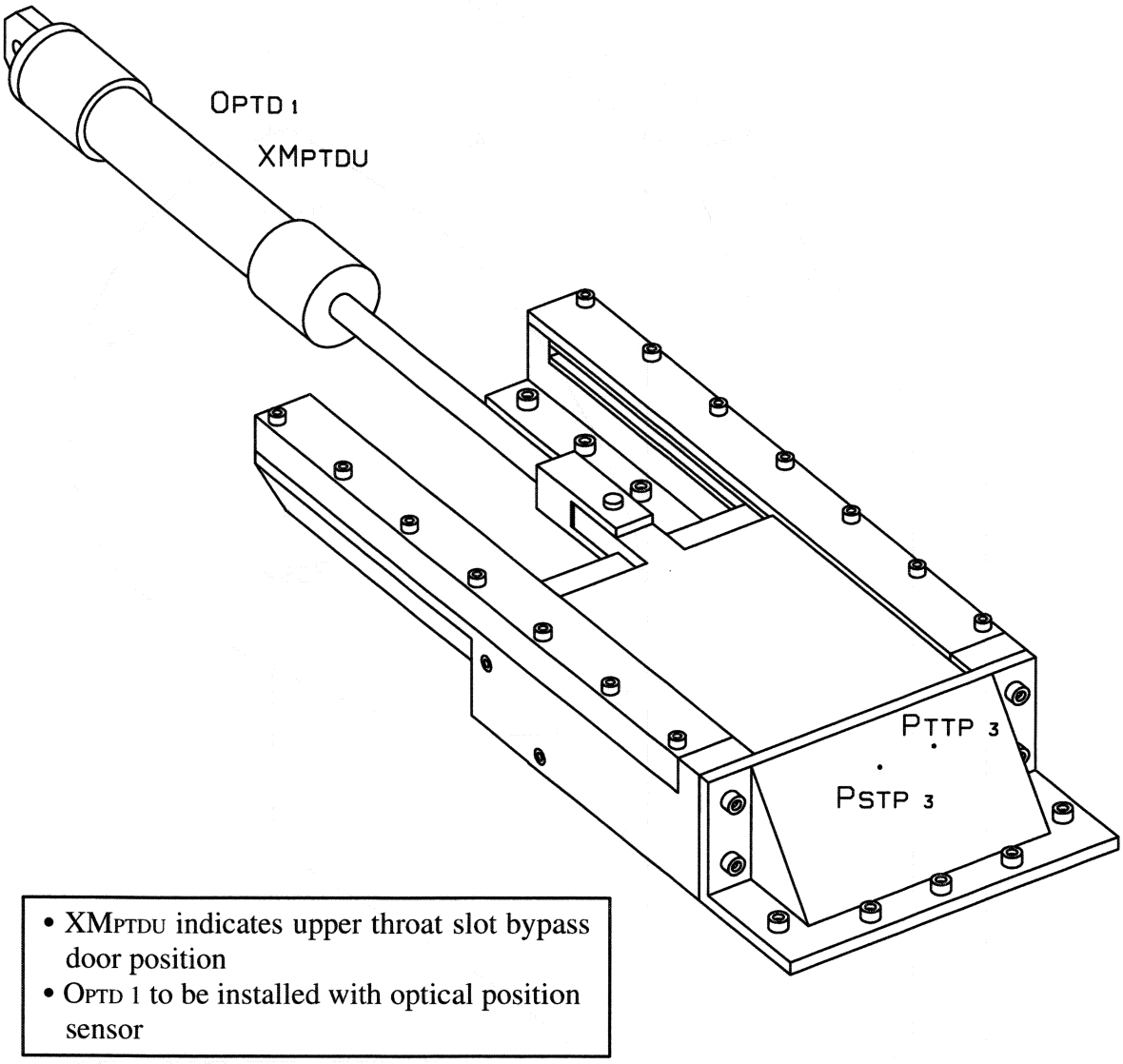

Figure 2–23. Throat Slot Bypass System Instrumentation (upper)

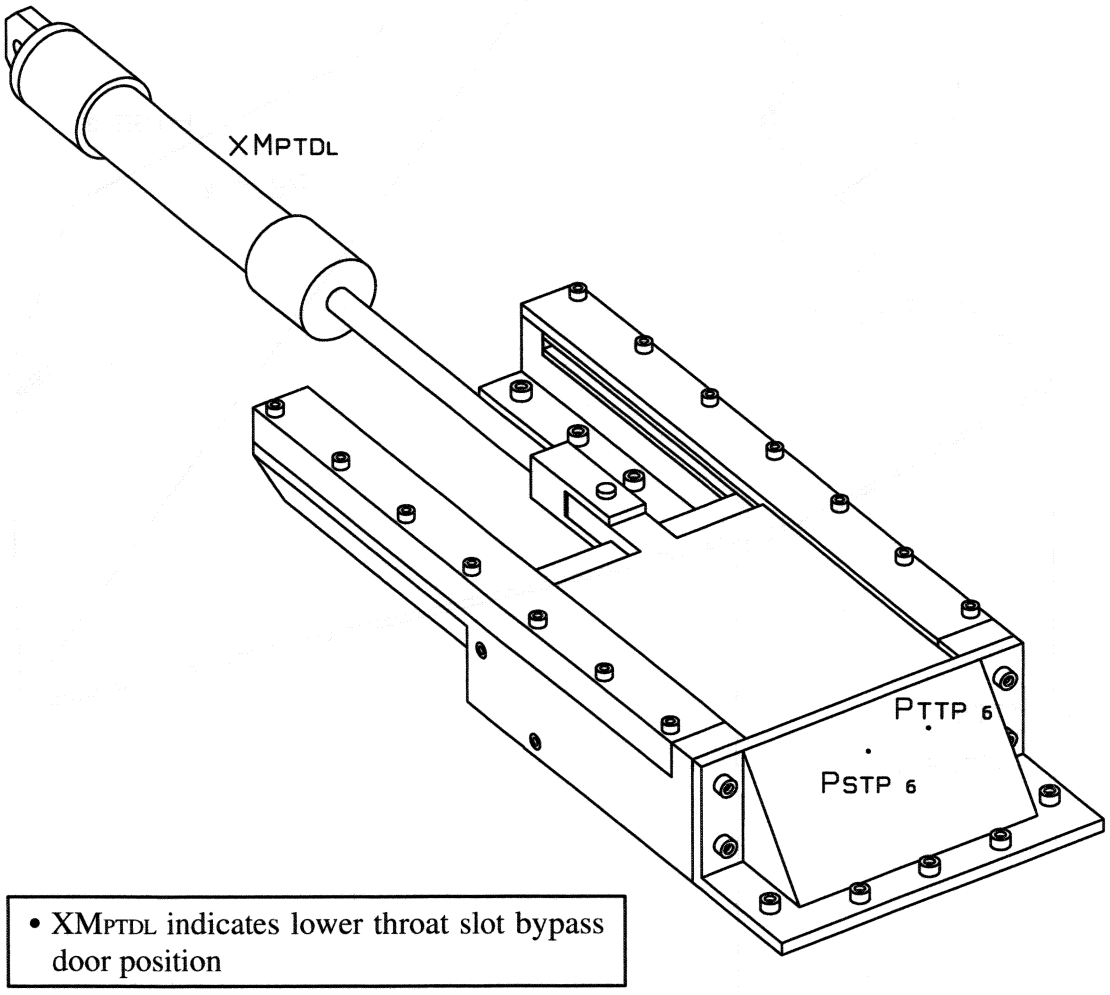

Figure 2–24. Throat Slot Bypass System Instrumentation (lower)

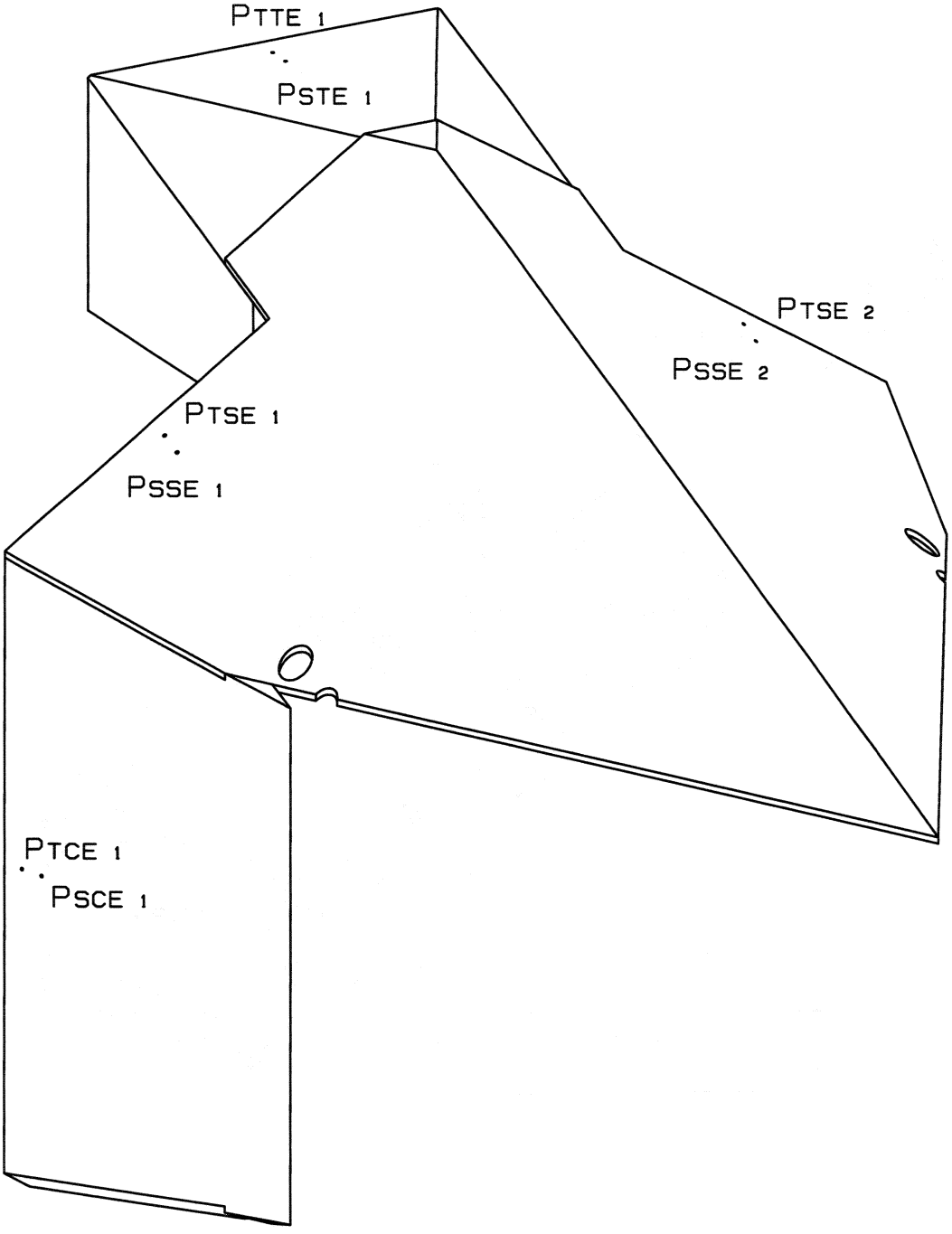

Figure 2–25. Exit Covers Instrumentation (upper/starboard)

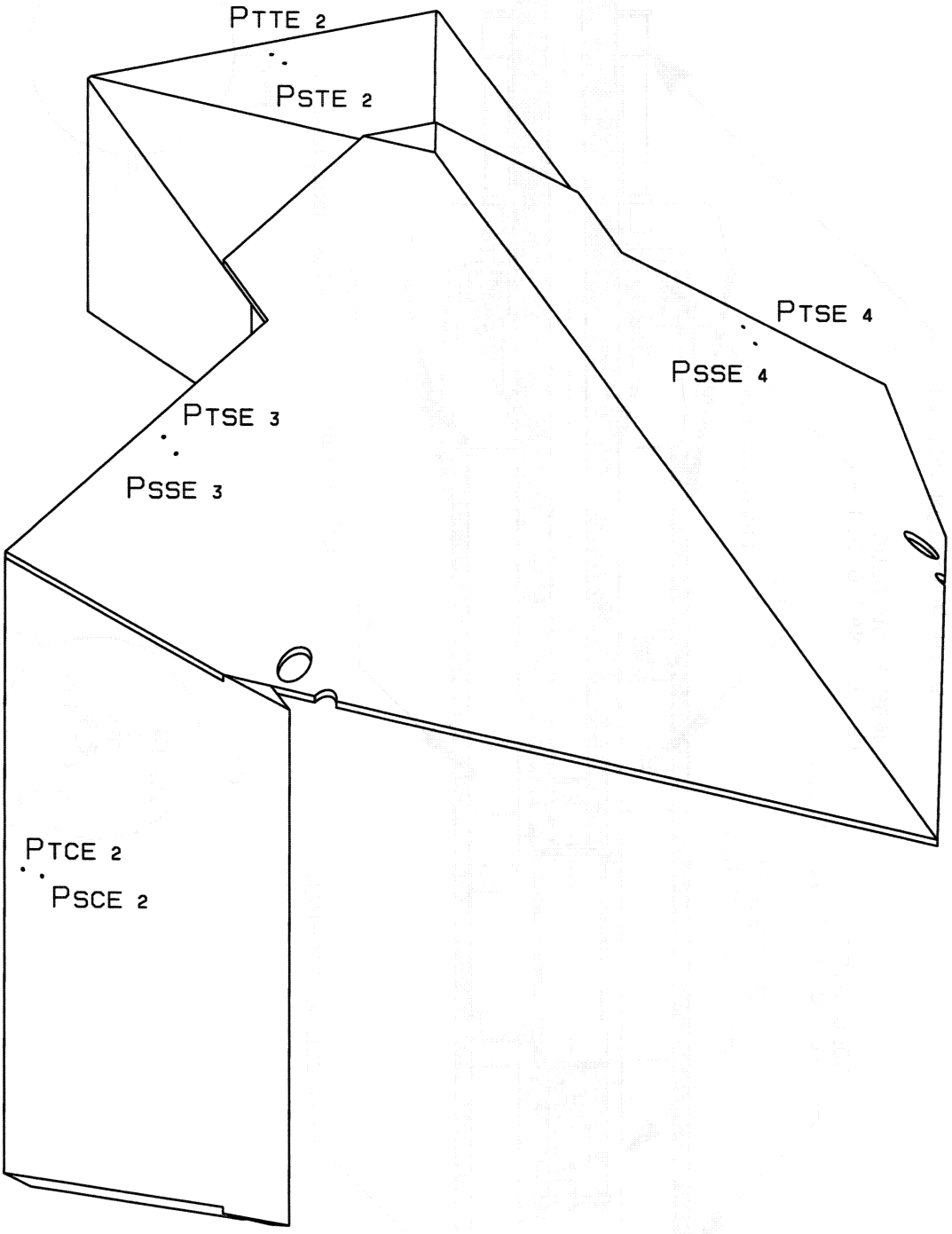

Figure 2–26. Exit Covers Instrumentation (lower/port)

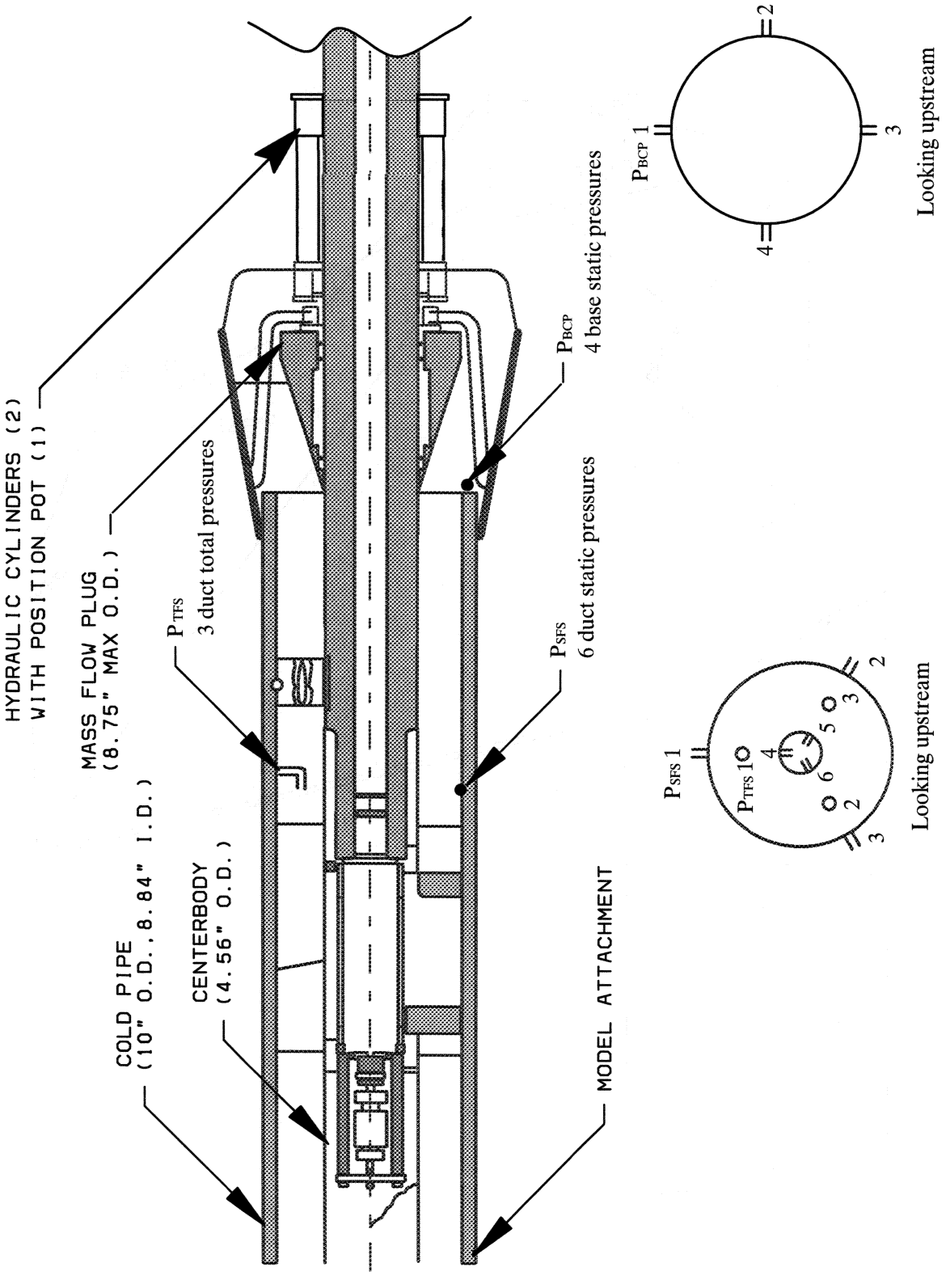

Figure 2–27. Cold Pipe Instrumentation

3. OPTIMIZATION

This section presents results from the configurational optimization phase of the test. The BTSSI inlet was equipped with several features to be experimentally optimized. These include the boundary layer bleed system, aft ramp leading edges, vortex generators, and forward and aft ramp positions. Optimization was performed parametrically, varying one parameter at a time in order to isolate effects of the configurational feature of interest.

3.1. BOUNDARY LAYER BLEED

A boundary layer bleed system was incorporated into the model design in order to remove part of the incoming boundary layer so that it does not separate due to the adverse pressure gradients produced by the shock waves, particularly the normal shock. The boundary layer bleed system is divided into three parts: (1) cowl bleed, (2) sidewall bleed, and (3) plenum bleed. The cowl and sidewall boundary layer is removed through 26% porous bleed plates at the locations shown in Fig. 2–4 and is designed to be operated under choking conditions. Boundary layer bleed analysis of the supersonic section of the inlet shows that a 26% porous plate will remove more than the required amount of the boundary layer to maintain attached flow through the normal shock. Excess bleed capacity is provided to compensate for possible inaccuracies in the analytical predictions. The porosity of the bleed plates was reduced in the test by filling rows of holes in order to determine the optimum bleed rates. The plenum bleed occurs through the throat slot and removes the forward ramp boundary layer.

The bleed optimization was conducted with the aim of producing high recovery with minimum bleed because excess bleed incurs a performance penalty for the inlet. A total of nine bleed configurations were tested and are shown in Fig. 3–1 through Fig. 3–18. The first several bleed patterns were attempts to achieve proper operation of the inlet, while the latter bleed patterns were optimization runs.

Fig. 3–19 shows the critical throat and engine face recovery for the nine bleed patterns along with the PARC predictions. As a compliment to this figure, Fig. 3–20 shows the corresponding bleed amounts for the bleed patterns and PARC. From these figures, it can be seen that the higher bleed patterns have higher recoveries which was expected. Bleed pattern 4 has the highest throat recovery of 0.9556, but has the second highest amount of bleed at 0.1464. Bleed pattern 5 has the highest engine face recovery of 0.9064, but has the third highest bleed rate of 0.1340. These bleed rates would be too high for a production inlet, but do indicate that the inlet concept is capable of providing the necessary performance. Bleed patterns 7–9 produced more realistic bleed amounts of 0.0856, 0.0838 and 0.0560 at the expense of lower engine face recovery values of 0.8675, 0.8840 and 0.8729.

The PARC results compare favorably to the bleed pattern 9 results, but with less bleed. PARC recoveries were computed based on the actual model engine face rake locations. The PARC bleed calculations use a constant surface mass flow to model the bleed which does not take into account roughness effects produced by the bleed in the test or the increase in bleed that occurs downstream of a normal shock that is in the middle of a bleed band. Both of these effects cause uncertainty in the PARC bleed modeling that requires further study. The bleed model has recently been improved by Boeing.[7,8]

Fig. 3–21 shows the critical engine face recovery as a function of bleed flow for the nine bleed patterns and the PARC calculations. The experimental results are along a band that trades en-

gine face recovery for boundary layer bleed. The desire to move the recovery towards the upper left corner of the plot could be viewed as being successful when comparing bleed pattern 1 with patterns 8 and 9. Fig. 3–22 shows similar results for the recovery at the throat. If Fig. 3–21 and Fig. 3–22 are compared, one can see that there is a 4% to 6% recovery loss between the throat rakes and the engine face rakes. Specifically, the losses in the subsonic diffuser were between 4% and 6%, which is rather high. Clearly, the inlet performance could be improved with a better subsonic diffuser.

Fig. 3–23 shows the pitot pressure corrected cowl and sidewall boundary layer profiles for each of the bleed patterns. Looking at the cowl profiles, one can see that bleed patterns 1–5 produce very full profiles. These would be profiles that produce good results in the subsonic diffuser, but at a high cost in terms of bleed drag. The profile for bleed #9 is close to separating and would produce lower subsonic diffuser performance. This is the case as found from comparing Fig. 3–21 and Fig. 3–22. These figures show that bleed #9 had over 6% total pressure loss between the throat and engine face, while the other bleeds had between 4% and 5%. The plots for bleed patterns 6–8 show more desirable boundary layer profiles that would give reasonable subsonic diffuser performance without excessive bleed.

The sidewall boundary layer profiles in Fig. 3–23 show similar trends as the cowl profiles. Bleed #9 has the lowest recovery, while bleed patterns 7 and 8 have a more reasonable shape. Bleed patterns 1–6 produced profiles that are too full. It should be noted that none of the sidewall profiles have a full well–rounded shape typical of a turbulent boundary layer. Bleeds 7 and 8 come closest to this type of shape, but are actually more like a laminar boundary layer profile. The complex nature of the boundary layer flow along the sidewall, where there are corner flows and several glancing shock interactions, makes it difficult to determine why the sidewall boundary layers behave as shown in the figure.

Fig. 3–24, Fig. 3–25, and Fig. 3–26 compare experimental and PARC total pressure profiles for the cowl and sidewall. The experimental results are for bleed patterns 1–9, while the PARC results are for the same bleed (same solution repeated) with the baseline aft–ramp leading edge and alternate #1 leading edge in the bleed pattern #8 plots. In the cowl comparisons, there is reasonable agreement for bleeds 6, 7, and 8. Bleed patterns 1–5 had larger amounts of cowl bleed that produced flat and full profiles that do not compare well to the rounded PARC profiles. Bleed pattern 9 has a shape similar to the PARC results but of a lower recovery. Like the experimental results, the PARC sidewall profiles have a flatter profile than the cowl profile. The PARC sidewall profile is in reasonable agreement with experiment for bleed patterns 1–6. There is less agreement for bleed patterns 7–9 as the experimental pressures become lower.

Reviewing Fig. 3–20 and the preceding boundary layer profile comparisons, one can conclude that the PARC boundary layer bleed is more effective for a given amount of bleed. Specifically, the PARC predicted boundary layers have similar shapes as the experimental, but require less amounts of bleed. The exact reason for this requires further study, but there are two likely causes. First, bleed roughness effects that occurred in the experiment are not modeled in the PARC computations. Secondly, the variation of bleed rate due to local conditions that took place in the experiment did not occur in the PARC analyses.

Fig. 3–27 shows the sidewall and cowl bleed rates versus engine face recovery during mass flow plug sweeps for bleed patterns 7, 8 and 9. In the figure, the plug sweep starts at the low recovery point and proceeds to the peak recovery (critical normal shock location), which is

followed by the unstart point. In general, the bleed rates remain nearly constant until just before the critical point where they increase. The figure shows that the bleed rates for bleed patterns 7 and 8 do not increase as much near the critical point as does bleed pattern 9. On the other hand, bleed patterns 7 and 8 show a more continuous increase in bleed rate up to the critical point, while the bleed rate for bleed pattern 9 is constant until near the critical point where the rate has a large increase. The reason for this difference can be determined from looking at the bleed patterns in Fig. 3–14 through Fig. 3–18. The bleed figures show that pattern 9 does not extend as far downstream as patterns 7 and 8. Noting that the bleed rate increases when the normal shock is over the bleed region, the difference in bleed rates can be explained as follows. Bleed patterns 7 and 8 bleed rates start to increase earlier than pattern 9 because they extend farther downstream which causes the normal shock to be over the bleed region sooner. Since bleed pattern 9 does not extend downstream very far, it "feels" the normal shock later in the plug sweep which produces the constant bleed rate up to that point. Once the normal shock is over the pattern 9 bleed region, the shock produces a large increase in the bleed rate.

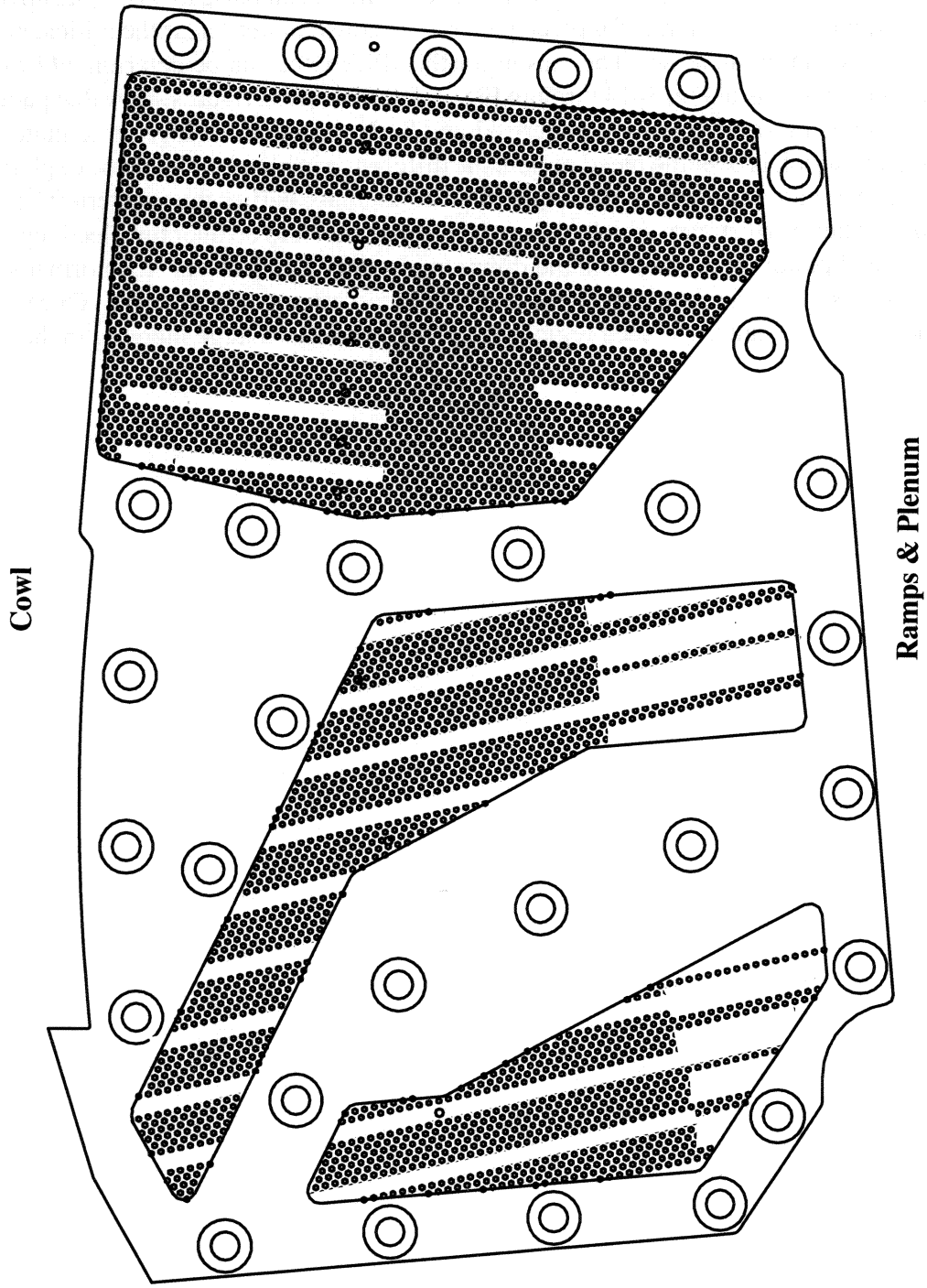

Figure 3–1. Sidewall Bleed Pattern #1

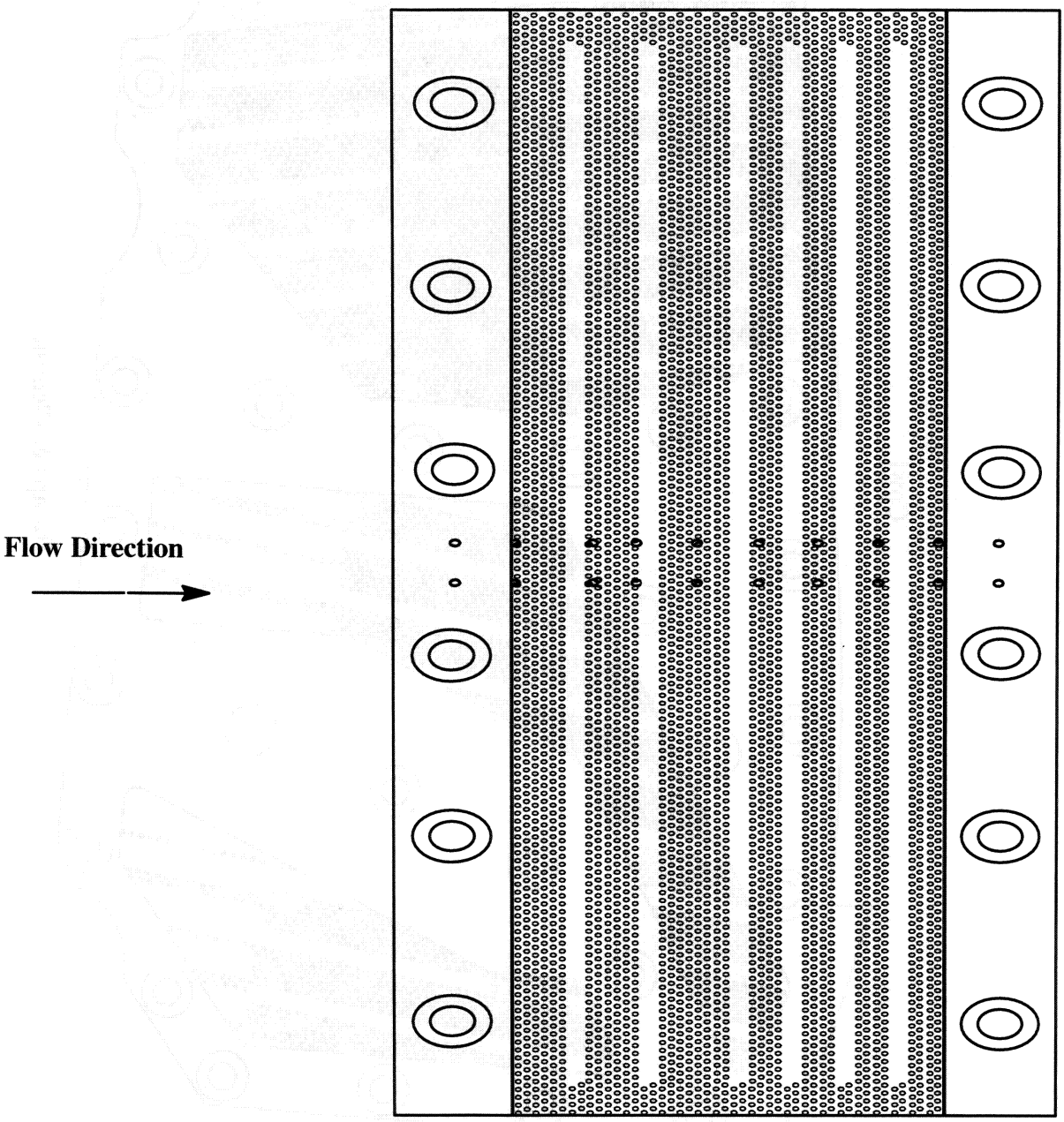

Figure 3–2. Cowl Bleed Pattern #1

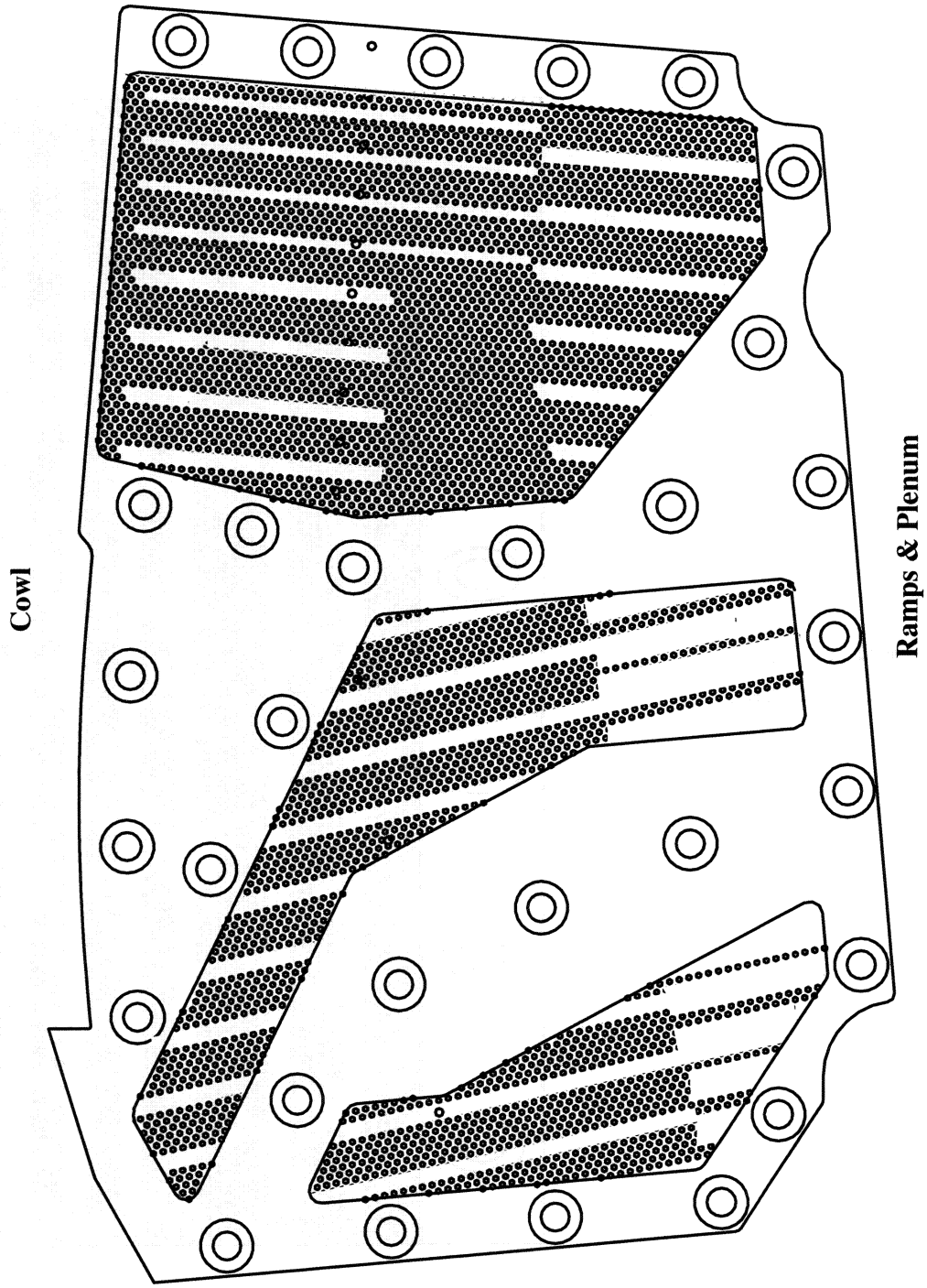

Figure 3–3. Sidewall Bleed Pattern #2

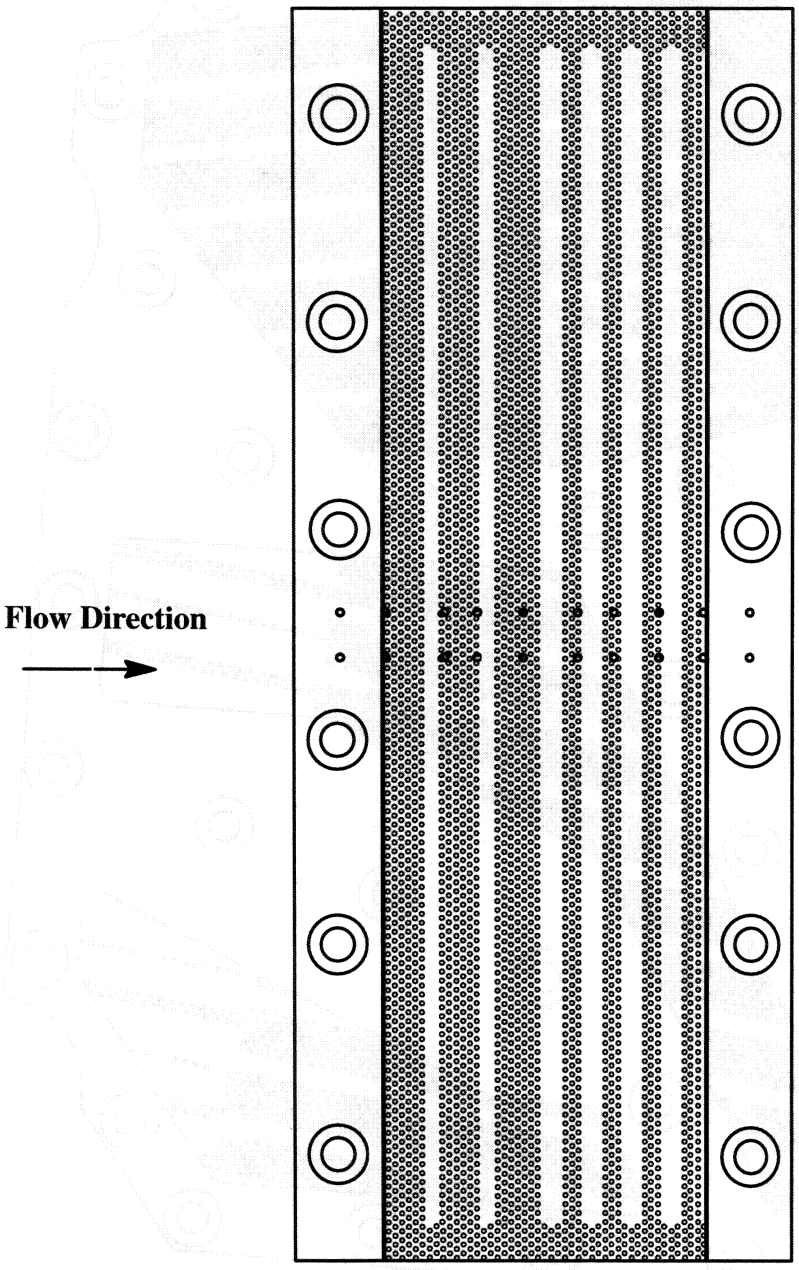

Figure 3–4. Cowl Bleed Pattern #2

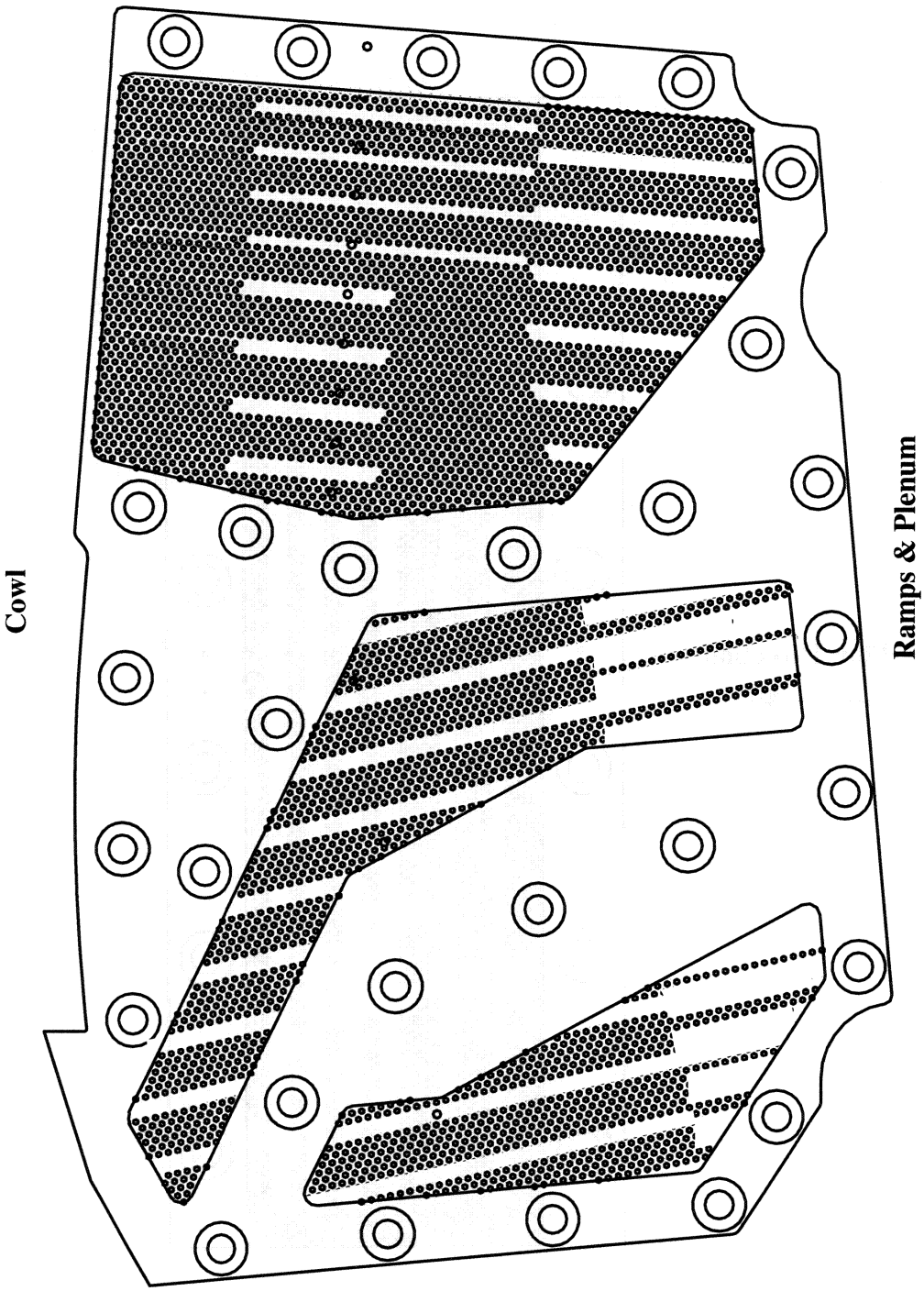

Figure 3–5. Sidewall Bleed Pattern #3

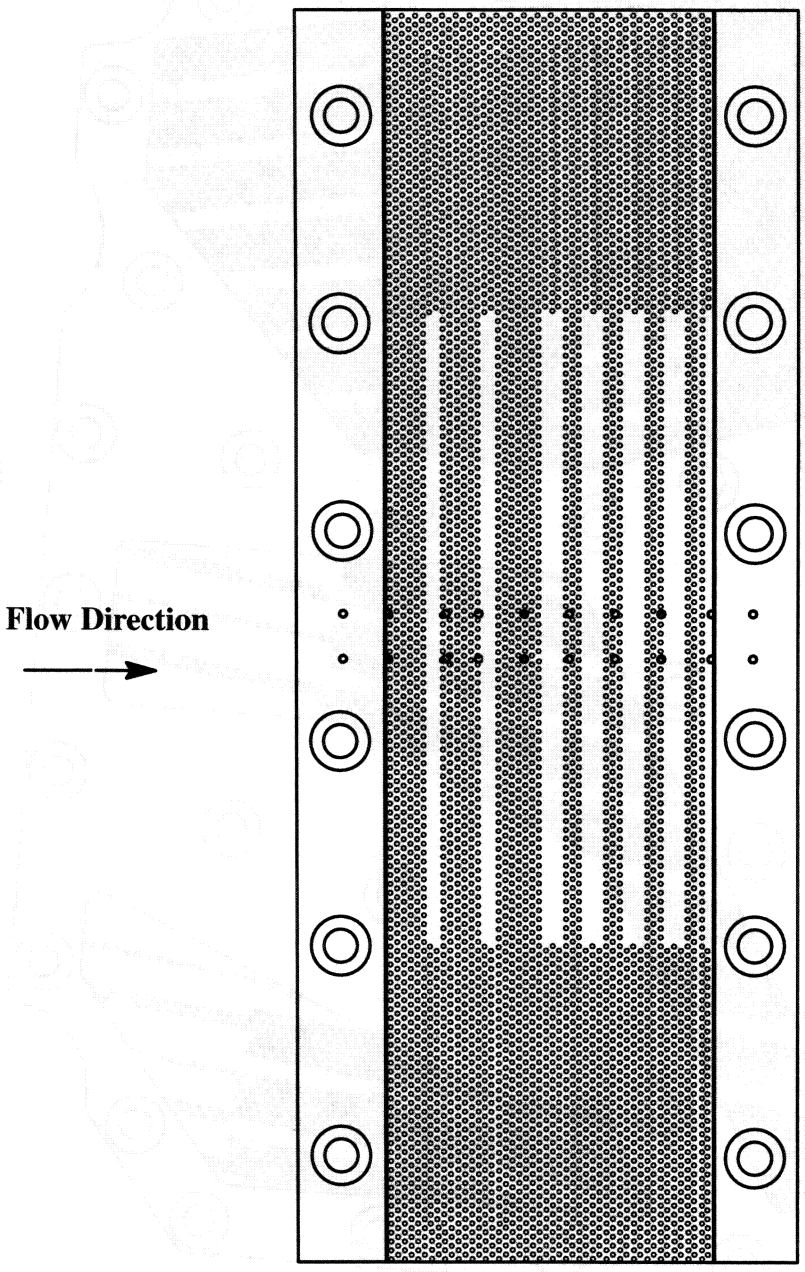

Figure 3–6. Cowl Bleed Pattern #3

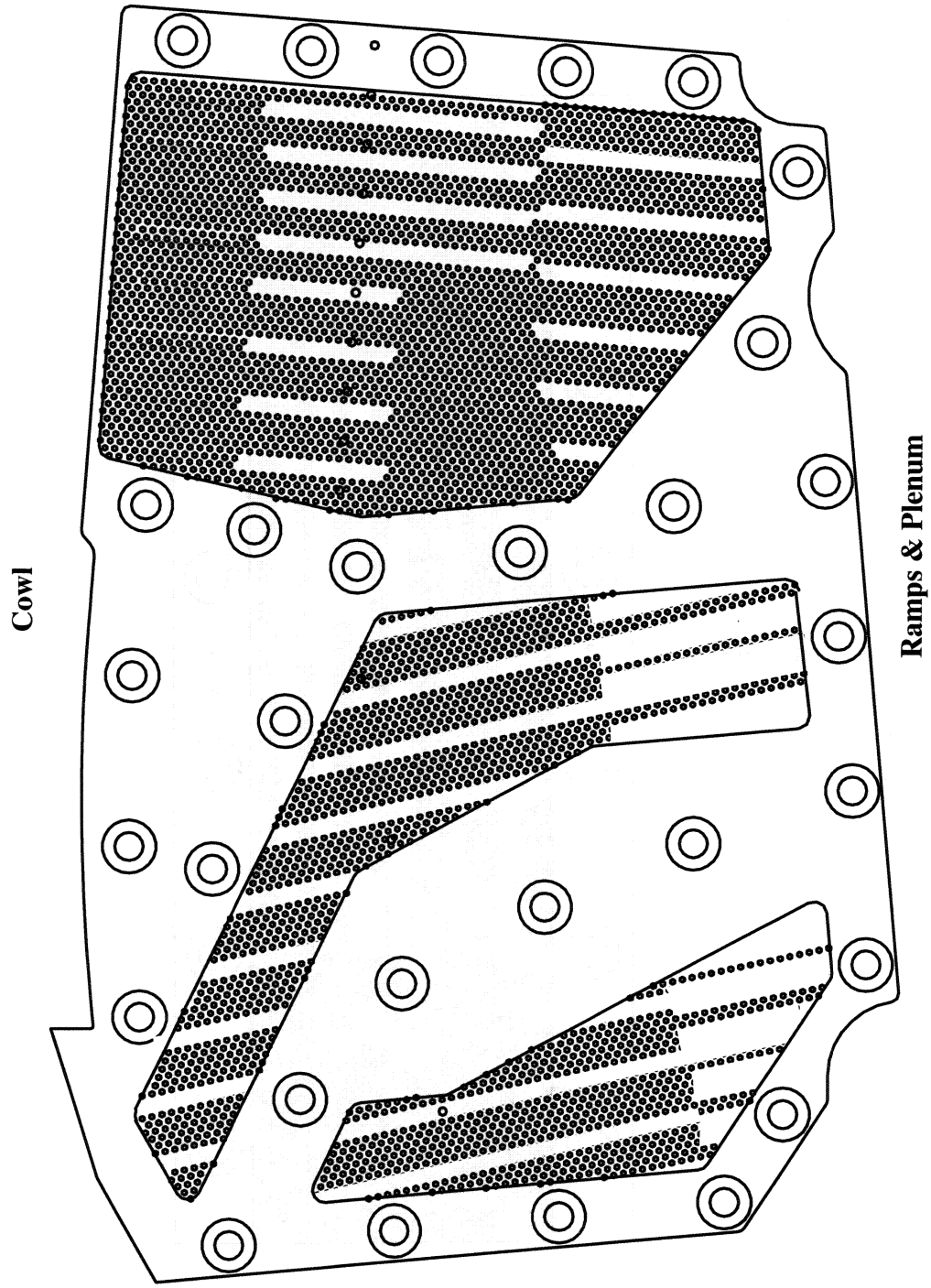

Figure 3–7. Sidewall Bleed Pattern #4

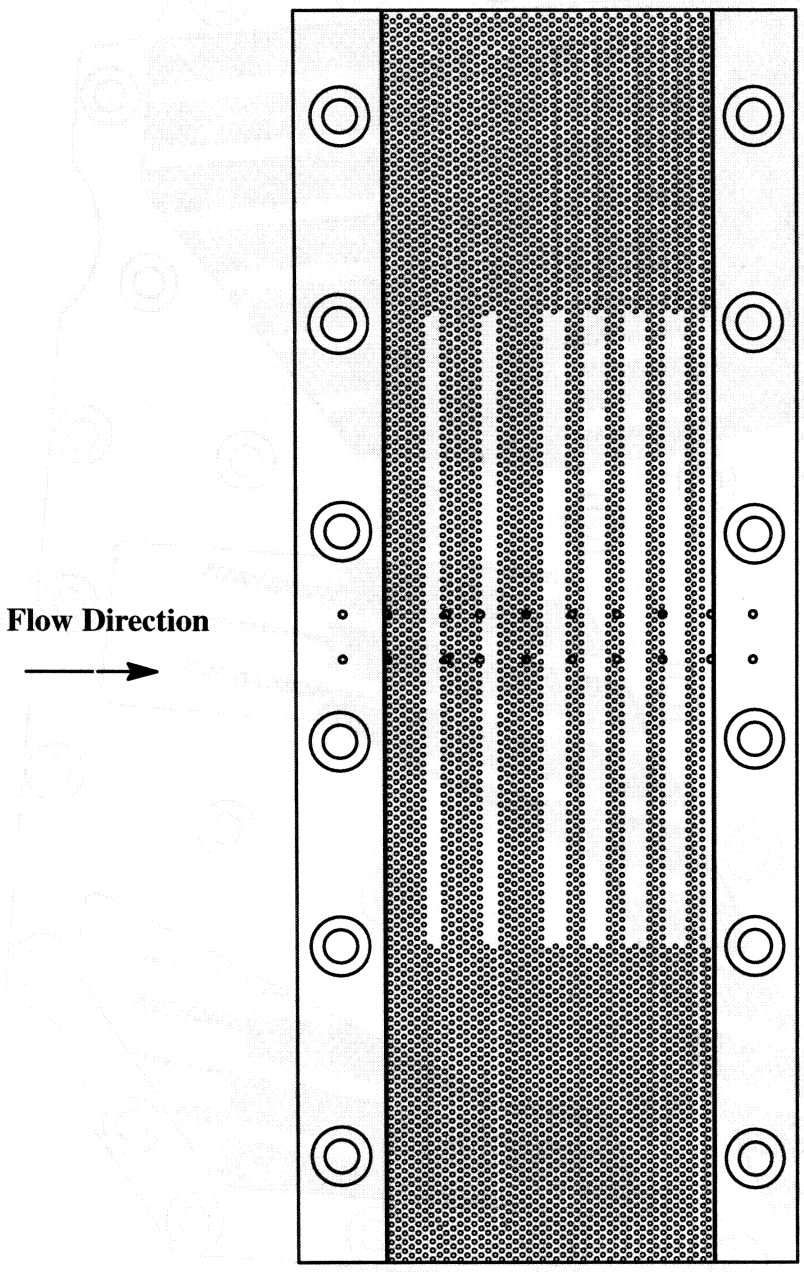

Figure 3–8. Cowl Bleed Pattern #4

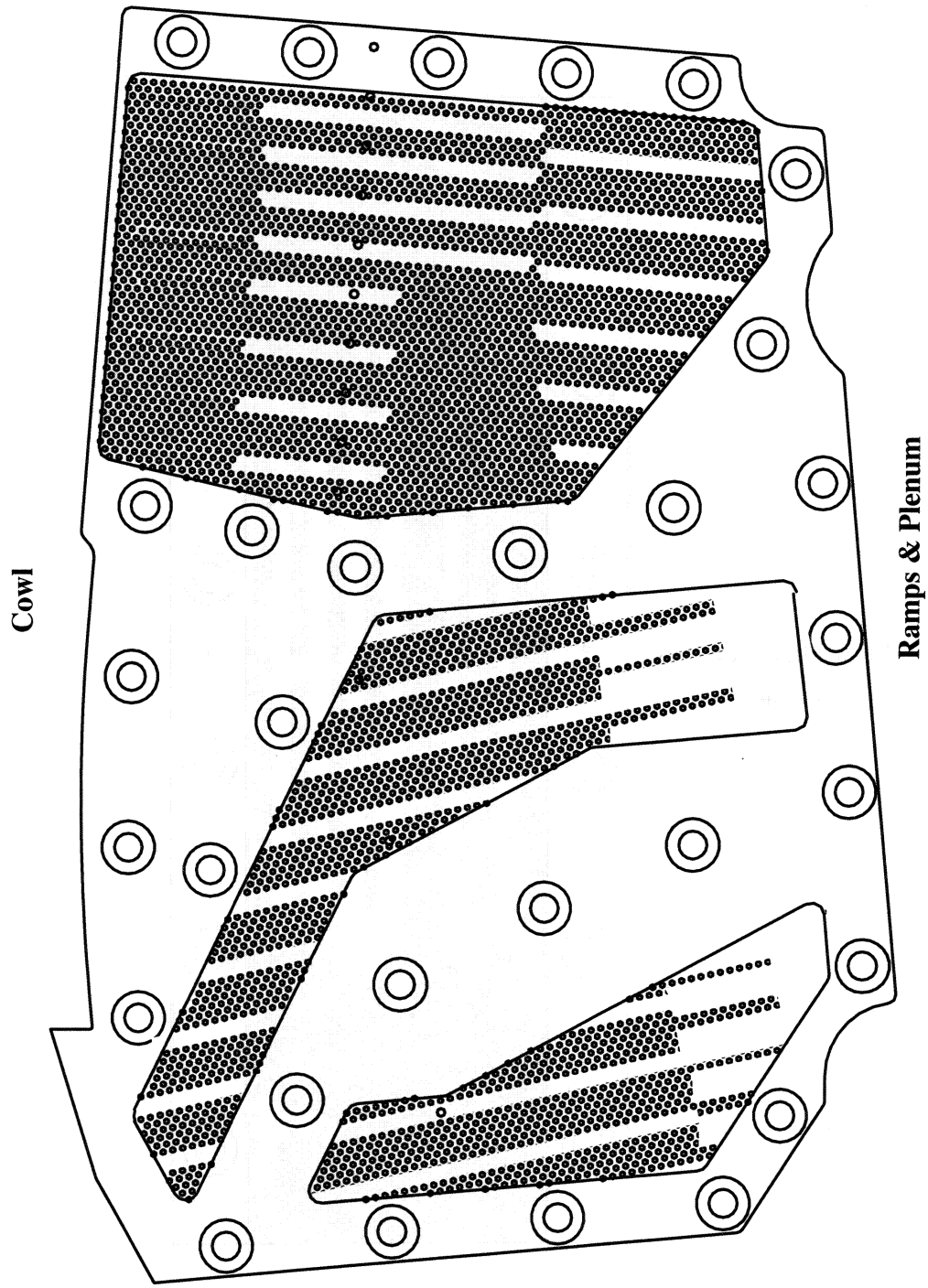

Figure 3–9. Sidewall Bleed Pattern #5

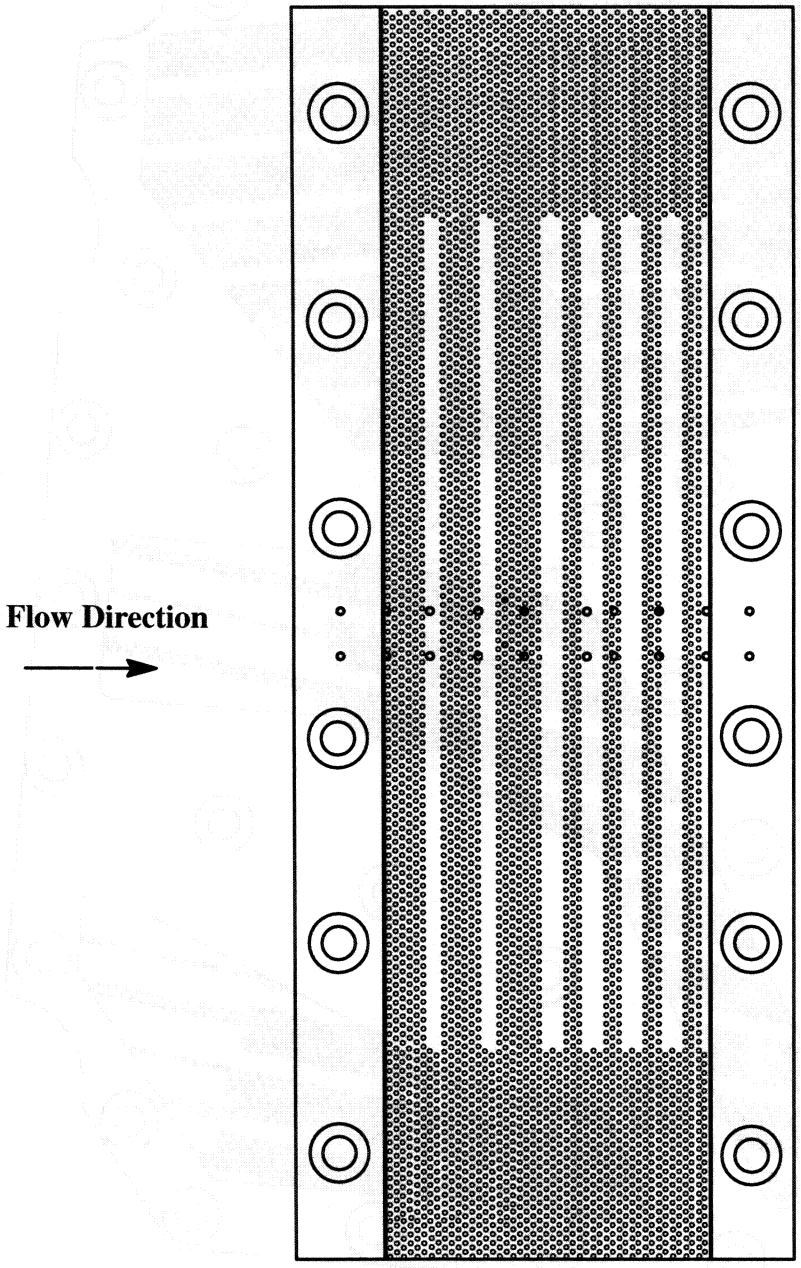

Figure 3–10. Cowl Bleed Pattern #5

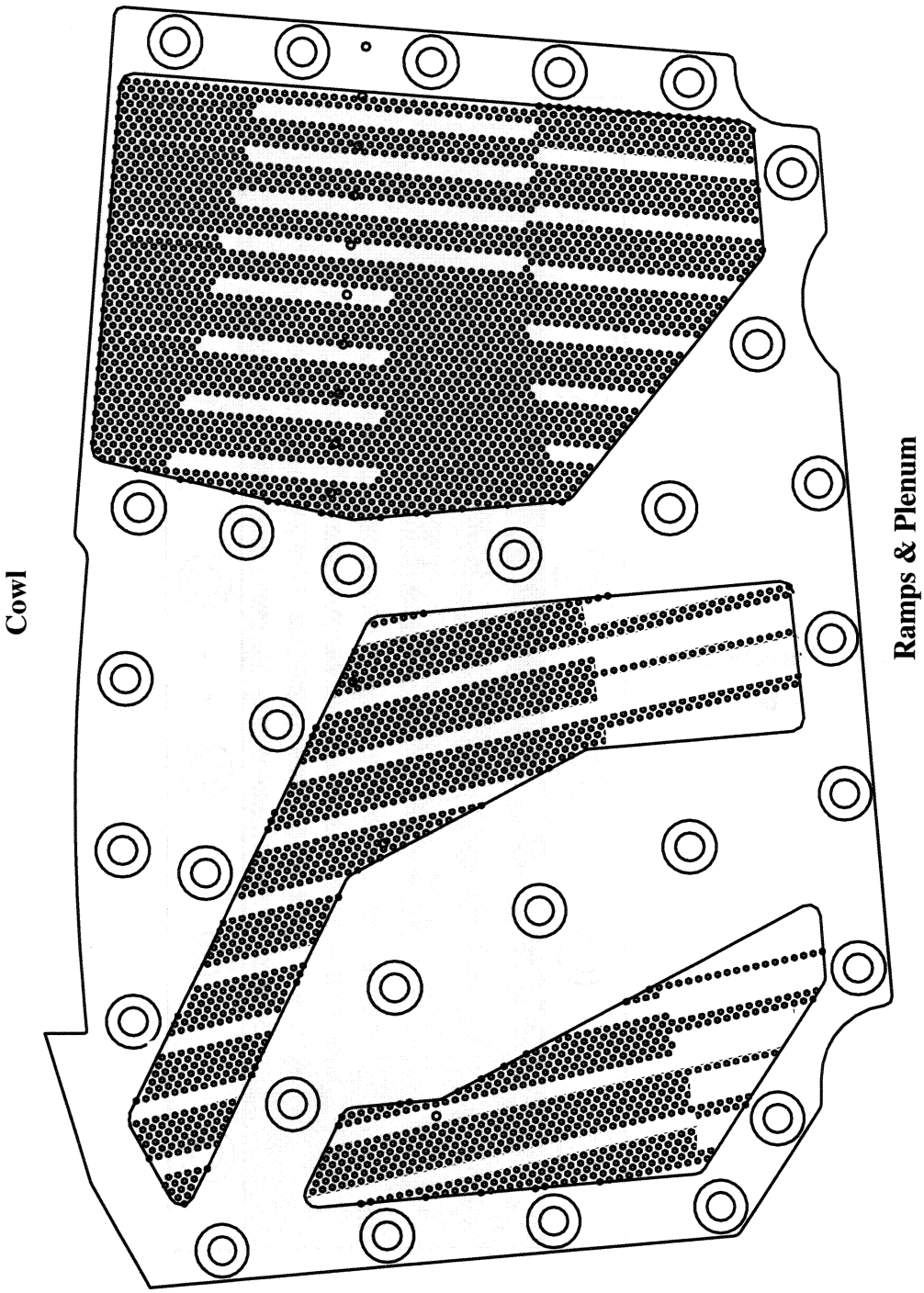

Figure 3–11. Sidewall Bleed Pattern #6

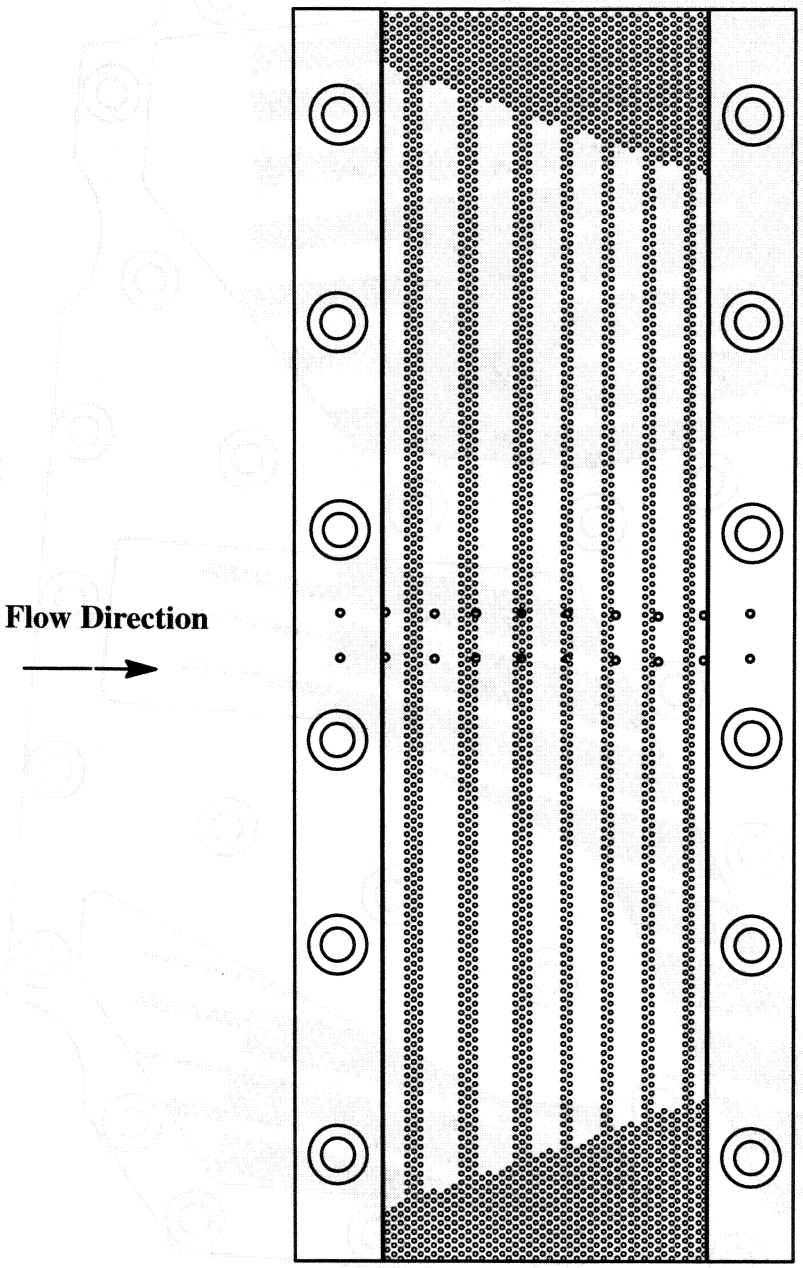

Figure 3–12. Cowl Bleed Pattern #6

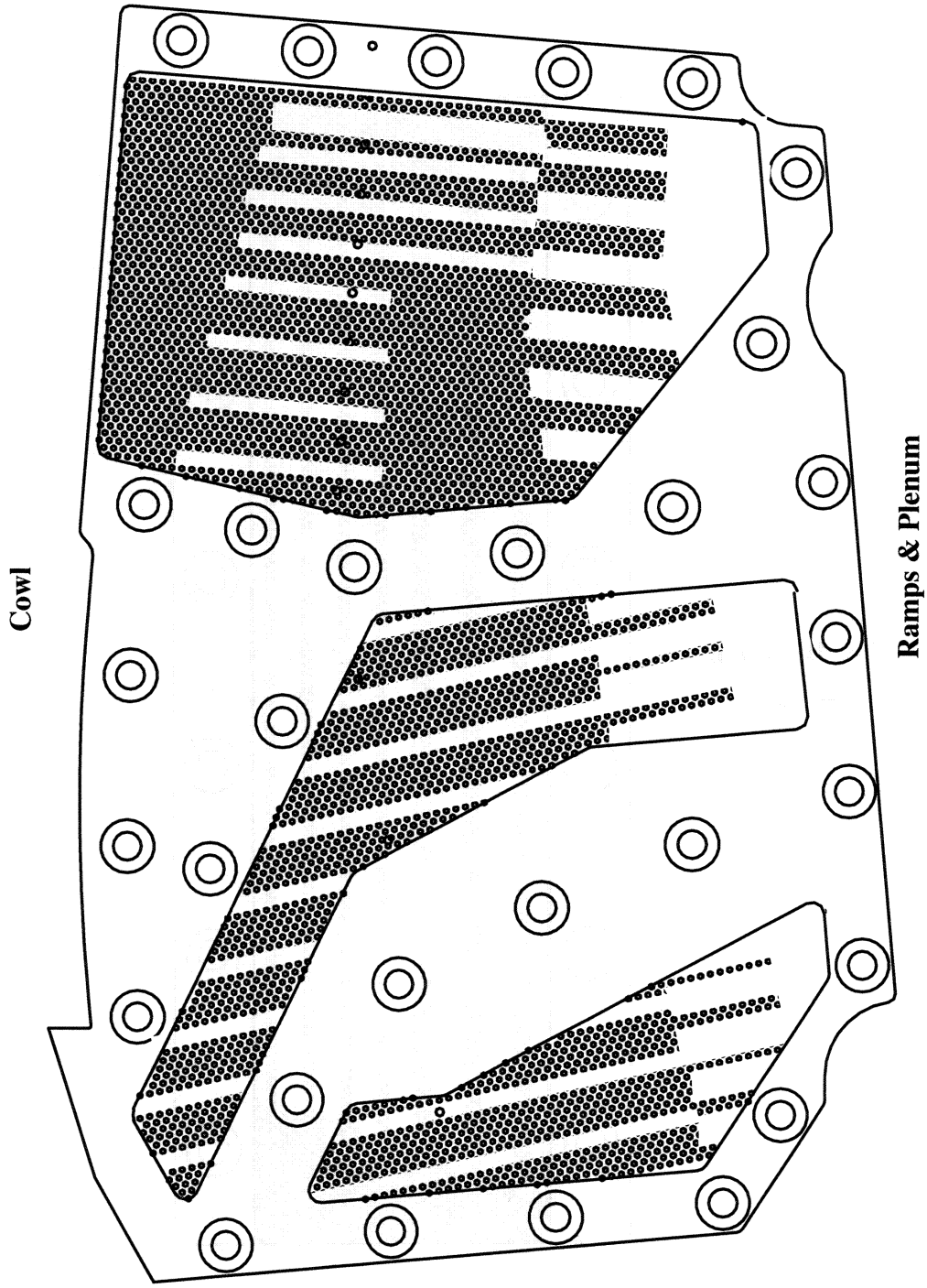

Figure 3–13. Sidewall Bleed Pattern #7

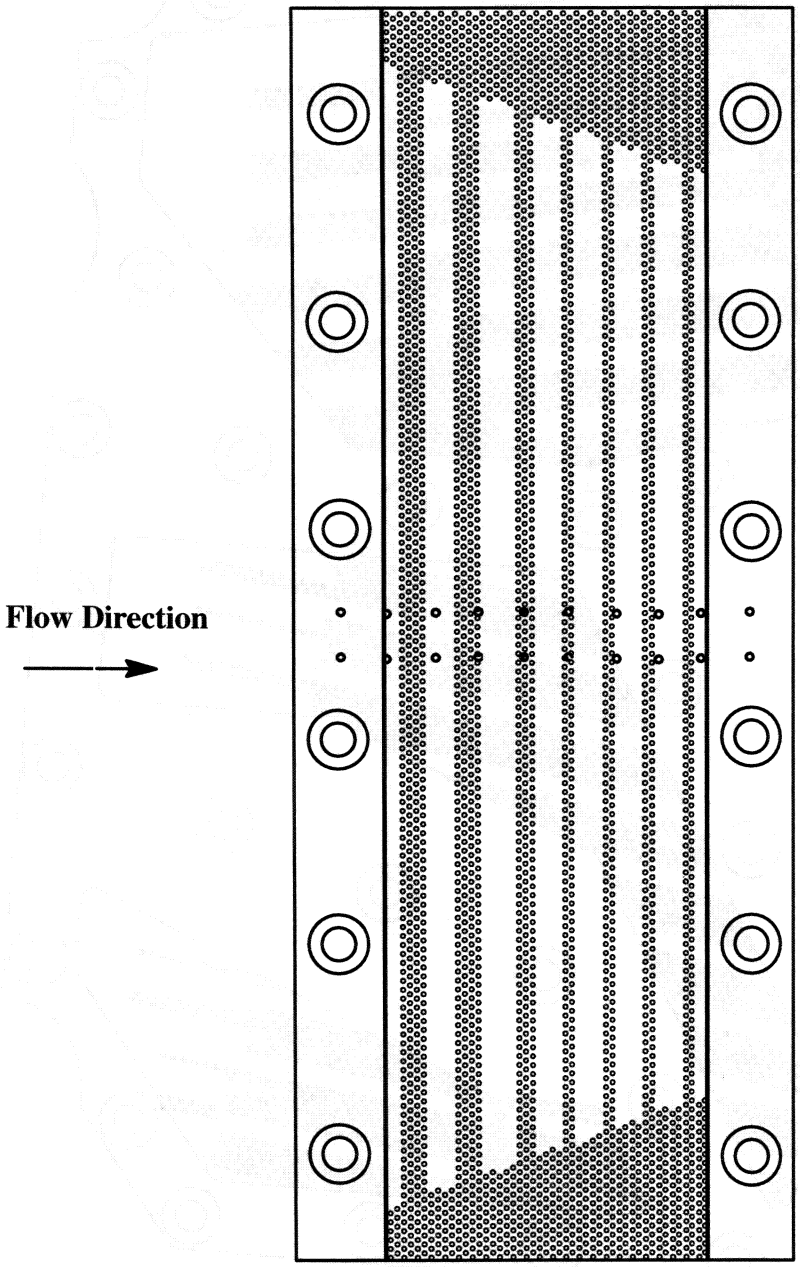

Figure 3–14. Cowl Bleed Pattern #7

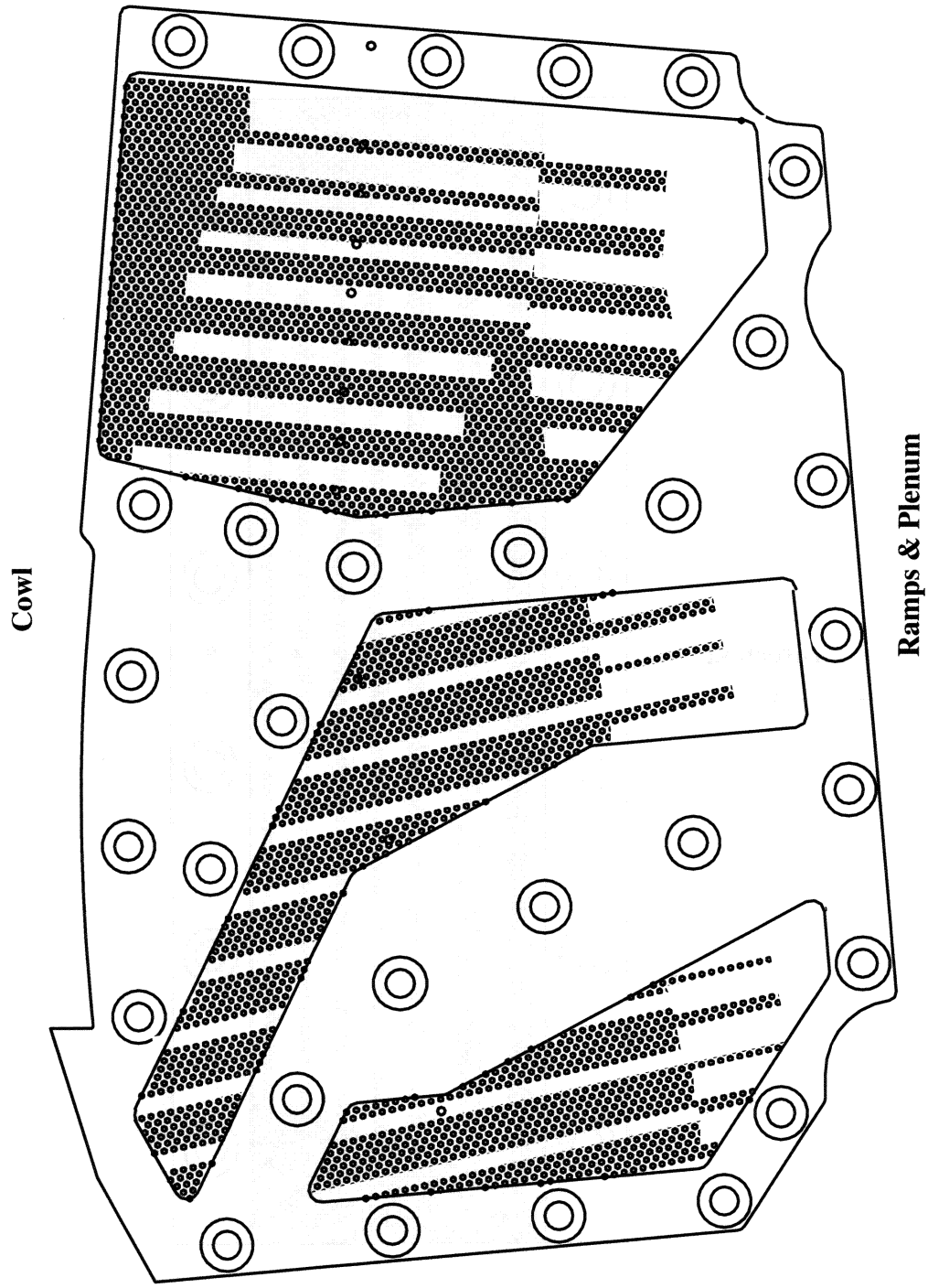

Figure 3–15. Sidewall Bleed Pattern #8

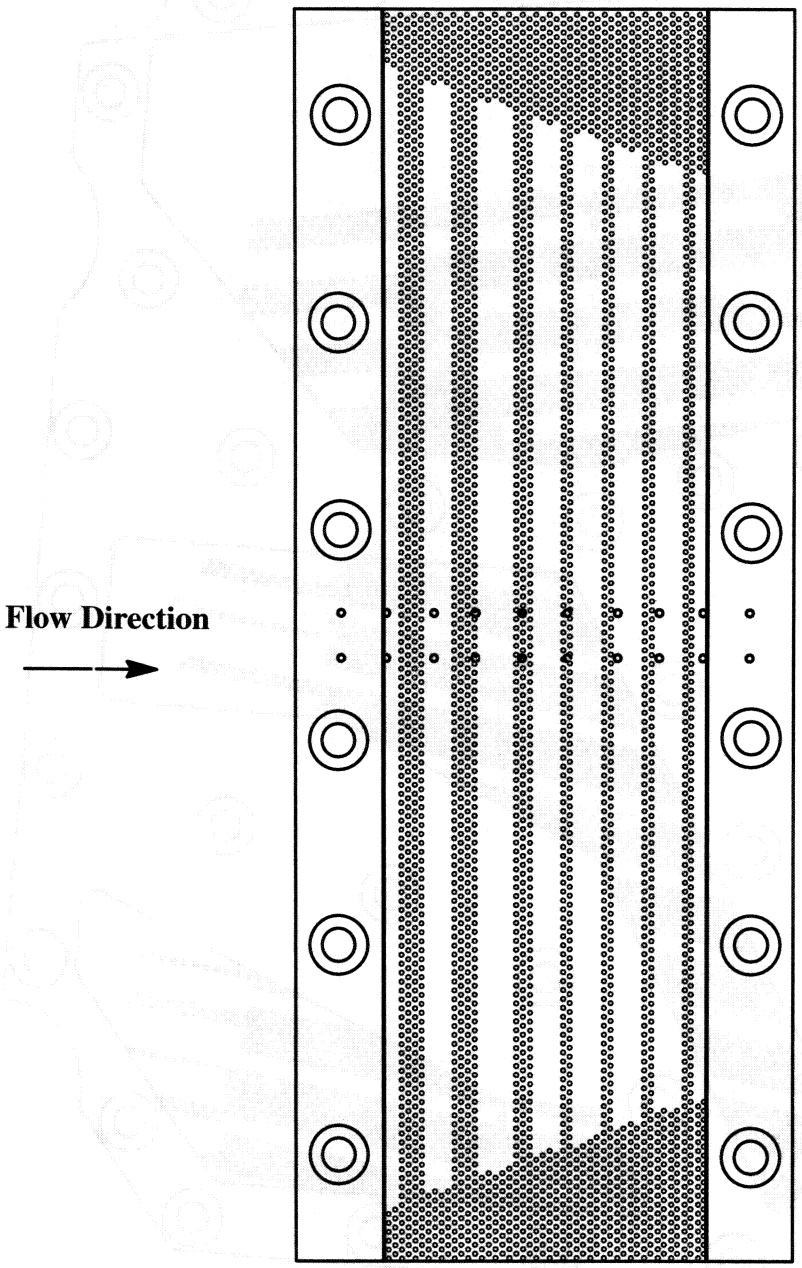

Figure 3–16. Cowl Bleed Pattern #8

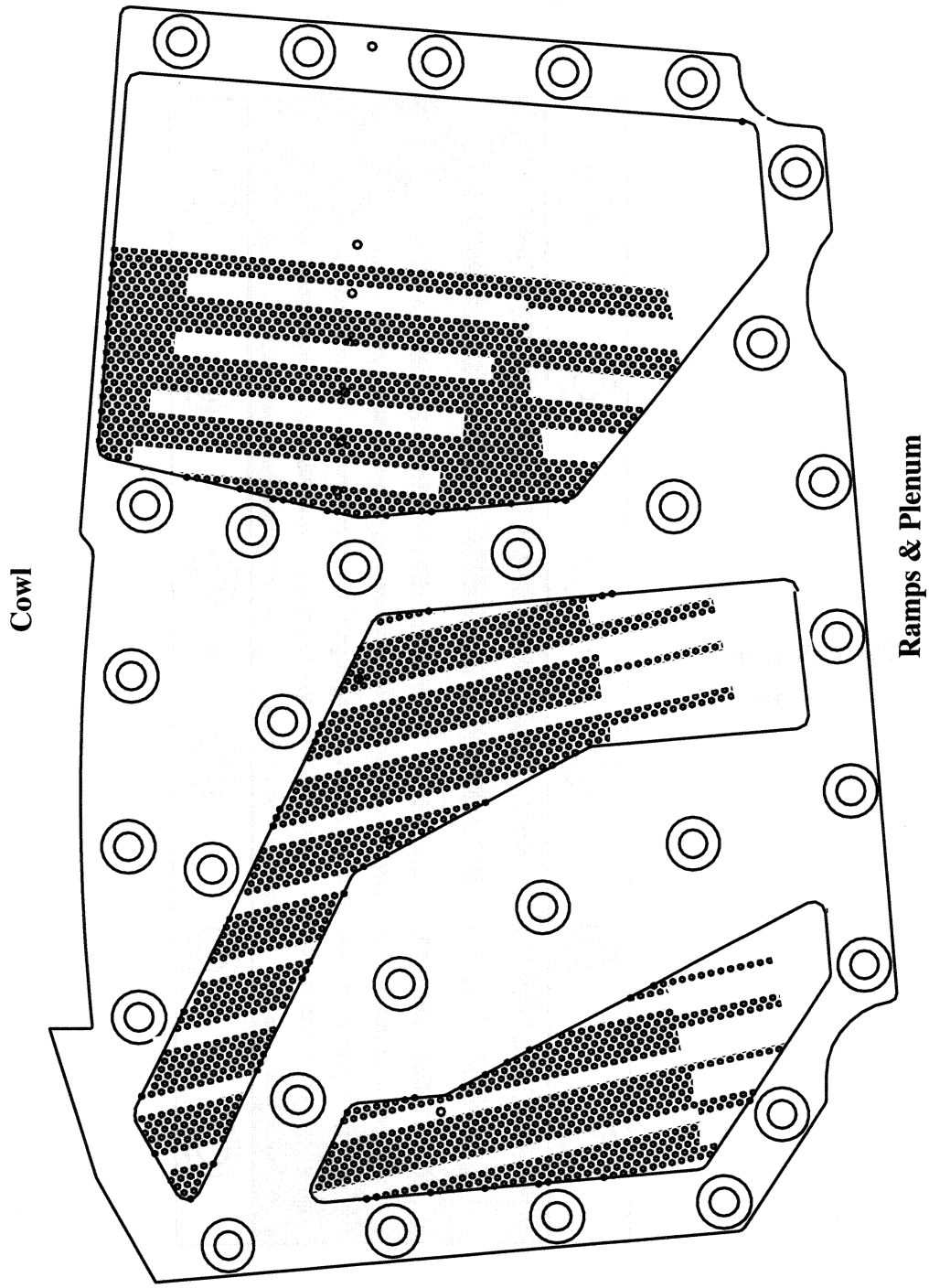

Figure 3–17. Sidewall Bleed Pattern #9

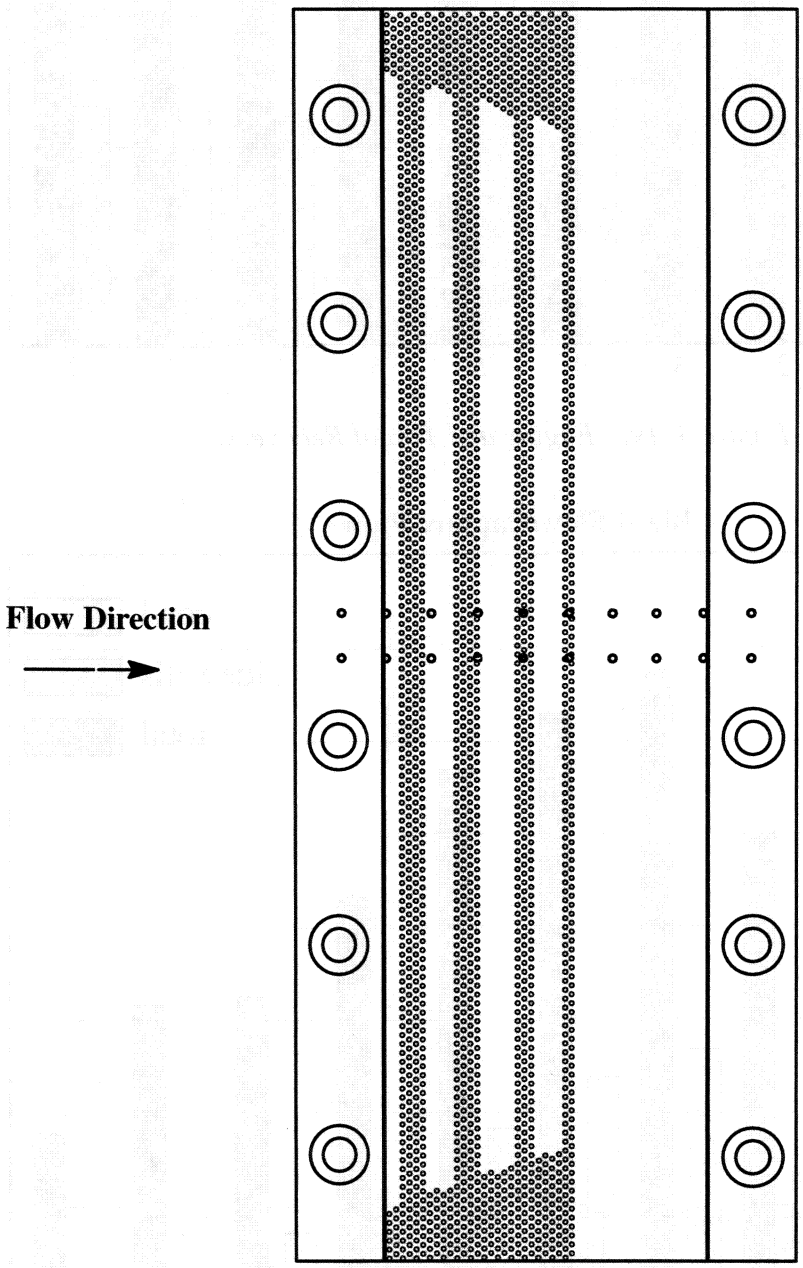

Figure 3–18. Cowl Bleed Pattern #9

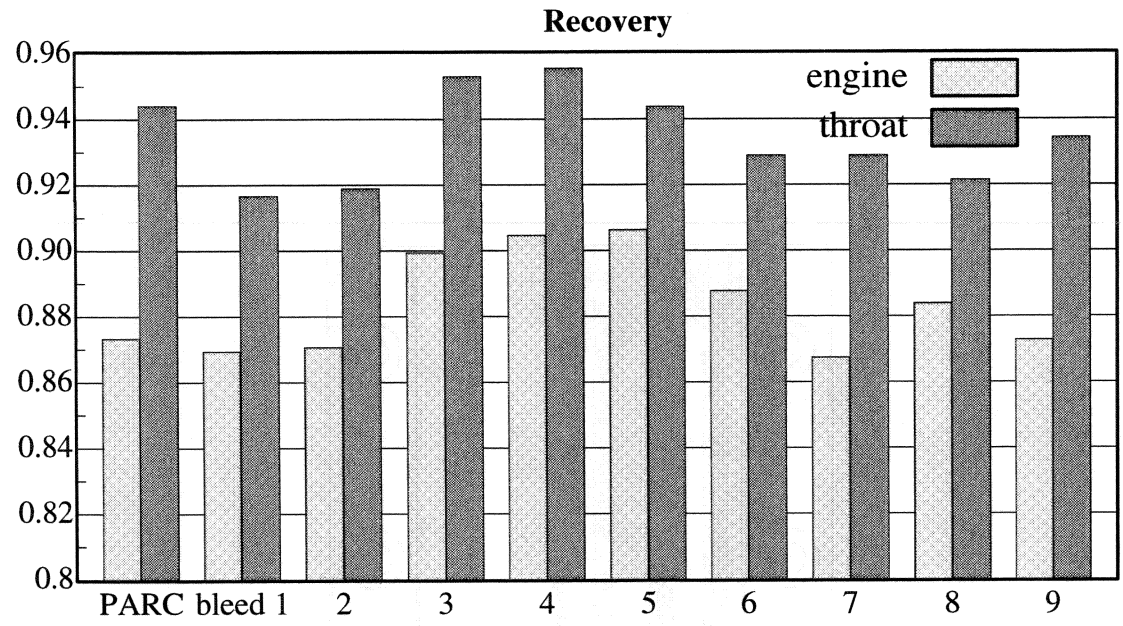

Figure 3–19. Engine and Throat Recovery.

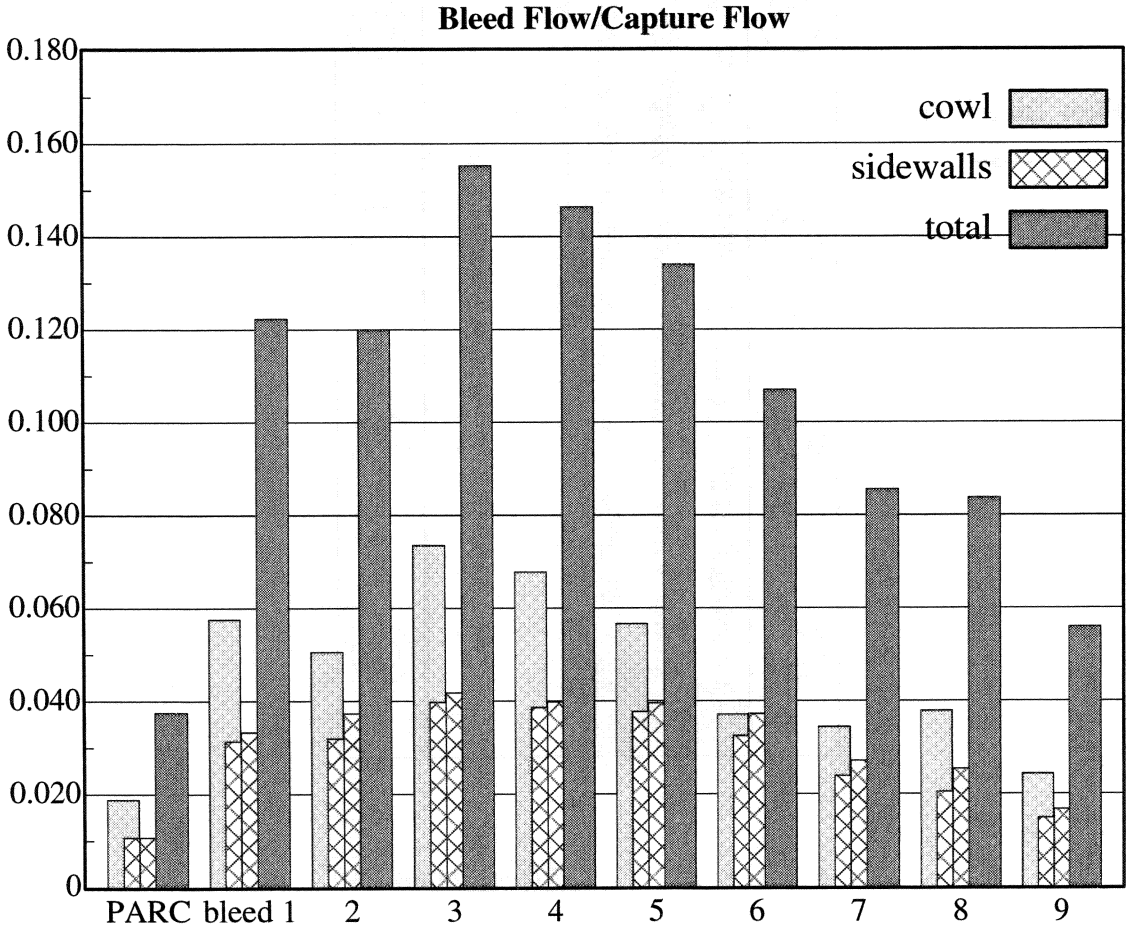

Figure 3–20. Bleed Mass Flow Ratios.

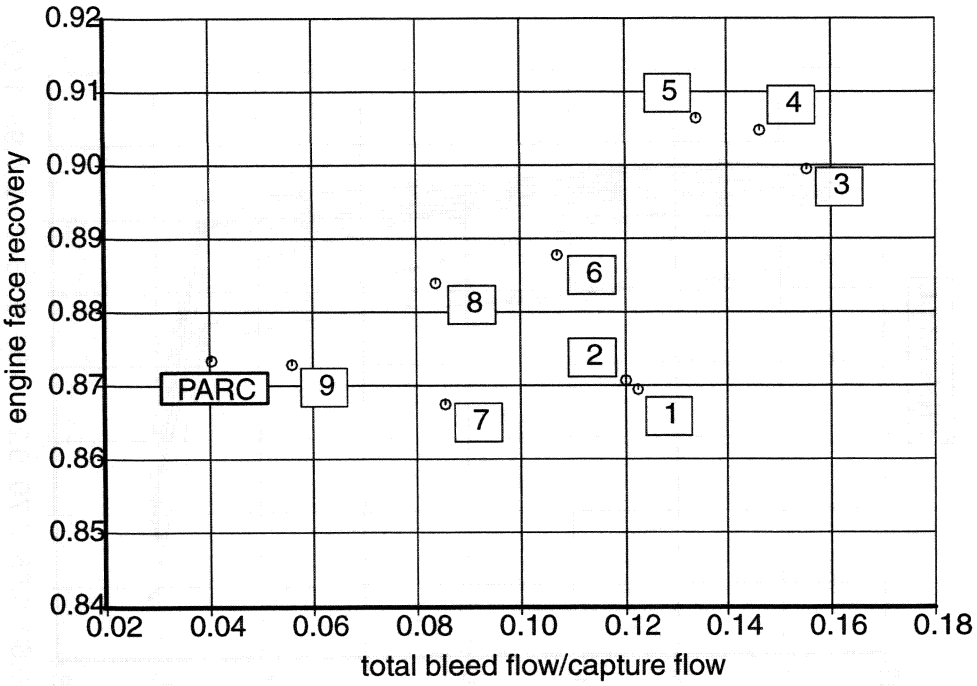

Figure 3–21. Total Bleed Flow vs. Engine Face Recovery for Bleed Patterns 1–9.

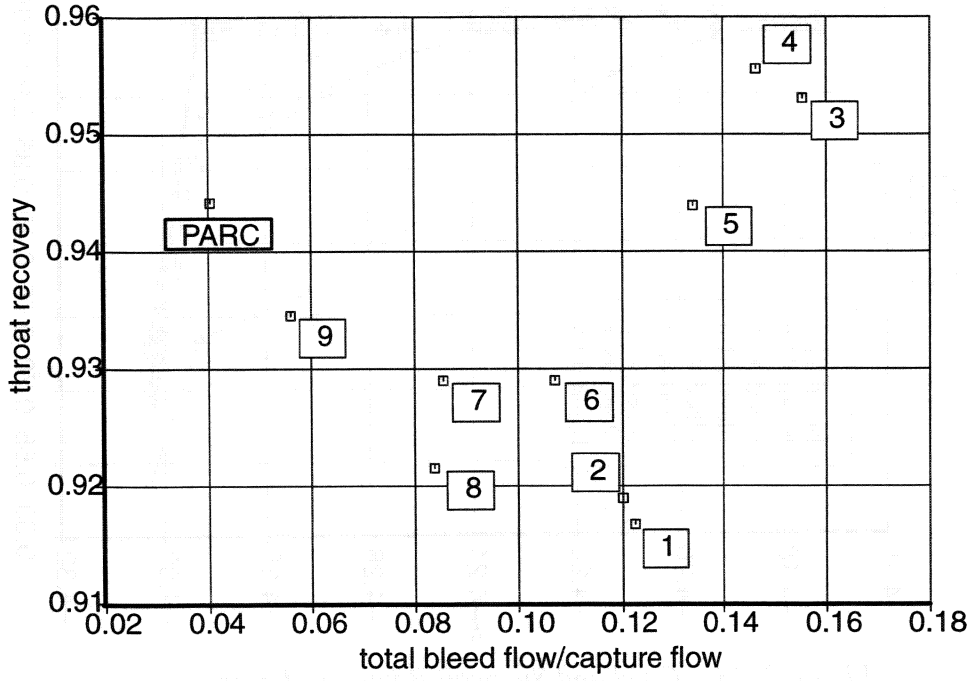

Figure 3–22. Total Bleed Flow vs. Throat Recovery for Bleed Patterns 1–9.

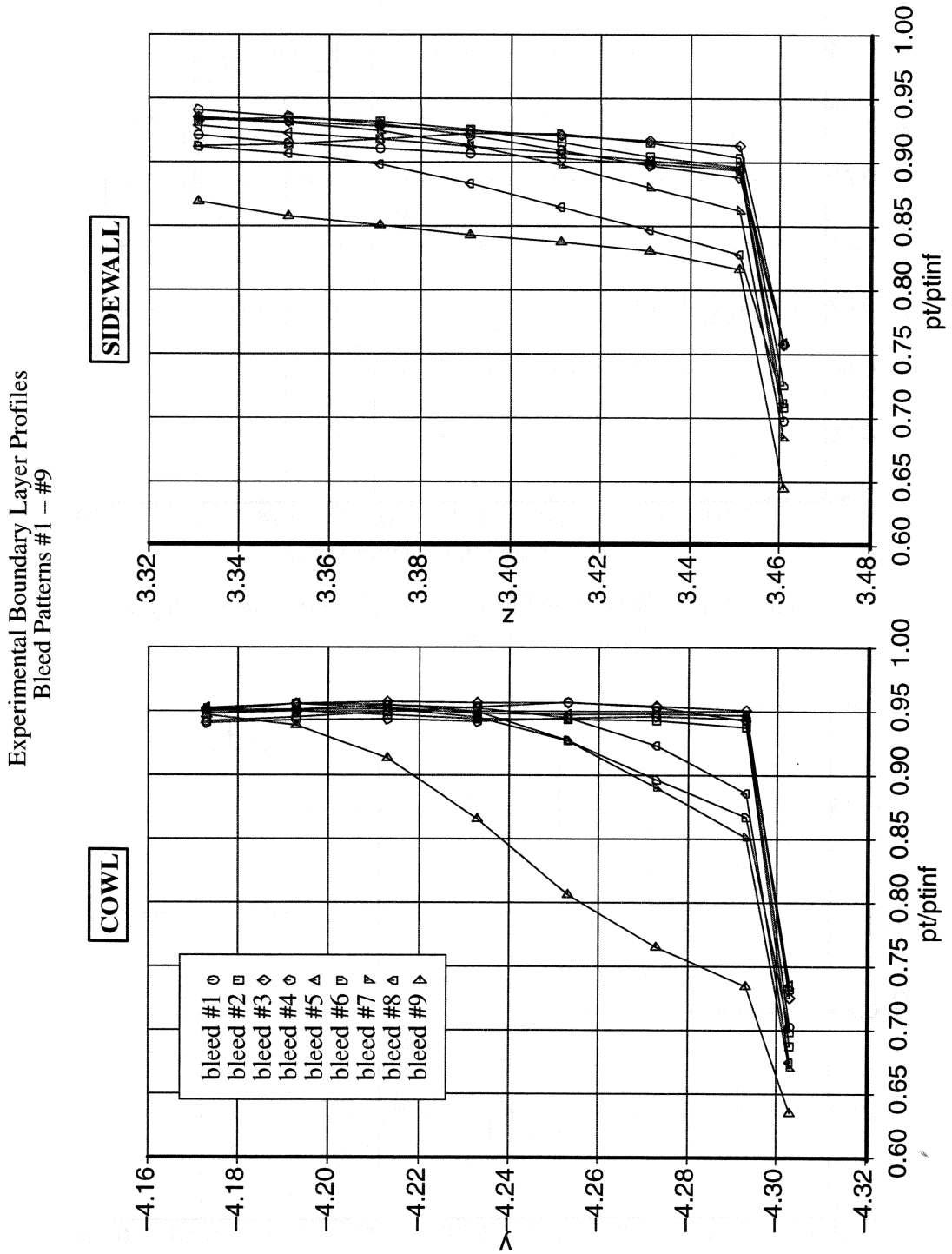

Figure 3–23. Cowl and Sidewall Boundary Layer Experimental Profiles.

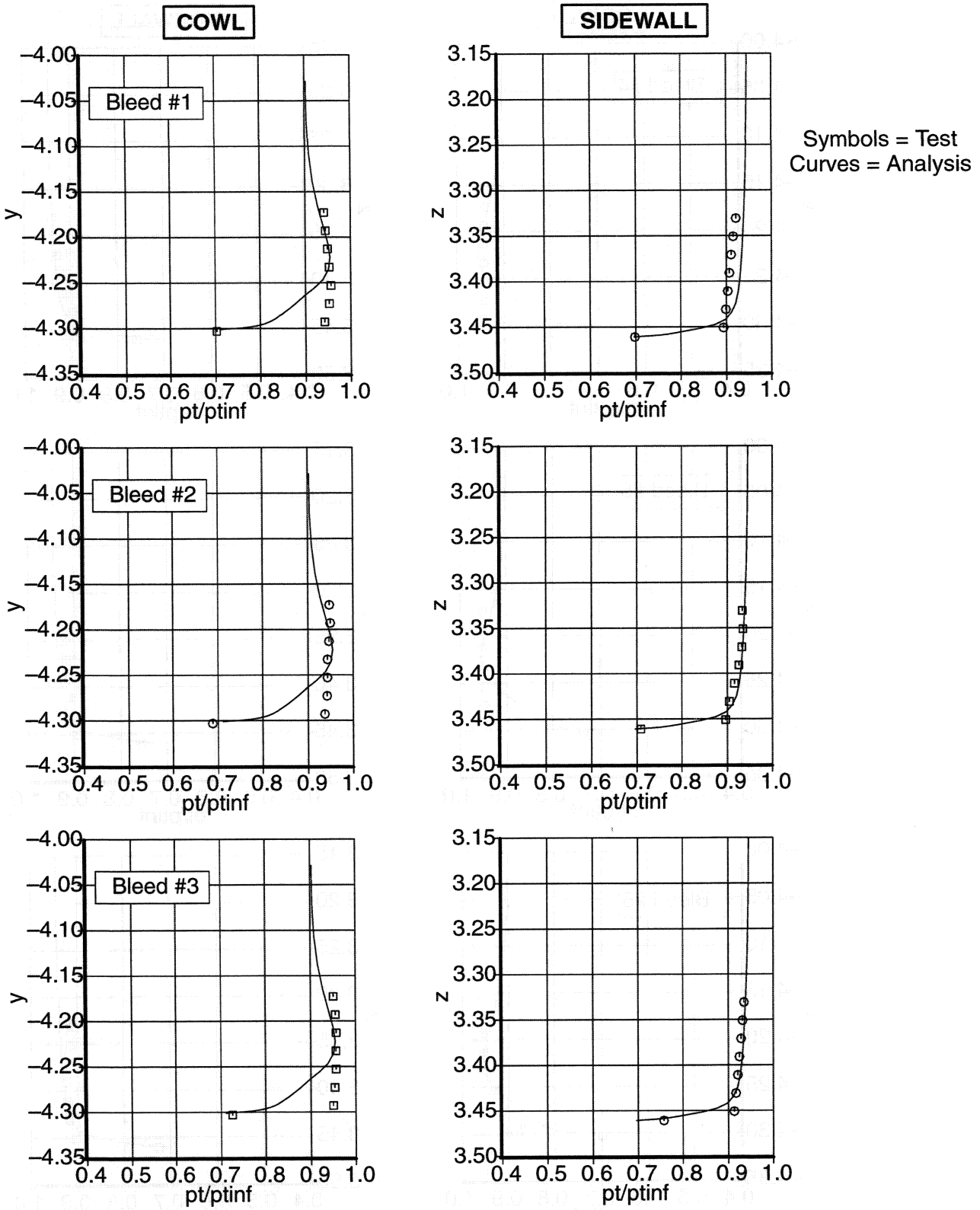

Figure 3–24. PARC and Experimental Boundary Layer Profile Comparison.

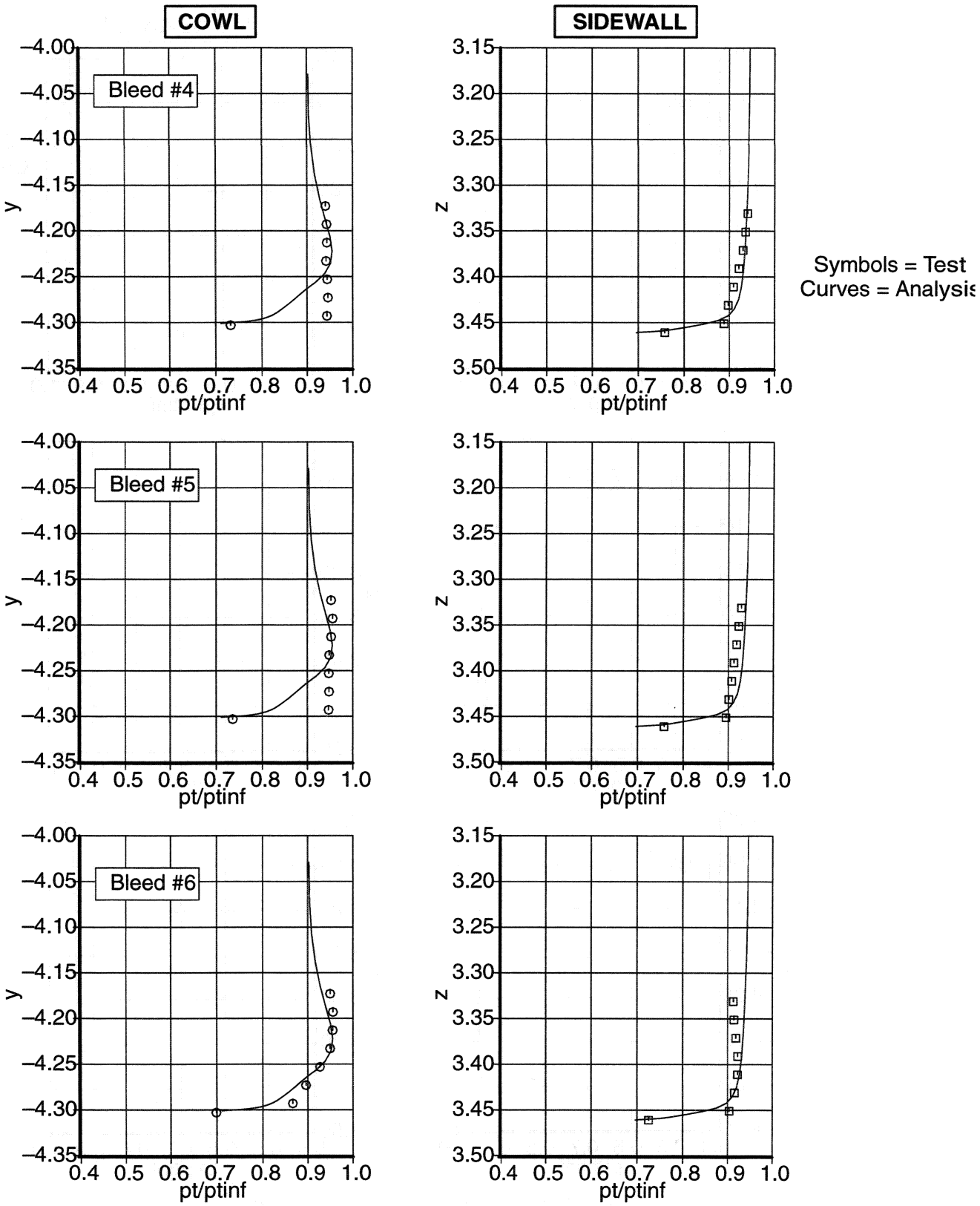

Figure 3–25. PARC and Experimental Boundary Layer Profile Comparison.

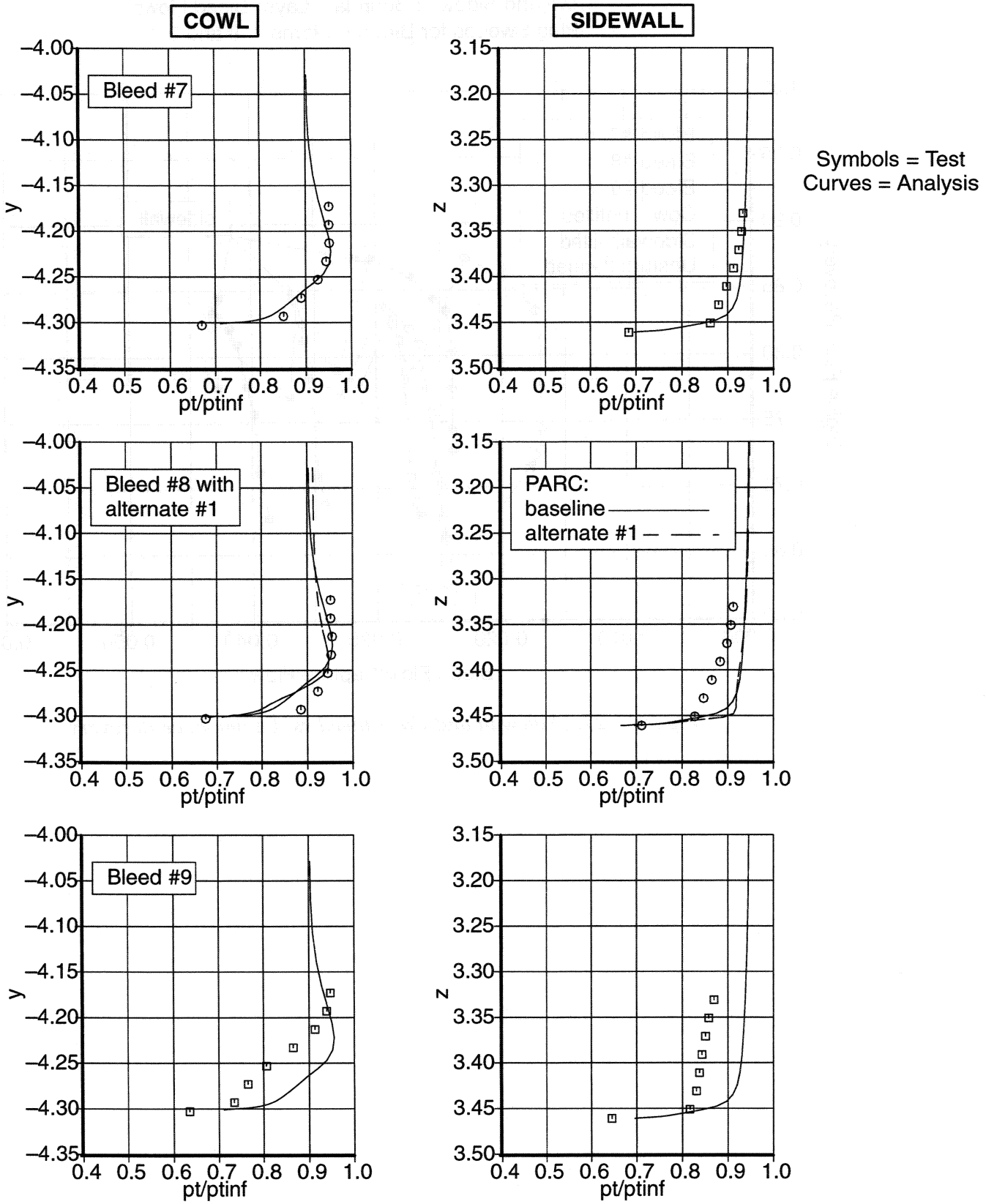

Figure 3–26. PARC and Experimental Boundary Layer Profile Comparison.

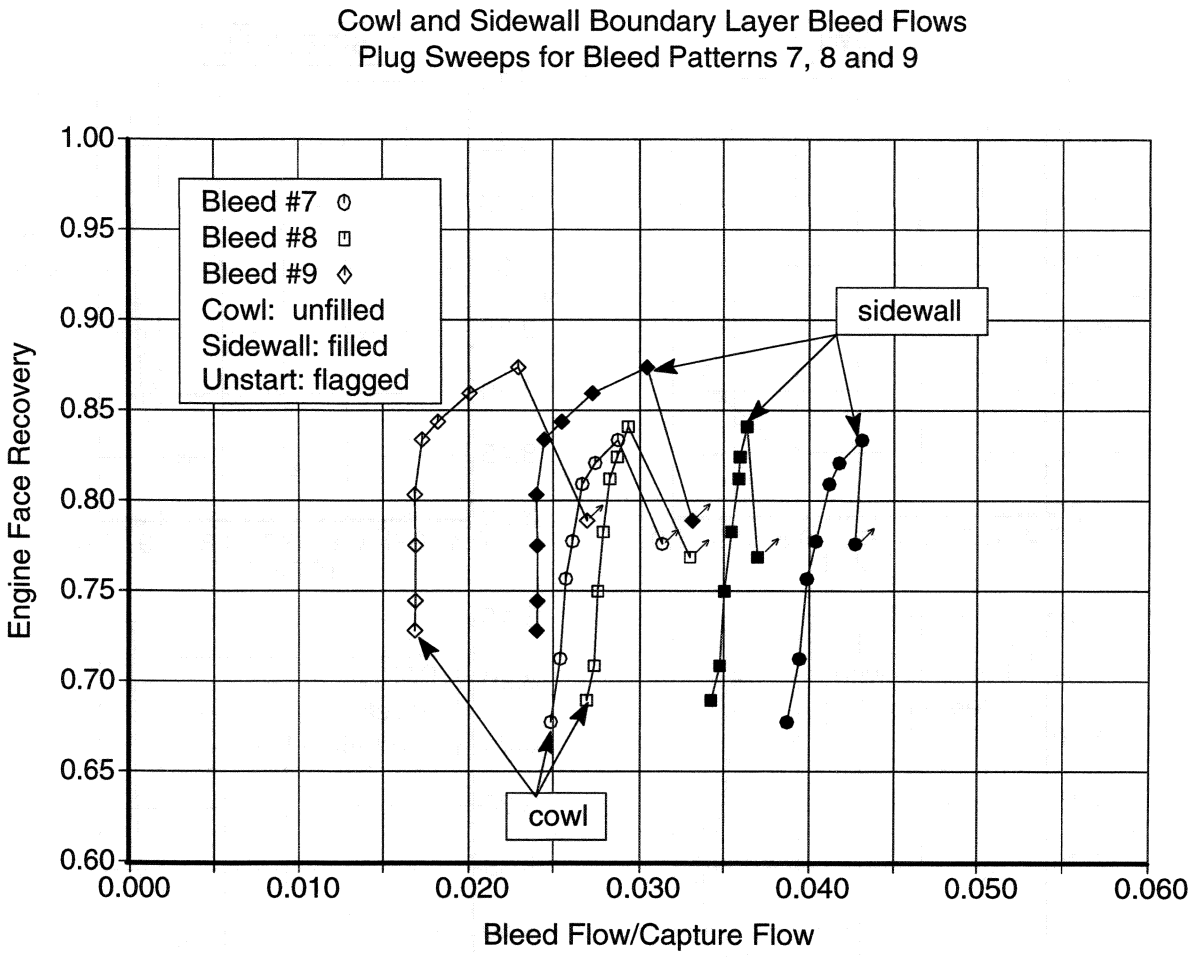

Figure 3–27. Sidewall and Cowl Bleed vs. Engine Face Recovery

3.2. AFT RAMP LEADING EDGE

Four different aft ramp leading edge geometries were studied in order to determine their effect on inlet performance. The importance of the aft ramp leading edge lies in the fact that it is located at the intersection of several key flow field phenomenon as shown in Fig. 3–28 . First, the slot shear layer terminates at this location and must move around the upper–half of the leading edge before entering the plenum. Second, the compressions waves generated by the cowl focus at the aft ramp leading edge. Also, when the inlet is operating at the critical point, the normal shock is located at the leading edge. Lastly, flow that is bleed into the plenum behind the normal shock interacts with the leading edge. All these interactions lead one to the conclude that the leading edge shape could be critical to the performance of the inlet. Since the effect of the leading edge on performance is not well understood, a parametric study was conducted during this test.

Fig. 3–29 shows a comparison of the four different leading edges. The baseline leading edge was a 2:1 ellipse with the highlight located at the focus of the cowl compression waves. Alternate #1 was thicker than the baseline with a longer transition from the highlight to the aft ramp surface. This longer transition resulted in less curvature and was meant to reduce any boundary layer separation that might occur with the baseline geometry. Alternate #2 was also a 2:1 ellipse but was located downstream of the baseline location in order to study the effect of streamwise positioning of the leading edge on inlet performance. Alternate #3 was designed to be similar to alternate #1 but with the highlight moved toward the plenum so that the stagnation point for the flow would more likely be at the highlight and not on the plenum side of the leading edge. Therefore, the alternate #3 geometry should result in less turning of the flow and reduce the possibility of boundary layer separation.

During the wind tunnel test, all four leading edge geometries were tested at different Mach numbers and side–slip angles. However, since the performance of alternate #2 was noticeably lower (it was difficult to keep the inlet started), only a limited amount of data was taken for this geometry. Not all of the leading edges were tested with the same boundary layer bleed pattern so that a direct comparison cannot be made between all geometries. The baseline, alternate #1, and alternate #2 leading edges were tested with bleed pattern #7, while alternate #1 and alternate #3 leading edges were tested with bleed pattern #8. The performance of the leading edges was determined from pressure distributions on the aft ramp, the throat total pressure rakes, and recovery at the engine face. Ideally, these measurements could be made more meaningful if flow visualization of the throat region were possible in order to determine the leading edge effects on the interactions taking place in that region. Currently, CFD provides a means to examine the flow field details at the leading edge and will be presented here to augment the experimental data.

For a true comparison, data for the following plots were selected from runs that had the most similar model and wind tunnel conditions. For the bleed #7 results, the baseline and alternate #1 readings had the same ramp positions and plenum door openings. Alternate #2 had slightly different ramp positions: forward ramps at 12.10 (port) and 12.29 (starboard) vs. 11.92 for the baseline; and aft ramps at 2.09 vs. 2.19 for the baseline. The plenum doors were larger at 1.20 than the baseline position of 0.80. These differences are small enough that it was felt that a direct comparison could be made between these three leading edges.

Fig. 3–30 shows the throat and engine face recoveries versus corrected engine flow for the baseline, alternate #1 and alternate #2 leading edges at Mach 2.35 with bleed pattern #7. Evident in the figure is that the alternate #1 leading edge produces a higher throat and engine face recov-

ery than the baseline or alternate #2. As the corrected flow is reduced (normal shock moves forward), the difference in recovery between the three inlets becomes less, but alternate #1 remains the highest. The alternate #2 data is offset to the left because of the larger plenum door opening which results in less engine corrected flow for a given normal shock position. One can see that the difference in recovery between alternate #1 (and the baseline) and alternate #2 is larger at the throat than at the engine face. The reason for this can be deduced from Fig. 3–31.

Fig. 3–31 shows the measured throat rake total pressures for the baseline, alternate #1 and alternate #2 leading edges along with 3D viscous PARC computational results of the throat rake total pressures for the baseline and alternate #1 leading edges. All the results are for when the normal shock is in the critical position. The figure shows that the profiles are relatively flat away from the cowl and aft ramp. Also, the experimental results show that the alternate #2 leading edge has low recovery near the aft ramp which results in the lower throat recovery shown in Fig. 3–30. The CFD results indicate that the lower recovery is confined to a region close to the walls. By using an area weighted averaging for the experimental throat recoveries, the recovery for alternate #2 is lower than the other recoveries due to one of its probes picking up the small low pressure region near the aft ramp. A more equitable comparison would be obtained using a mass flux based method. As the flow is mixed in the subsonic diffuser, a more accurate average is obtained at the engine face and so the difference in recovery for alternate #2 at the engine face becomes less than at the throat. The difference between the PARC and experimental results is due to, in part, different amounts of boundary layer bleed and the fact that the normal shock is farther upstream in the PARC calculations as shown in Appendix A.1.

Fig. 3–32 shows the surface static pressure distributions on the port aft ramp for the baseline, alternate #1, and alternate #2 leading edges along with PARC results for the baseline and alternate #1 leading edges. The figure shows that for the experimental results, the alternate #1 pressures are the highest, while the alternate #2 pressures are the lowest. This agrees with the recovery findings shown previously. The PARC results are shown from the end of the forward ramp, along the slot, and along the aft ramp. The PARC aft ramp pressures are higher than the experiment due to the shock being farther upstream in the PARC calculations. The alternate #1 PARC aft ramp pressures are lower than the PARC baseline due to an expansion that is occurring along the forward part of the slot which causes the flow to turn slightly into the plenum. This expansion results in larger normal shock losses and additional turning around the aft ramp leading edge that combine to produce lower pressures along the aft ramp. More PARC analysis is required to understand this flow condition.

For the bleed #8 results of the alternate #1 and #3 leading edges, the starboard ramps of the model and the upper and lower plenum bleed doors were set the same. The port forward ramp for alternate #1 was 11.4 degrees, while for alternate #3 it was 11.6 degrees. The port aft ramp for alternate #1 was set at 2.09", while for alternate #3 it was set at 2.13". These differences were felt to be small enough for direct comparison of the two leading edges, especially since the throat total pressure rakes were on the starboard side which was at the same position for both readings.

Fig. 3–33 shows the throat and engine face recoveries versus corrected engine flow for the alternate #1 and alternate #3 leading edges at Mach 2.35 with bleed pattern #8. One can see from the figure that there is little difference in recovery between the two leading edges, with alternate #3 having a slightly better engine face recovery.

Fig. 3–34 shows the measured throat rake total pressures for the alternate #1 and alternate #3 leading edges along with 3D viscous PARC computational results of the throat rake total pressures for the baseline and alternate #1 leading edge. Both sets of data are at the critical normal shock position. The experimental results show similar trends for both leading edges. The PARC results are in reasonable agreement for the middle and sidewall rakes, while for the centerline rake they are lower than experiment.

Fig. 3–35 shows the surface static pressure distributions on the port aft ramp for the alternate #1 and alternate #3 leading edges along with PARC results for the baseline and alternate #1 leading edges. As can be seen in the figure, the alternate #3 aft ramp surface pressures are slightly higher than the alternate #1 pressures. Both sets of experimental data are similar to the baseline PARC predictions The alternate #3 pressures are slightly lower due to the shock being further downstream as shown in Appendix A.1. The alternate #1 PARC pressures are lower than experiment due to the reasons discussed earlier.

A leading edge that extends farther upstream was not tested because it was felt that it would cause poor performance due to restricting bleed behind the normal and would interfere with the convergence of the compression waves off the cowl. From Fig. 3–30 and Fig. 3–33 it can be concluded that of the four leading edges, alternate #3 provides slightly better performance. The data plots in this section substantiate this finding by showing alternate #3 results in good recovery at the throat and high pressures in the subsonic diffuser. Another conclusion that can be drawn from the data is that aft ramp leading edge shape is less important than its location. This comes from the fact that the baseline, alternate #1 and alternate #3 leading edges had different shapes with similar highlight locations but produced similar recoveries, while the baseline and alternate #2 had the same shape with different highlight locations but produced different recoveries.

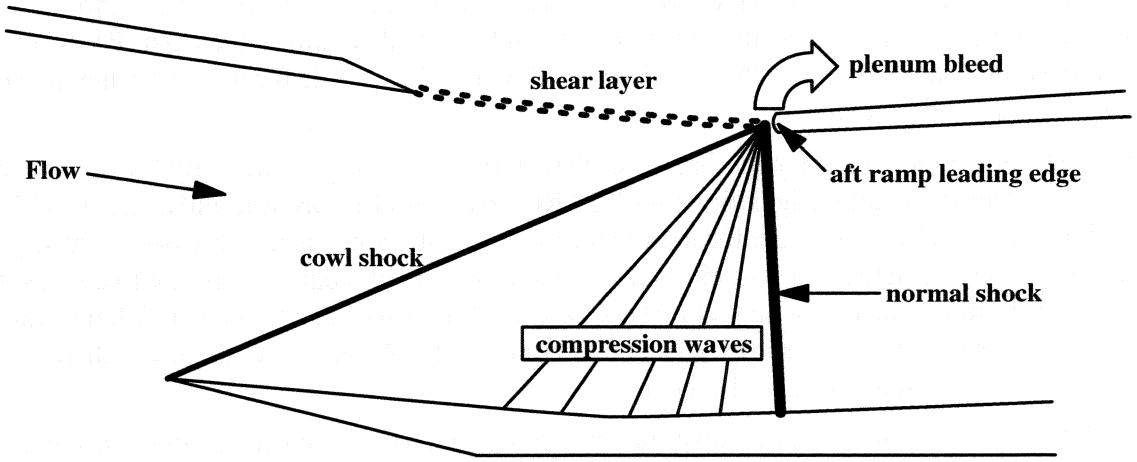

Figure 3–28. Aft Ramp Leading Edge Flow Field

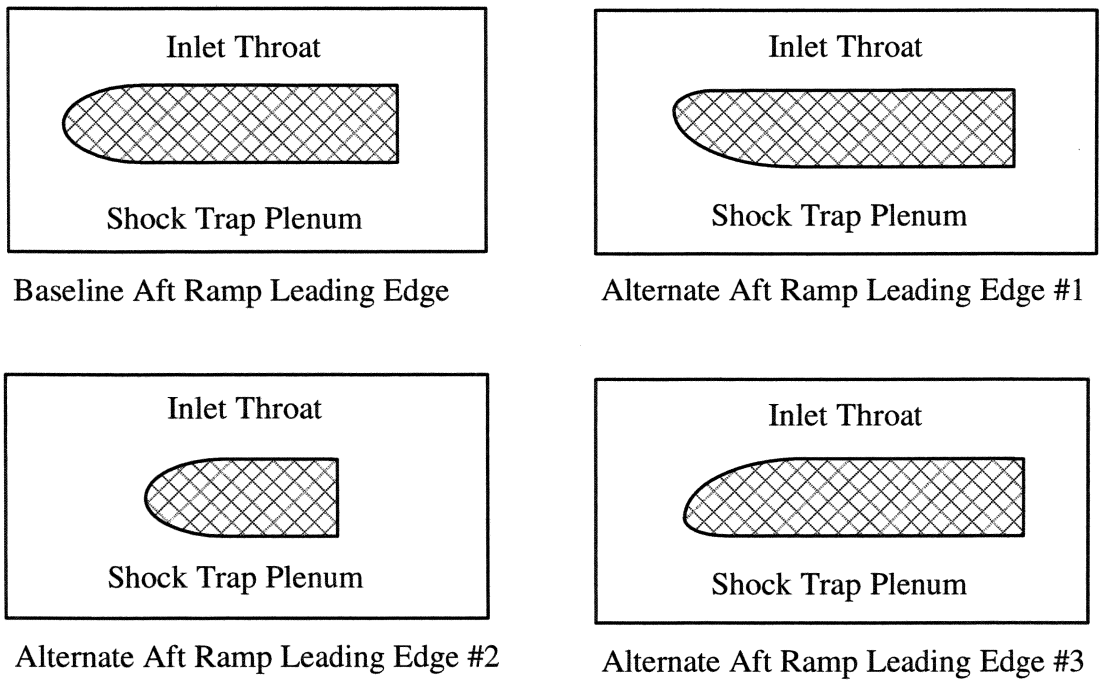

Figure 3–29. Aft Ramp Leading Edge Configurations

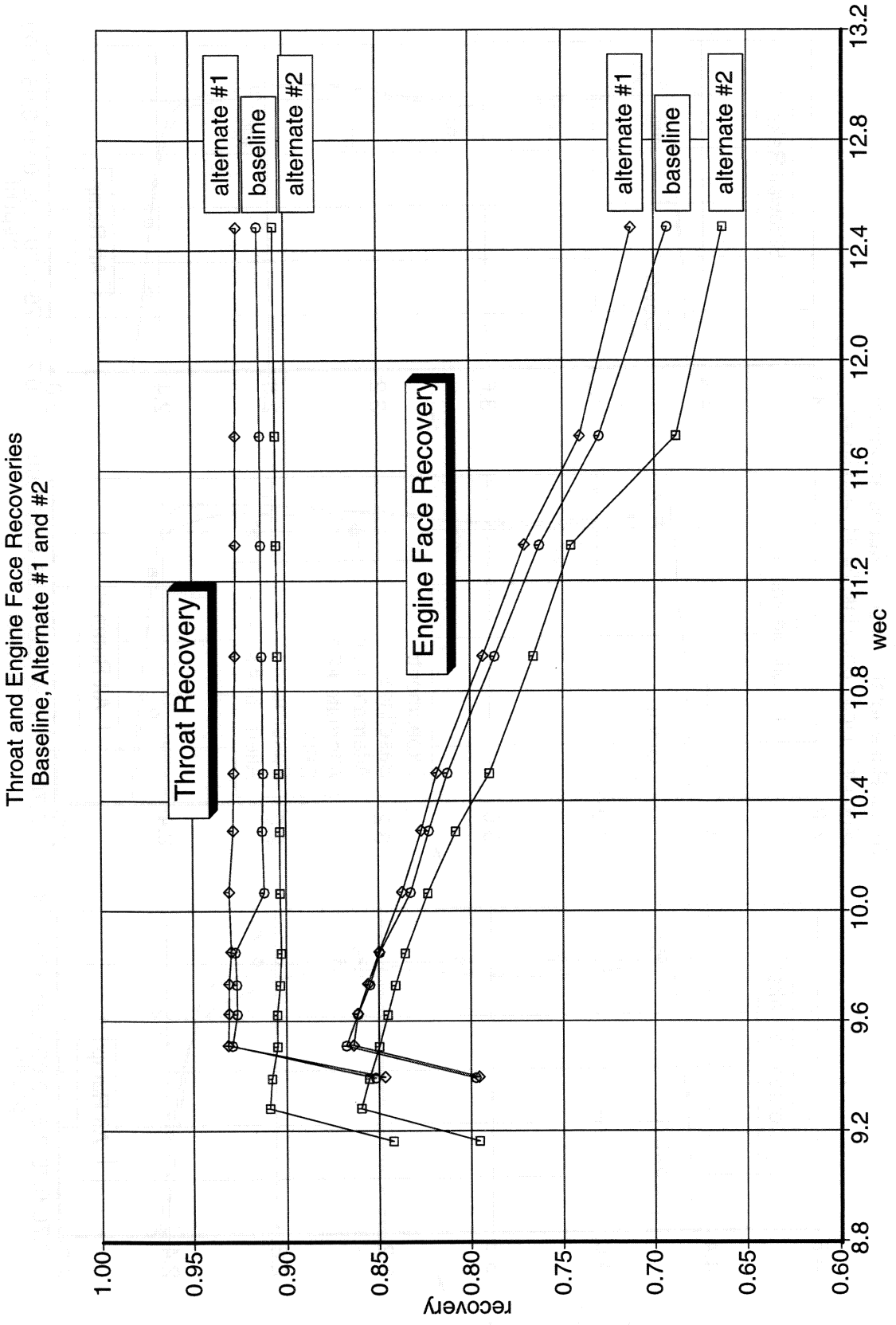

Figure 3–30. Throat and Engine Face Recovery vs. Corrected Air Flow

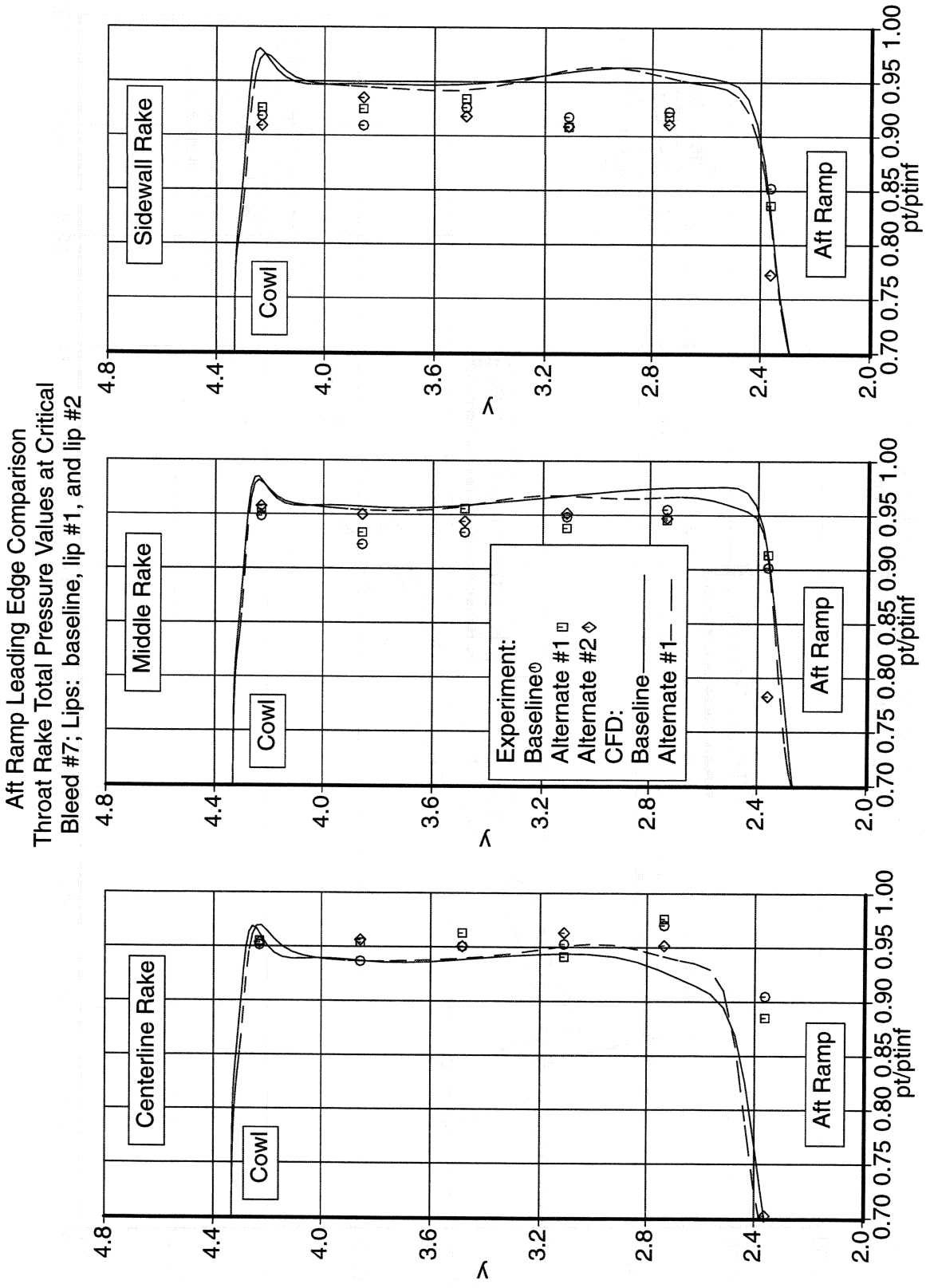

Figure 3–31. Throat Rake Total Pressure Profiles Comparison.

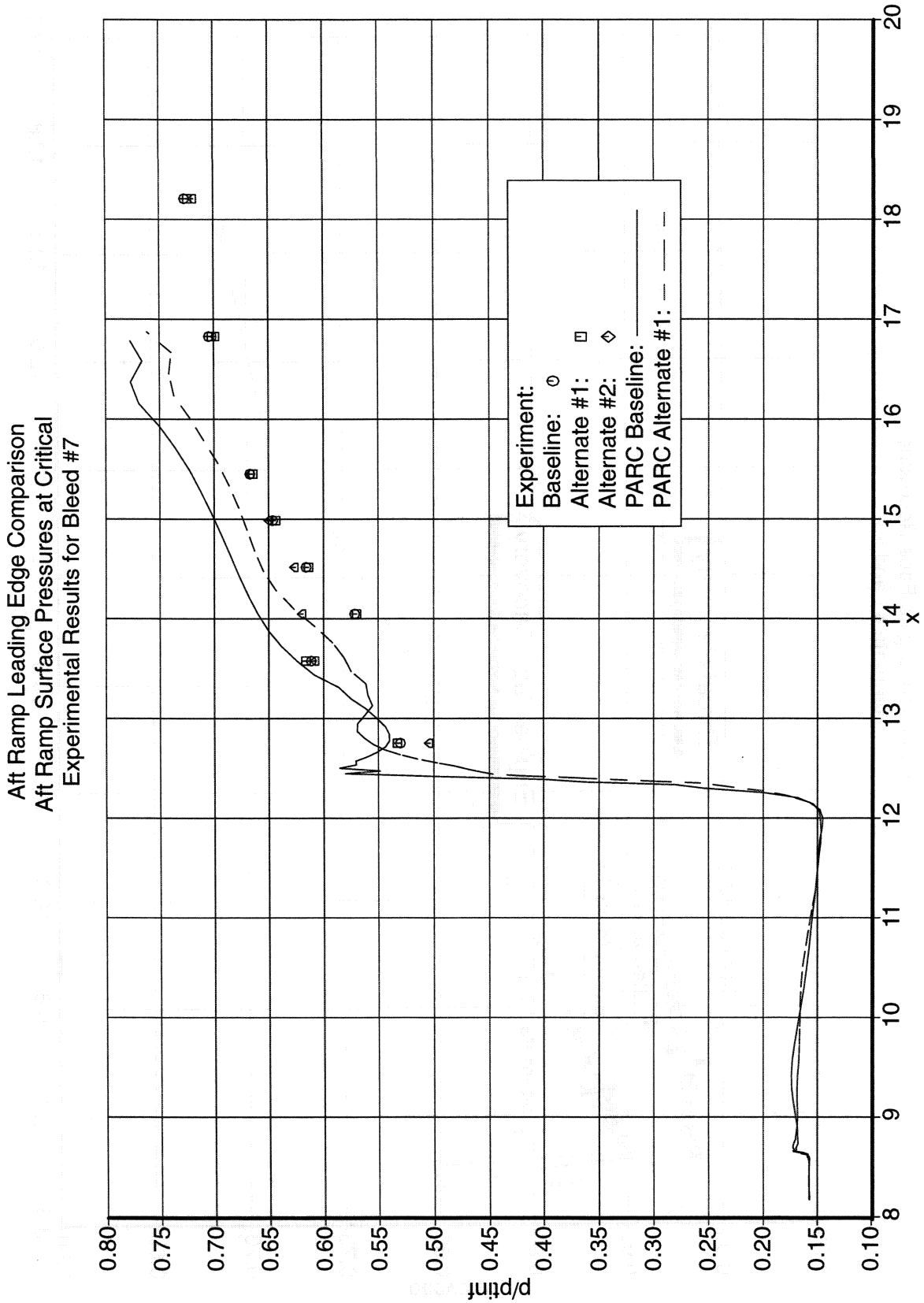

Figure 3–32. Aft Ramp Surface Pressure Comparison.

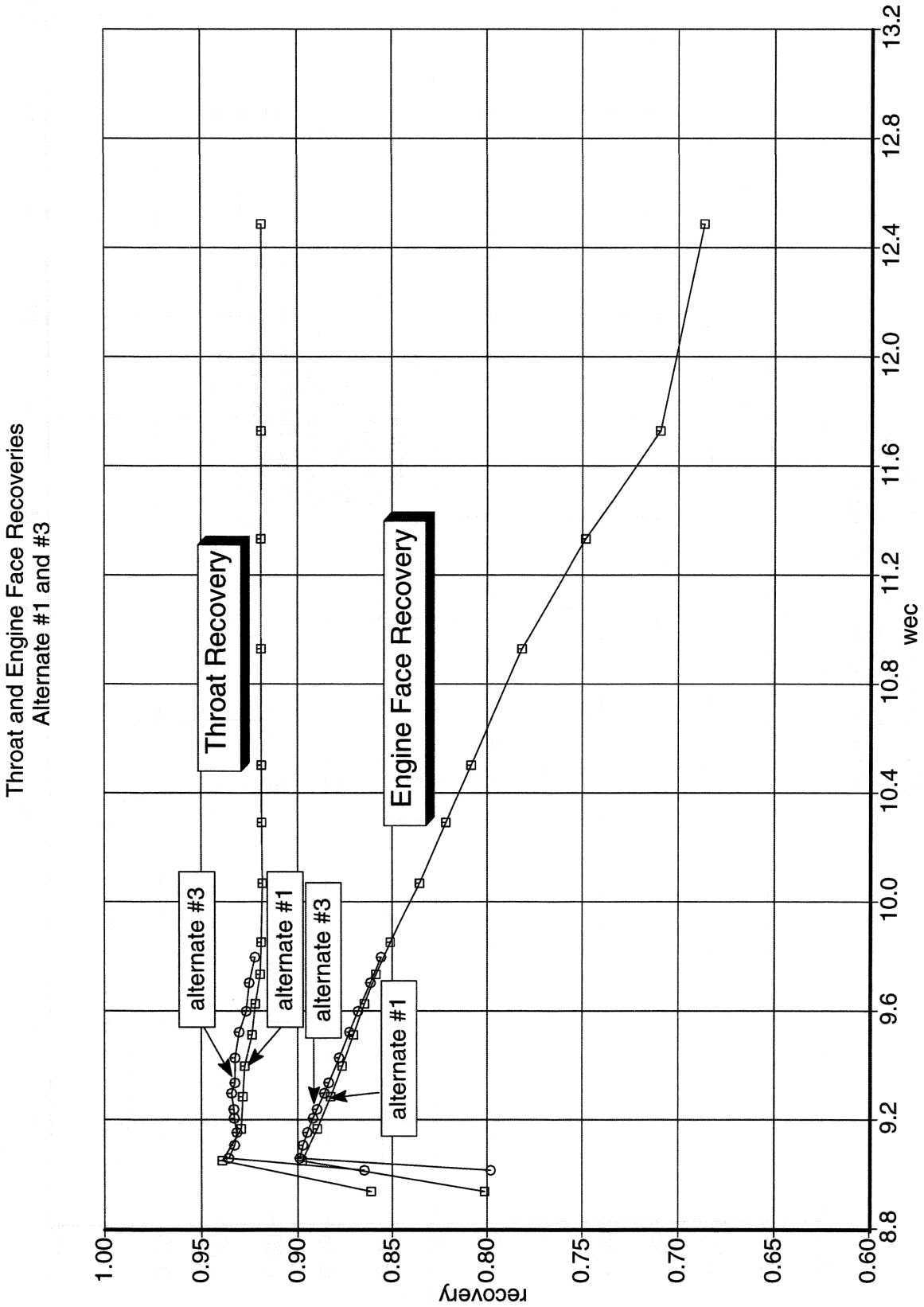

Figure 3–33. Throat and Engine Face Recovery vs. Corrected Air Flow.

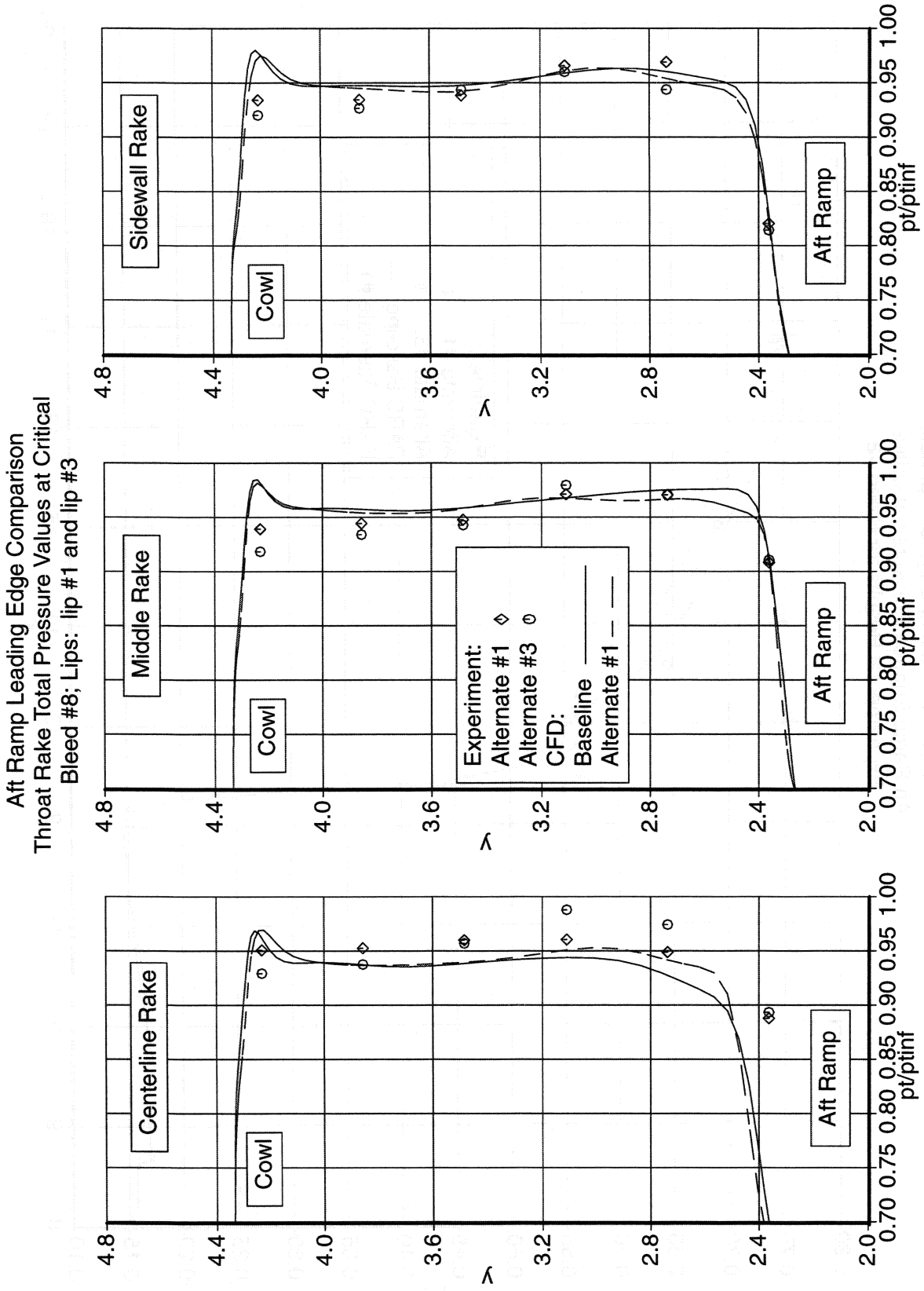

Figure 3–34. Throat Rake Total Pressure Profiles Comparison.

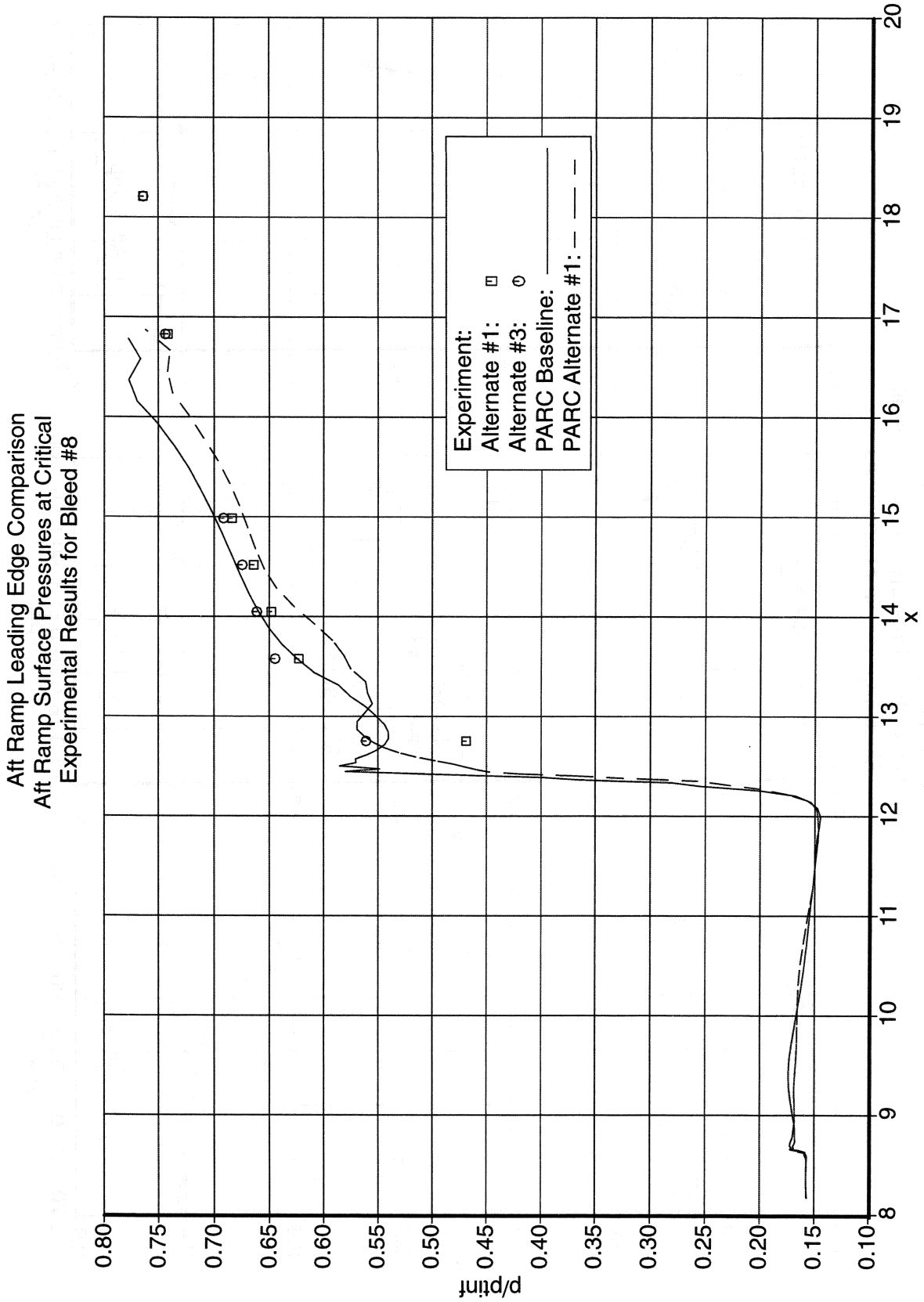

Figure 3–35. Aft Ramp Surface Pressure Comparison

3.3. VORTEX GENERATORS

Three different vortex generator patterns were studied in order to determine their effect on subsonic diffuser performance. Vortex generators are used to prevent separation and minimize distortion. These benefits, however, need to be traded against the performance losses they introduce. The optimal vortex generator pattern is the one that yields the highest recovery with an acceptable distortion level.

The three sets of vortex generator configurations investigated are shown in Figs. 3–36, 3–37, and 3–38. The baseline concept uses 8 pairs of rectangular tabs generating counter–rotating vortices. Alternate pattern #1 is the same as the baseline configuration except the two mid–ramp vortex generator pairs are removed. Alternate pattern #2 uses 8 pairs of triangular tabs in the same arrangement as the baseline pattern.

Due to a poor subsonic diffuser design, achieving an acceptable level of distortion was not possible with any of the vortex generator configurations. The lowest level of distortion achieved was over 18% where a level on the order of 10% is acceptable, based upon $(Pt_{max}–Pt_{min})/Pt_{avg}$. Fig. 3–39 presents a performance summary for the three configurations. This performance comparison is for the design condition of Mach 2.35, bleed configuration #9, zero angle–of–attack, zero angle–of–yaw, and minimum shock trap flow. Data for the corresponding critical point is summarized in Figs. 3–40 and 3–41. Using area averaged total pressure recovery and $(Pt_{max}–Pt_{min})/Pt_{avg}$ distortion as metrics, there is little difference between each of the vortex generator configurations. Performance is poor for all three. The baseline concept was selected for the rest of the test as "optimum" since recovery is relatively high and distortion is relatively low.

Recovery contour plots for each set of vortex generators at the Mach 2.35 critical point are shown in Figs. 3–42, 3–43, and 3–44. The influence of the throat rake on the starboard side of the inlet is apparent in each of the contour plots. Further examination of the starboard side distortion indicates the throat rakes have a greater influence on the distortion pattern than any of the vortex generator sets tested.

Examination of the port side recovery contours indicates a modest difference in the type of distortion resulting from each set of vortex generators. Both configurations using the rectangular tabs result in predominantly radial distortion, whereas distortion resulting from the triangular tabs has an added circumferential characteristic. The radial distortion in a 2D, bifurcated inlet may be a result of the very large bullet nose at the inlet/engine interface. The circumferential characteristic resulting from the triangular tabs may suggest less mixing than is generated by the rectangular tabs.

Due to the poor subsonic diffuser design and resulting poor performance, an attempt to refine comparisons beyond these qualitative assessments has not been made.

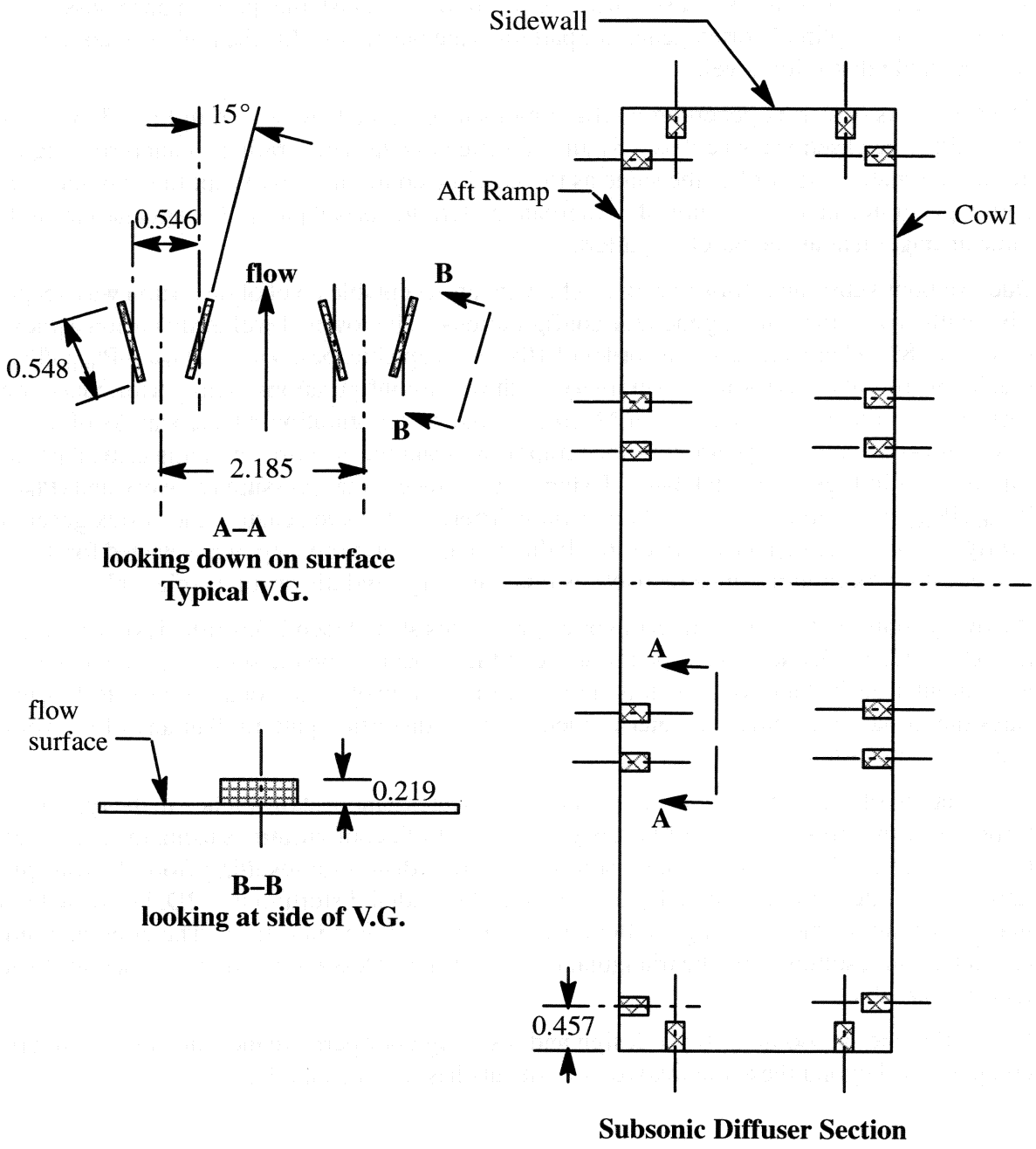

Figure 3–36. Baseline Vortex Generator Pattern (No. 0)

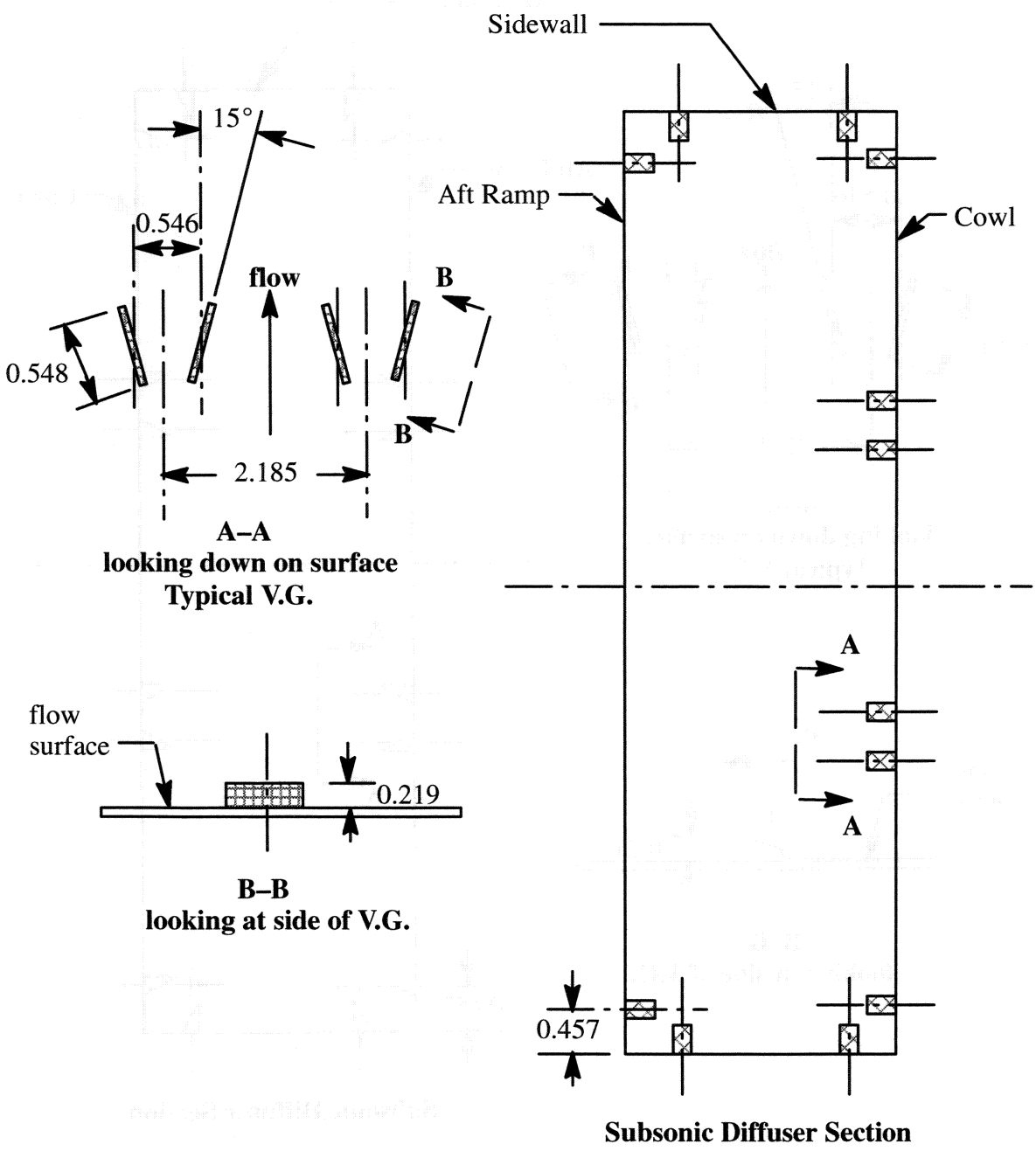

Figure 3–37. Alternate Vortex Generator Pattern #1

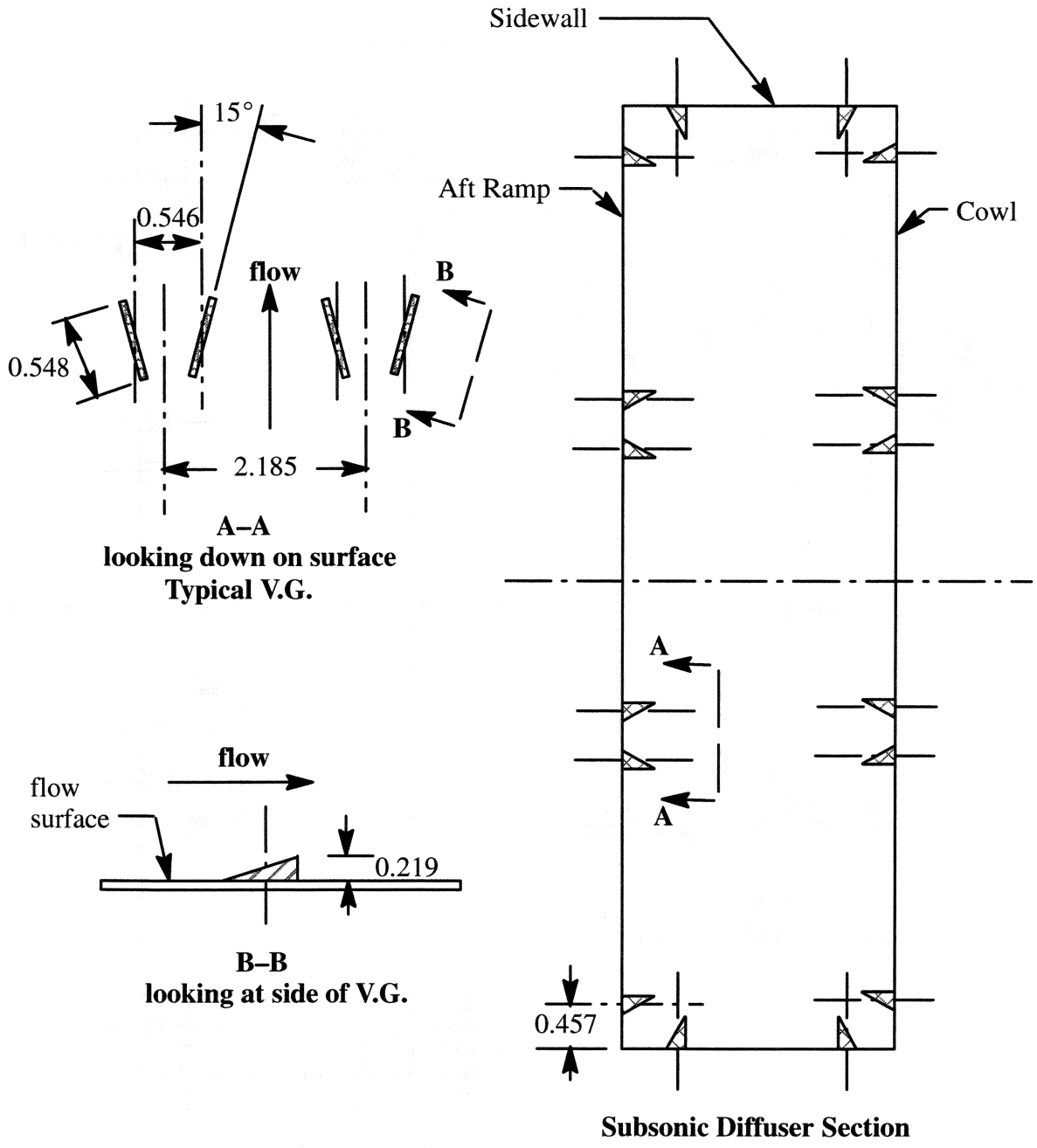

Figure 3–38. Alternate Vortex Generator Pattern #2

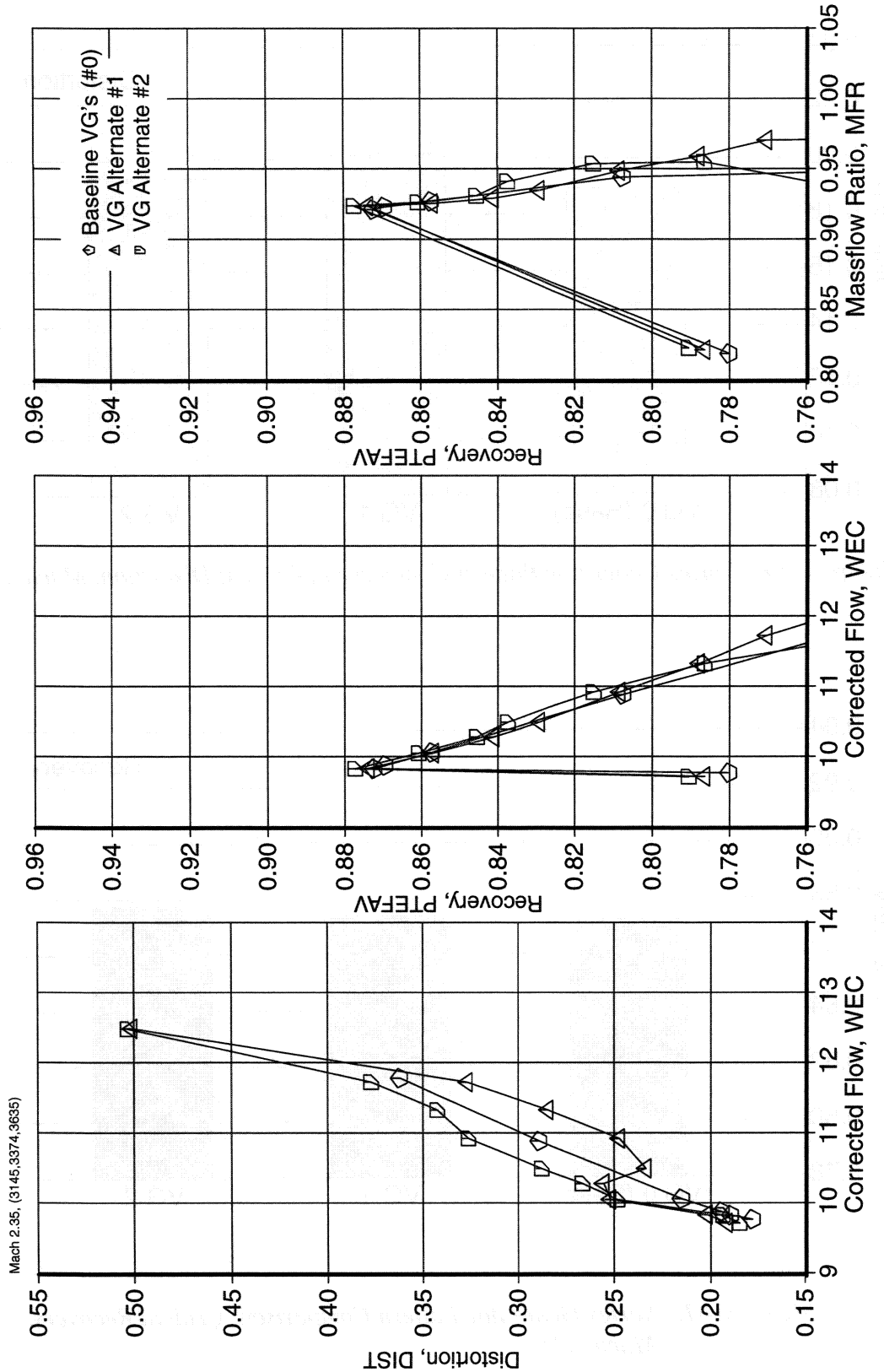

Figure 3–39. Vortex Generator Configuration Effects, Mach 2.35, Bleed No. 9, Zero Angle–of–Attack, Zero Angle–of–Yaw.

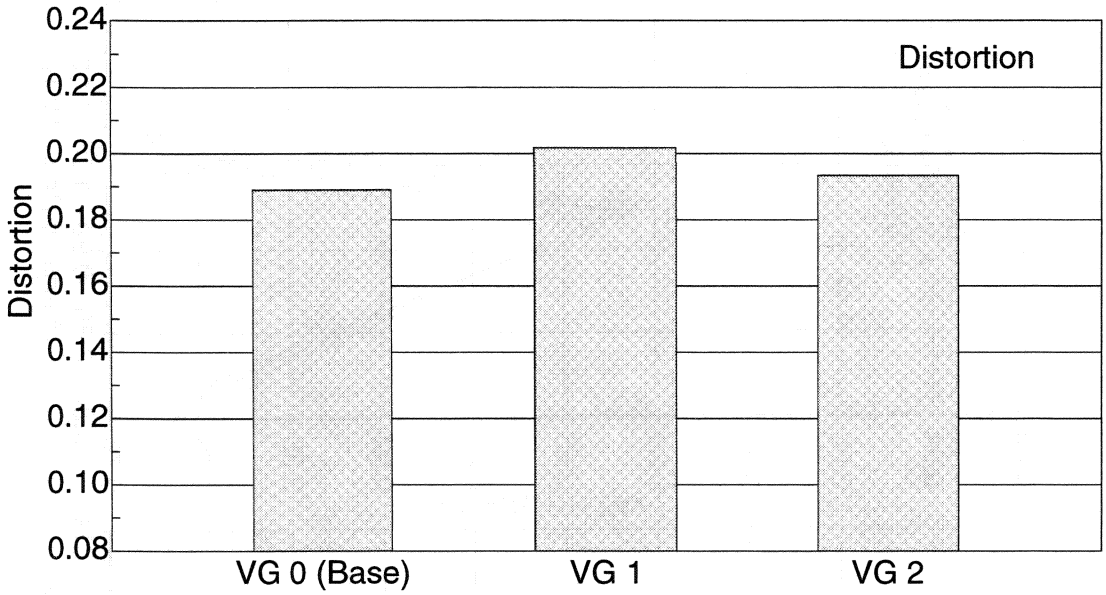

Figure 3–40. Vortex Generator Pattern Comparison, Critical Distortion, Mach 2.35.

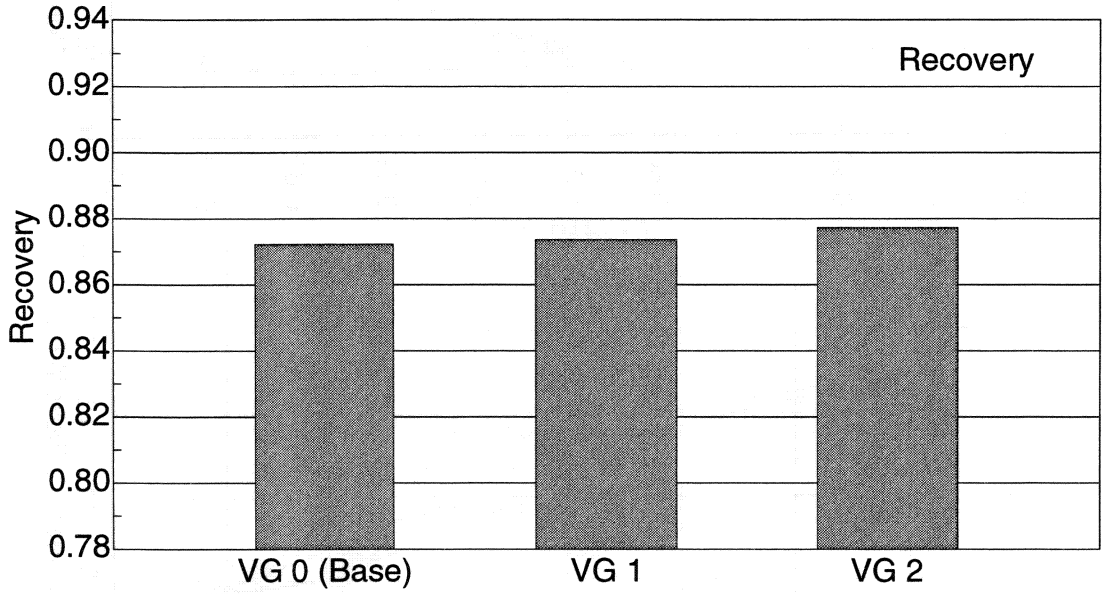

Figure 3–41. Vortex Generator Pattern Comparison, Critical Recovery, Mach 2.35

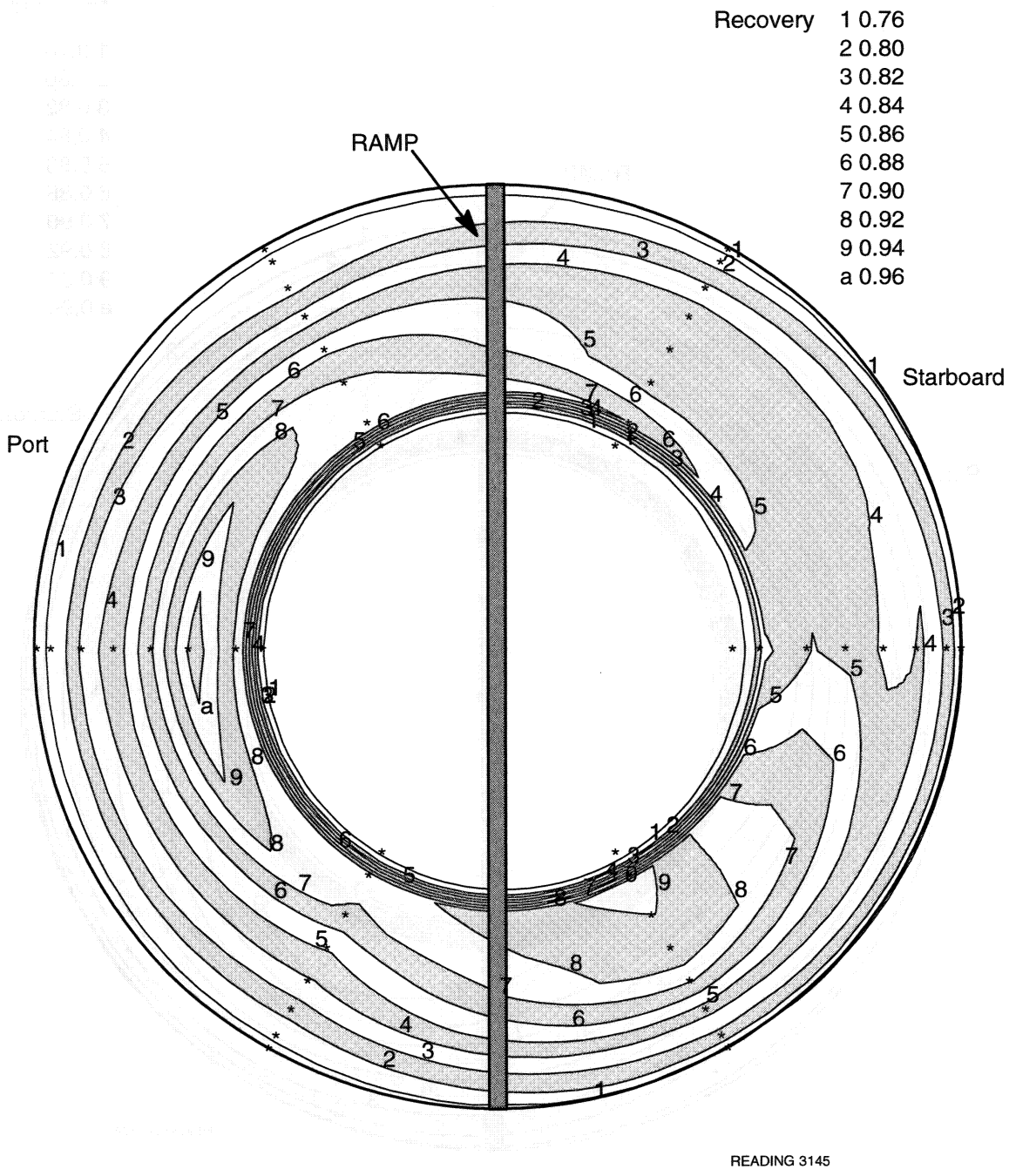

Figure 3–42. Engine Face Recovery Contours with Baseline Vortex Generator Pattern (#0) at Mach 2.35 Critical Point.

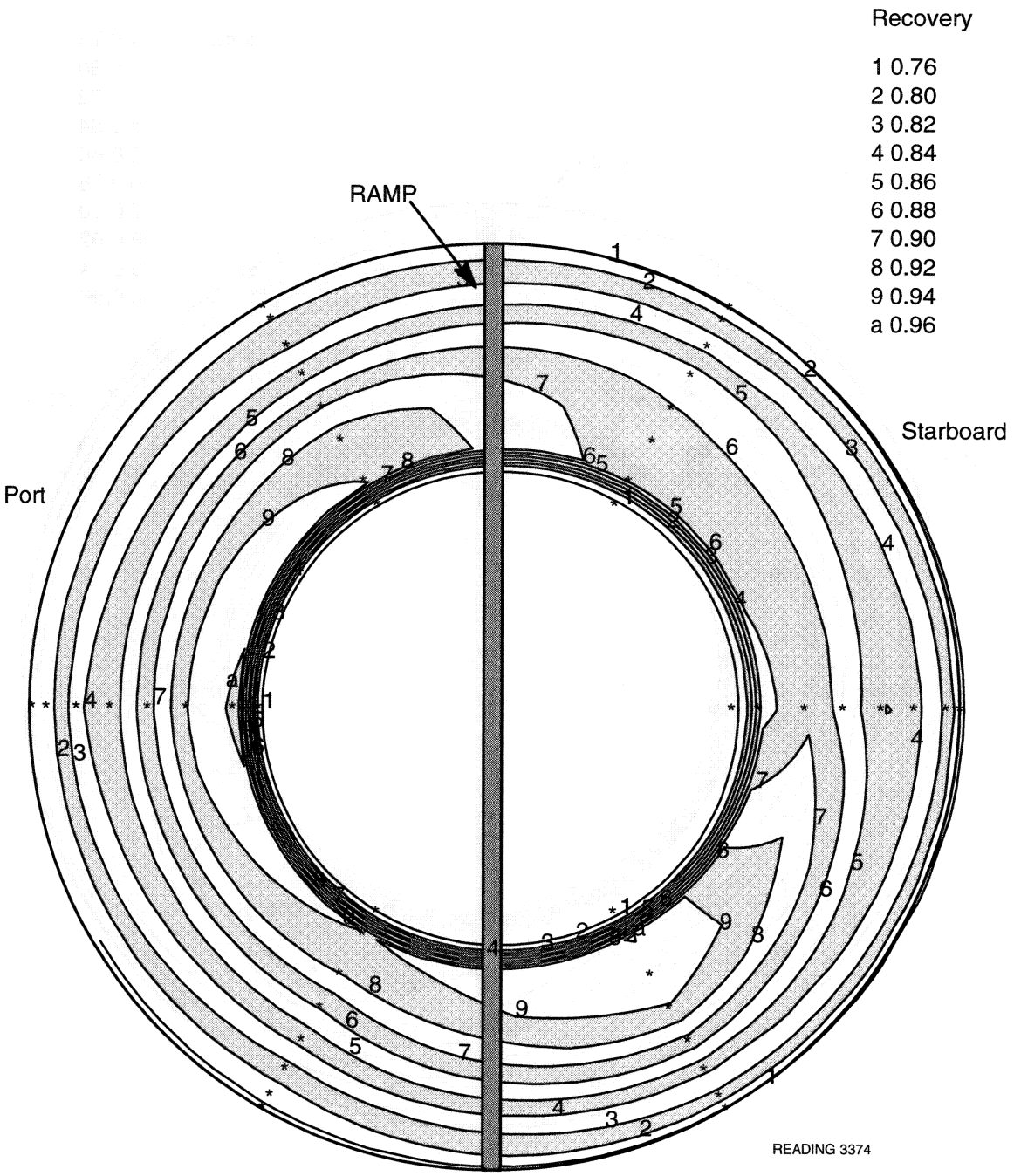

Figure 3–43. Engine Face Recovery Contours with Alternate Vortex Generator Pattern #1 at Mach 2.35 Critical Point.

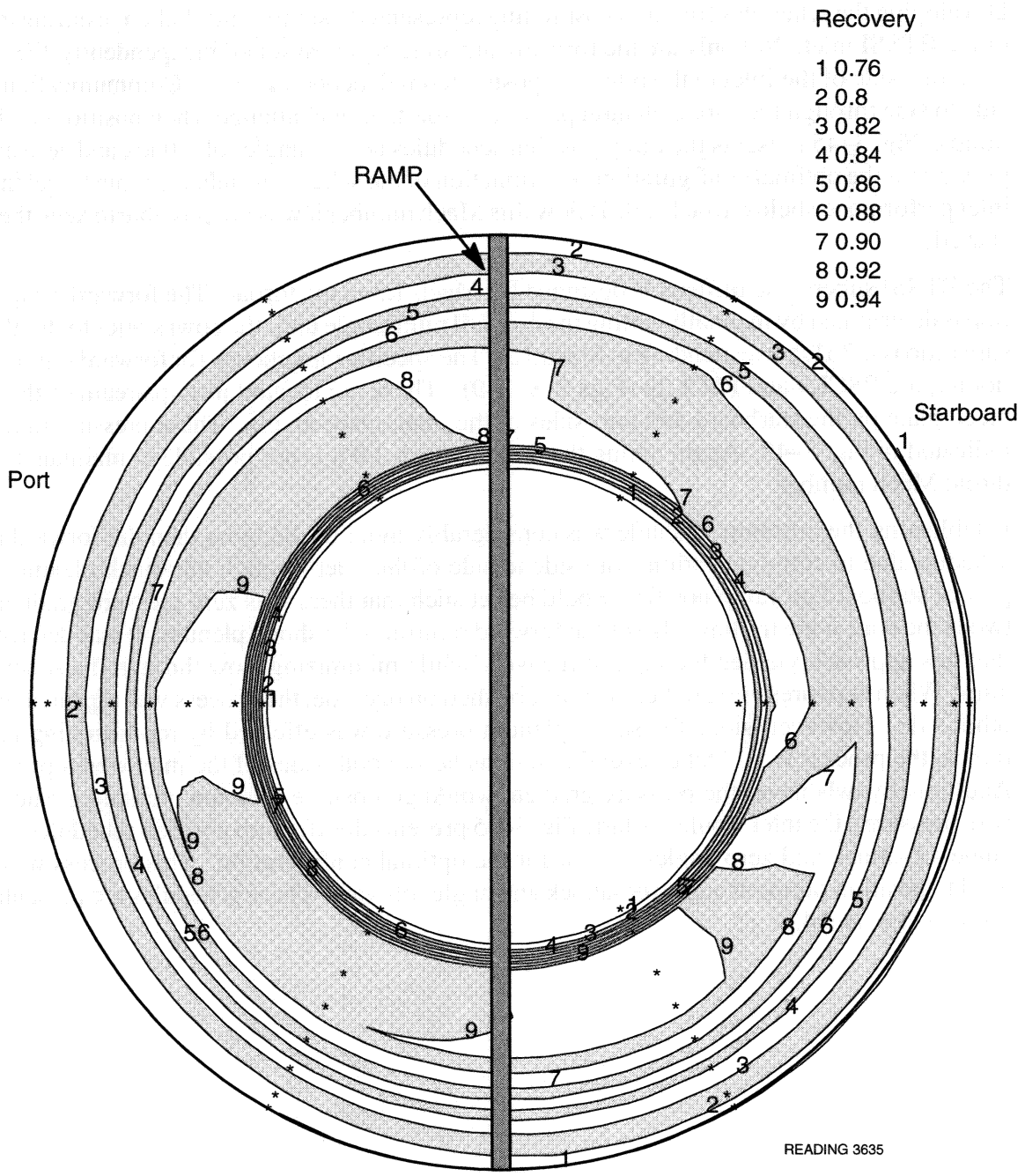

Figure 3–44. Engine Face Recovery Contours with Alternate Vortex Generator Pattern #2 at Mach 2.35 Critical Point.

3.4. FORWARD AND AFT RAMP SCHEDULES

Developing the schedules for ramp positioning represented a significant challenge during testing of the BTSSI inlet. Not only are the forward and aft ramps positioned independently, the ramps from one side of the inlet to the other are positioned independently also. Communication from side to side through the shock plenum presented a particular challenge when positioning the aft ramps. Fig. 3–45 presents the ramp position schedules at zero angle–of–attack and zero angle–of–yaw for the optimal configuration. Examination of the schedules indicate ramp travel limited inlet performance below Mach 2.0. Below this Mach number it was not possible to keep the inlet started.

The BTSSI supersonic diffuser is designed for Mach 1.3 in the throat. The forward ramp position is determined by manually setting the forward ramp angle until the cowl static–to–total pressure ratio is 0.361, corresponding to Mach 1.3. The specific taps chosen for forward ramps positioning are PSCL9 and PSCL29 (Figs 2–8, 2–9). These are located just upstream of the cowl bleed plate on the starboard and port sides of the inlet, respectively. These pressure ratios are indicated in Fig. 3–45. Again noting that below Mach 2.0 it is not possible to maintain the 1.3 throat Mach number.

Establishing the aft ramp schedule was considerably more challenging than the forward ramp schedule due to communication from side to side of the inlet through the shock plenum. The port or starboard aft ramp position would be set such that there was zero pressure gradient between the core at the trailing edge of the forward ramp and the shock plenum. It was determined that this approach yielded the highest recovery while minimizing flow through the shock plenum. When zero pressure gradient was established on one side, the process was repeated for the other side. However, since the shock plenum pressure was effected by repositioning the aft ramps, the process would take several iterations before both sides of the inlet were optimized. Additionally, whenever the pressure gradient would go positive (plenum pressure greater than core pressure), the inlet would unstart. Fig. 3–45 presents the aft ramp position schedules at zero angle–of–attack and zero angle–of–yaw for the optimal configuration. This process was also used to position ramps at angle–of–attack and angle–of–yaw. These schedules are presented in sections 4.6. and 4.7.

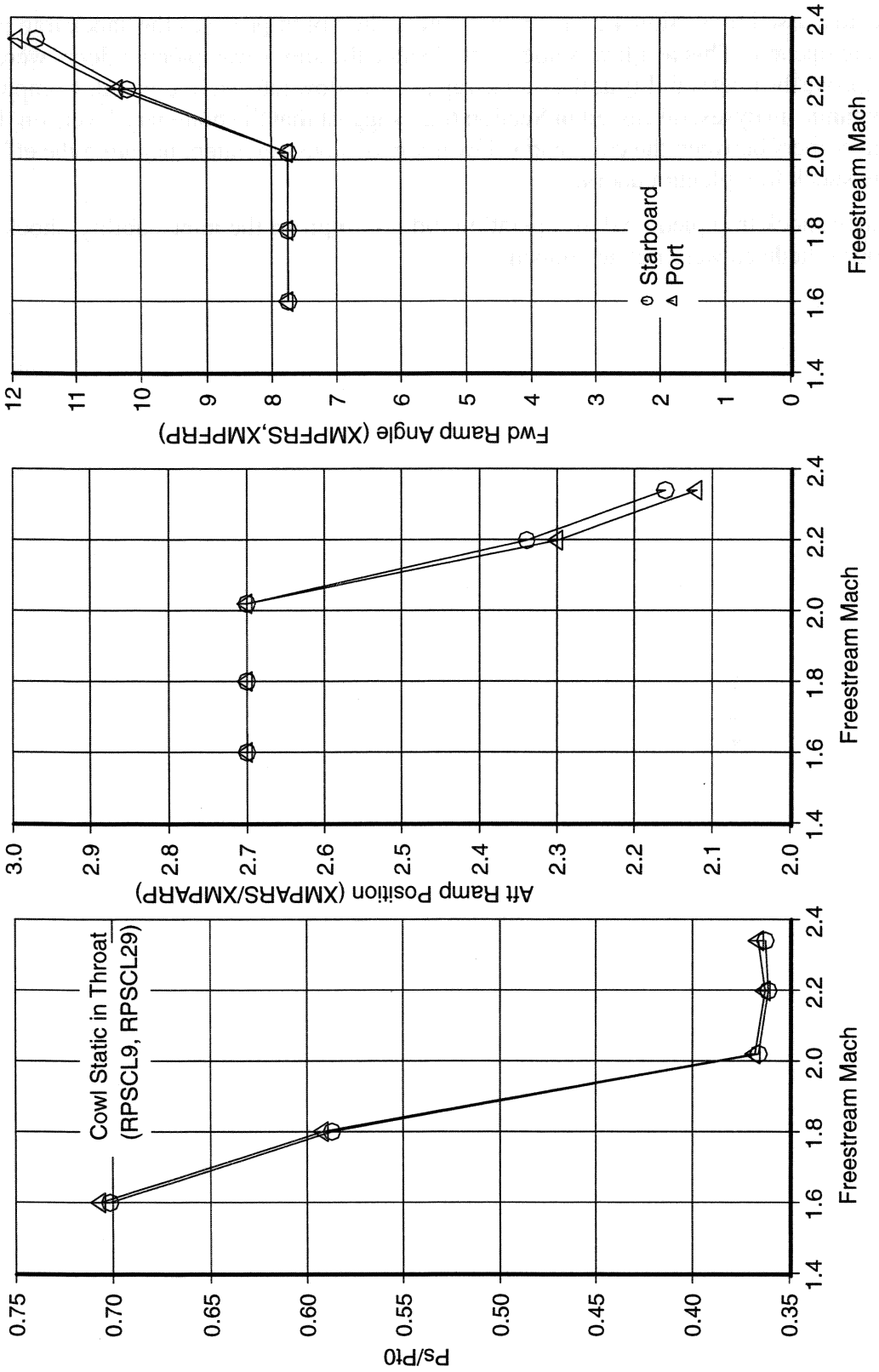

Figure 3–45. Ramp Positioning Schedule, Critical Operation

3.5. SHOCK TRAP PLENUM DOOR SCHEDULE

As discussed in Section 4.2. the inlet stability did not improve as the shock trap plenum doors were opened. This result was unexpected since the shock trap plenum doors were designed to improve the inlet stability as the shock trap plenum flow rate was increased. Computational fluid dynamic analyses, discussed in Section 6.2., suggest that the boundary layers on the cowl or in the corners between the cowl and sidewalls may have separated, negating the effectiveness of the shock trap plenum doors.

Since shock trap plenum door operation did not improve the inlet stability, shock trap plenum door schedules were not developed.

4. PERFORMANCE

This section presents performance data for the BTSSI inlet. Following a discussion of the normal operation characteristics, performance of the optimal configuration at varying angles of attack and yaw, inlet massflow ratio, and shock plenum flow rate is presented.

4.1. NORMAL OPERATION

Normal operation is defined as critical operation of the optimal configuration inlet. This corresponds to the inlet configuration with bleed No. 9, aft ramp lip No. 3, and vortex generator configuration No. 0 operating at zero angle–of–attack and zero angle–of–yaw. Fig. 4–1 is a summary of the inlet performance during normal operation as a function of freestream Mach number. The inlet is started above Mach 1.8. At the design condition of Mach 2.35, average throat recovery is 93.8%. This agrees fairly well with predictions made for the supersonic diffuser. An extremely poor subsonic diffuser design resulted in a predictably poor engine face recovery of 87.1% with an engine face distortion of 18%, where distortion is defined as (Ptmax–Ptmin)/Ptavg. The corresponding engine face total pressure contour map is shown in Fig. 4–2. Somewhat surprising is the radial nature of the distortion for a 2D bifurcated inlet. This may be a result of the very large bullet nose at the inlet/engine interface. However, an investigation into the significance of engine face characteristics has not been made given the poor subsonic diffuser design.

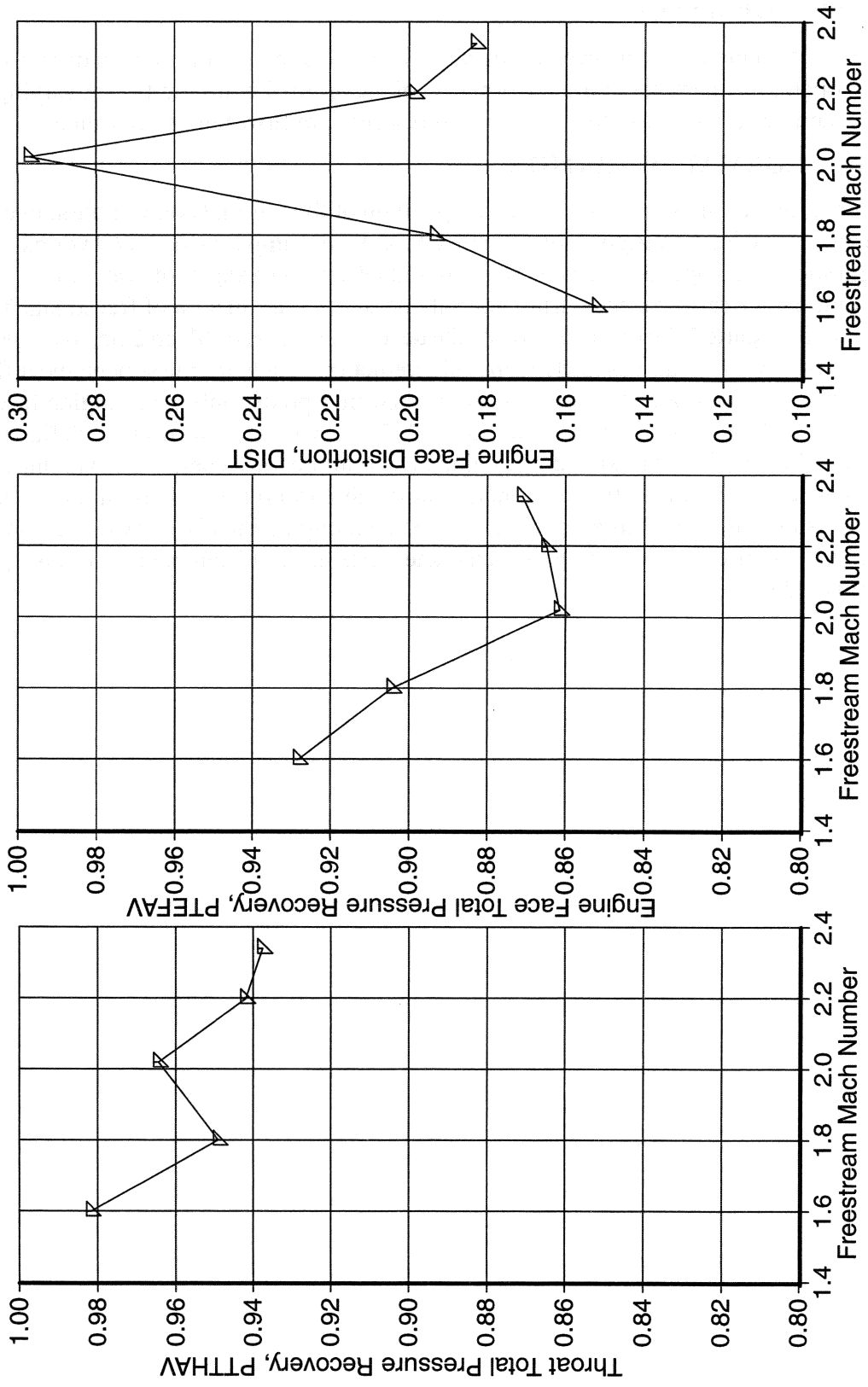

Figure 4–1. Critical Performance as a function of freestream Mach number for the Optimal Inlet Configuration.

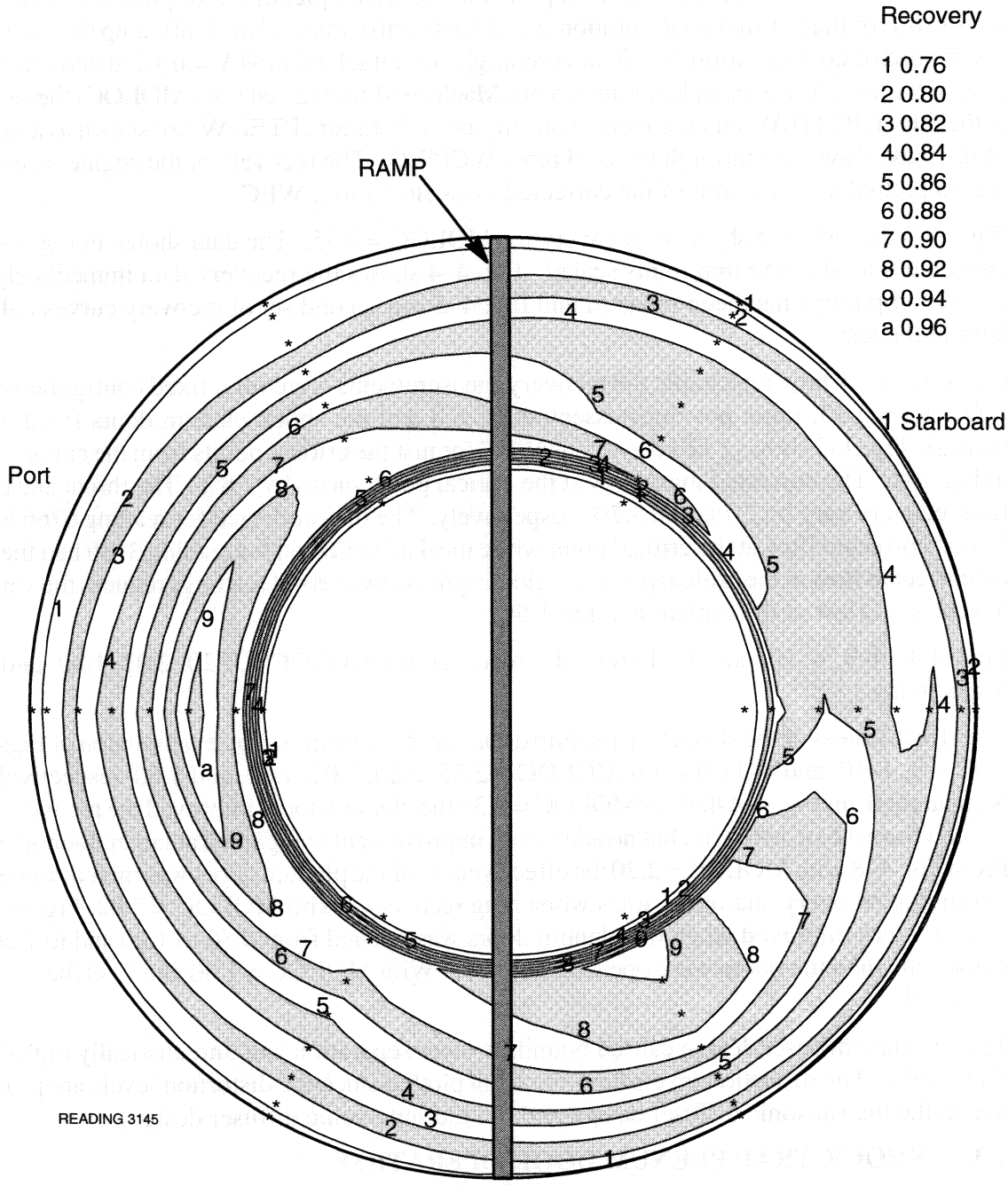

Figure 4–2. Engine Face Total Pressure Recovery Contours. Mach 2.35, Critical Operation. Optimal Configuration.

4.2. STABILITY MARGIN

The stability margin of the inlet is shown through plots of the total pressure recovery as a function of the mass flow through the cold pipe and the shock plenum door position. These plots are shown for the optimal configuration (i.e., bleed configuration No. 9, aft ramp No. 3, and vortex generator configuration No. 0) at zero angle–of–attack (ALPHA = 0.) and zero angle–of–yaw (BETA = 0.). For each local freestream Mach condition tested (i.e., MOLOC) the recovery at the throat, PTTHAV, and recovery at the engine face station, PTEFAV, are shown as a function of the mass flow ratio through the cold pipe, WCPWO. The recovery at the engine face station is also plotted as a function of the corrected mass flow ratio, WEC.

Figs. 4–3 through 4–5 show the recovery for MOLOC = 2.35. The data shown in Fig. 4–3 was collected with the aft ramp joints sealed. Fig. 4–4 shows the recovery data immediately after the aft ramp joints had been repaired and Fig. 4–5 is a second set of recovery curves collected later in the test.

Fig. 4–6 shows how repeatable the recovery measurements were for a fixed configuration (i.e., MOLOC = 2.35, ramp positions essentially fixed and the shock plenum doors fixed at 0.60 inches). Fig. 4–7 shows PTEFAV versus WEC for just the critical points from the curves shown in Fig. 4–6. The corrected mass flow at the critical point varies by 7.8%. The throat and engine face recovery vary by 2.7% and 3.7%, respectively. The data collected for reading 6766 had the lowest corrected flow at the critical point while the data collected for reading 3136 had the highest corrected flow at the critical point. Neglecting these two sets of readings reduces the variation in corrected flow at the critical point to 1.5%.

Figs. 4–8, 4–9, 4–10, and 4–11 show the recovery for MOLOC = 2.20, 2.02, 1.80, and 1.60, respectively.

The effectiveness of the shock trap plenum doors can be determined by examination of Figs. 4–4, 4–8, 4–9, 4–10, and 4–11 (i.e. for MOLOC = 2.35, 2.20, 2.02, 1.80, and 1.60, respectively). It is apparent from Fig. 4–4 that for MOLOC = 2.35 the plenum doors improved the recovery when opened from 0.6 in. to 0.8 in., but no additional improvement was gained at larger door openings. From Fig. 4–8 with MOLOC = 2.20 the effectiveness of the plenum doors was mixed, sometimes improving recovery and other times worsening recovery. With MOLOC = 2.02, Fig. 4–9, the recovery was improved when the plenum doors was opened from 0.80 to 1.00 and to 1.50, but worsened when the doors were opened to 2.00 in. With MOLOC = 1.80 and 1.60 the inlet was unstarted.

The subsonic diffuser design caused boundary layer separation and unrealistically high distortion levels. The distortion levels have not been plotted since the distortion levels are primarily due to the the subsonic diffuser design and not the supersonic diffuser design.

4.3. SHOCK TRAP PLENUM DOOR OPERATION

The shock trap plenum door operation is shown through plots of the pressure difference across the starboard and port forward ramp trailing edges, DELSTR and DELPRT, normalized by the local freestream stagnation pressure, PTOLOC, as a function of the corrected mass flow at the engine face station, WEC, and the shock trap plenum door position, XMPTD. Note that the pressure difference values are the static pressures in the shock trap plenum minus the static pressure at the forward ramp trailing edges (i.e., DELSTR = PSTP1 − PSFR3 and DELPRT = PSTP4 − PSFR12). The recovery at the engine face station, PTEFAV, as a func-

tion of the corrected mass flow ratio is also shown for reference. These plots are for the optimal configuration (i.e., bleed configuration No. 9, aft ramp No. 3, and vortex generator configuration No. 0) at zero angle–of–attack (ALPHA = 0.) and zero angle–of–yaw (BETA = 0.).

Figs. 4–12, 4–13, 4–14, 4–15, and 4–16 show the pressure difference across the forward ramp trailing edges and the recovery for MOLOC = 2.35, 2.20, 2.02, 1.80, and 1.60, respectively.

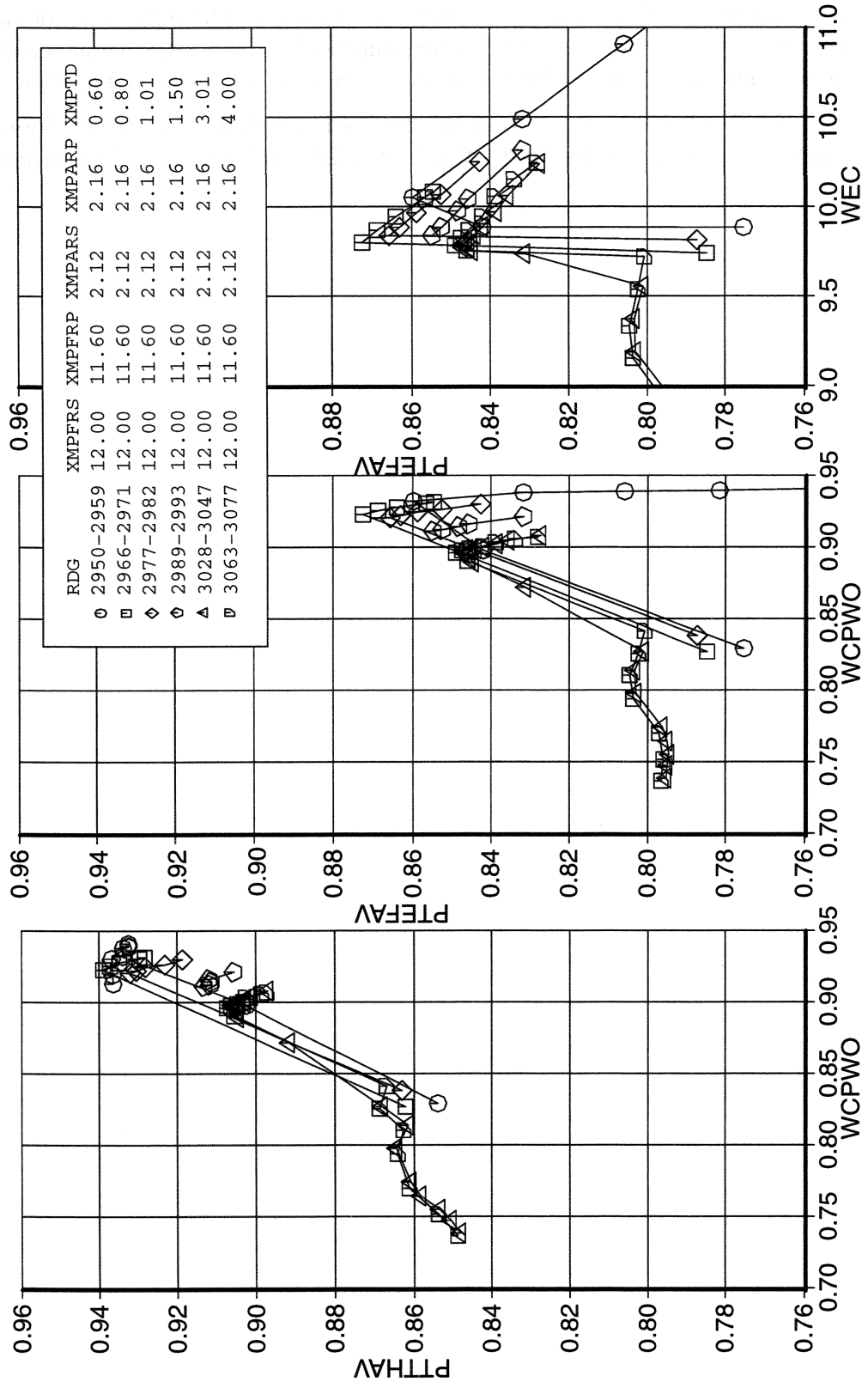

Figure 4–3. Recovery for Bleed Configuration 9, Aft Ramp 3, Vortex Generator 0, MOLOC = 2.35, ALPHA = 0., BETA = 0., Aft Ramps Sealed

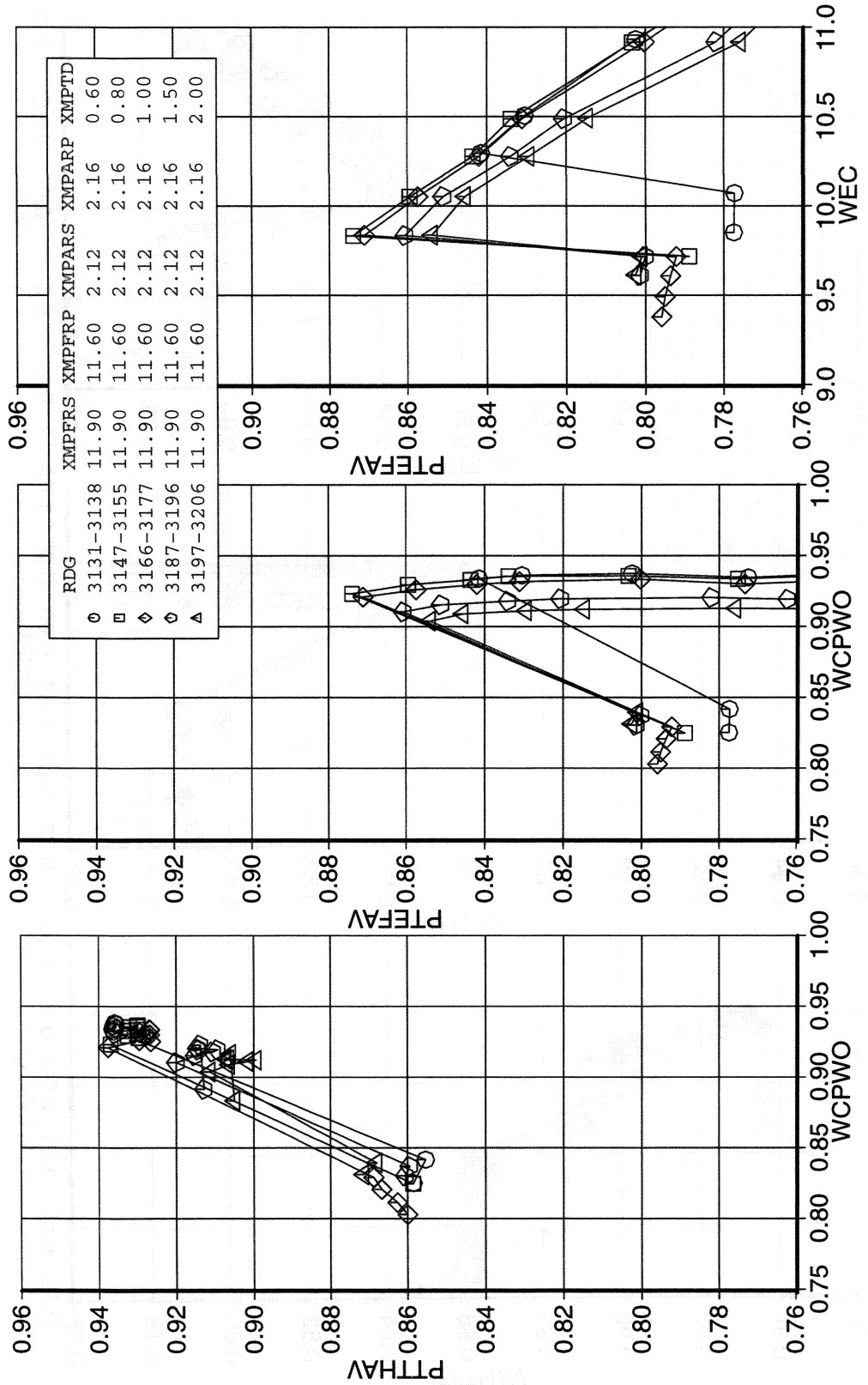

Figure 4–4. Recovery for Bleed Configuration 9, Aft Ramp 3, Vortex Generator 0, MOLOC = 2.35, ALPHA = 0., BETA = 0., After Repair

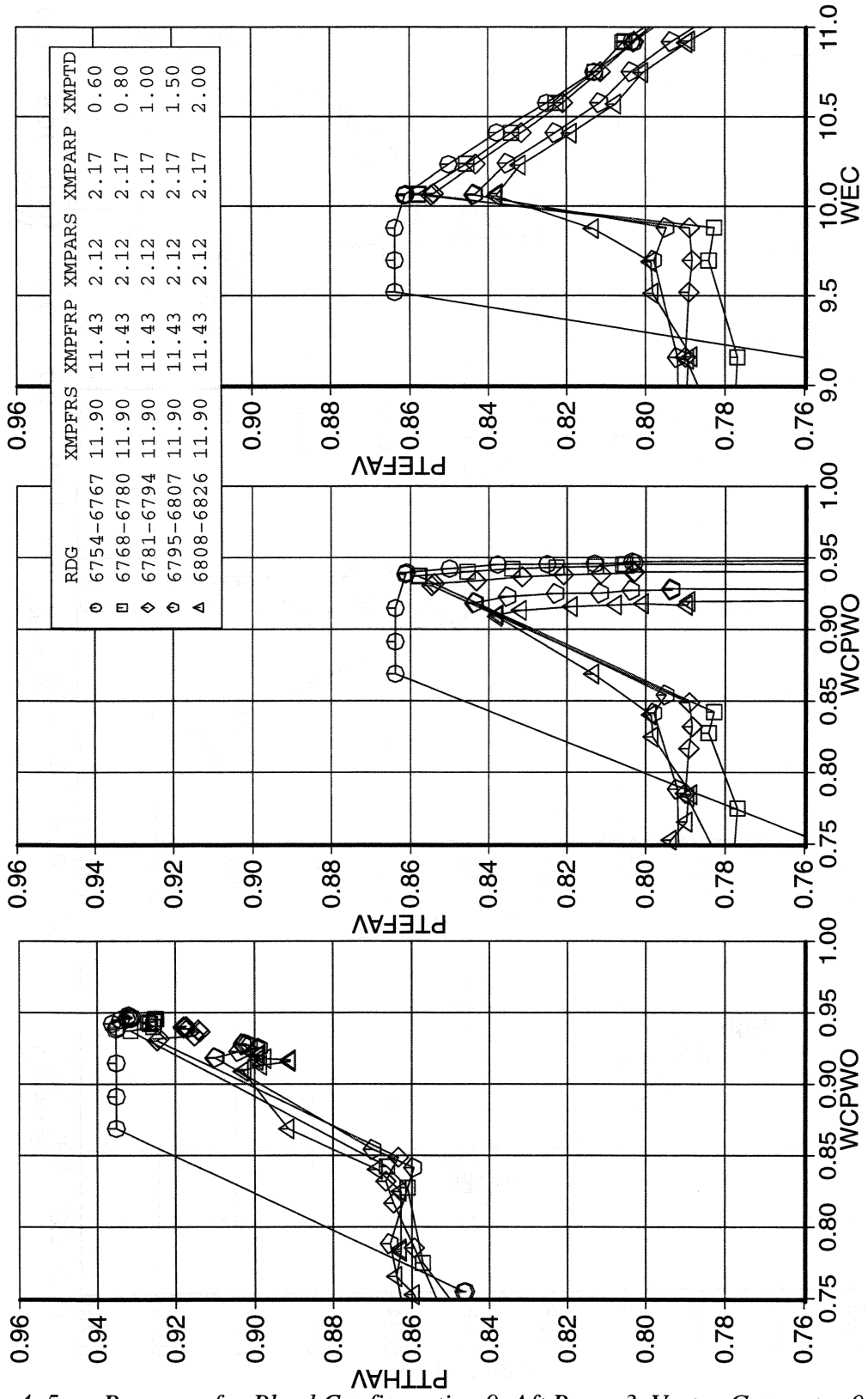

Figure 4–5. Recovery for Bleed Configuration 9, Aft Ramp 3, Vortex Generator 0, MOLOC = 2.35, ALPHA = 0., BETA = 0., After Repair (Repeat)

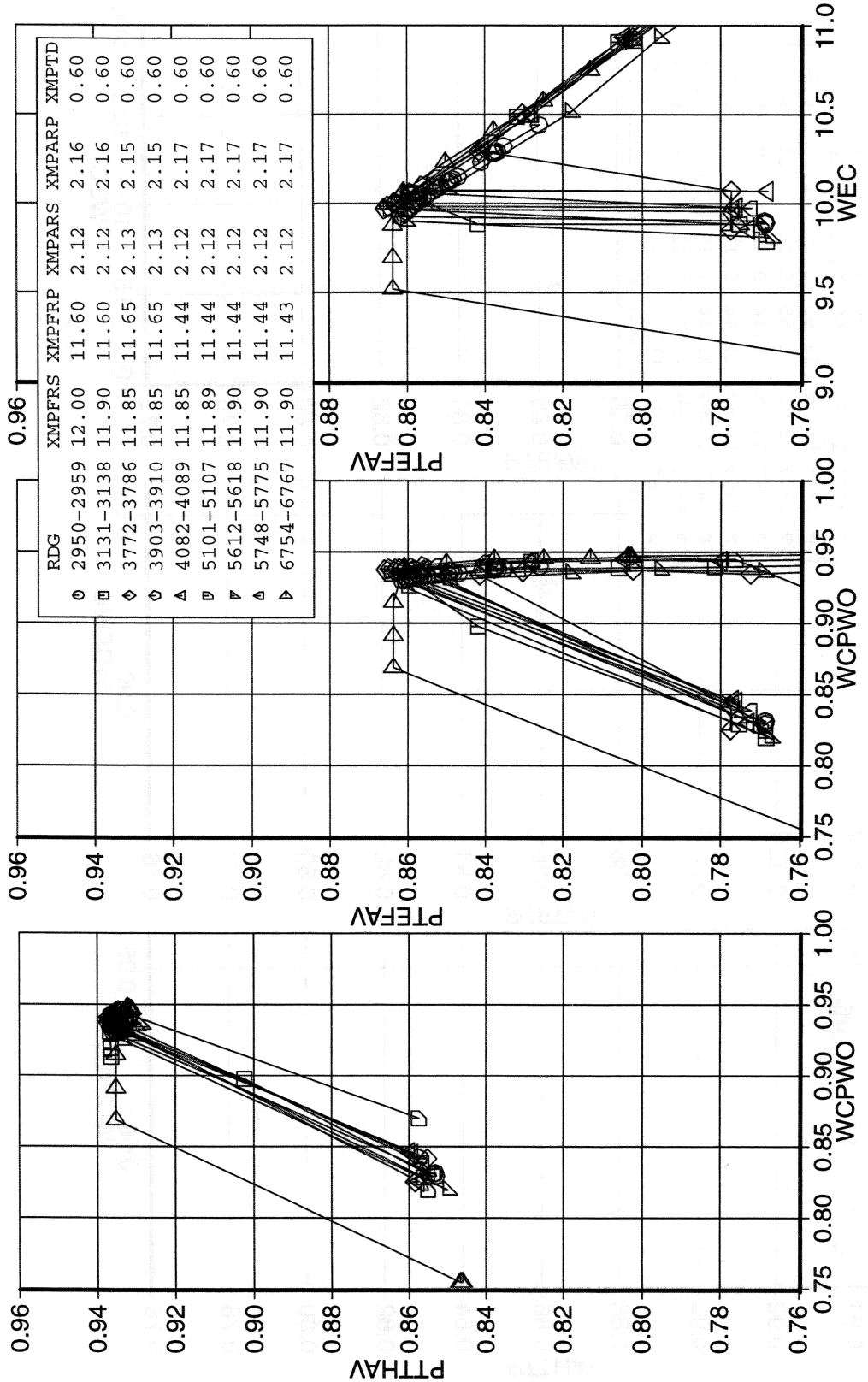

Figure 4–6. Recovery for Bleed Configuration 9, Aft Ramp 3, Vortex Generator 0, MOLOC = 2.35, ALPHA = 0., BETA = 0., (Repeatability Check)

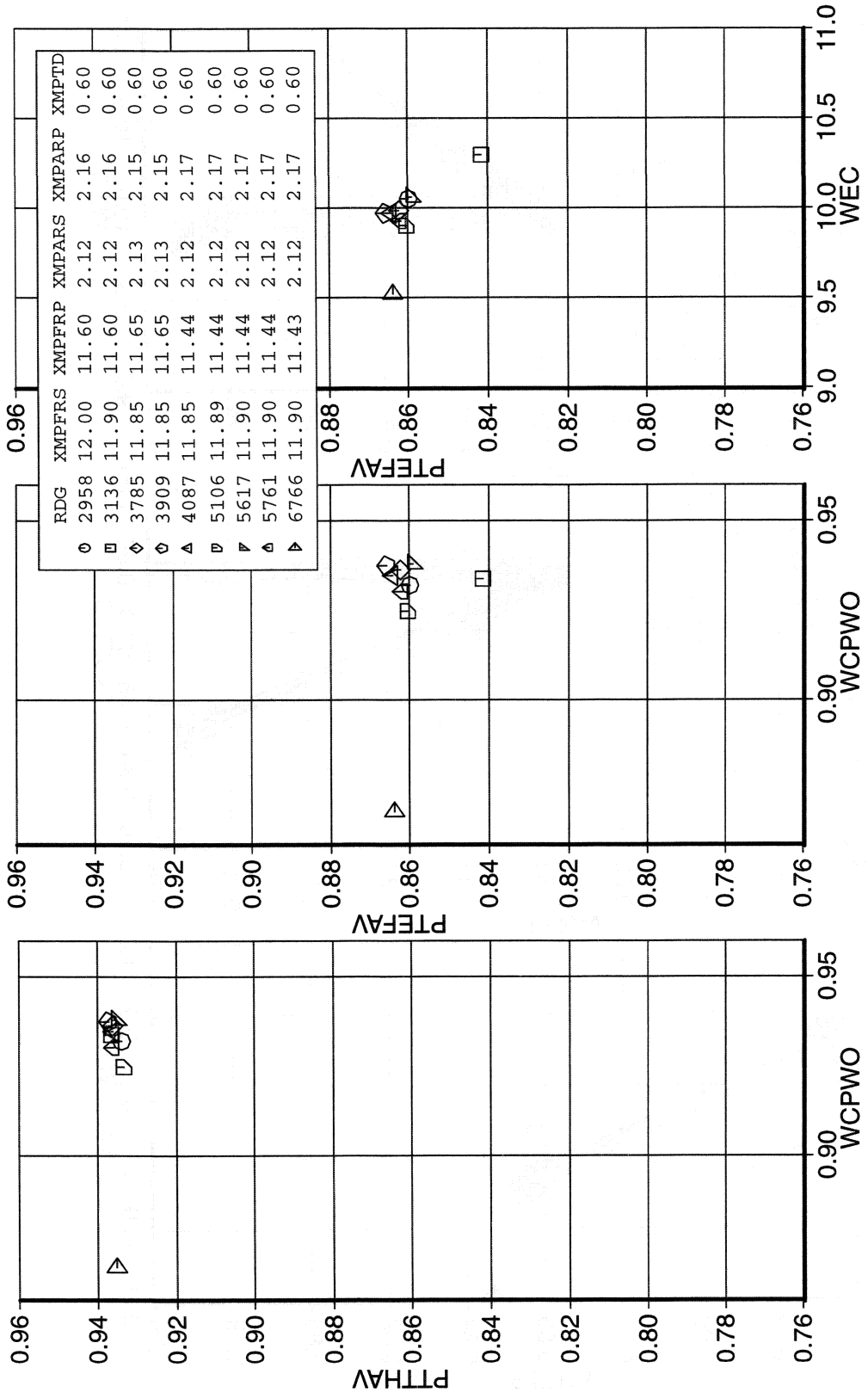

Figure 4–7. Recovery for Bleed Configuration 9, Aft Ramp 3, Vortex Generator 0, MOLOC = 2.35, ALPHA = 0., BETA = 0., Critical Point Repeatability

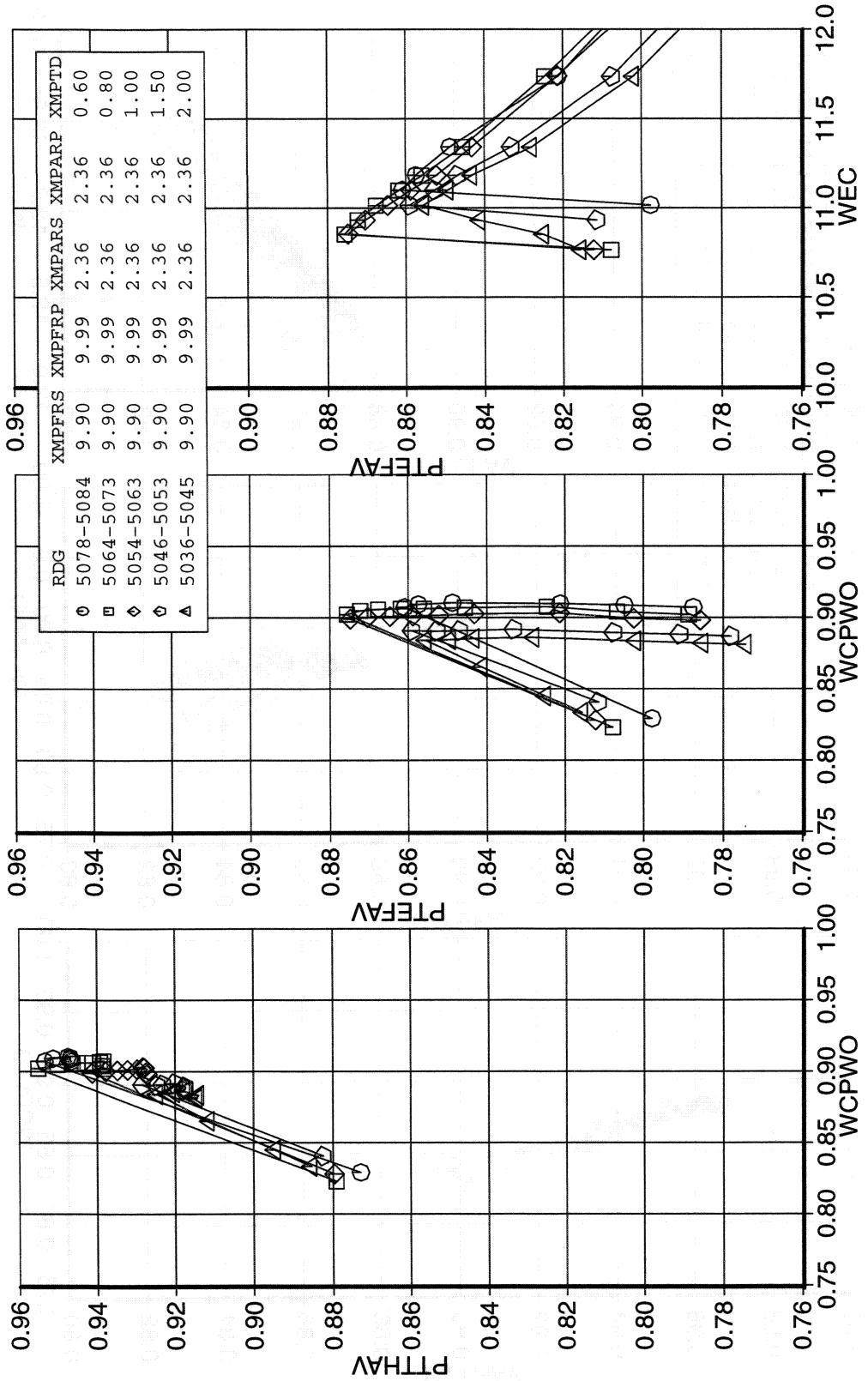

Figure 4–8. Recovery for Bleed Configuration 9, Aft Ramp 3, Vortex Generator 0, MOLOC = 2.20, ALPHA = 0., BETA = 0.

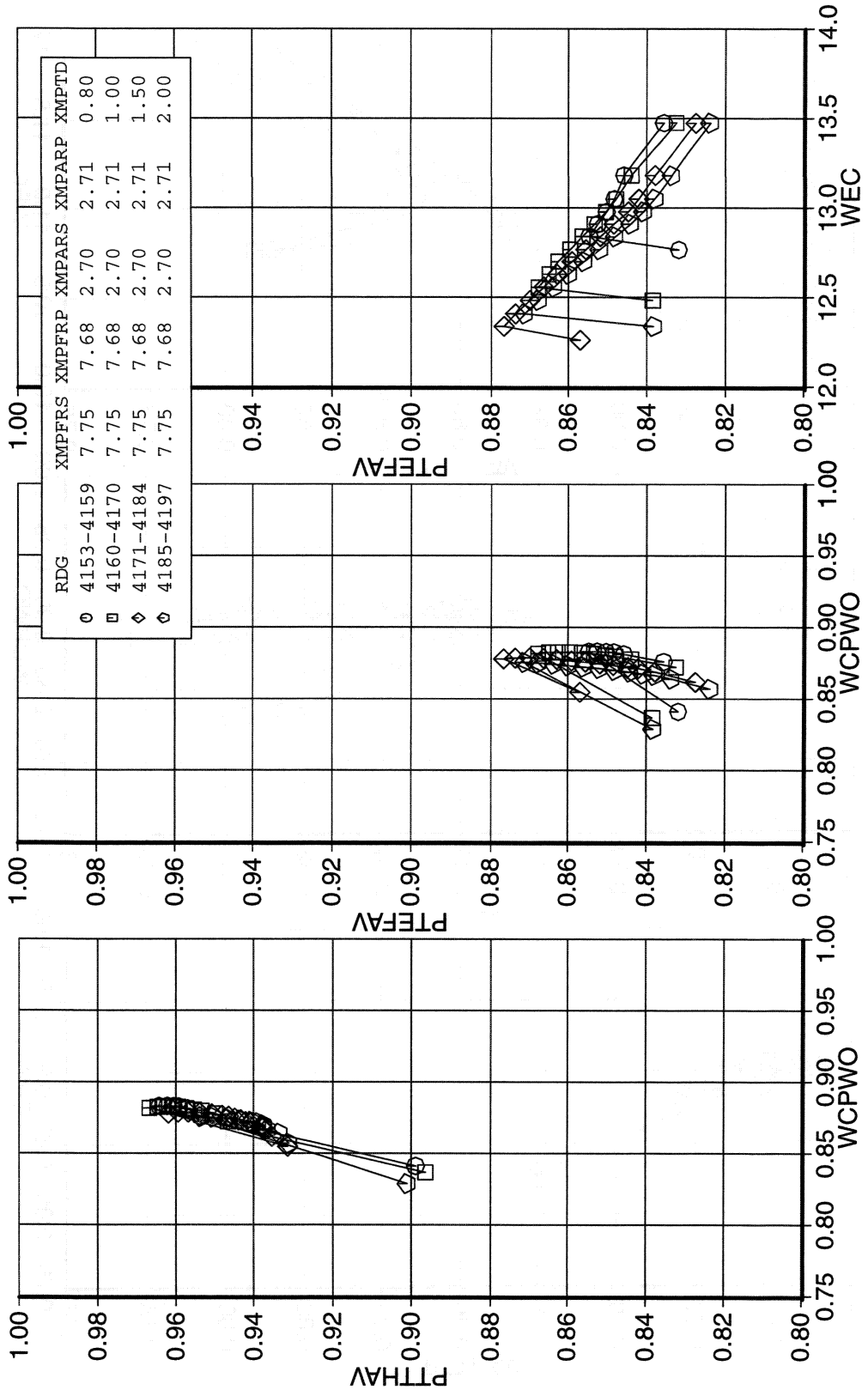

Figure 4–9. Recovery for Bleed Configuration 9, Aft Ramp 3, Vortex Generator 0, MOLOC = 2.02, ALPHA = 0., BETA = 0.

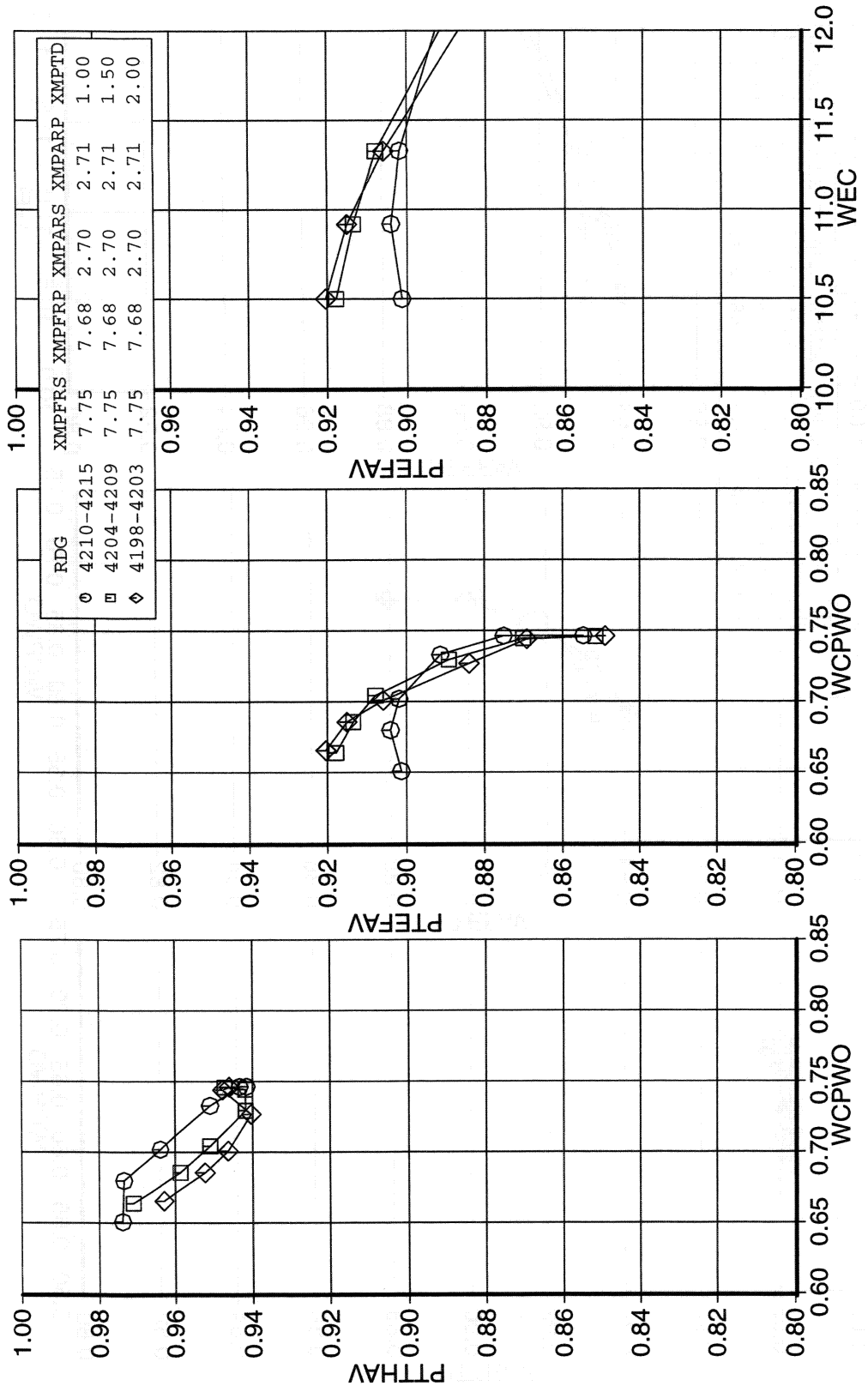

Figure 4–10. Recovery for Bleed Configuration 9, Aft Ramp 3, Vortex Generator 0, MOLOC = 1.80, ALPHA = 0., BETA = 0.

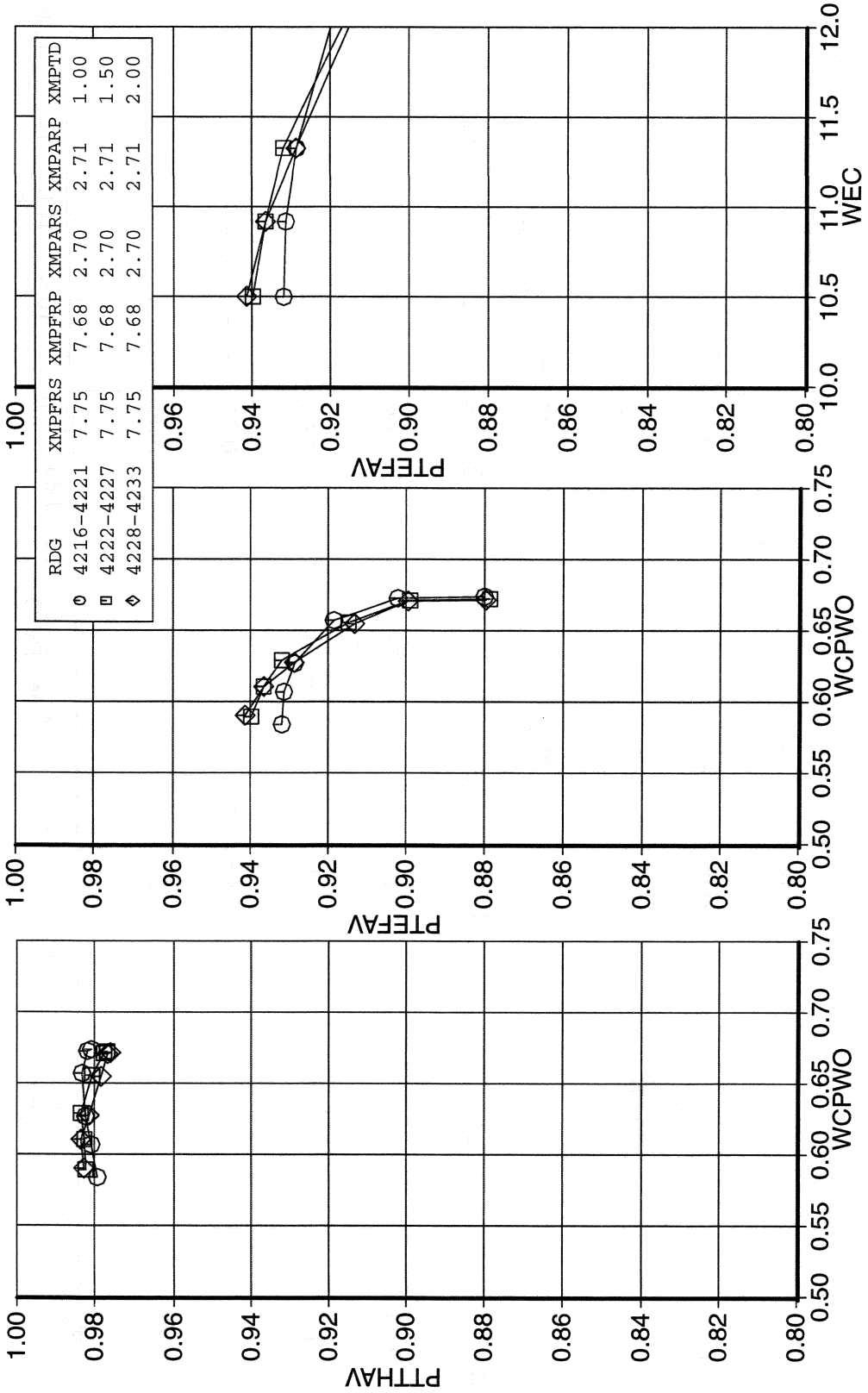

Figure 4–11. Recovery for Bleed Configuration 9, Aft Ramp 3, Vortex Generator 0, MOLOC = 1.60, ALPHA = 0., BETA = 0.

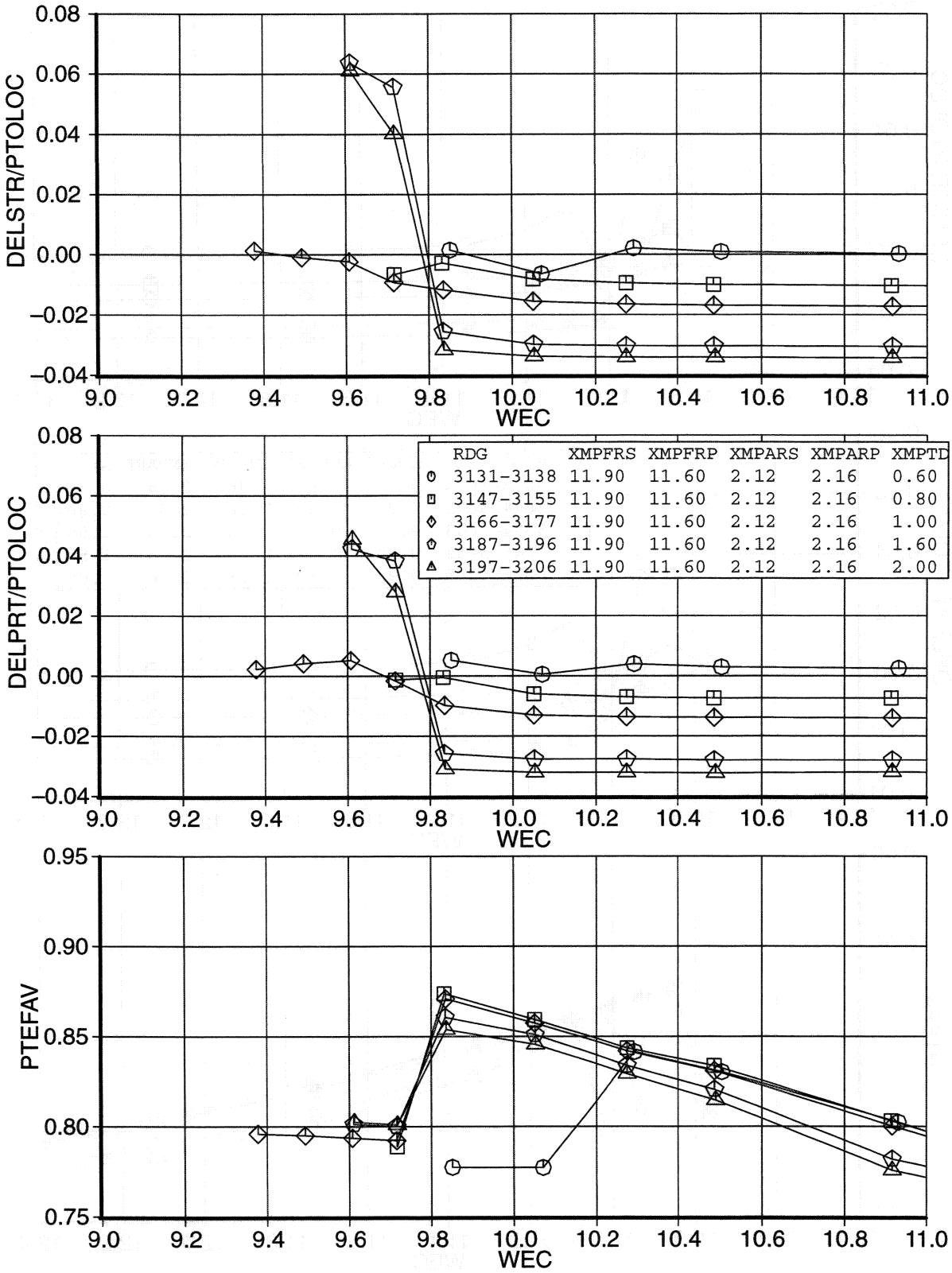

Figure 4–12. Shock Trap Plenum Door Operation for Bleed Configuration 9, Aft Ramp 3, Vortex Generator 0, MOLOC = 2.35, ALPHA = 0., BETA = 0.

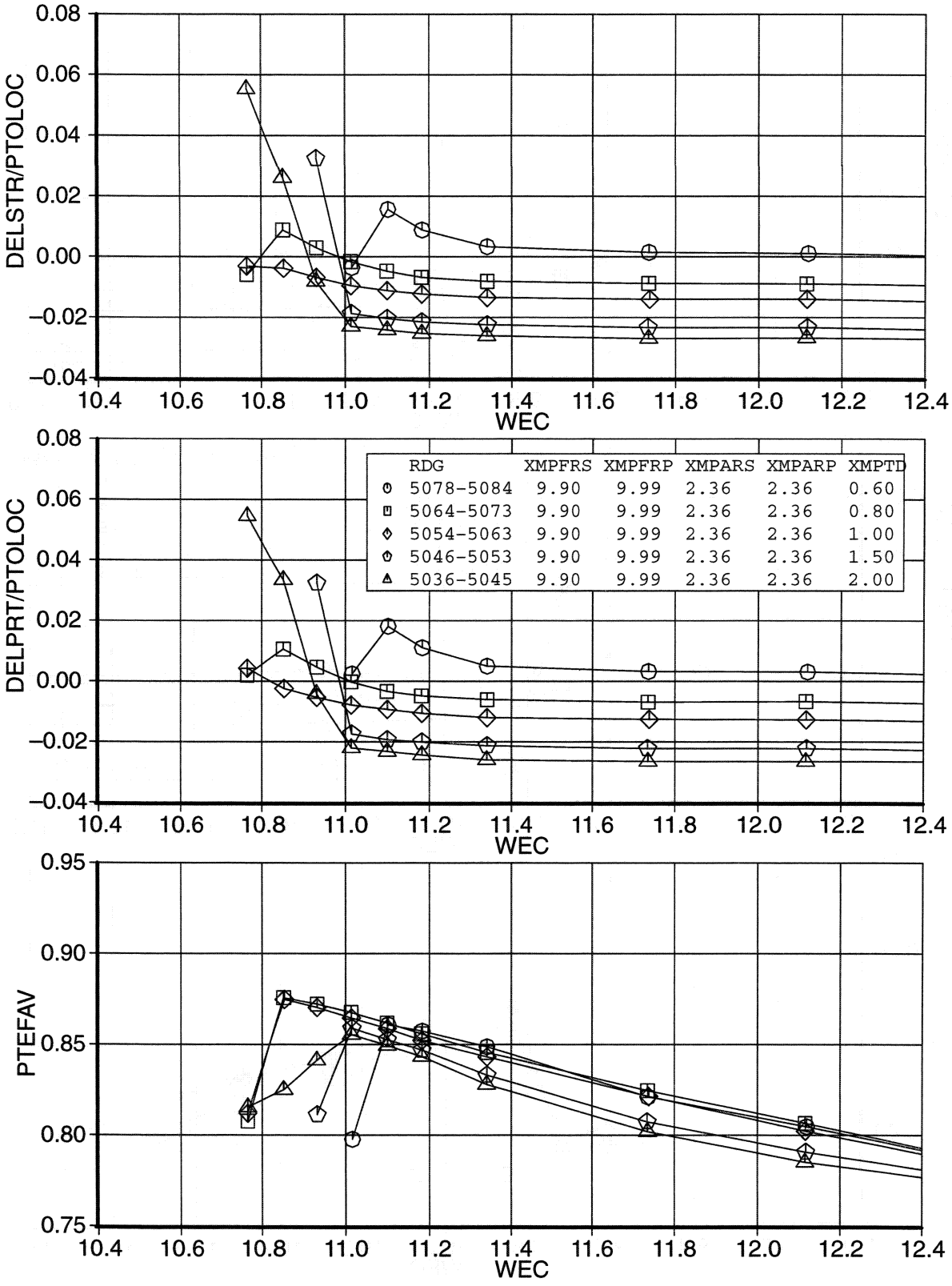

Figure 4–13. Shock Trap Plenum Door Operation for Bleed Configuration 9, Aft Ramp 3, Vortex Generator 0, MOLOC = 2.20, ALPHA = 0., BETA = 0.

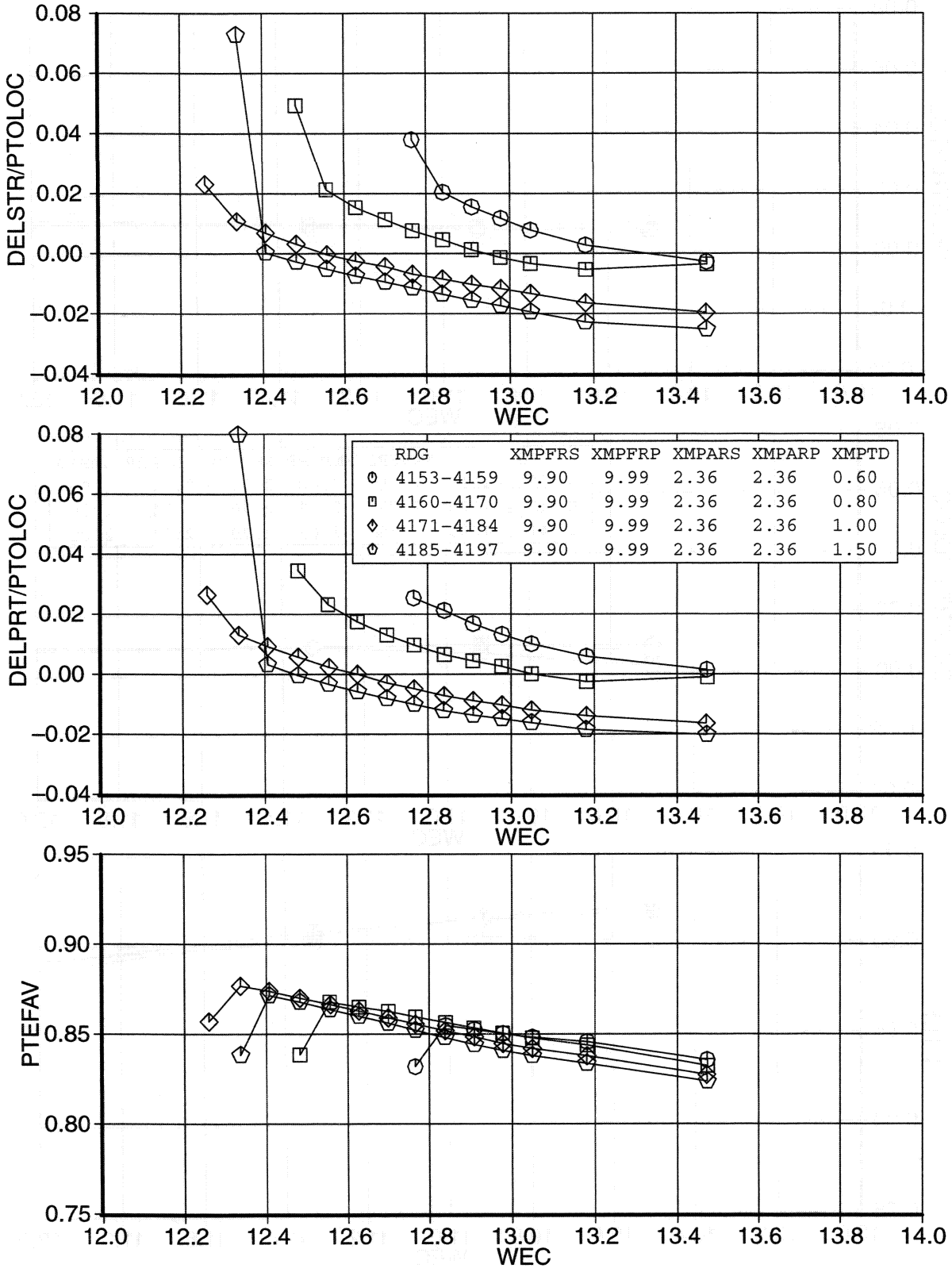

Figure 4–14. Shock Trap Plenum Door Operation for Bleed Configuration 9, Aft Ramp 3, Vortex Generator 0, MOLOC = 2.02, ALPHA = 0., BETA = 0.

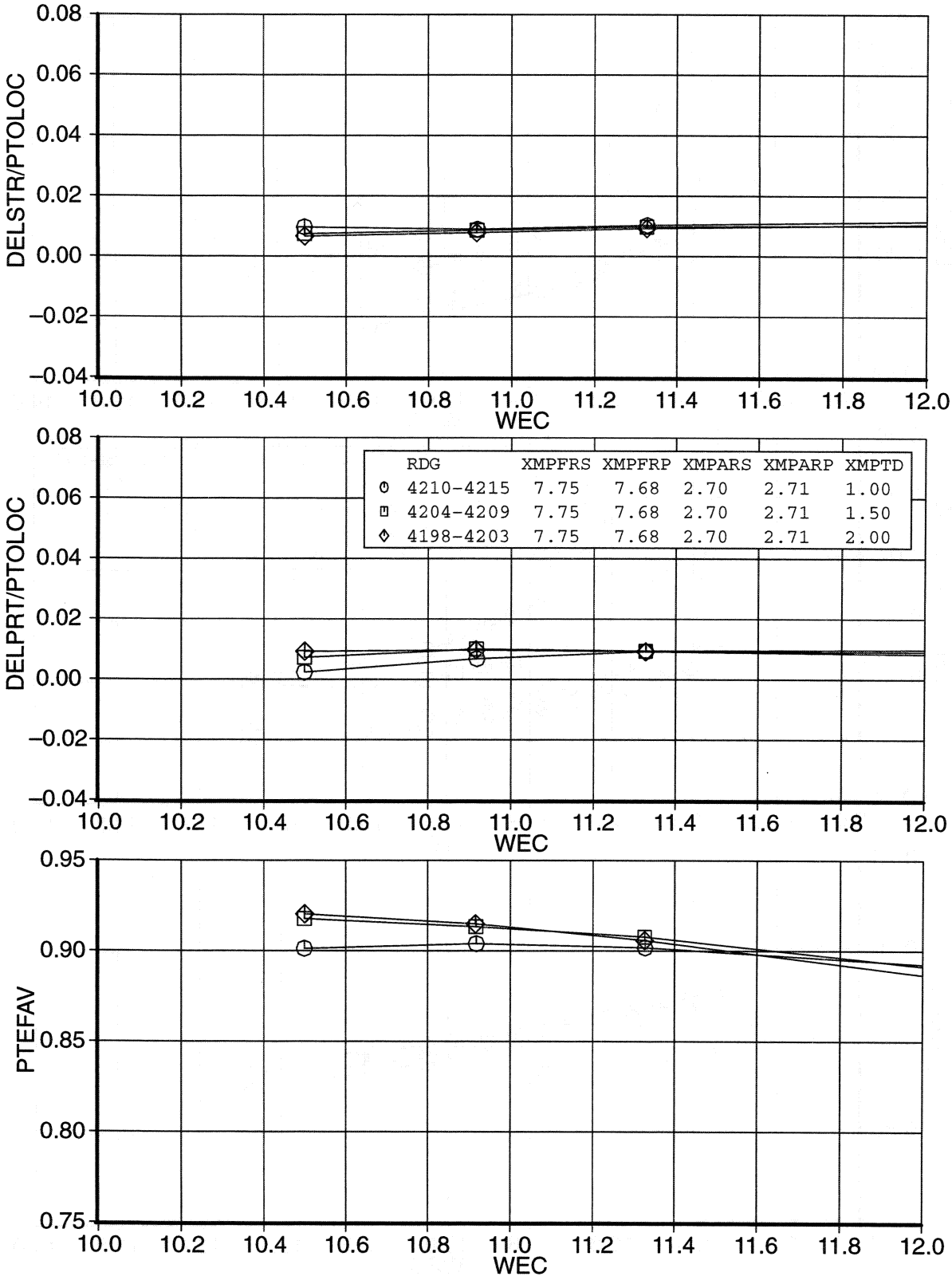

Figure 4–15. Shock Trap Plenum Door Operation for Bleed Configuration 9, Aft Ramp 3, Vortex Generator 0, MOLOC = 1.80, ALPHA = 0., BETA = 0.

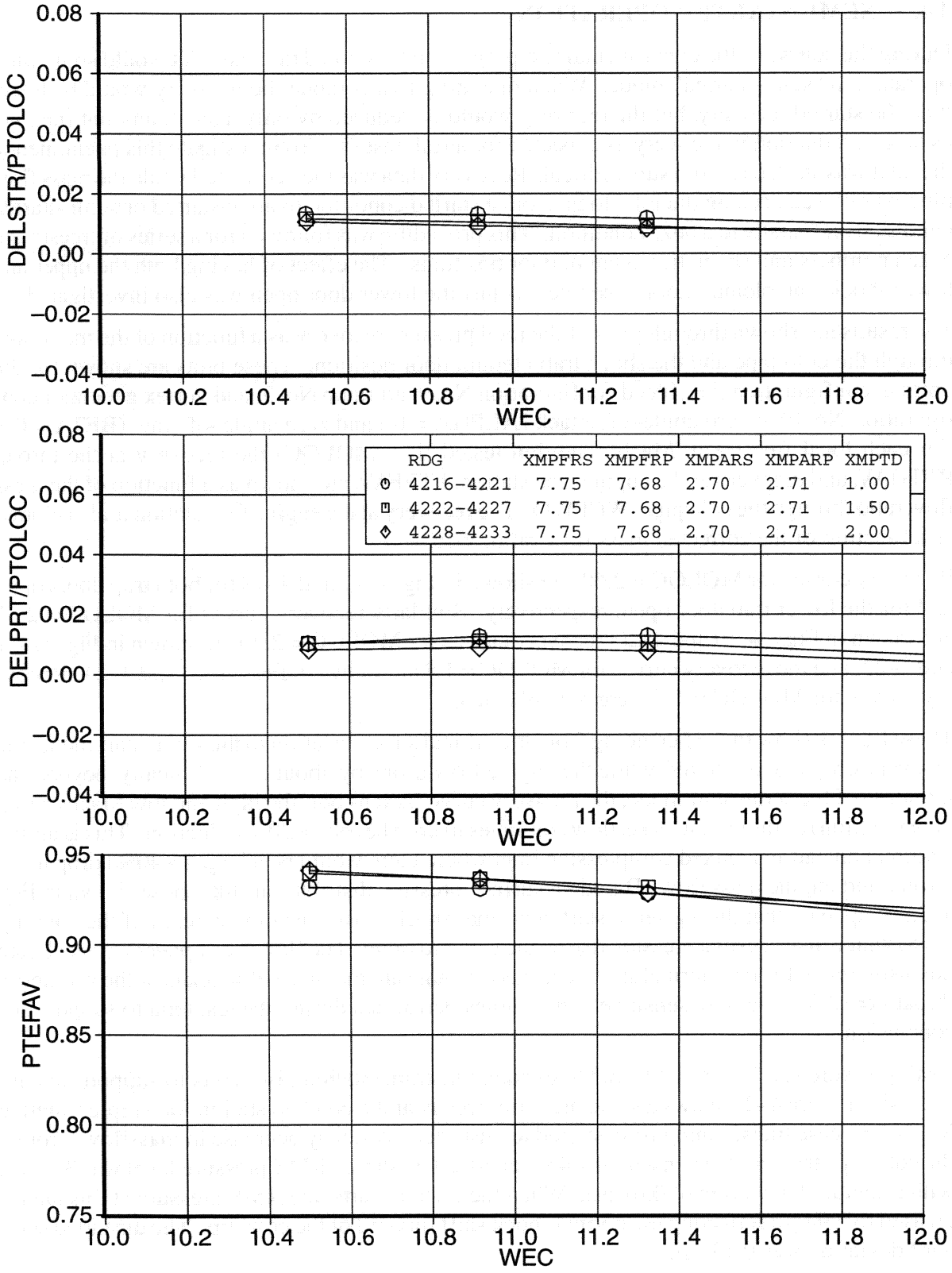

Figure 4–16. Shock Trap Plenum Door Operation for Bleed Configuration 9, Aft Ramp 3, Vortex Generator 0, MOLOC = 1.60, ALPHA = 0., BETA = 0.

4.4. SEMI–STARTED OPERATION

During the course of the experimental test program it was noted that the inlet would sometimes operate in a "semi–started" mode. When operating in this mode the recovery would be lower than the started recovery, but the recovery would be reduced by only a small amount (i.e., not as large a reduction in recovery as expected for a full unstart). To investigate this phenomenon the inlet was started and run supercritical. Recovery data was then collected while the mass flow plug was closed causing the inlet to go from a started condition to an unstarted or semi–started condition and finally to a buzz condition. This procedure was followed for a series of freestream Mach numbers and shock trap plenum door positions. The effect of having both the upper and lower shock trap plenum doors open versus just the lower door open was also investigated.

The results are shown through plots of the total pressure recovery as a function of the mass flow through the cold pipe and the shock trap plenum door position. These plots are shown for the optimal configuration (i.e., bleed configuration No. 9, aft ramp No. 3, and vortex generator configuration No. 0) at zero angle–of–attack (ALPHA = 0.) and zero angle–of–yaw (BETA = 0.). For each local freestream Mach condition tested (i.e., MOLOC) the recovery at the throat, PTTHAV, and recovery at the engine face station, PTEFAV, are shown as a function of the mass flow ratio through the cold pipe, WCPWO. The recovery at the engine face station is also plotted as a function of the corrected mass flow ratio, WEC.

Recovery curves for MOLOC = 2.60 are shown in Fig. 4–17 and 4–18 for both trap doors open and for the lower trap door open, respectively. Similarly recovery curves for MOLOC = 2.35 are shown in Figs. 4–19 and 4–20, recovery curves for MOLOC = 2.20 are shown in Figs. 4–21 and 4–22, and the recovery curves for MOLOC = 1.8 are shown in Figs. 4–23 and 4–24. Recovery curves for MOLOC = 1.6 were not collected.

These figures show that when going from the critical shock location to the semi–start mode, the recovery drops by 6% to 8% while the engine flow drops by about 5%. Typically, beyond the initiation of the semi–start mode, the recovery curve flattens out (the high and low Machs being the exception) as the engine mass flow continues to drop beyond a 20% reduction. This is unlike a normal unstart in a mixed compression inlet where there would be a large (> 40%) drop in recovery and engine mass flow. Based on surface pressure distributions like those shown in Fig. 4–25, it appears that during semi–start, a normal shock exists just downstream of the cowl lip (x=8) which also causes a pressure rise on the forward ramp. The flow then appears to accelerate downstream of this first normal shock and pass through another normal shock near the geometric throat (x=12.5). Pressure sensitive paint studies performed during the test tend to support this conclusion.

RMS pressure levels derived from the dynamic instrumentation also tends to support this hypothesis. Figure 4–26 shows a static pressure trace near the cowl lip station for a representative Mach 2.35 case transitioning from started to unstarted. A steady decrease in massflow through the cold pipe triggered the unstart at 4.45 seconds. The started RMS pressure level was 3.35 psi with a standard deviation of 0.01 psi. When the inlet unstarts, the RMS pressure at this tap increased to 5.94 psi reflecting the normal shock shift forward of the cowl lip. The unstarted standard deviation was 0.15 psi.

Figure 4–27 shows a similar trace at the same station during a transition from started to semi–started. In this case, the shock trap plenum doors have been fully opened. The RMS pressure level during the started mode was 3.30 psi, approximately the same as above and with the same

standard deviation. During the semi–started mode, the RMS pressure increased to 4.46 psi. This is lower than the started pressure level and tends to support the conclusion that a normal shock is generated upstream of the critical point, but short of a full unstart. However, further inspection of the absolute pressure levels in Figure 4–27 suggests an alternate conclusion. Additionally, the standard deviation increased by an order of magnitude to 1.30 psi.

Figure 4–27 shows a large, cyclic pressure variation during the semi–start mode. When the time scale is expanded to show more detail, as shown in Figure 4–28, it is noted that the pressure level at the bottom of each cycle is about the same as the started pressure. At the cycle peaks, the pressure level is about the same as for a full unstart. Based on this characteristic, a revised theory is that during semi–start, the inlet is cycling between fully started and fully unstarted. The frequency of this event ranges from approximately 0.2 Hz to 20 Hz. An intriguing feature of this phenomenon was the ability to precisely control the frequency of the unstart/re–start cycles.

The potential impact of this behavior on either the inlet itself or on an engine may be significant. Further investigation of the phenomenon is required before understanding all implications, especially since the subsonic diffuser is separated in this inlet. Figure 4–29 shows a total pressure trace at the engine face (PDTEF1) recorded during the same unstart event as in Figure 4–26. Figure 4–30 is the corresponding engine face total pressure trace recorded during the semi–start event.

From started to unstarted, the RMS total pressure decreased 8% at the probe being considered. From started to semi–started, the RMS total pressure decreased by only 3%, a trend consistent with the reduced increase in static pressure at the cowl lip. However, what is different at the engine face as compared to the cowl lip, is that the standard deviation in total pressure during semi–start is only modestly higher than the started (and unstarted) levels. The standard deviation for the started and unstarted cases were approximately equivalent at 0.28 psi. However, the order–of–magnitude increase in standard deviation at the cowl lip when transitioning to semi–start translated to a more modest increase to 0.42 psi at the engine face. Figure 4–31 compares the cowl lip static pressure to the engine face total pressure at an expanded time scale. The influence of the unstart/re–start cycles is evident at both locations, but is more pronounced at the cowl lip. Whether this effect is acceptable to an engine is an issue that would have to be resolved upon continued investigation of this inlet concept.

Figure 4–32 and 4–33 show the effects of unstart and semi–start at a different engine face tap location (PDTEF6). Absolute levels differ from those in the previous figures, but a similar trend in overall behavior is noted. Figure 4–34 shows the effect of semi–start at a freestream Mach number of 2.20. Again, similar behavior is observed.

High speed video recorded during both semi–start and unstart modes of operation does not provide additional information. It is not possible to synchronize events observed in the high speed video with the respective dynamic data.

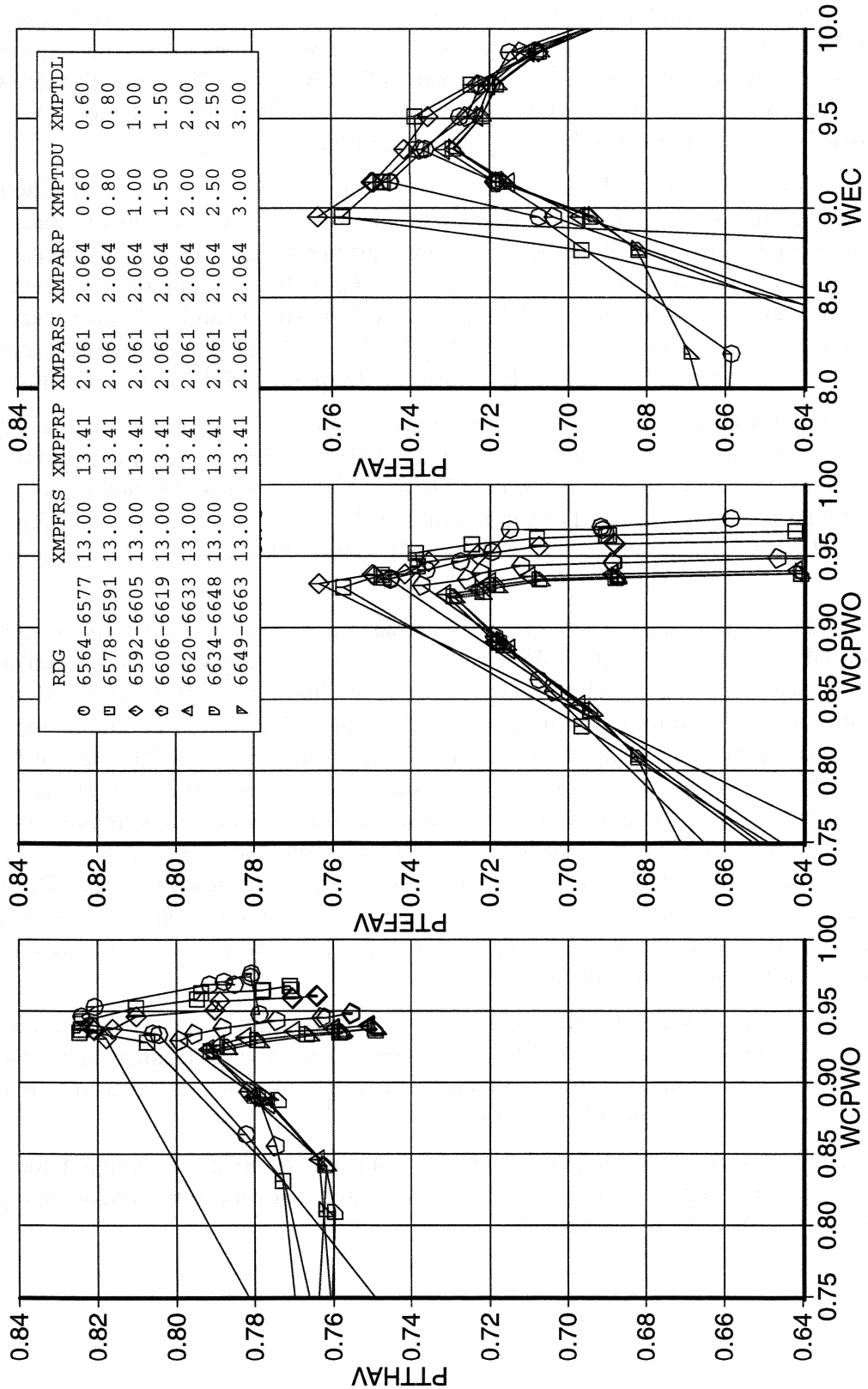

Figure 4–17. Recovery Curves for Started Through Buzz Condition, Bleed Configuration 9, Aft Ramp 3,Vortex Generator 0, Both Plenum Doors Open, MOLOC = 2.60, ALPHA = 0., BETA = 0.

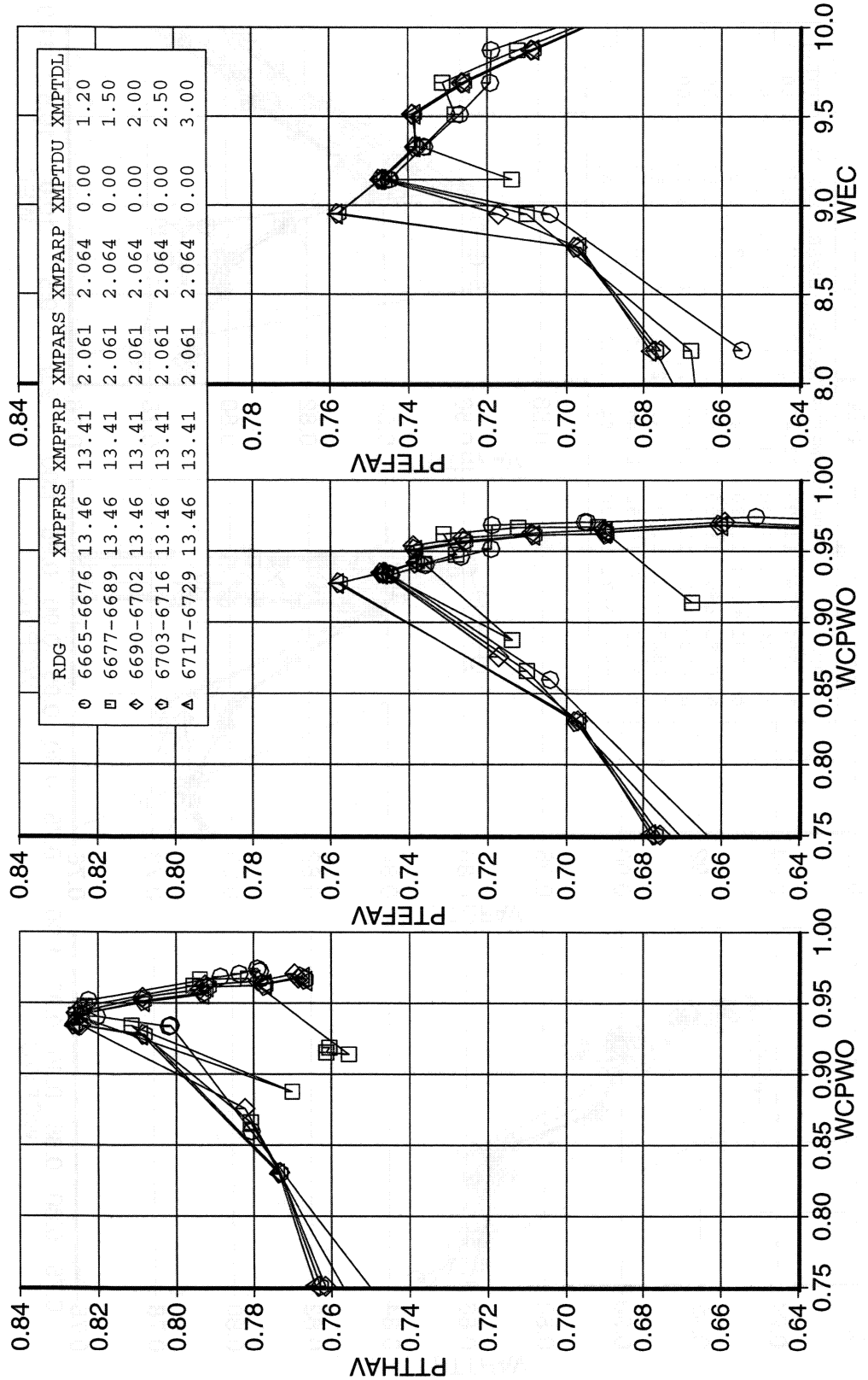

Figure 4–18. Recovery Curves for Started Through Buzz Condition, Bleed Configuration 9, Aft Ramp 3, Vortex Generator 0, Single Plenum Door Open, MOLOC = 2.60, ALPHA = 0., BETA = 0.

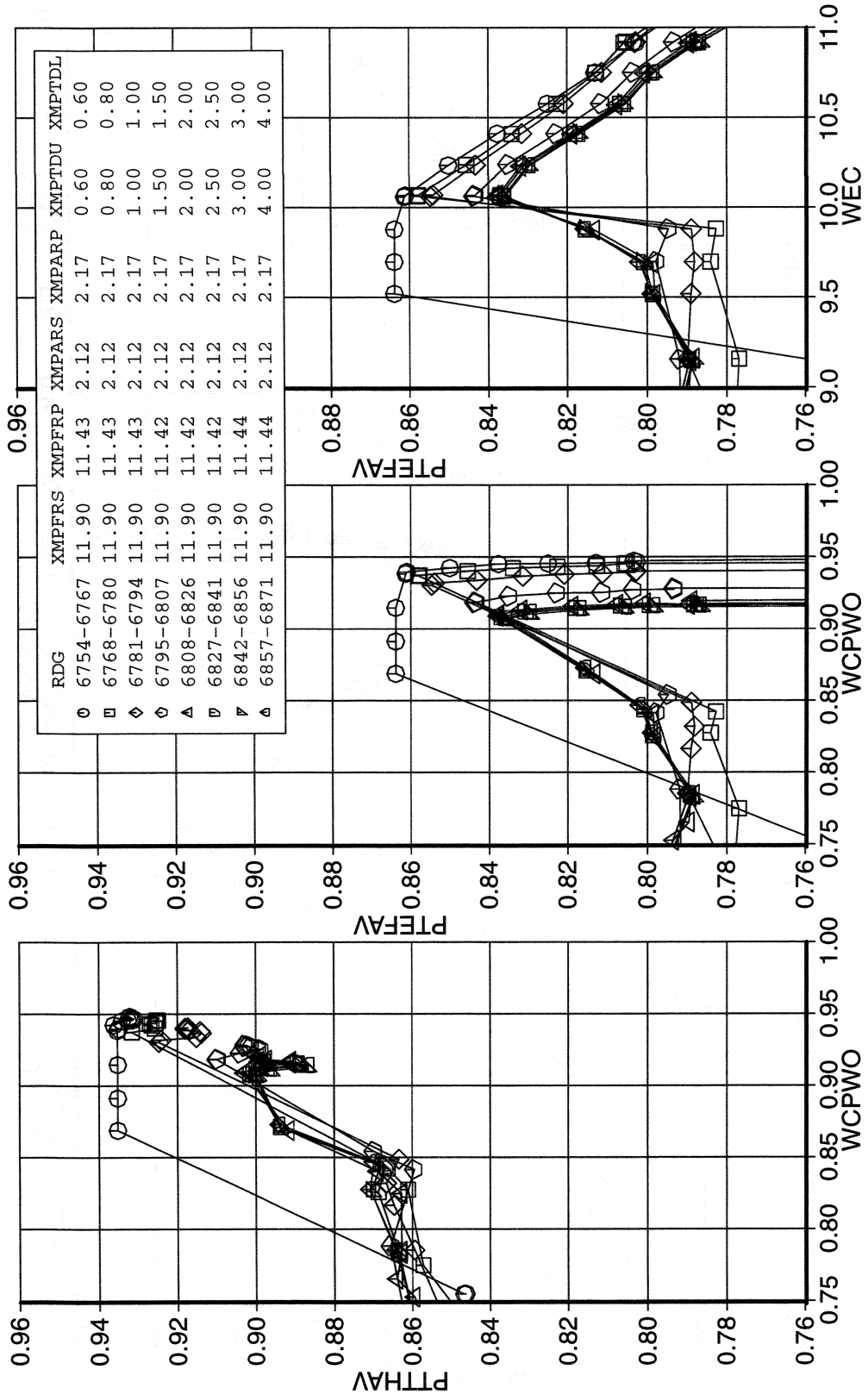

Figure 4–19. Recovery Curves for Started Through Buzz Condition, Bleed Configuration 9, Aft Ramp 3, Vortex Generator 0, Both Plenum Doors Open, MOLOC = 2.35, ALPHA = 0., BETA = 0.

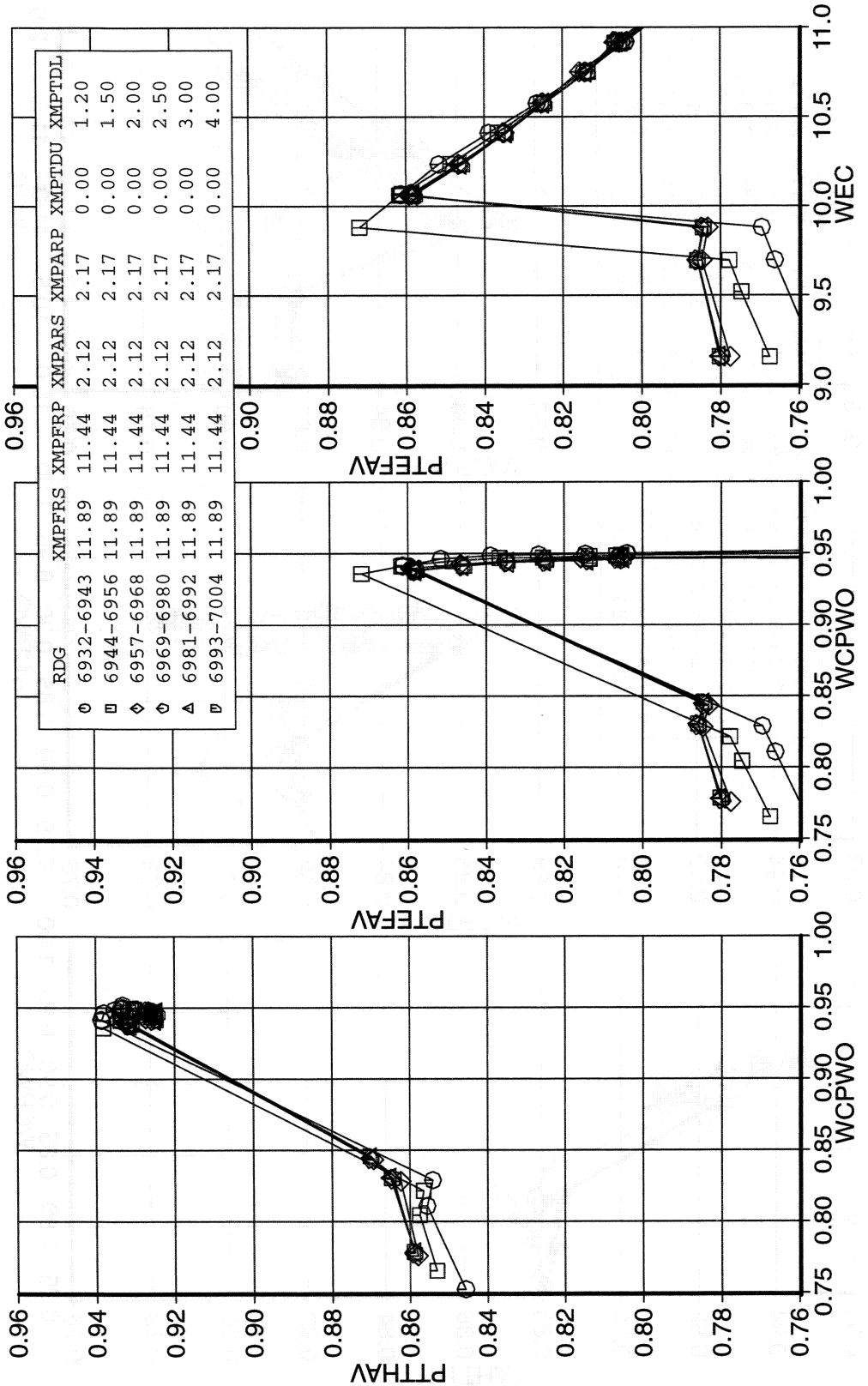

Figure 4–20. Recovery Curves for Started Through Buzz Condition, Bleed Configuration 9, Aft Ramp 3, Vortex Generator 0, Single Plenum Door Open, MOLOC = 2.35, ALPHA = 0., BETA = 0.

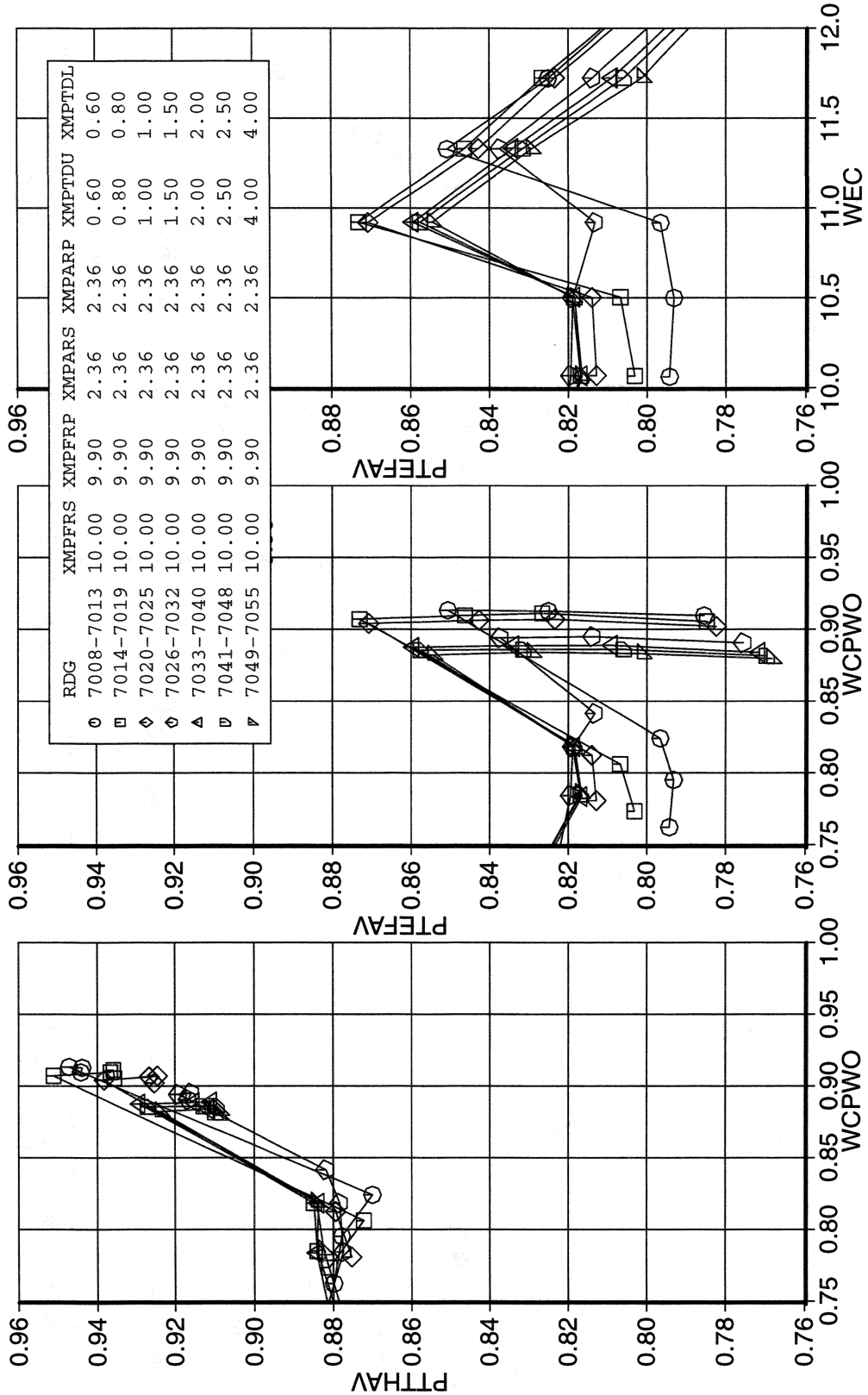

Figure 4–21. Recovery Curves for Started Through Buzz Condition, Bleed Configuration 9, Aft Ramp 3, Vortex Generator 0, Both Plenum Doors Open, MOLOC = 2.20, ALPHA = 0., BETA = 0.

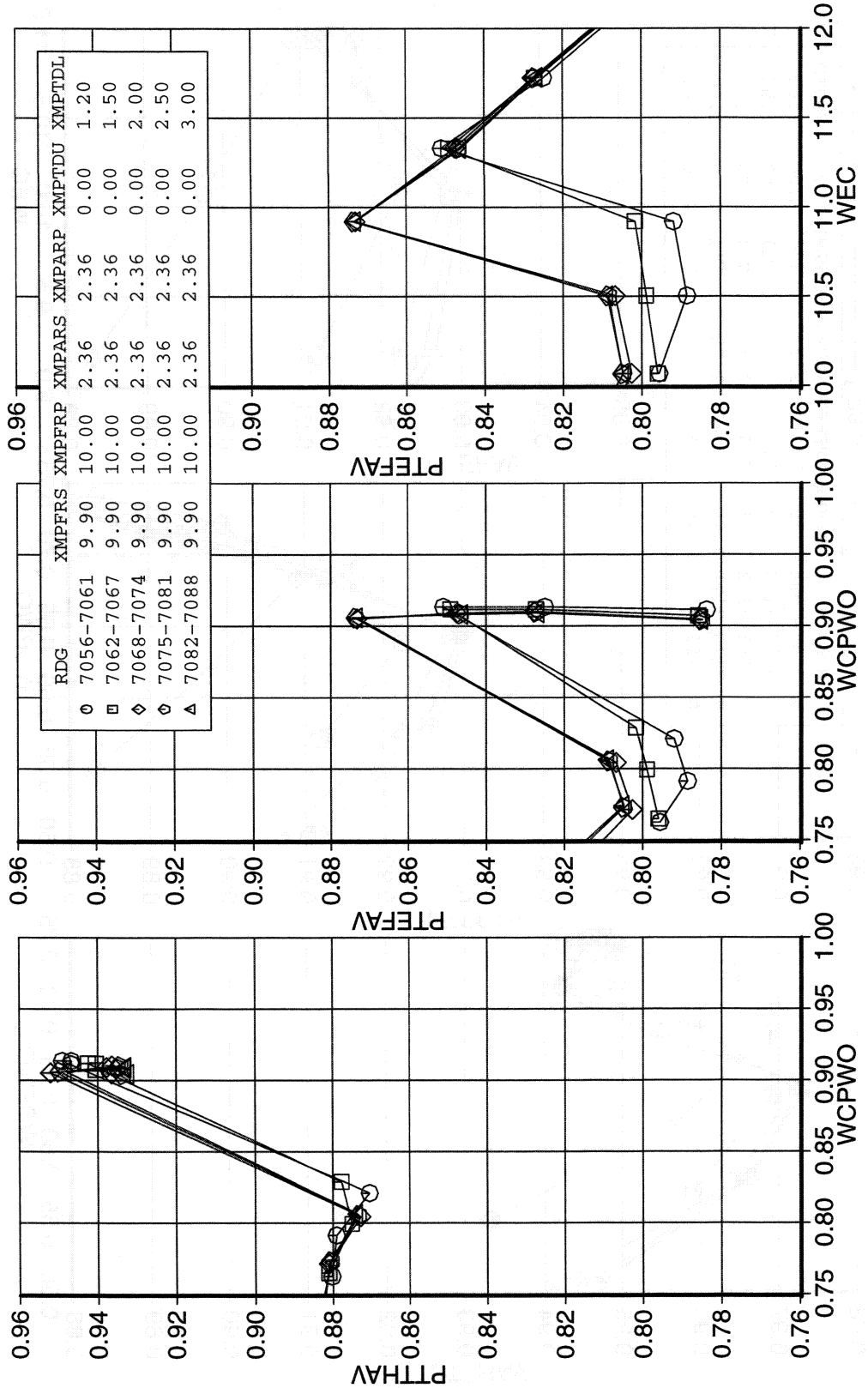

Figure 4–22. Recovery Curves for Started Through Buzz Condition, Bleed Configuration 9, Aft Ramp 3, Vortex Generator 0, Single Plenum Door Open, MOLOC = 2.20, ALPHA = 0., BETA = 0.

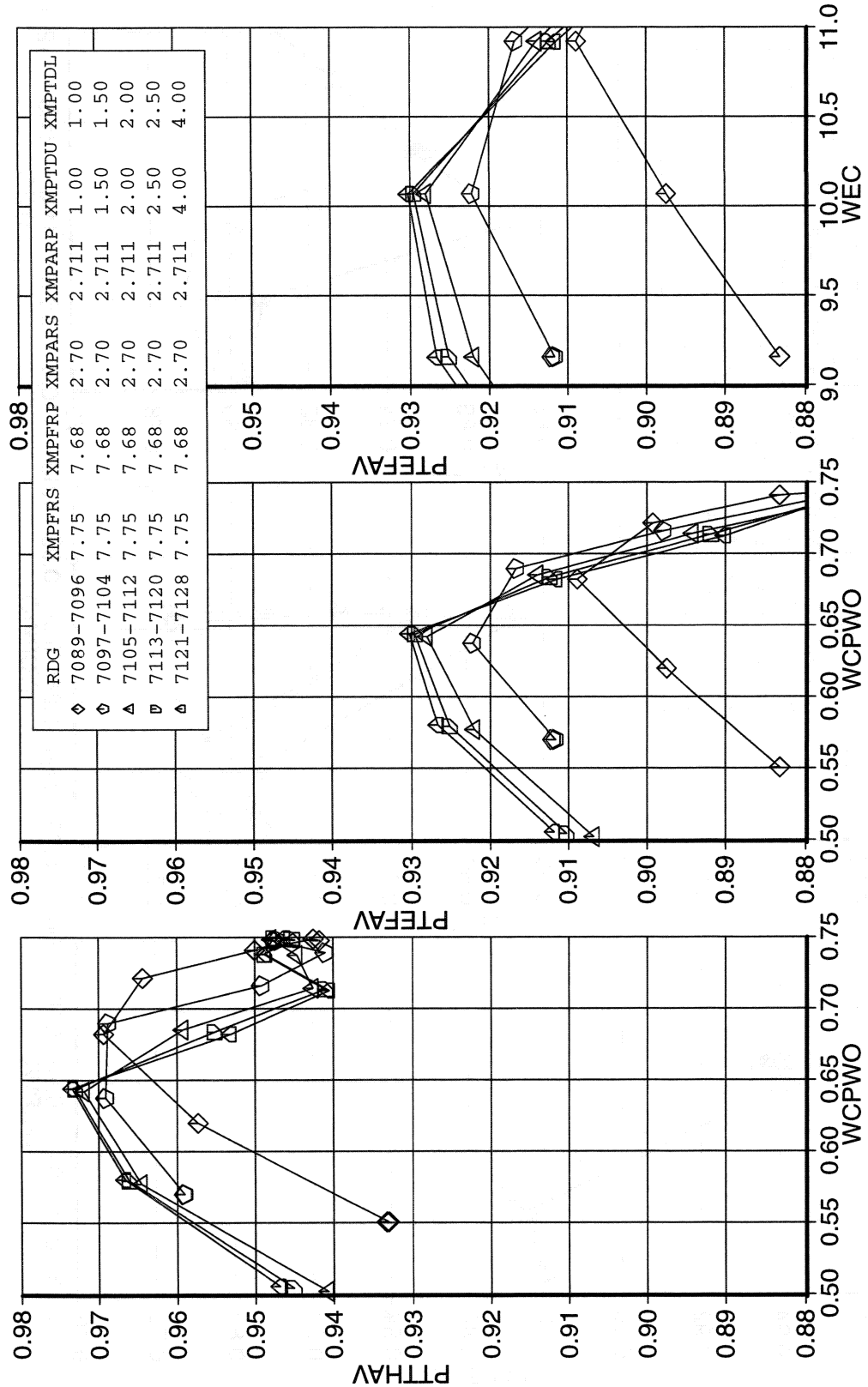

Figure 4–23. Recovery Curves for Started Through Buzz Condition, Bleed Configuration 9, Aft Ramp 3, Vortex Generator 0, Single Plenum Door Open, MOLOC = 1.80, ALPHA = 0., BETA = 0.

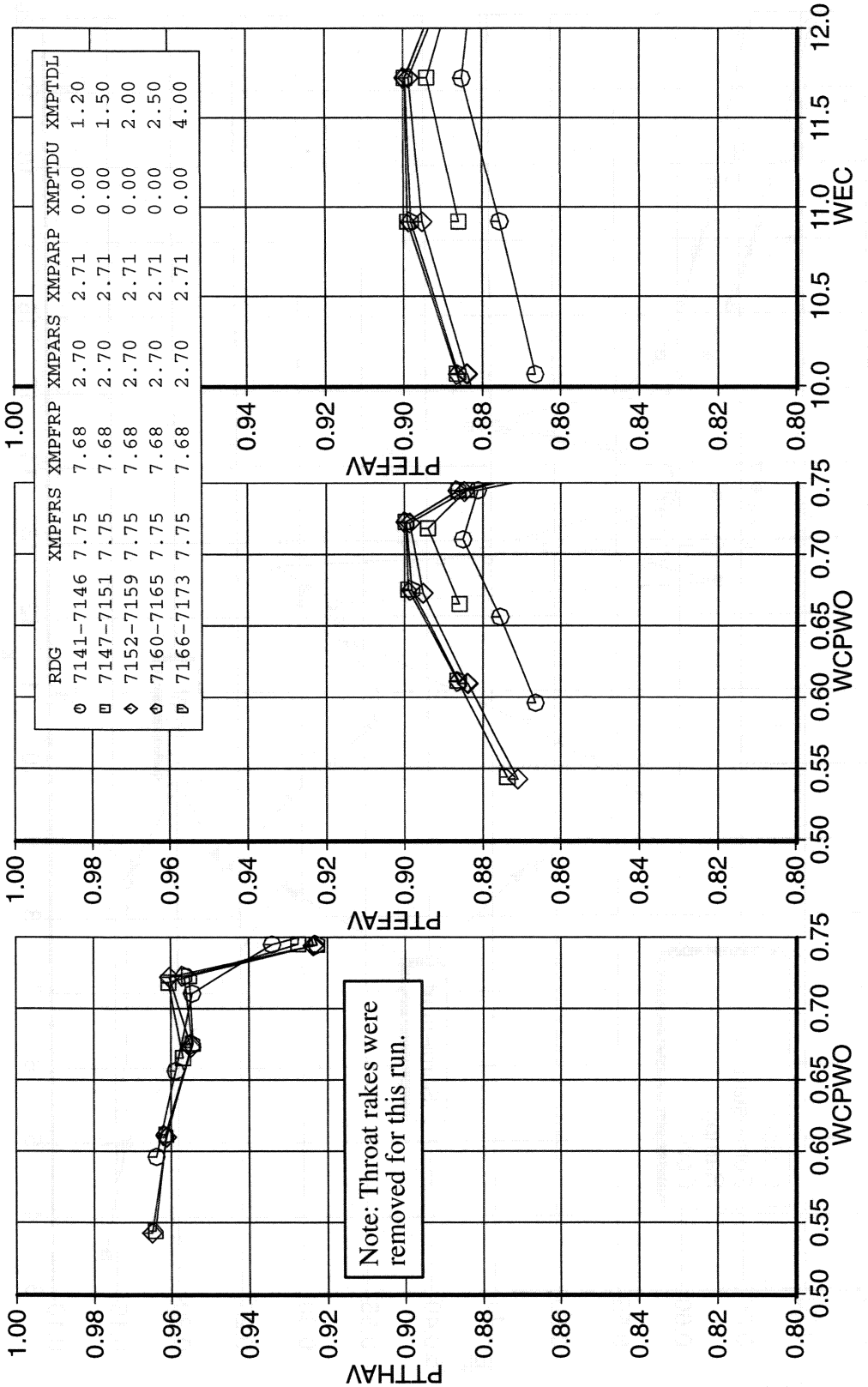

Figure 4–24. Recovery Curves for Started Through Buzz Condition, Bleed Configuration 9, Aft Ramp 3, Vortex Generator 0, Single Plenum Door Open, MOLOC = 1.80, ALPHA = 0., BETA = 0.

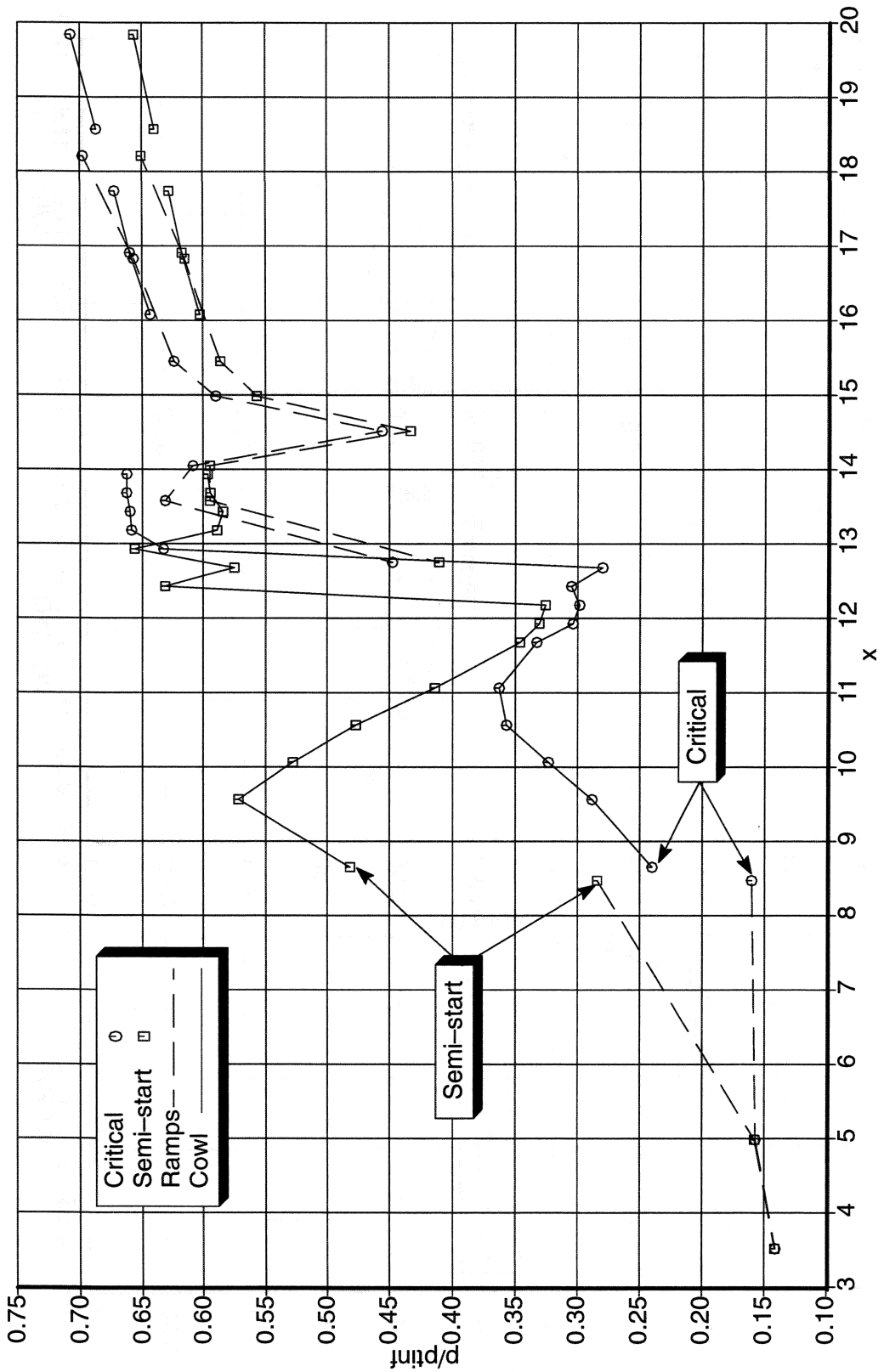

Figure 4–25. Surface Pressure Comparison for Critical and Semi–start conditions, MOLOC = 2.35, ALPHA = 0., BETA = 0., Rdg. 6778 and 6779

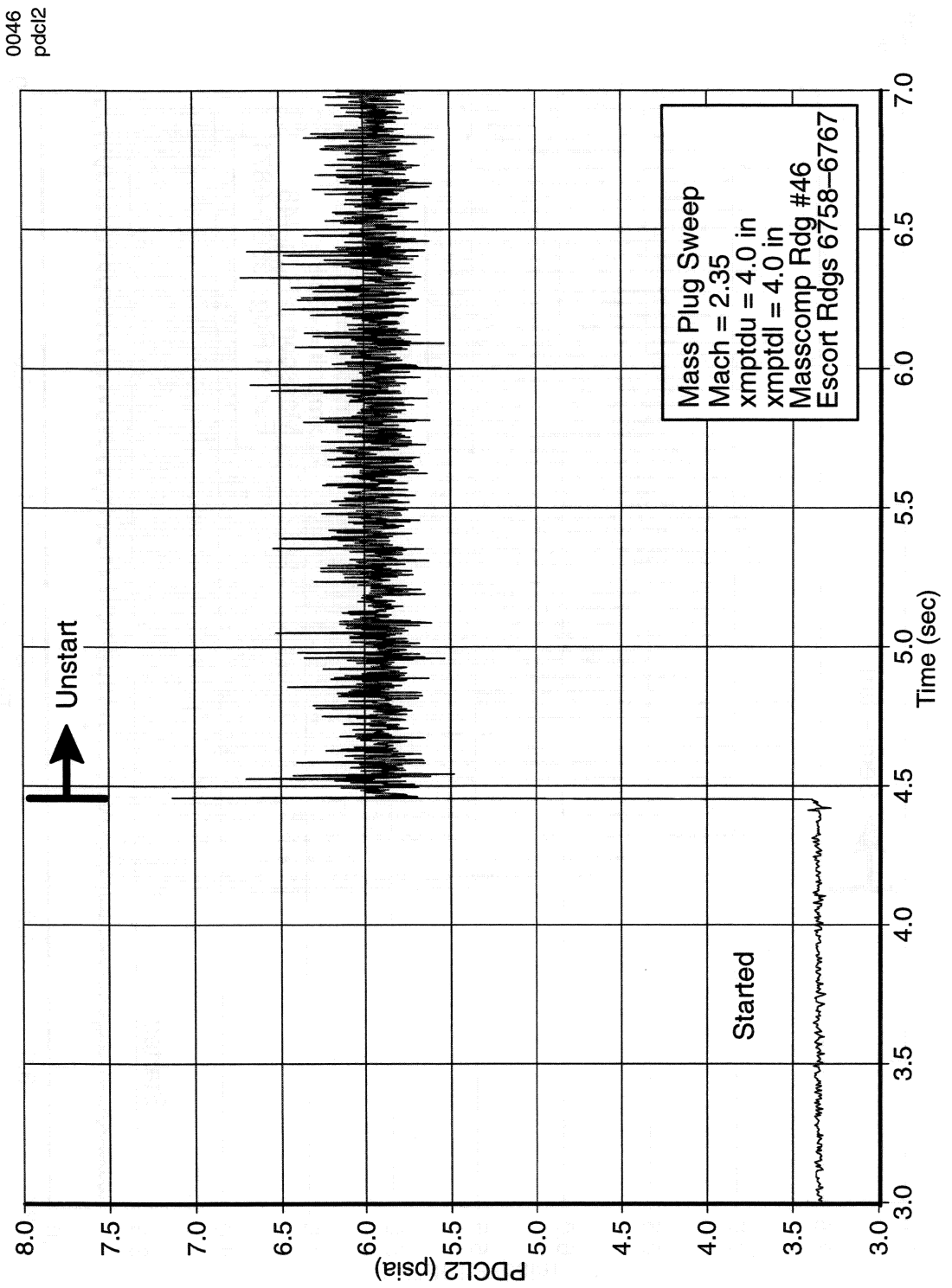

Figure 4–26. Dynamic Static Pressure, Cowl Lip (Port Side) MOLOC = 2.35, ALPHA = 0., BETA = 0.

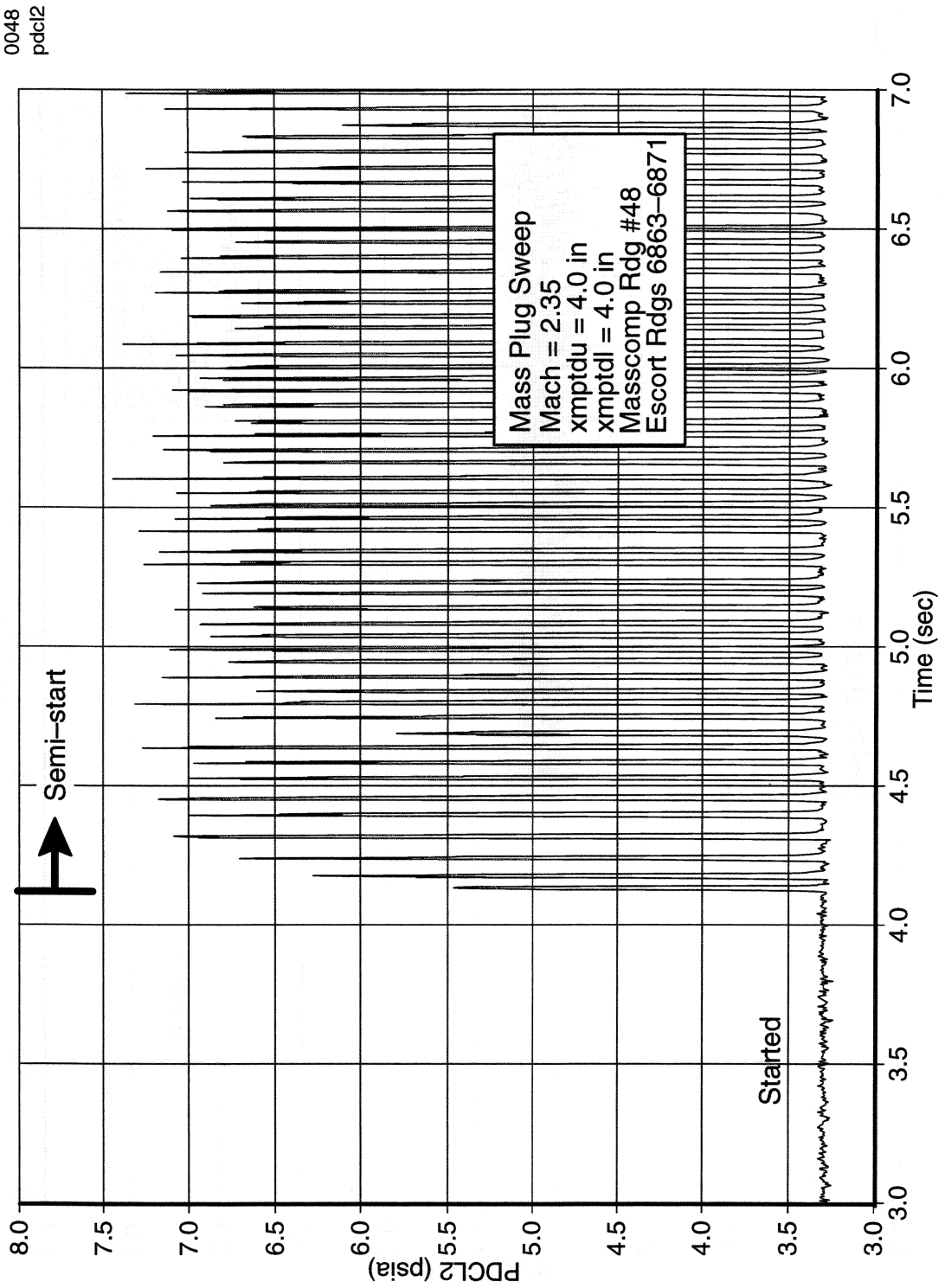

Figure 4–27. Dynamic Static Pressure, Cowl Lip (Port Side) MOLOC = 2.35, ALPHA = 0., BETA = 0.

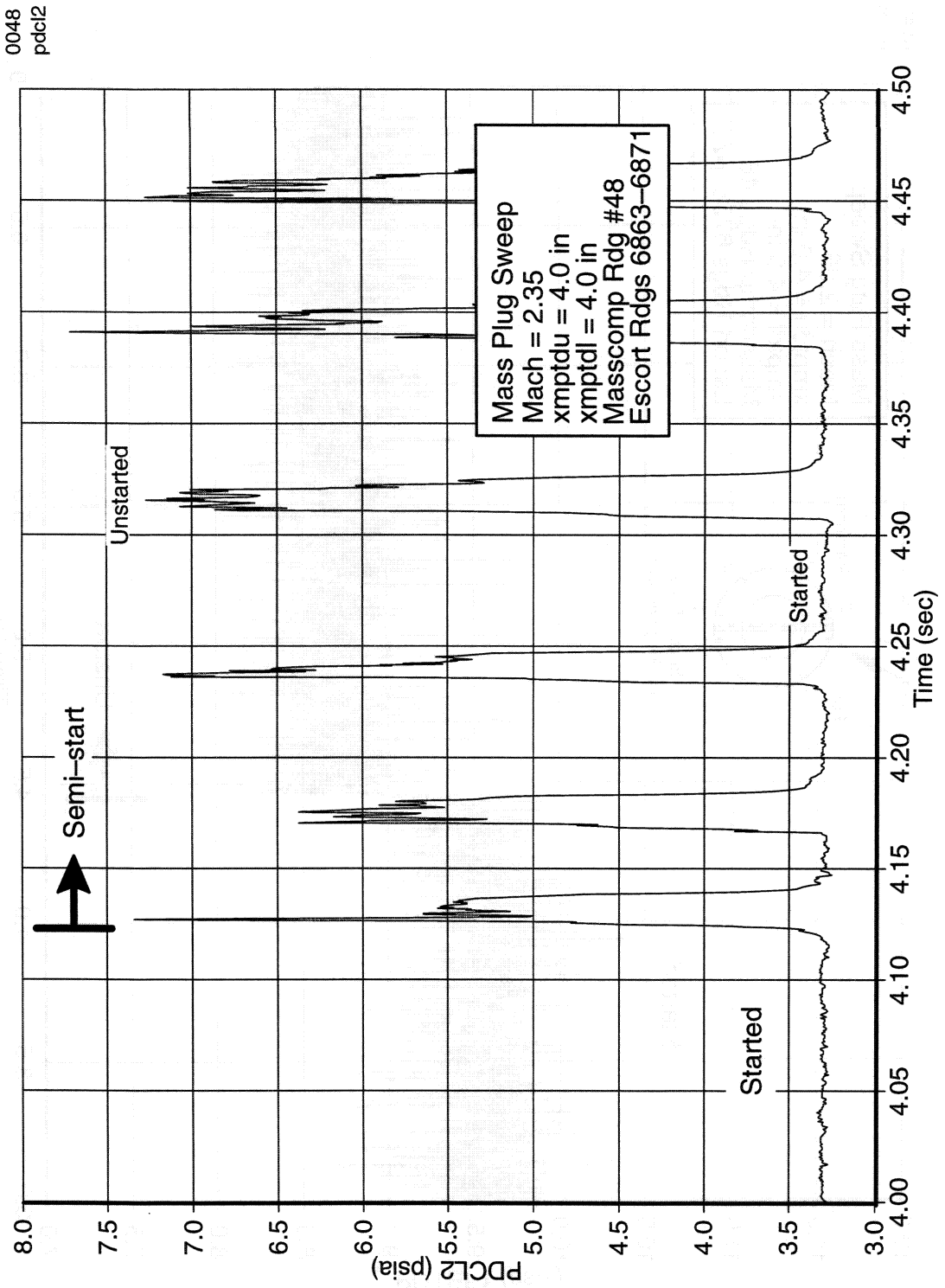

Figure 4–28. Semi–Start Buzz, Cowl Lip (Port Side)
MOLOC = 2.35, ALPHA = 0., BETA = 0.

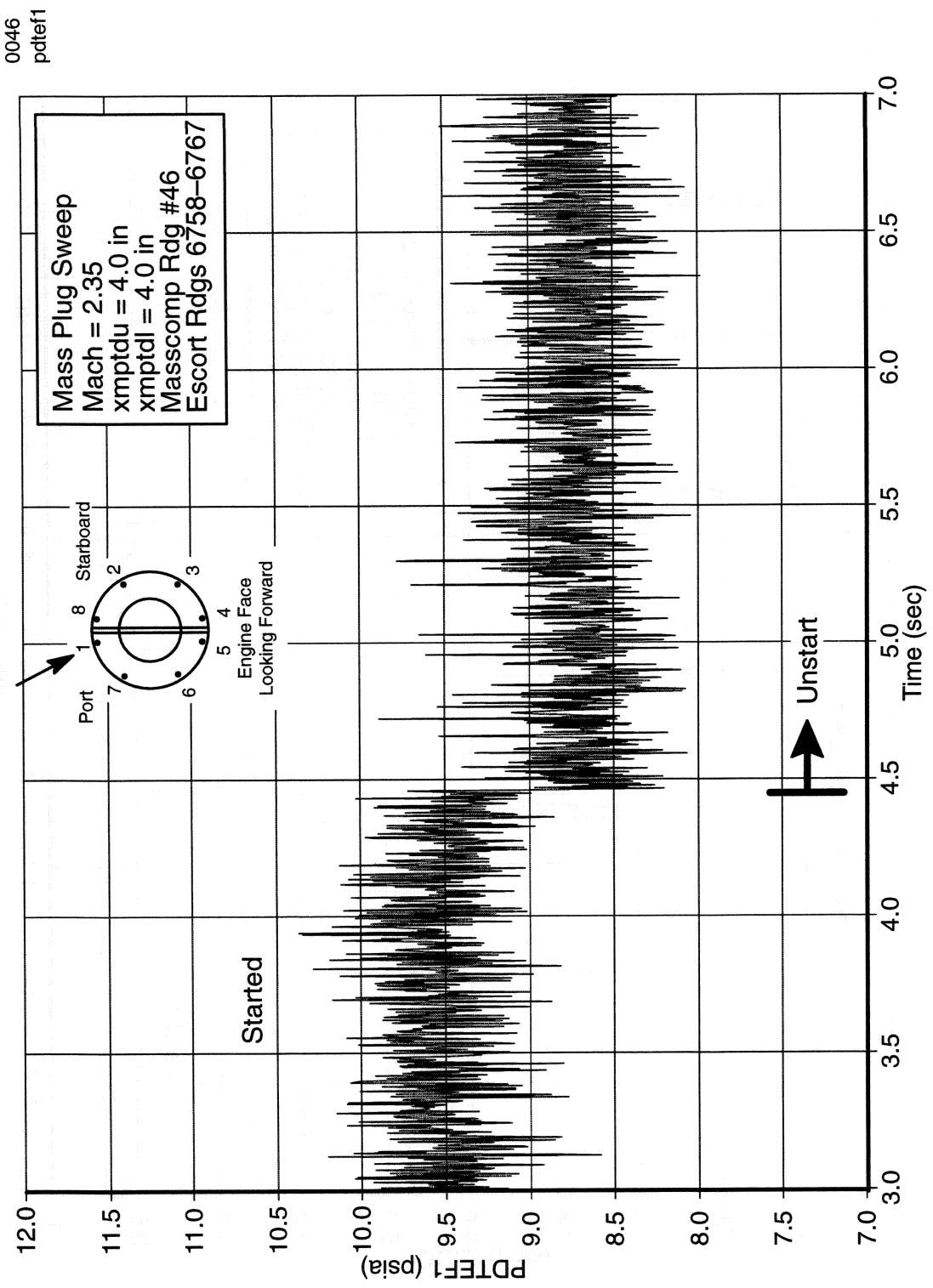

Figure 4–29. Dynamic Total Pressure, Engine Face (Port Side #1) MOLOC = 2.35, ALPHA = 0., BETA = 0.

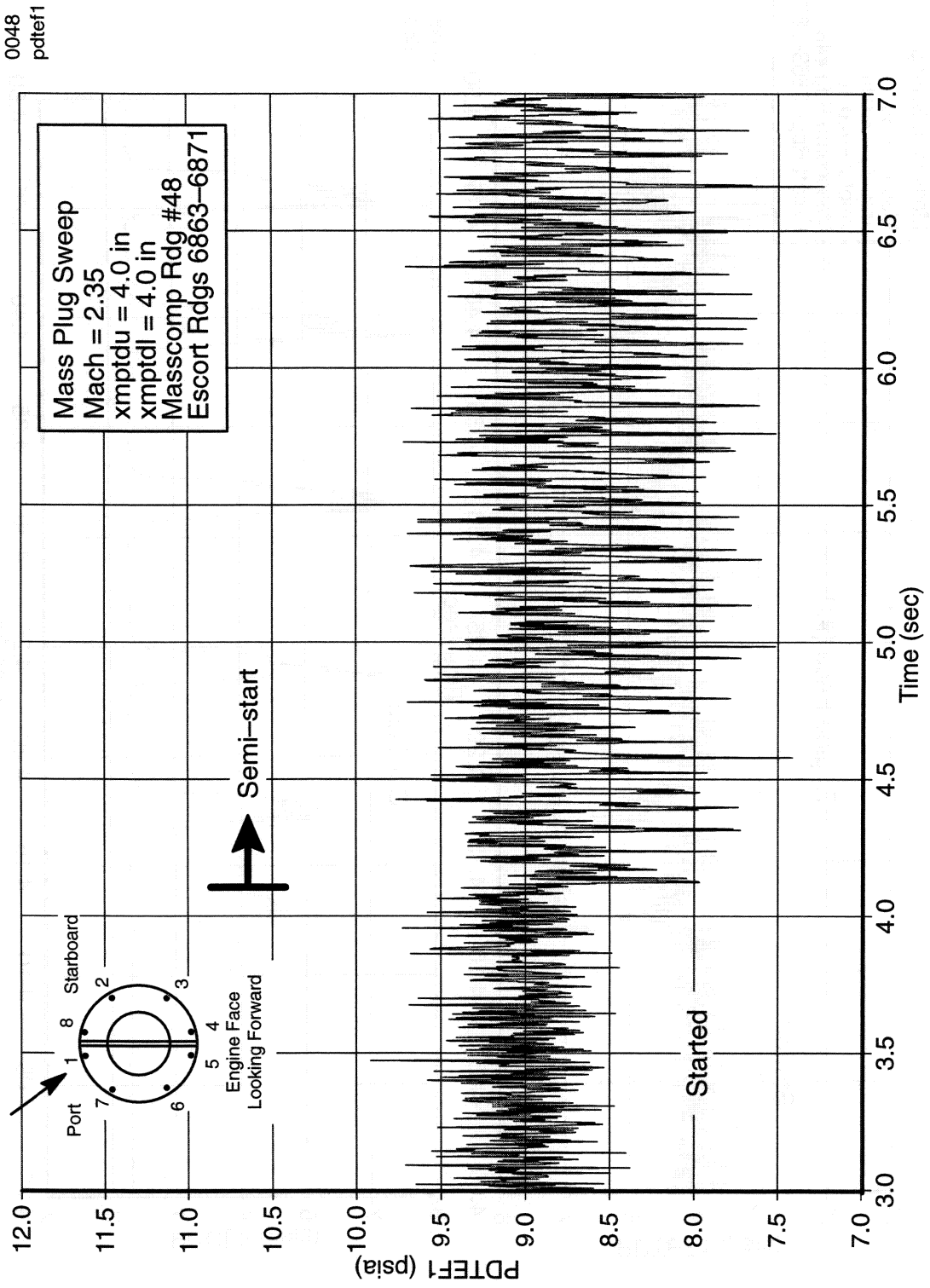

Figure 4–30. Dynamic Total Pressure, Engine Face (Port Side #1) MOLOC = 2.35, ALPHA = 0., BETA = 0.

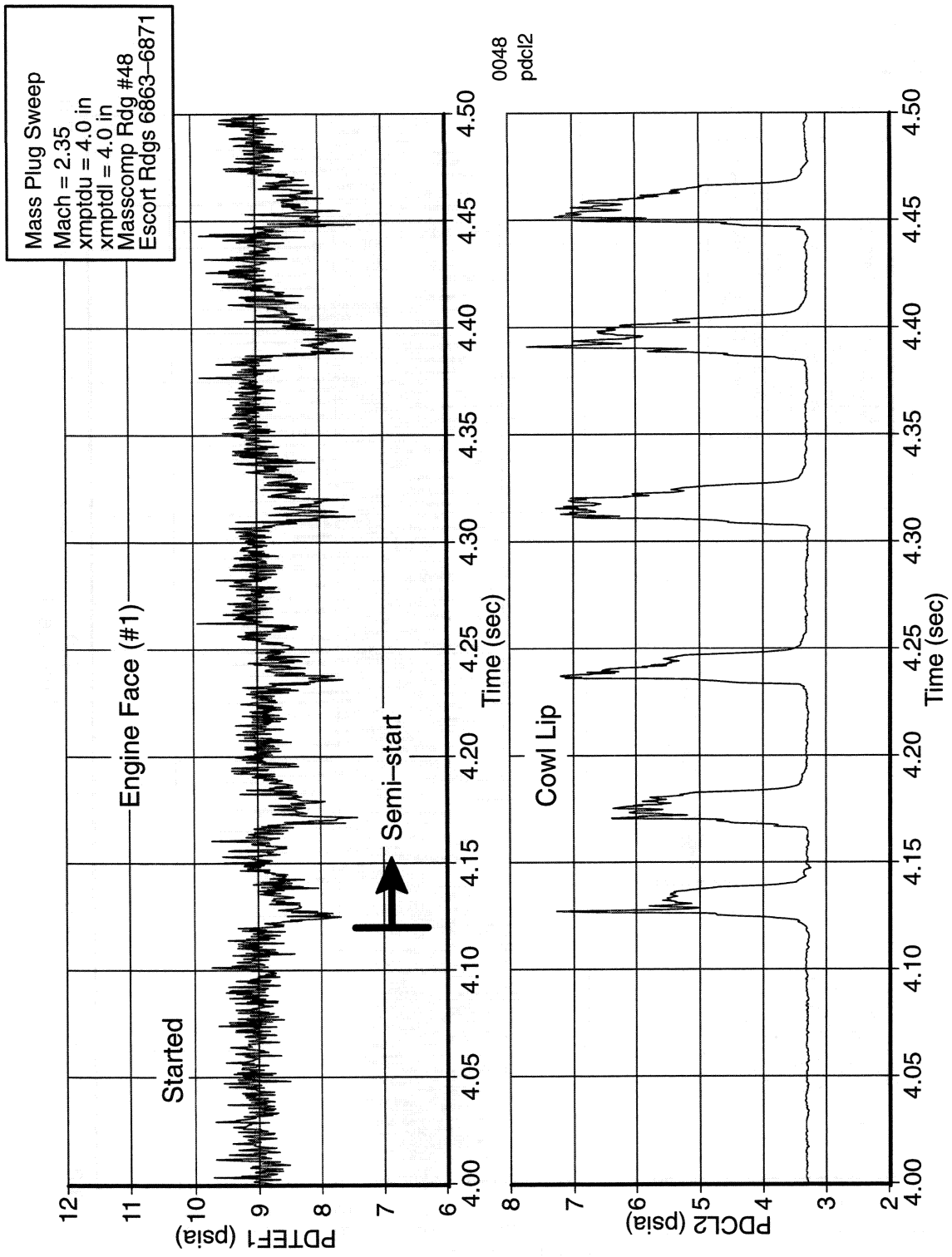

Figure 4–31. Comparison of Engine Face Total to Cowl Lip Static Pressures, MOLOC = 2.35, ALPHA = 0., BETA = 0.

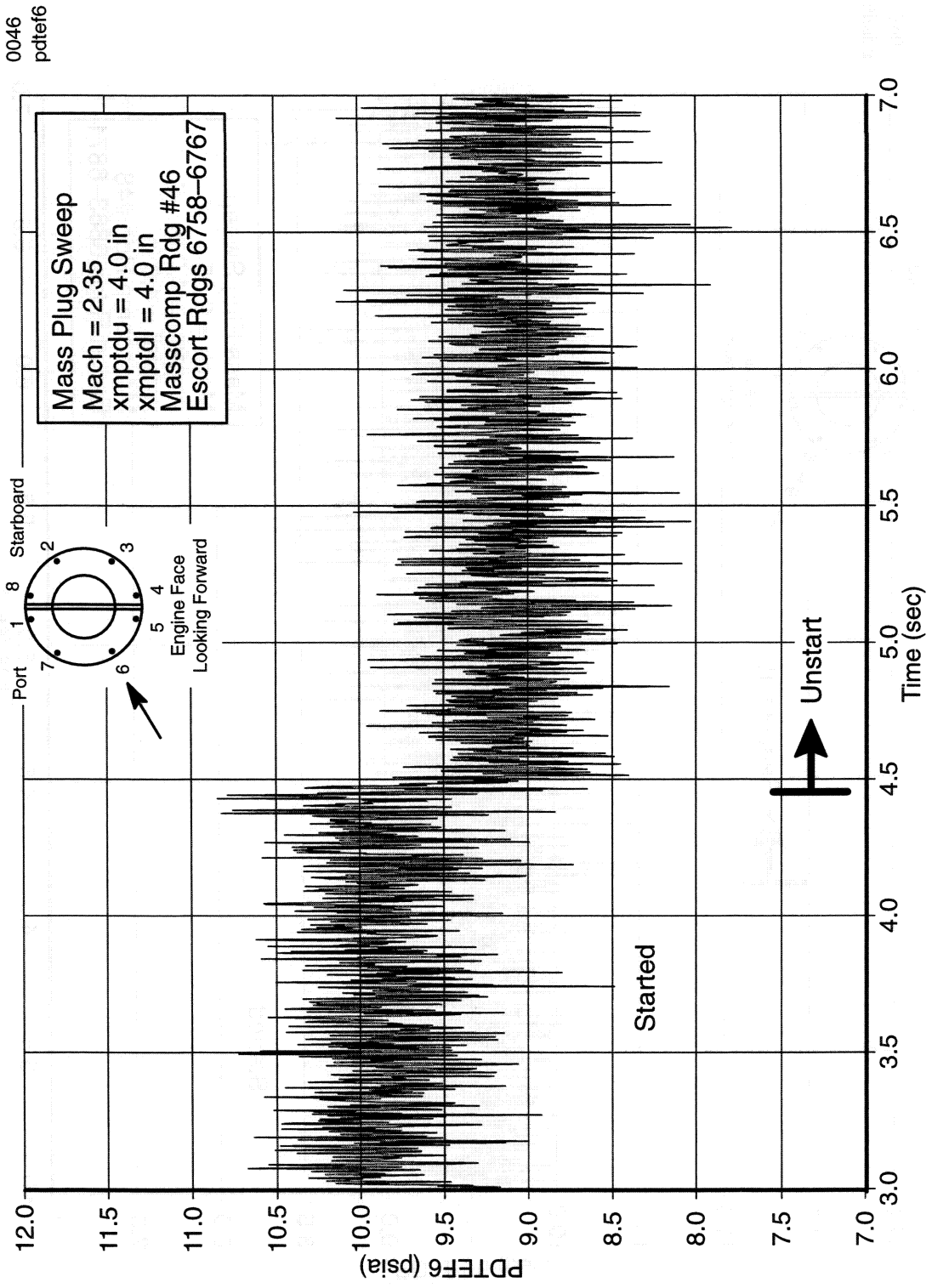

Figure 4–32. Dynamic Total Pressure, Engine Face (Port Side #6) MOLOC = 2.35, ALPHA = 0., BETA = 0.

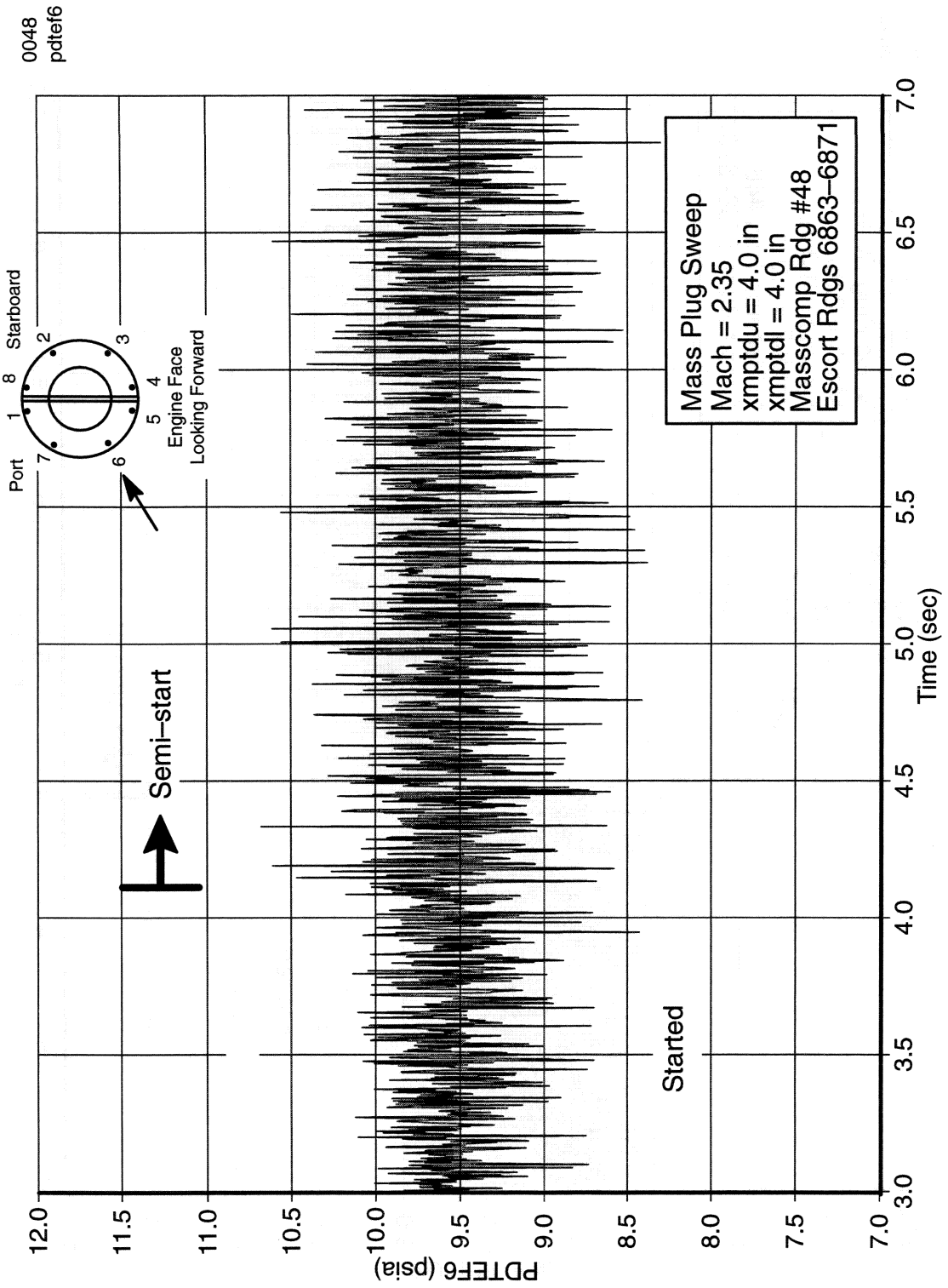

Figure 4–33. Dynamic Total Pressure, Engine Face (Port Side #6) MOLOC = 2.35, ALPHA = 0., BETA = 0.

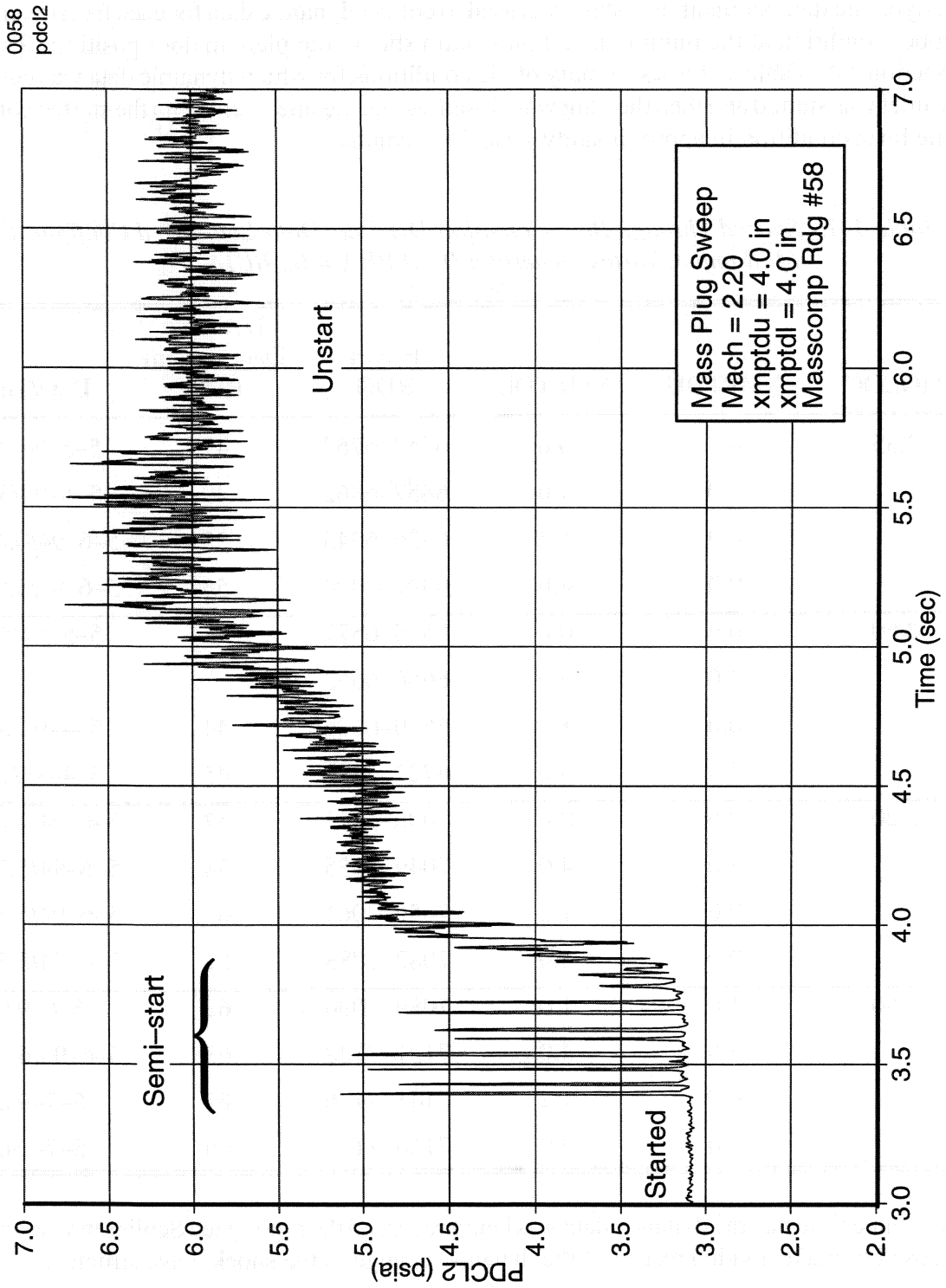

Figure 4–34. Dynamic Static Pressure, Cowl Lip (Port Side)
MOLOC = 2.20, ALPHA = 0., BETA = 0.

4.5. UNSTART DYNAMICS

The dynamic data acquisition system was used to collect dynamic data for each freestream Mach number condition at the minimum and maximum shock trap plenum door positions discussed in Section 4.4. Table 4–1 is a summary of the conditions for which dynamic data was collected. The inlet was started and then the plug was closed so that the inlet went from the started condition to the buzz condition in approximately 10 to 15 seconds.

Table 4–1. Started Through Buzz Condition Dynamic Data Log, Bleed Configuration 9, Aft Ramp 3, Vortex Generator 0, ALPHA = 0., BETA = 0.

MOLOC	XMPTDU	XMPTDL	Escort RDG	Dynamic Data System RDG	Date/Time
2.35	0.6	0.6	6758–6767	47	5–5–94/2:32
	4.0	4.0	6857–6862	49	5–5–94/3:46
	0.0	1.2	6936–6943	55	5–6–94/0:49:44
	0.0	4.0	6997–7004	56	5–6–94/3:01:07
2.60	0.6	0.6	6570–6577	43	5–5–94/5:18
	3.0	3.0	6656–6663	–	–
	0.0	1.2	6670–6676	44	5–4–94/6:47
	0.0	3.0	6722–6729	45	5–4–94/7:20
2.20	0.6	0.6	7008–7013	57	5–6–94/4:07:51
	4.0	4.0	7049–7055	58	5–6–94/5:29:12
	0.0	1.2	7056–7061	60	5–6–94/5:38:20
	0.0	4.0	7082–7088	61	5–6–94/5:54:40
1.80	1.0	1.0	7089–7096	62	5–6–94/?
	4.0	4.0	7121–7128	63	5–6–94/6:45:44
	0.0	1.2	7141–7146	65	5–7–94/?
	0.0	4.0	7166–7173	66	5–7–94/?

At the same time that the dynamic data was being recorded the high speed Schlieren video system was used to make a video record of the dynamic change in the shock wave structure.

The recorded dynamic data comprises a significant volume of material. Some of this data is presented in the previous section to discuss the semi–start phenomenon. The remaining data is available for review upon request.

4.6. ANGLE OF ATTACK OPERATION

The angle of attack effects on inlet performance was investigated by pitching the model relative to the gust plate and observing the change in engine face recovery and distortion. Mach numbers of 2.6, 2.35, 2.20, 2.00, 1.80 and 1.60 were studied at angles of attack from 0° to ±5°. Each Mach number was run with various throat slot bypass door settings. All data was taken with aft ramp leading edge #3 and bleed pattern #9.

Fig. 4–35 shows the engine face recovery, distortion, mass flow plug position (xmfp) and forward ramp positions (xmpfrs and xmpfrp) versus angle of attack for Mach 2.60. The figure shows that the recovery and distortion are symmetrical about $\alpha = 0°$. The mass flow plug position was also symmetrical and was opened with angle of attack to keep the inlet started. The forward ramps remained fixed. The figure shows that the recovery dropped from 0.75 to 0.60, while the distortion increased from about 0.20 to 0.60 when the angle of attack changed from 0° to ±5°. The bypass doors are shown to not have a significant effect on the angle of attack behavior of the inlet. Their main effect is to change the recovery and distortion levels while the shape of the curves remain the same.

Fig. 4–36 shows the results for Mach 2.35 which are similar to the Mach 2.60 results. For this Mach number, the forward ramp angles were decreased as the angle of attack was increased. However, the recovery still drops from 0.85 to 0.67, while the distortion rises from 0.2 to 0.7. Also, the bypass door effect is similar to the Mach 2.60 results.

Fig. 4–37 shows the recovery, distortion, mass flow plug position and forward ramp positions results for Mach 2.20. The plot shows the same type of behavior for Mach 2.20 as was shown for Mach 2.60 and 2.35. The recovery drops from 0.87 to 0.71, while the distortion increases from 0.20 to 0.60. In Fig. 4–38 the Mach 2.00 results are shown and one can see that the inlet recovery and distortion are similar to the previous Mach numbers. The recovery drops from 0.85 to 0.77 for the bypass doors at 2.0" and down to 0.67 for the doors at 1.0". The distortion varies from 0.30 at 0° to 0.60 at ±5°. The figure shows that the forward ramps were fixed for this Mach number.

Fig. 4–39 contains the results for Mach 1.80 and shows that the recovery and distortion have less change at angle of attack than the previous Mach numbers. The plots of the Mach 1.60 results in Fig. 4–40 show more similarity to the Mach 1.80 results than the other Mach numbers.

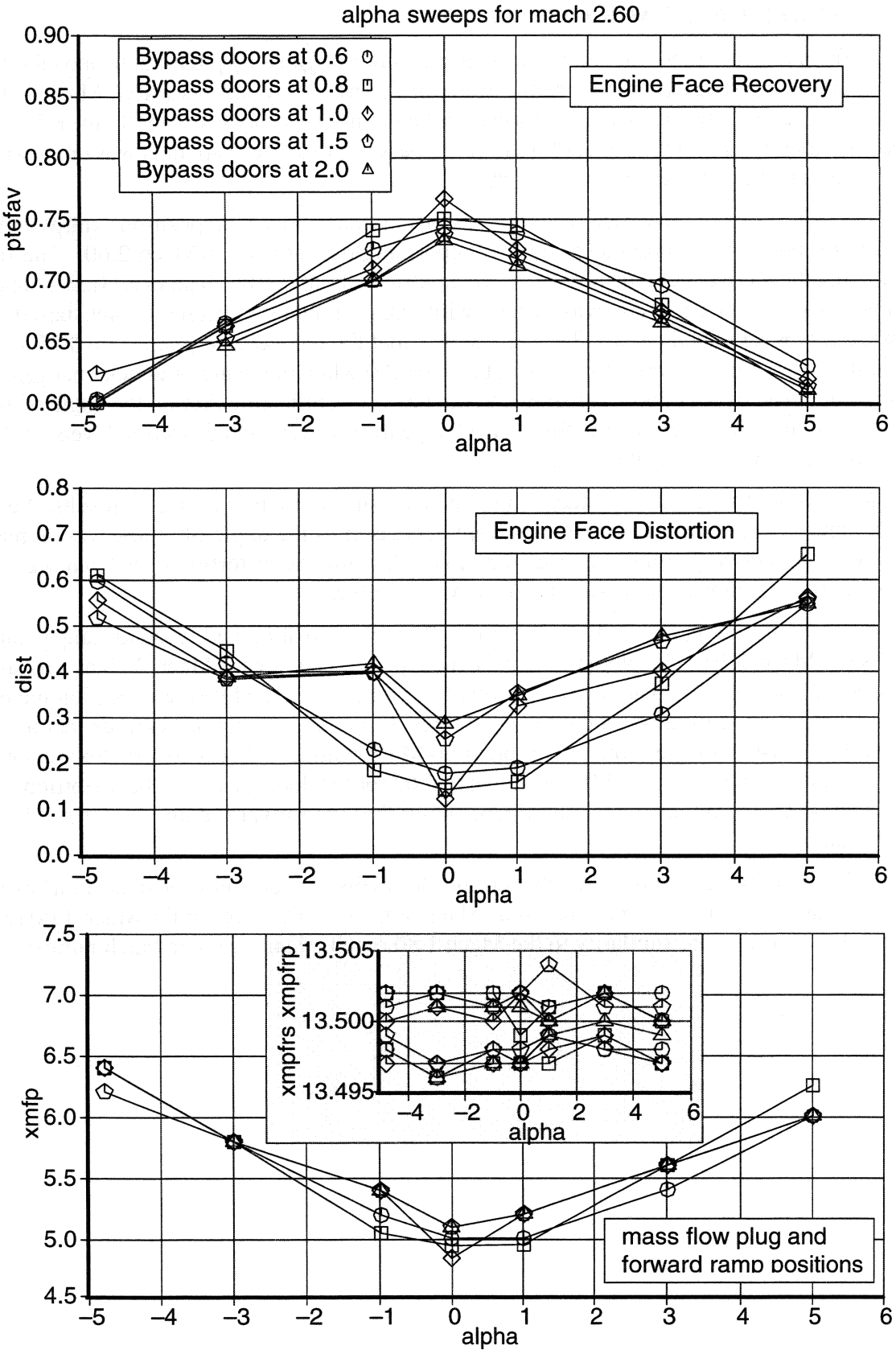

Figure 4–35. Mach 2.60 Angle of Attack Results.

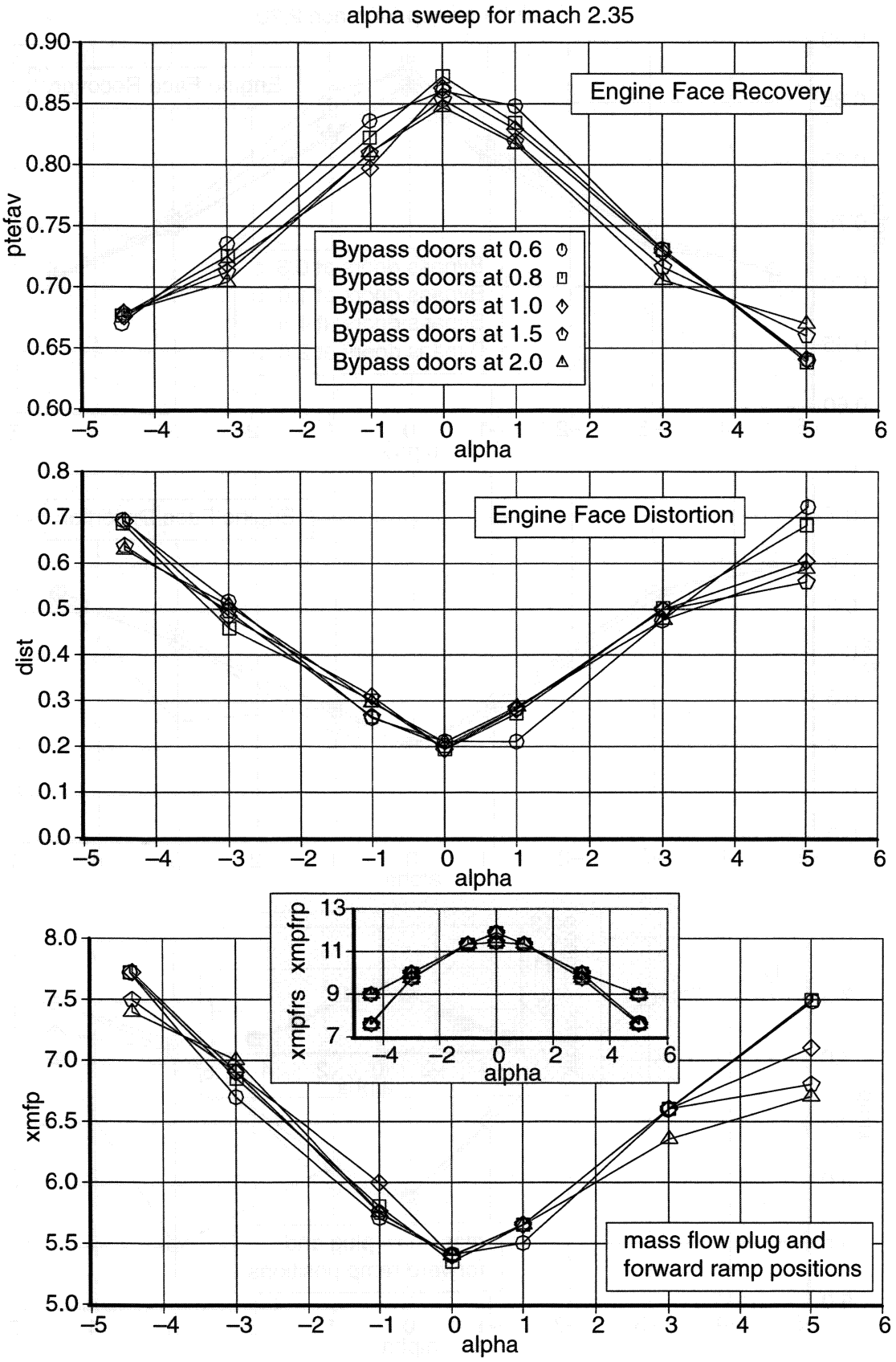

Figure 4–36. Mach 2.35 Angle of Attack Results.

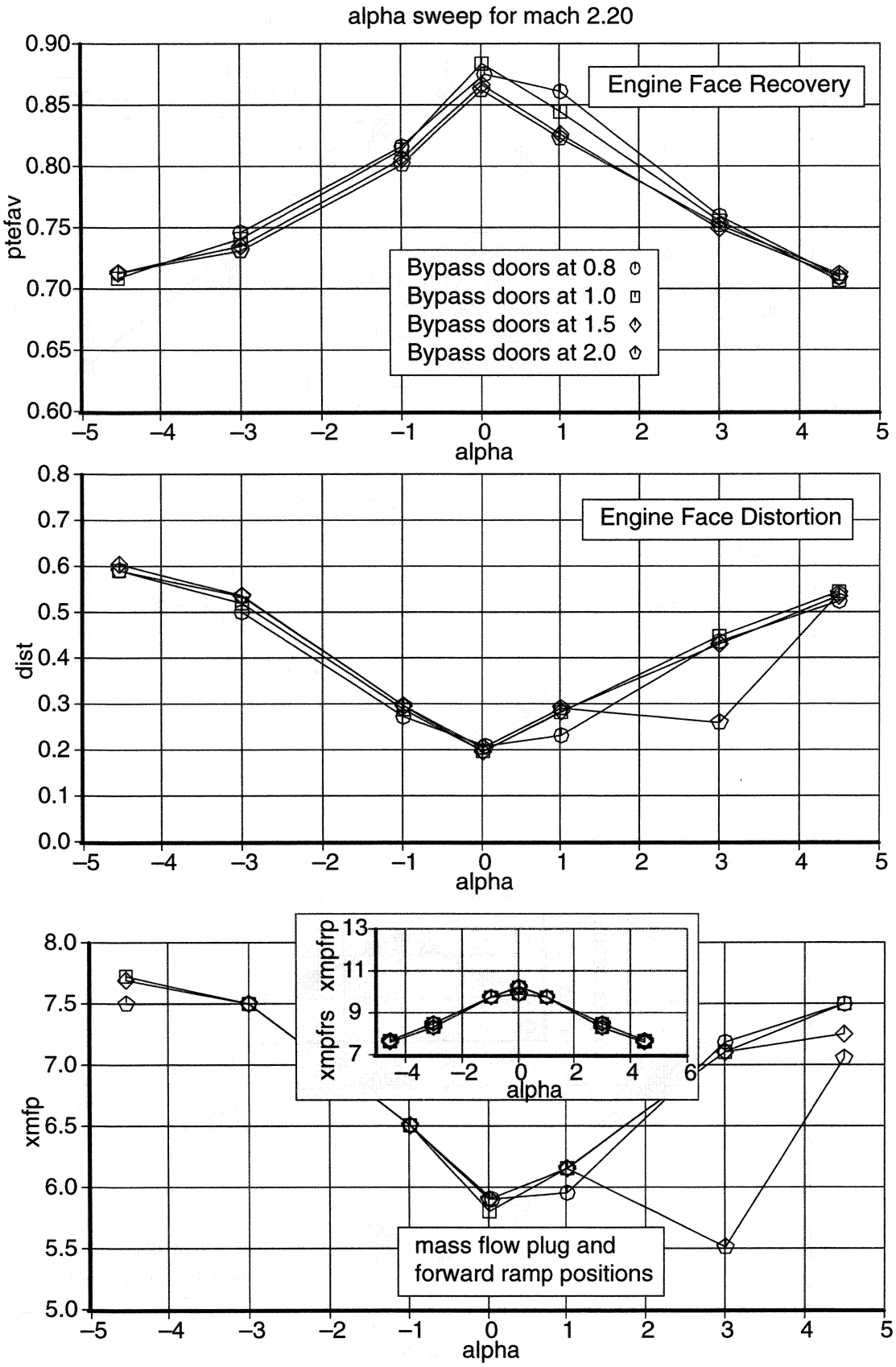

Figure 4–37. Mach 2.20 Angle of Attack Results.

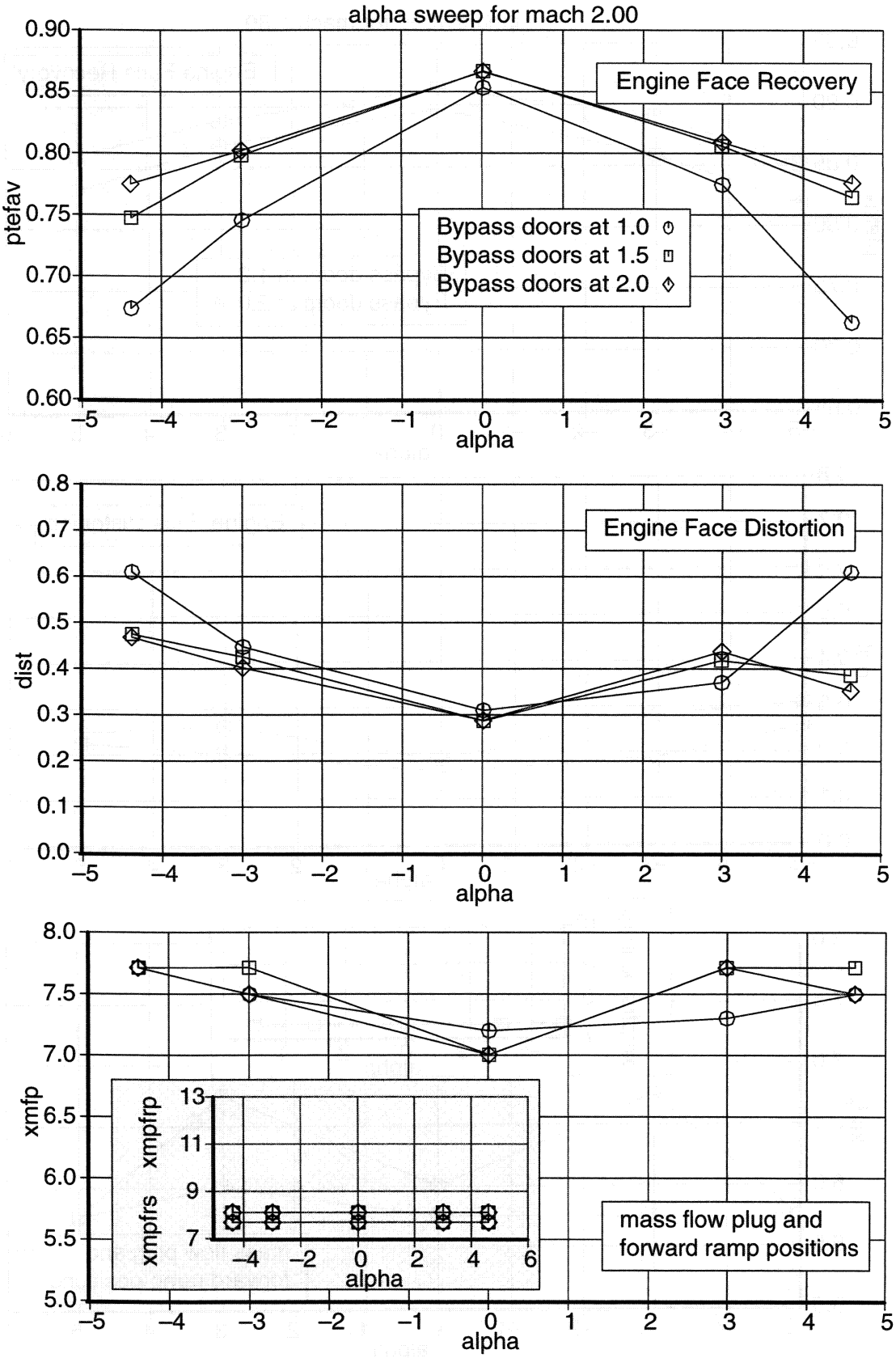

Figure 4–38. Mach 2.00 Angle of Attack Results.

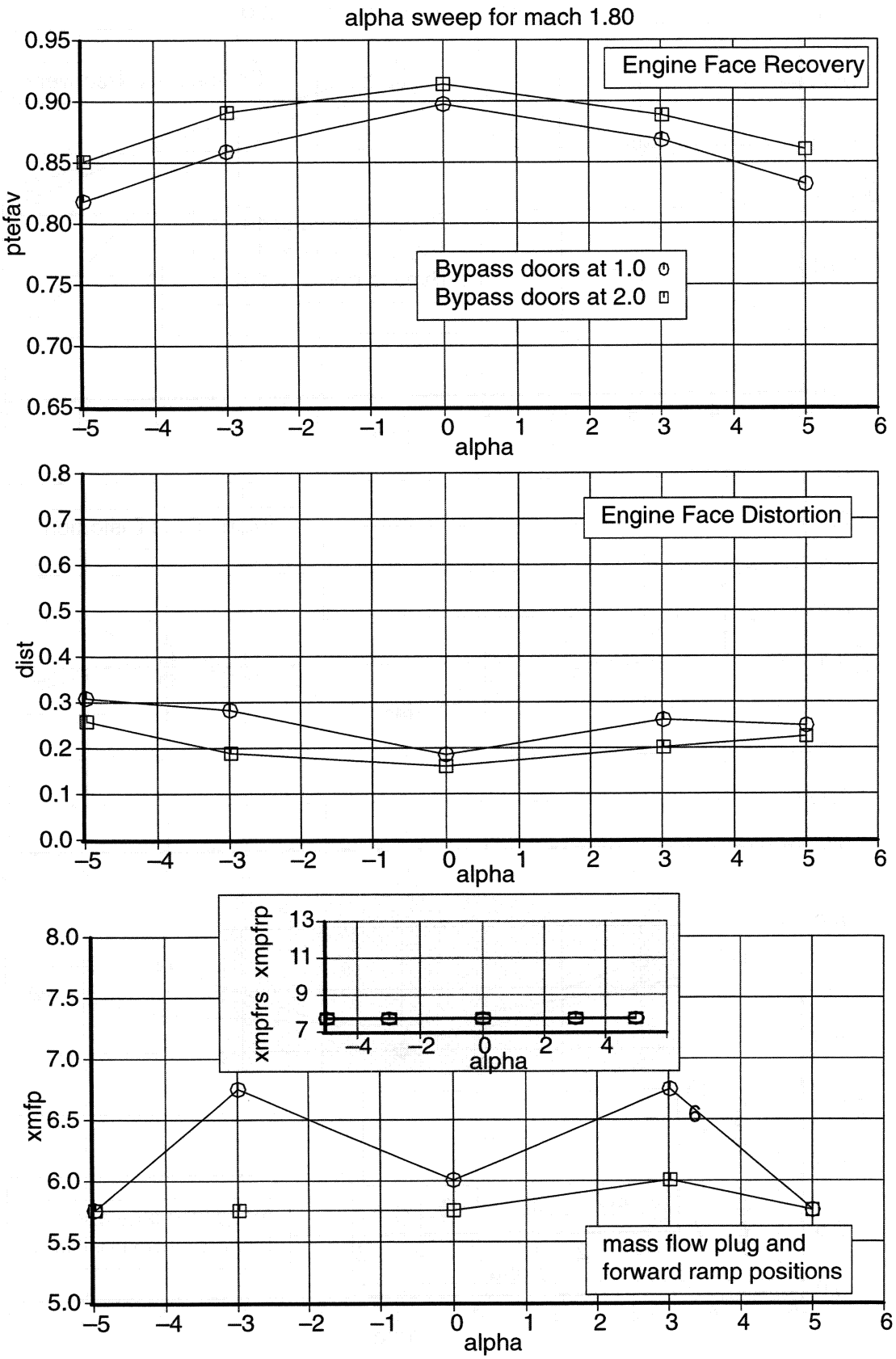

Figure 4–39. Mach 1.80 Angle of Attack Results.

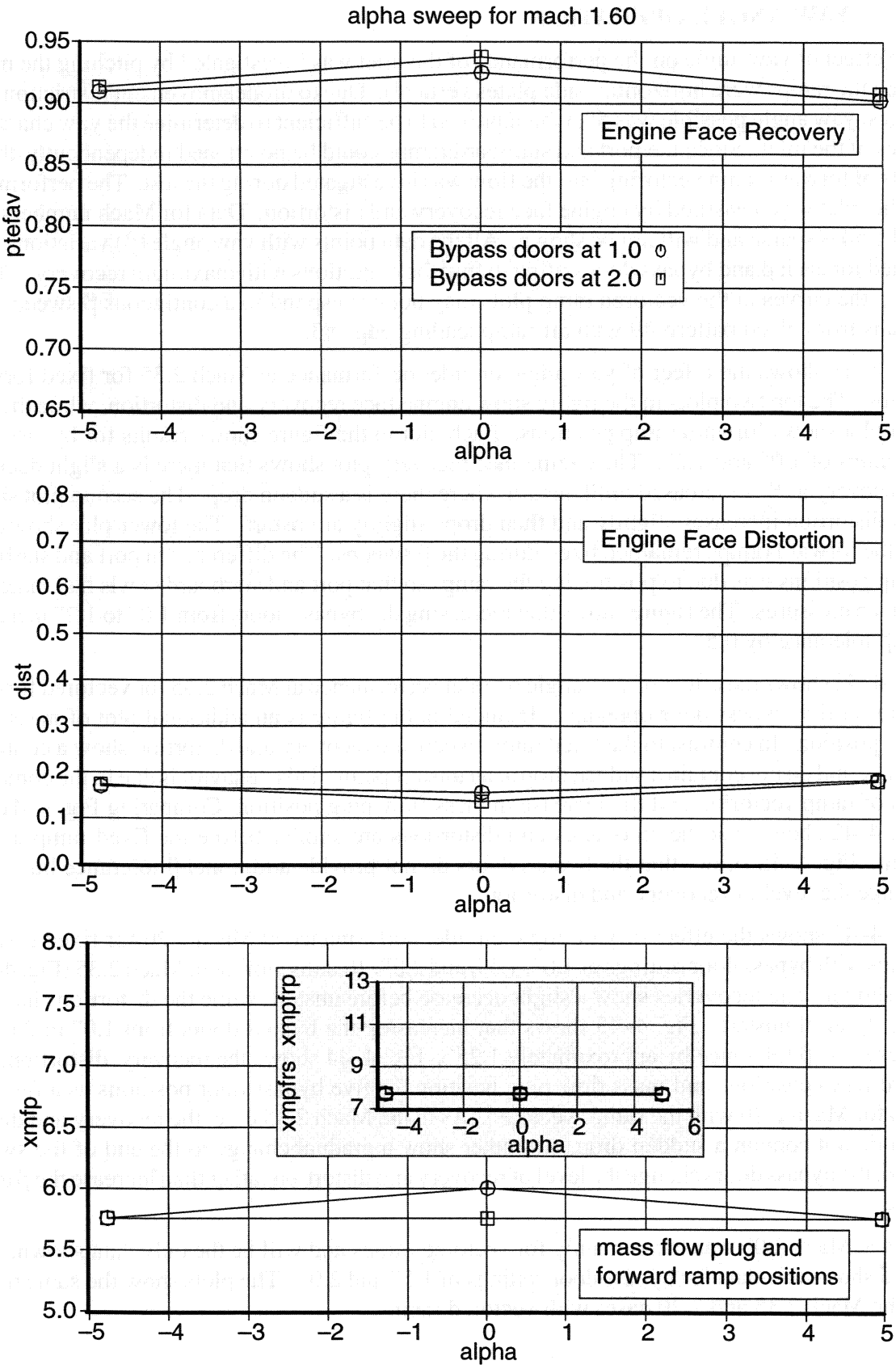

Figure 4–40. Mach 1.60 Angle of Attack Results.

4.7. YAW ANGLE OPERATION

The effect of yaw angle on the performance of the inlet was investigated by pitching the model when the ramps were horizontal (side plates vertical). Due to model movement restrictions, the largest yaw angle possible was 5°, which proved to be sufficient to determine the yaw characteristics of the inlet. Since the port and starboard ramps could be positioned independently, the effects of forward ramp vectoring into the flow was investigated during the test. The performance of the inlet was measured by engine face recovery and distortion. Data for Mach numbers 1.80 and 1.60 is sparse and will not be shown. All the data points with yaw angle (β) variations were sorted for each β and bypass door setting to find the conditions with maximum recovery. Therefore, the curves in the vectored ramp plots may not correspond to a continuous β sweep. The data is from bleed pattern #9 with aft ramp leading edge #3.

Fig. 4–41 shows the effect of yaw angle on inlet performance at Mach 2.35 for fixed forward ramps. The top two plots in the figure show engine face recovery and distortion, while the bottom plot shows forward ramp positions. Each plot in the figure shows results for bypass door openings of 1.0" and 1.2". The engine face recovery plot shows that there is a slight decrease in recovery as β is increased until unstart where there is a sudden drop. The second plot shows that distortion increases slightly and then drops slightly at unstart. The lower plot shows that the the forward ramps remained fixed during the β sweeps. The difference in port and starboard ramp positions was due to positioning the ramps so that port and starboard cowls had matching surface pressures. The figure shows that increasing the bypass doors from 1.0" to 1.2" increases the β tolerance by 0.5°.

Fig. 4–42 shows the effect of yaw angle on inlet performance at Mach 2.35 for vectored forward ramps at five bypass door openings. Included in the figure is an additional plot of mass flow plug position. In contrast to the fixed ramp sweep, the recovery and distortion show a continual change and do not contain a sudden drop at an unstart point. This behavior is due to the combination of ramp vectoring and the increase in mass flow plug position. Comparing Fig. 4–41 and Fig. 4–42 shows that the recoveries and distortions are similar before the fixed ramp unstart point. Fig. 4–42 shows that the bypass doors do not provide additional β tolerance but rather change the level of recovery and distortion.

Fig. 4–43 shows the effect of yaw angle on inlet performance at Mach 2.20 for fixed forward ramps with bypass door settings of 1.0", 1.5", and 2.0". Results similar to Mach 2.35 (Fig. 4–41) are shown. The recoveries show a slight decrease before unstart, while the distortions increase slightly until unstart. Fig. 4–43 shows that increasing the bypass doors from 1.0" to 2.0" increases the β tolerance by approximately 1.25°. Fig. 4–44 shows the recovery, distortion, forward ramp positions and mass flow plug position for five bypass door positions as a function of β for Mach 2.20 with the ramps vectored. As in the Mach 2.35 case, the recovery and distortion do not contain a sudden drop, but rather show a gradual change to the end of the sweep. Also, the bypass doors change the level of recovery and distortion rather than increase the β tolerance.

Data at Mach 2.00 was taken mainly for vectored ramps and will be the only data shown. Fig. 4–45 shows this data for bypass door settings of 1.5" and 2.0". The plots show the same trends as the Mach 2.35 and 2.20 cases with vectored ramps.

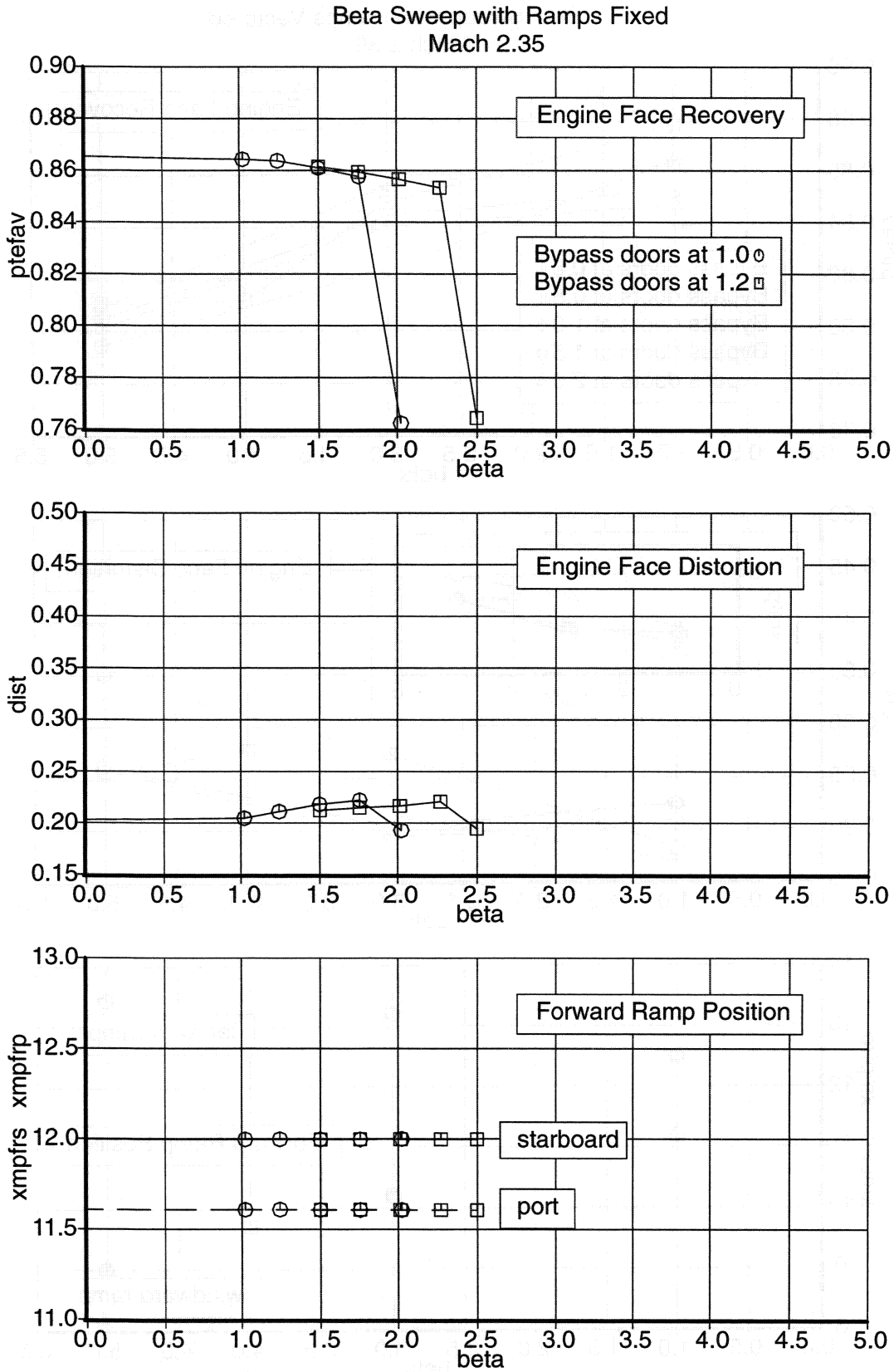

Figure 4–41. Mach 2.35 Beta Sweep with Fixed Ramps.

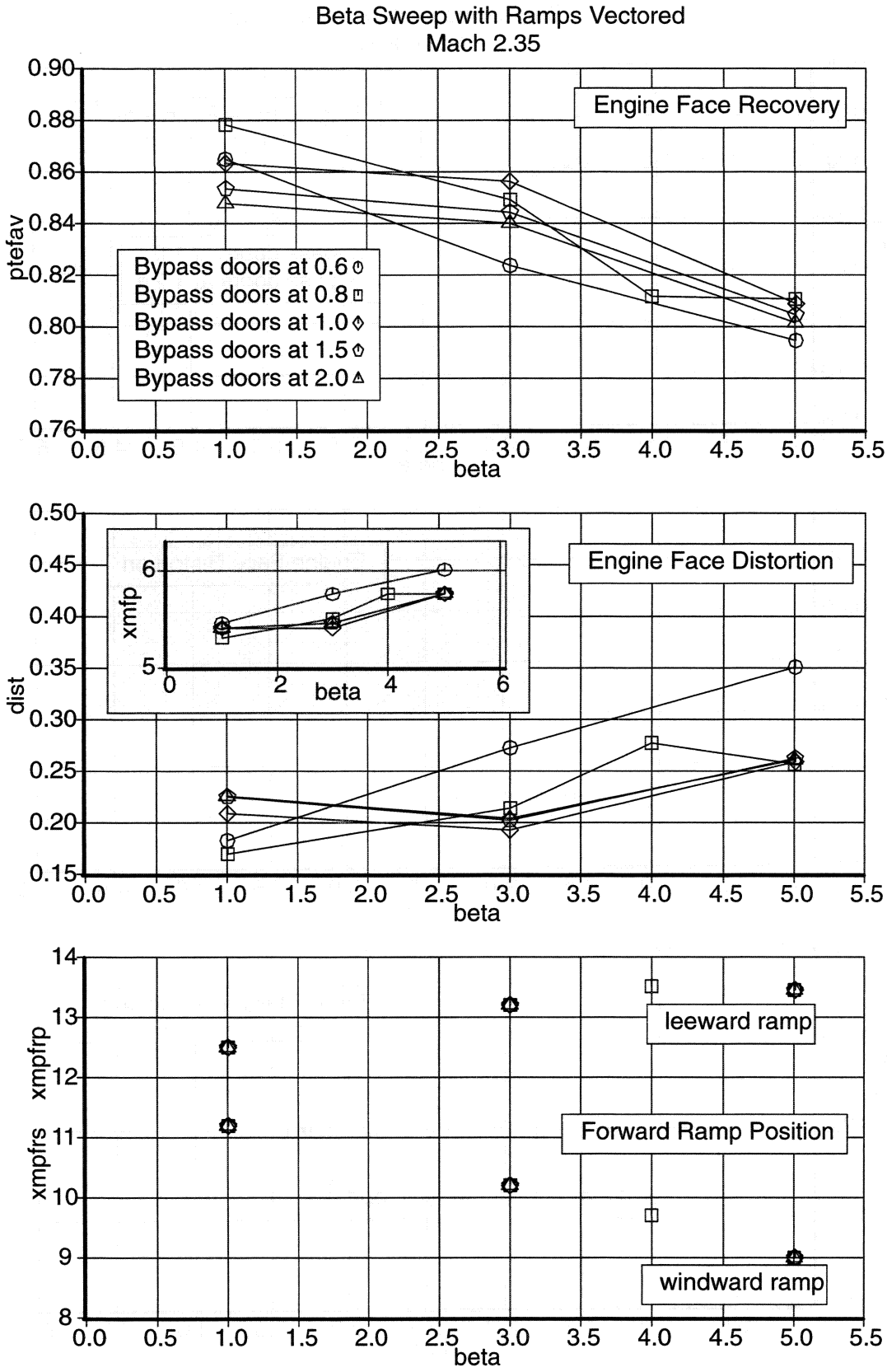

Figure 4–42. Mach 2.35 Beta Sweep with Vectored Ramps.

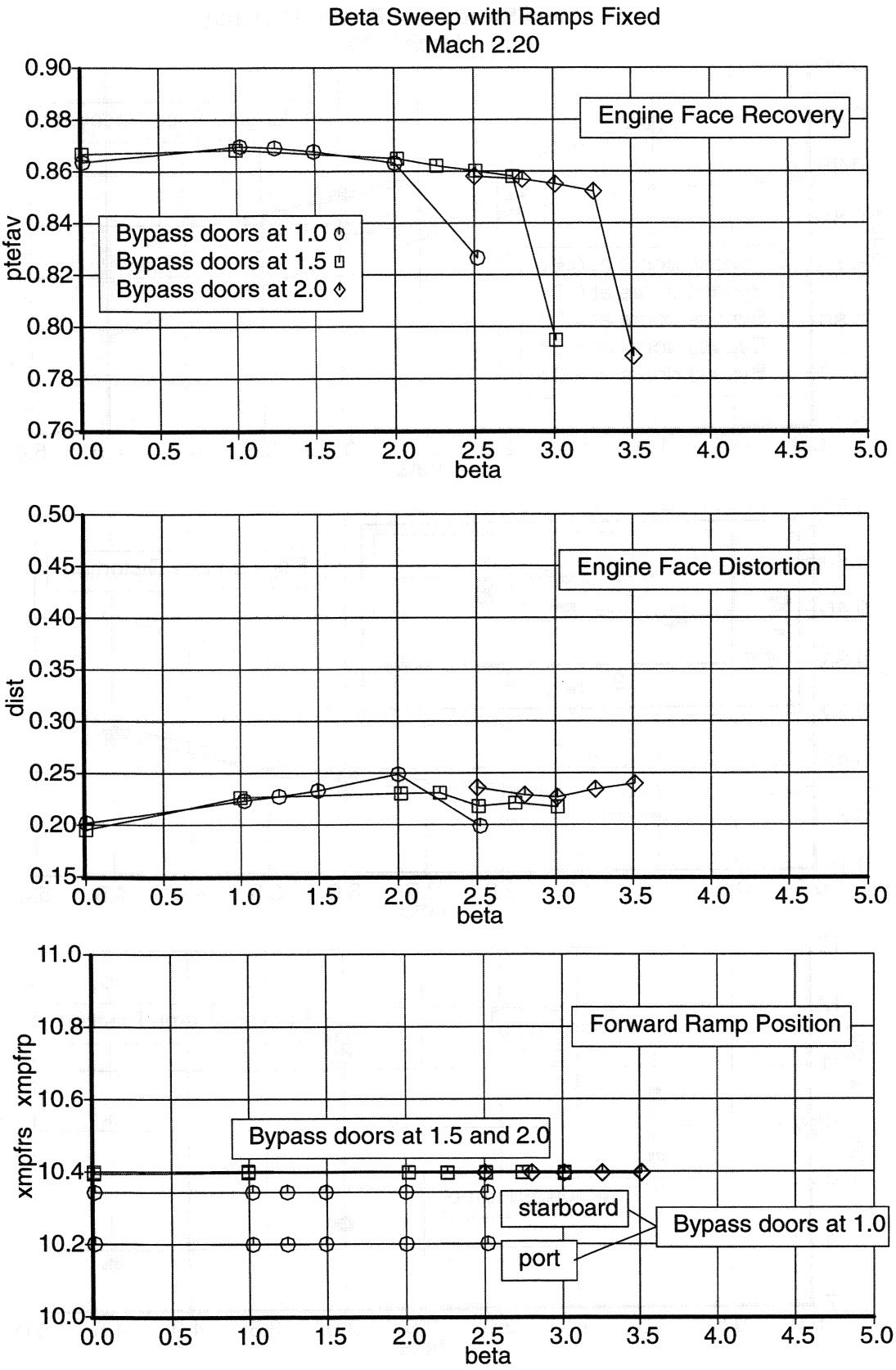

Figure 4–43. Mach 2.20 Beta Sweep with Fixed Ramps.

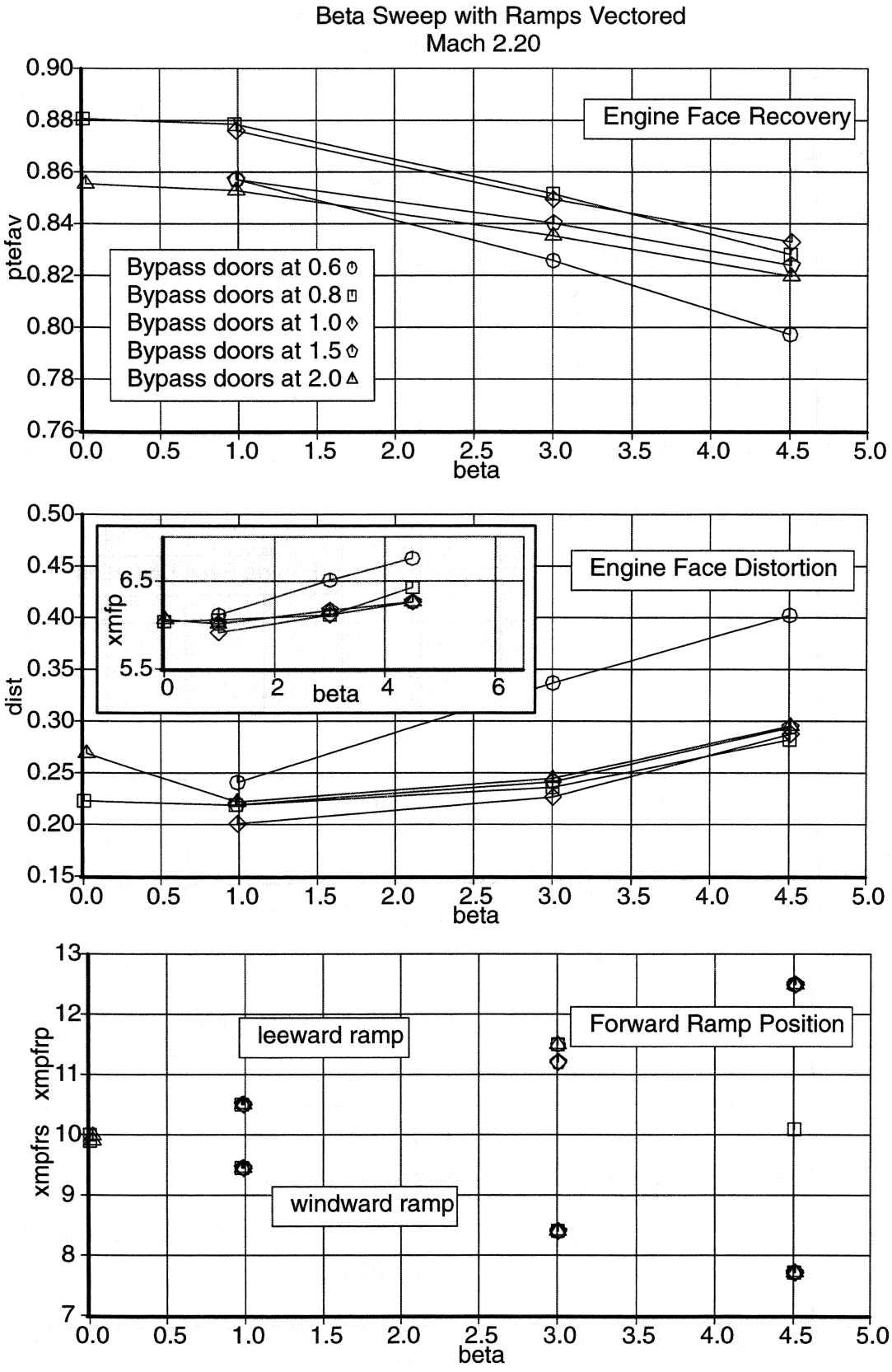

Figure 4–44. Mach 2.20 Beta Sweep with Vectored Ramps.

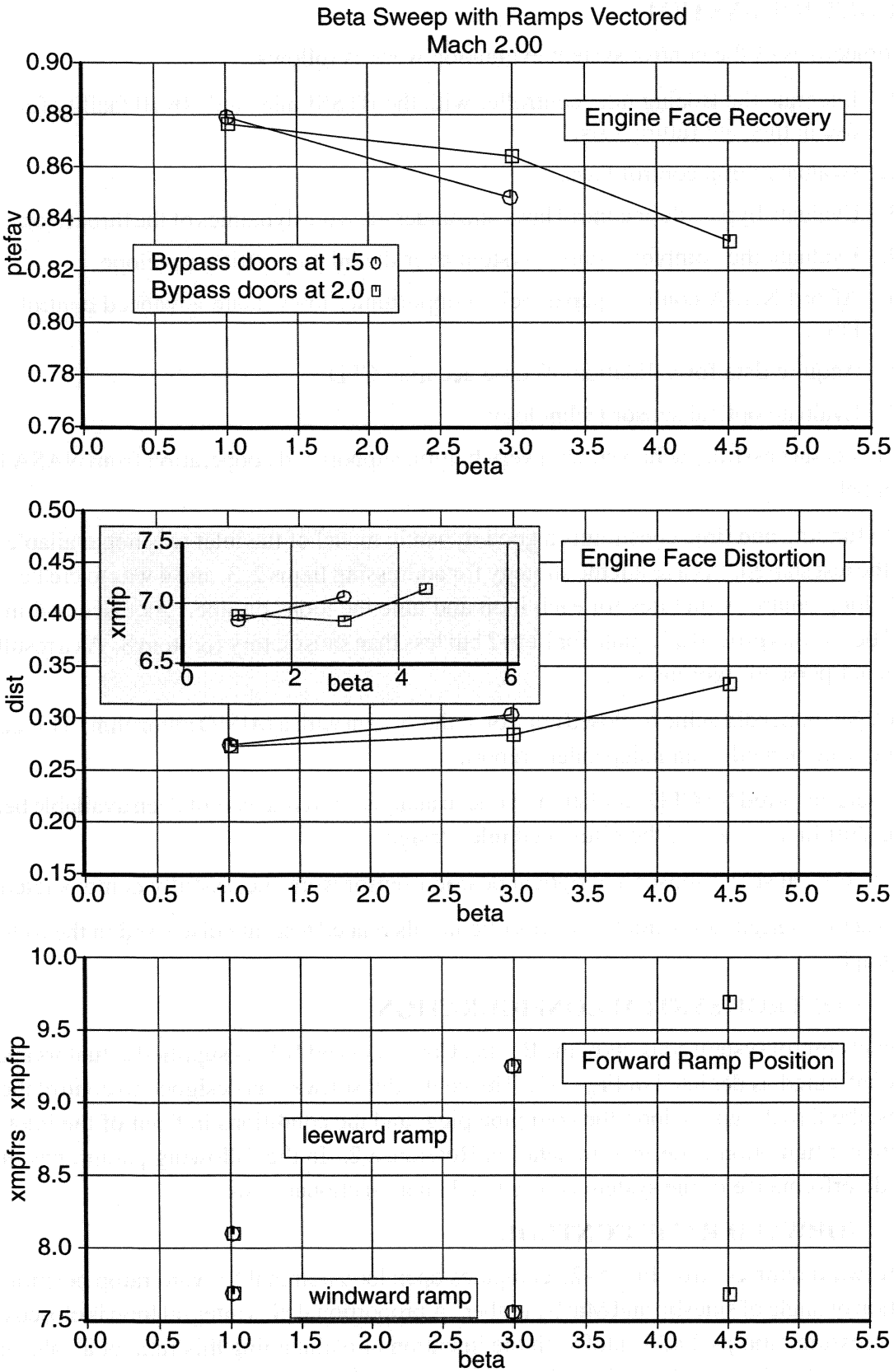

Figure 4–45. Mach 2.00 Beta Sweep with Vectored Ramps.

5. CONTROL SYSTEM

The objectives of the control system evaluation were as follows:

1. Integrate the Boeing inlet controller with the BTSSI inlet and 10x10 facility for use in this and future tests.
2. Evaluate ramp control laws.
3. Evaluate bypass door control laws and understand the dynamics of the throat slot.
4. Evaluate the complete control system over the inlet operating envelope.
5. Afford NASA controls personnel an opportunity to evaluate advanced control laws.
6. Acquire data for validation of time accurate CFD.
7. Evaluate optical sensor technology.

Item 1 was successfully achieved with very helpful support and cooperation from NASA Lewis personnel.

Due to funding and time constraints a good dynamic model of the inlet was not available at the time the test started. As a result the strategy for addressing Items 2, 3, and 4 was to create simple single loop control structures for each loop and tune the loops on line. As discussed in more detail below this proved adequate for Item 2 but less than satisfactory for Item 3. As a result Item 4 was not pursued rigorously.

NASA personnel did achieve closed control of the system with a MIMO algorithm. This activity will be documented in an independent report.

Data were acquired for CFD validation. Time to analyze this data has not been available because of the shift in direction of the bifurcated inlet design.

Both an optical shock sensor and optical position sensor were successfully demonstrated.

The system configuration and the results of controls related tests are discussed in the following paragraphs.

5.1. CONTROL SYSTEM CONFIGURATION

The inlet control system consists of the Boeing Controller and NASA supplied actuators and sensors configured as depicted in Fig. 5–1. The controller software is designed to control the inlet ramps, the throat bypass door, the cold pipe plug, and the conditions in front of the inlet. The system configuration is defined in detail in Reference 2. In the following paragraphs the observed performance of the system is discussed on a functional basis.

5.2. FORWARD RAMP CONTROL

The forward ramp control, Fig. 5–2, computes open loop nominal forward ramp positions as a function of angle of sideslip and Mach number. A proportional plus integral loop is closed on the cowl pressure ratio pscl9(29)/ptof with the intention of maintaining this ratio at a value corresponding to Mach 1.3 in the region of these static taps. The delta actuator position computed by the loop closure is added to the base schedule to form the total actuator position command. Loop

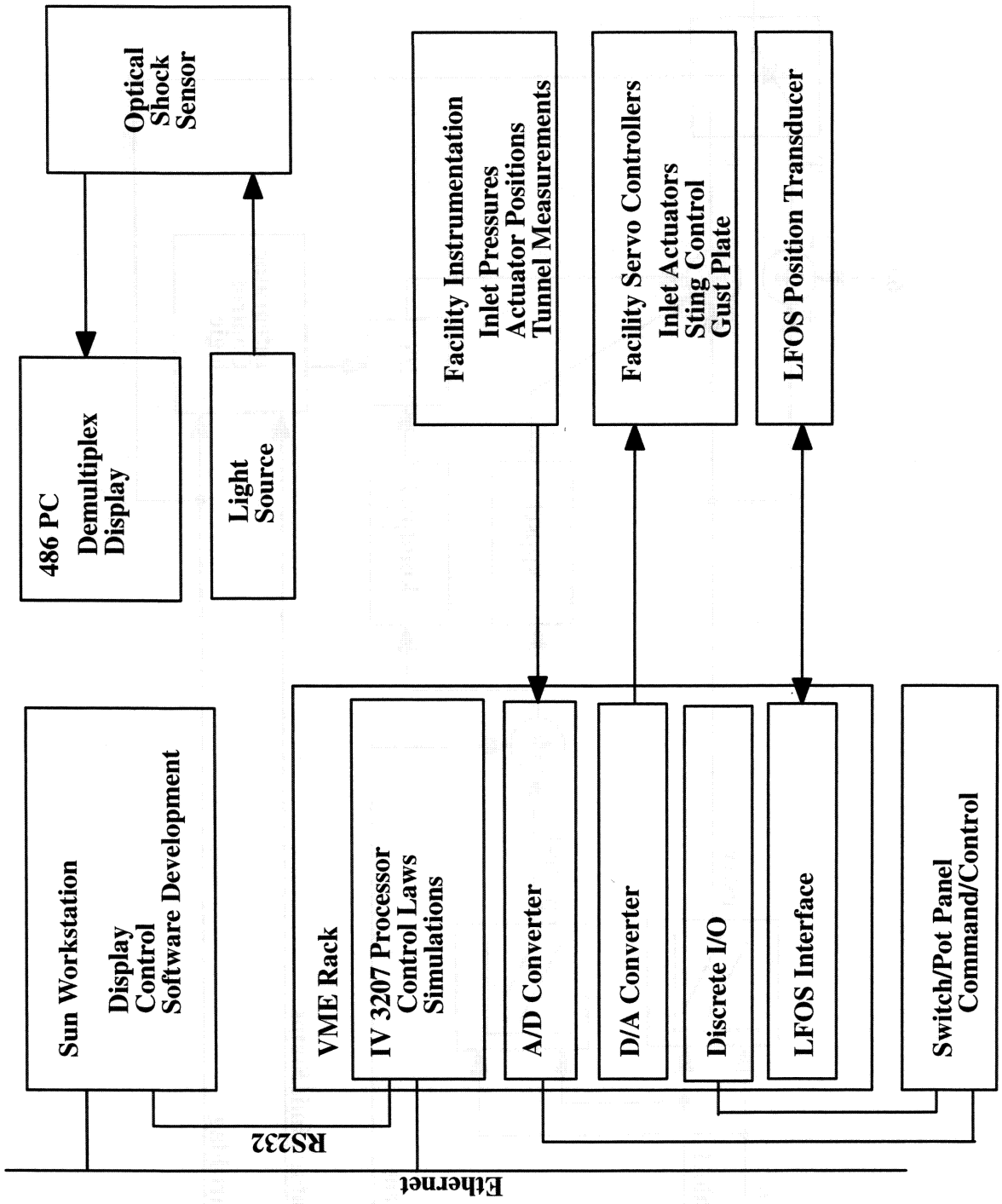

Figure 5–1. Inlet Control Hardware Block Diagram

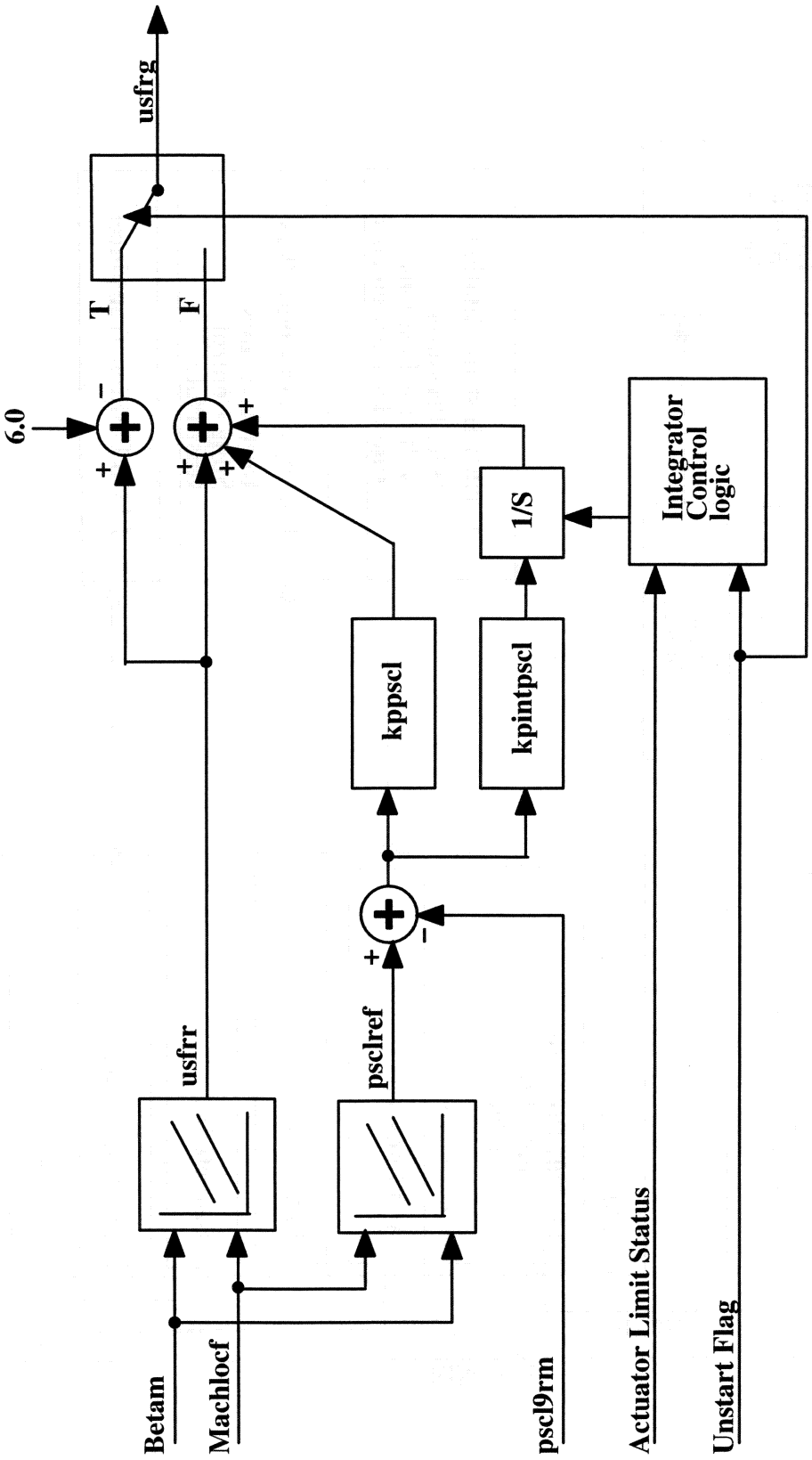

Figure 5–2. Starboard Forward Ramp Control (typ)

closure gains were chosen to achieve 6 dB gain margin and keep noise generated ramp activity to low levels.

The loop closure scheme functioned well over the available range of travel of the ramps. Automatic operation of the inlet over the angle of sideslip range –5 to 5 degrees was demonstrated. Fig. 5–3 illustrates the operation of the system at Mach 2.35. Evaluation at lower Mach numbers was also conducted. Integrator anti wrap–up logic was included in the logic. As can be seen in the figure it functioned adequately for the limited testing done.

Two significant problems were encountered in the operation of this loop. First the original total pressure feedback used in the system was that measured at the throat, ptth. This was replaced, as a test expedient at least, by ptof, the tunnel total pressure, because the aerodynamic noise on the throat pressure signal was unacceptably large. In general the problem of aerodynamic noise on pressure signals was the limiting constraint on operating close to the critical point. Second the stability/accuracy of the Kulite transducers incorporated in the model was found to be inadequate.

The early portions of the test were run with throat rakes in one side of the inlet and no throat rakes in the other side. As a result the inlet ramps were configured asymmetrically to achieve the same cowl pressure ratio pscl9(29)/ptof on each side of the inlet. When the throat rakes were removed some asymmetry still remained. Comparison of steady state and control dynamic transducers and observation of unstart margins eventually revealed that a 0.1 psi offset in the kulites was sufficient to create a significant asymmetry in automatic operation and eliminate most of the design point Mach margin on one side of the inlet. Had the problem been identified early in the test more stringent calibration and data cross–checking schemes might have been invoked. In fact the problem was isolated late in the test. The major conclusion to be drawn from this is that for the next test and flight applications more accurate and stable pressure transducers will be required to measure the feedback Mach number for use in the control system.

Lack of an ability to automatically cross correlate steady state and controls data as seen by the control system is an additional deficiency requiring correction. Both deficiencies will be corrected in subsequent tests.

In spite of these problems the control mode proved to be an adequate scheme for ramp control.

Initial control testing was performed with the region between the ramps open so that slot flow from both sides entered a common plenum and exited through both throat bypass doors. In this configuration rapid opening of the throat bypass doors was sufficient to restart the inlet if the flow control plug was simultaneously reset to a stable operating point. Subsequently a splitter plate was installed in the region between the ramps such that each bypass door was essentially dedicated to venting one throat slot. In this configuration opening the throat bypass doors alone was not adequate to restart the inlet. Control logic was therefore added to automatically move the ramps down while opening the bypass doors and opening the plug until the inlet restarted. This logic worked satisfactorily. However the arrangement is less desirable from an airplane system design standpoint since it implies moving more surfaces rapidly and thus incurring larger transient hydraulic power requirements at a critical point in aircraft operation.

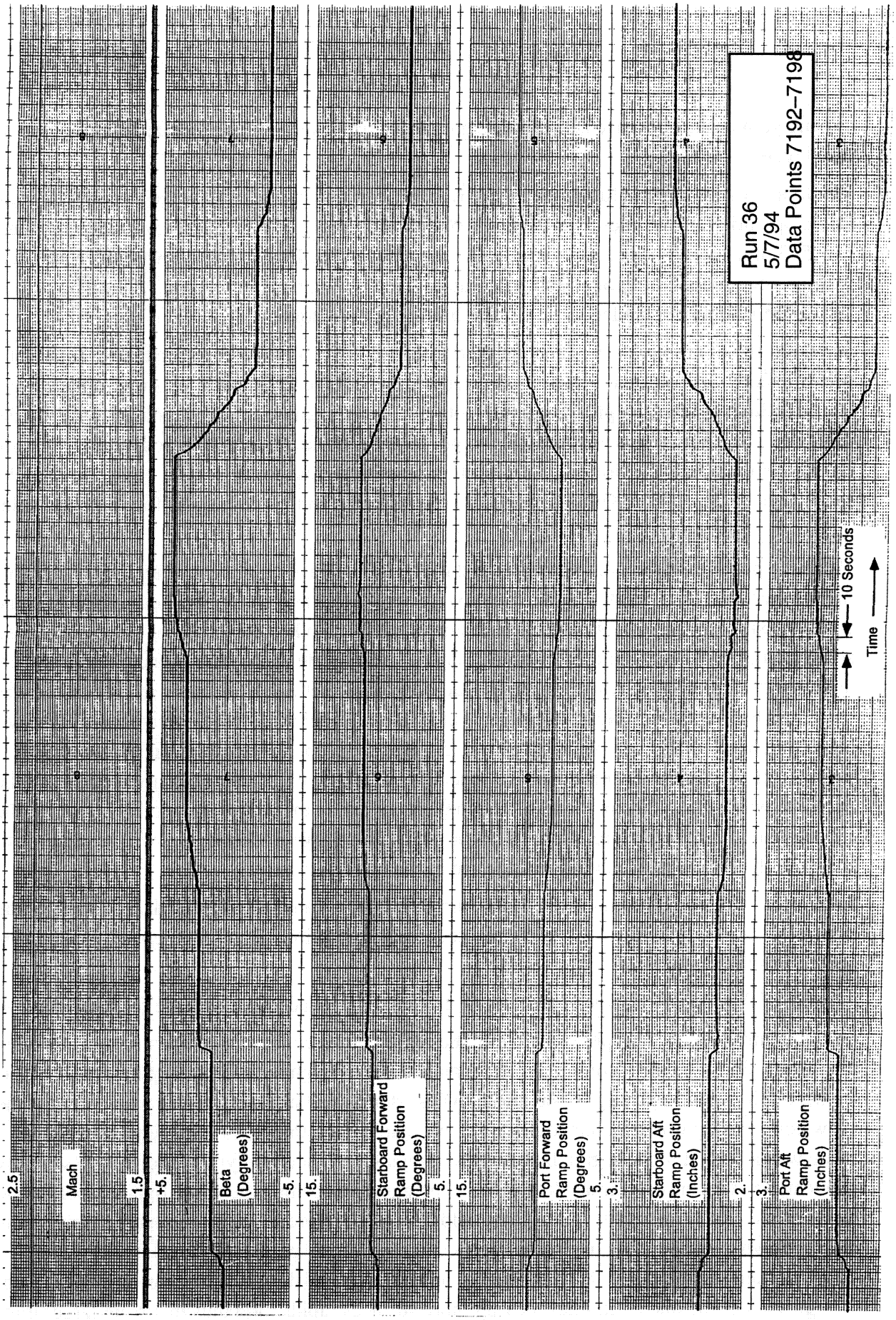

Figure 5–3. Ramp Control Operation

5.3. AFT RAMP CONTROL

The aft ramp control mode slaved the aft ramp position to forward ramp position through a gearing schedule. This arrangement appeared to work satisfactorily although prior tests have suggested that coupling aft ramp and forward ramp together in this manner may lead to sustained limit cycles. These could be avoided through scheduling the aft ramp directly off freestream Mach and angle of sideslip. Time did not permit exploring the pros and cons of the two approaches.

5.4. THROAT BYPASS DOOR CONTROL

Three different approaches to controlling normal shock position were evaluated. The results of the evaluations are outlined in the following paragraphs.

5.4.1. Baseline Control Mode

The nominal throat bypass door control mode, Fig. 5–4, adjusted the doors through a base schedule and regulator loop closure similar to that for the forward ramp. For reasons outlined below the test was conducted using various manual and automatic base schedules. No completely satisfactory schedule was developed. The regulator loop maintained forward ramp delta p at a setpoint near zero. The theory of the mode is that a delta p of zero corresponds to the shear line in the throat slot flowing back off the forward ramp and grazing the forward edge of the aft ramp.

Significant time and effort were spent attempting to make this mode work, with limited success. Two features of the system were found to interfere with operation of this mode. First, high noise levels on the delta p signal and inadequate control loop stability margin near the critical operating point precluded increasing the gain enough to make the loop work, or filtering the data enough to suppress its tendency to auto unstart. Second, efforts at developing small signal linear models by perturbing all surfaces small increments around the operating point to produce the elements of a "D" matrix revealed that the contribution of bypass door motion to shock position motion in the started condition was negligible. Only when the shock detached itself from the aft ramp did the bypass door actually become effective in controlling the shock.

This mode does however have the interesting property that the throat bypass doors automatically adjust to accommodate upstream flow field variations quite satisfactorily.

An example of system operation in this mode is shown in Fig. 5–5. In this particular case the system is operating right at the unstart limit, so that unstarts are occurring about once per second. The system was placed at the unstart limit by adjusting setpoint schedules. The cyclic behavior in the started condition results from having set the loop gains extremely high to maximize speed of response to the unstart. Because of sensor noise it was difficult to establish a loop stability limit in the classic sense. The high frequency low amplitude cycling appears to be a limit cycle stabilized by the actuator rate limit.

The interesting property of the operation of the system in this condition is that the apparent loss in recovery when the inlet unstarts is only on the order of 10% because the unstart only occurs momentarily. The shock detaches from the aft ramp and reestablishes itself on the forward ramp briefly. Thus these data demonstrate that the shock is transitioning from one stable state to anoth-

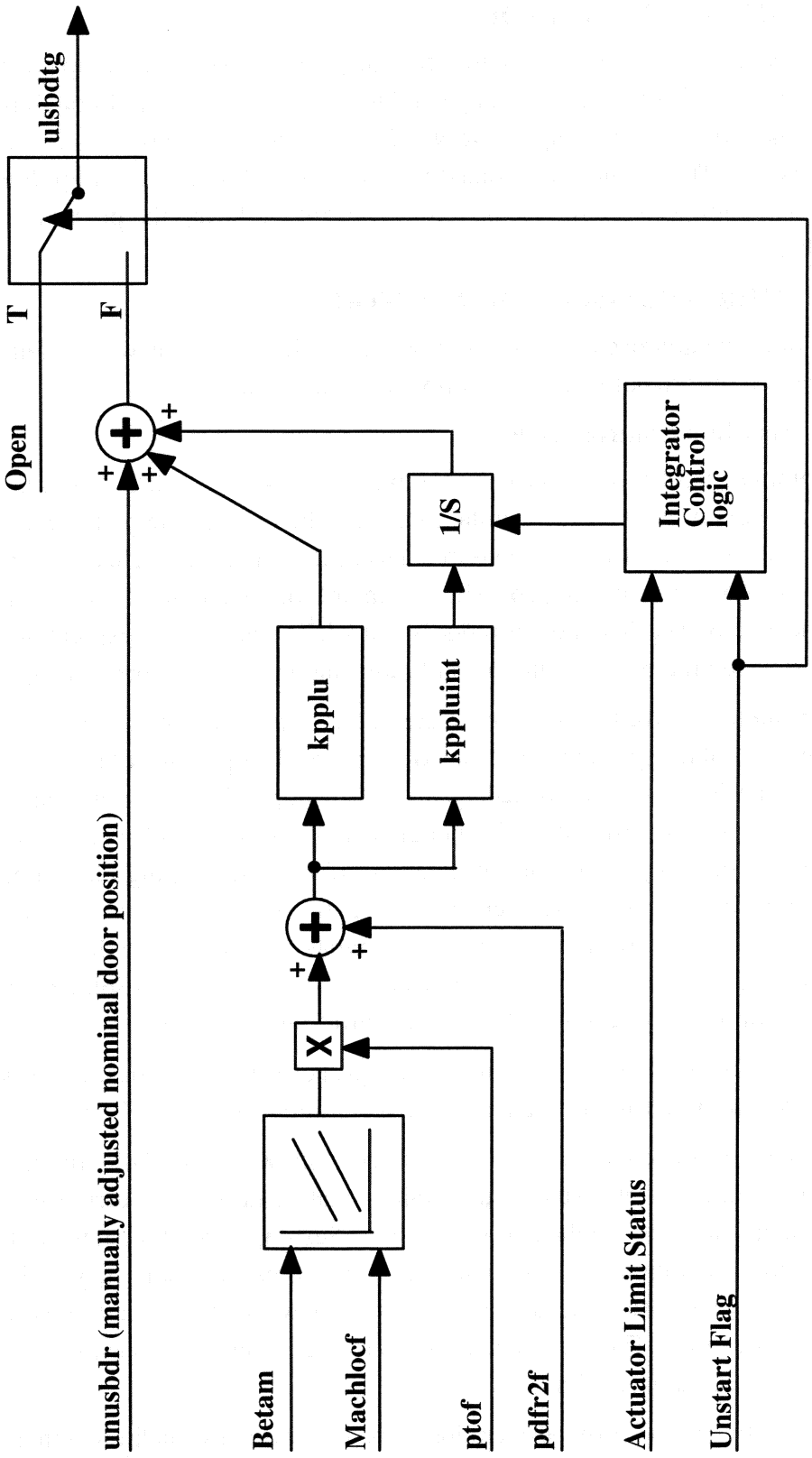

Figure 5–4. Lower Throat Bypass Door Control (typ)

er through a region of linear instability. Control of the shock in this unstable region would require sample rates much higher than the 10 milliseconds used for this test and probably higher bypass door slew rates. An attempt was made to implement a 1 millisecond control loop but it proved impractical with the resources available.

With the fast acting bypass doors the unstart restart cycle only requires about 40 milliseconds. The acceptability of this mode of operation depends on the ability of the engine to tolerate the resulting variation in pt2 and distortion and the practicality of exercising the bypass door frequently. Because of the poor subsonic diffuser performance it was not possible to tell whether this behavior was acceptable from a compressor standpoint or not.

5.4.2. Optional Control Mode

An optional normal shock control feedback based on a perforated manifold running fore and aft in the region of the normal shock was also evaluated. The signal from this pickup provides a useful indication of normal shock position but again the throat door is only effective in controlling the shock after it detaches from the aft ramp.

5.4.3. Plug Control Mode

When it was determined that the throat doors were poorly suited as effectors to control the normal shock a limited attempt was made to control normal shock using the flow plug and both of the above feedbacks. This wasn't a configuration we had planned on using, therefore no prior analysis had been done of it. Unfortunately the complex dynamics of the cold pipe and plug made it difficult to develop compensation for this configuration. We were able to achieve stable started operation at an operating point about 3% supercritical. Operation at lower supercritical margins led to unstarts apparently caused by noise propagation through the control laws.

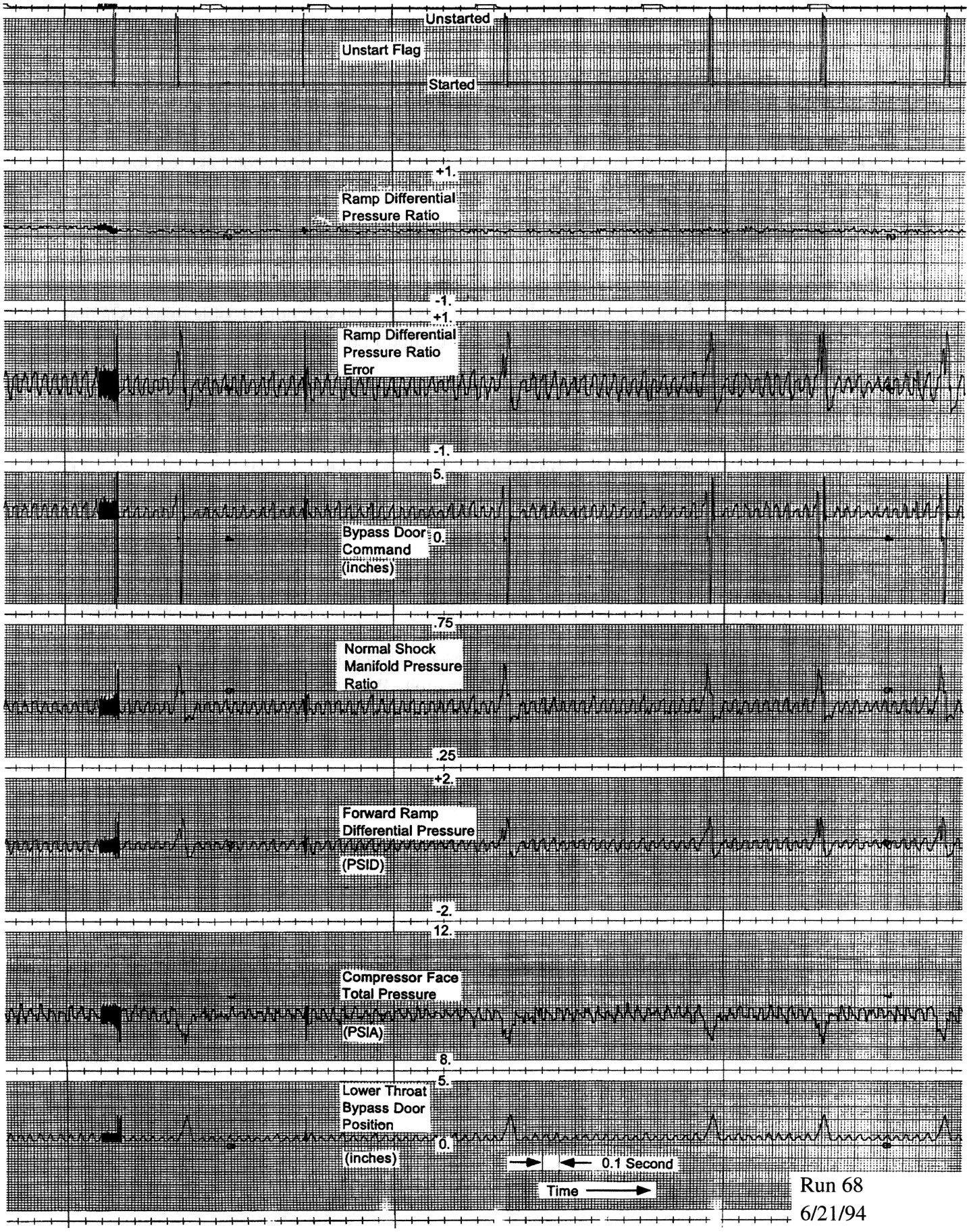

Figure 5–5. Bypass Control Operation

5.5. LFOS TRANSDUCER

A Boeing developed fiber optic linear position transducer was mounted on the bypass actuator in order to evaluate its performance in the wind tunnel environment. The interface characteristics of the transducer are documented in the ICD. Due to the research nature of the transducer the LFOS output was differenced with the conventional LVDT feedback and the error between the two monitored on a strip chart recorder. The LFOS transducer was not used to provide an active feedback.

The first time the actuation system was operated with the wind tunnel active the LFOS failed mechanically. Review of the situation showed that the LFOS design, created for a somewhat different application, featured a stainless steel shaft running through an unbushed hole in the stainless steel case. In this installation the shaft rubbed on the housing. When the actuator was slewed at high rates this almost instantly led to galling and jammed the shaft into the housing. The actuator was sufficiently powerful to bend the jammed shaft. The unit was removed and returned to its developers who repaired the shaft and installed a Teflon bushing. No further mechanical problems were encountered with the system.

Subsequent monitoring of the transducer output showed substantial differences between the LVDT and LFOS output during rapid transients. Consultation with the designers revealed that this was to be expected given the glitch and fault detection logic built into the transducer processing software, the 7 millisecond update rate for the transducer and our very rapid slew rate capability. Given this information and the test priority to understand the behavior of the throat slot we elected to continue monitoring the transducer but did not bother to correct the glitches.

The major results of the LFOS assessment then were: A proper bushing is required in this type of transducer to preclude galling in high slew rate applications. Software revisions are required to accommodate high slew rate operation. Third, and most importantly, the fiber optic signals were passed over roughly 200 feet of cable and operated in the wind tunnel low pressure environment with no noticeable degradation in transducer output. No optical fiber failures or contamination problems were observed.

5.6. OPTICAL SHOCK SENSOR

An optical shock sensor was designed under PAIT Task 15 and tested on the BTSSI inlet. The design and bench testing of the shock sensor is documented in Reference 3.

The optical shock sensor operates by establishing a shadowgraph on the inlet sidewall. The shadowgraph is frequency encoded by an optical filter, introduced into a single multimode fiber, and transmitted over the fiber from the model to the control room where it is decoded by an optical spectrometer.

A number of problems were encountered and corrected in installing and operating the transducer. These were as follows:

1. The fitting to which the sensor mounting link clamps was epoxied to the sensor body. The epoxy failed as a result of unstart pressure transients and probably poor process control in fabrication. The problem was corrected by incorporating

mechanical fasteners in the design. NASA machine shops were instrumental in turning this modification around quickly.

2. The transducer installation permitted angular adjustment about the x axis but not in the z axis. When the installation was designed no adjustment was perceived to be necessary in the z axis because the bleed plates were expected to be parallel within extremely tight tolerances. Unfortunately the bleed plate apparently was locally deformed due to installation stresses. The result was that the sensor heads were misaligned sufficiently to destroy signal transmission across the inlet. The problem was corrected by shimming one end of the transducer by .008 inches.

Once securely installed and aligned the sensor was demonstrated to successfully detect a shadow generated by a small physical obstruction, Fig. 5–6. When operated at altitude with the inlet operating in the started mode the behavior of the transducer was somewhat different than anticipated.

The normal shock was expected to appear as variation in the center frequency of the absorption peak associated with the shadow of the shock. This phenomena was observed once or twice during unstart transients which were not recorded. Steady state data, Fig. 5–7, revealed an entirely different phenomena, namely a variation in absorption peak strength as a function of cold pipe flow. Assuming that the optical system was operating correctly, as pre test calibration indicated, these phenomena are explained as follows. The absorption peaks at X= 12.1 and X=12.58 represent oblique shocks. The activity at X=12.9 appears to represent the normal shock. As the downstream flow was reduced the three peaks varied in amplitude presumably because the shock strengths or profile varied without any significant displacement of the shock. When the normal shock detached from the aft ramp and moved abruptly forward it was observable as a singleframe transient displacement of the peak before the shock moved forward and out of range of the transducer. The other observable but unfortunately unrecordable phenomena was that as the inlet approached the critical point the magnitude and frequency of shadowgraph signal variation at X=12.9 increased – in other words the signal became significantly noisier.

The conclusion from these data is that the shock sensor will work as designed as a frequency modulated system in an inlet which permits the normal shock to travel with variations in downstream airflow. It also is, at least in theory, possible to make it operate as a amplitude modulated device. Unfortunately in practice the usual problems with signal to noise ratio of AM systems would probably be insurmountable.

5.7. MISSION SIMULATION

It was our intent to fly the inlet over complete supersonic missions to demonstrate control system operation and evaluate random variations in freestream conditions over time. A simple point mass simulation of the airplane was included for this purpose as well as noise generators to provide random disturbances. These systems were never evaluated, largely because of the difficulties involved in developing an acceptable control mode for which such tests would have been meaningful. An additional restriction was identified in that Mach variation above Mach 2.0 requires adjustment of tunnel operating condition which was not available to the control computer.

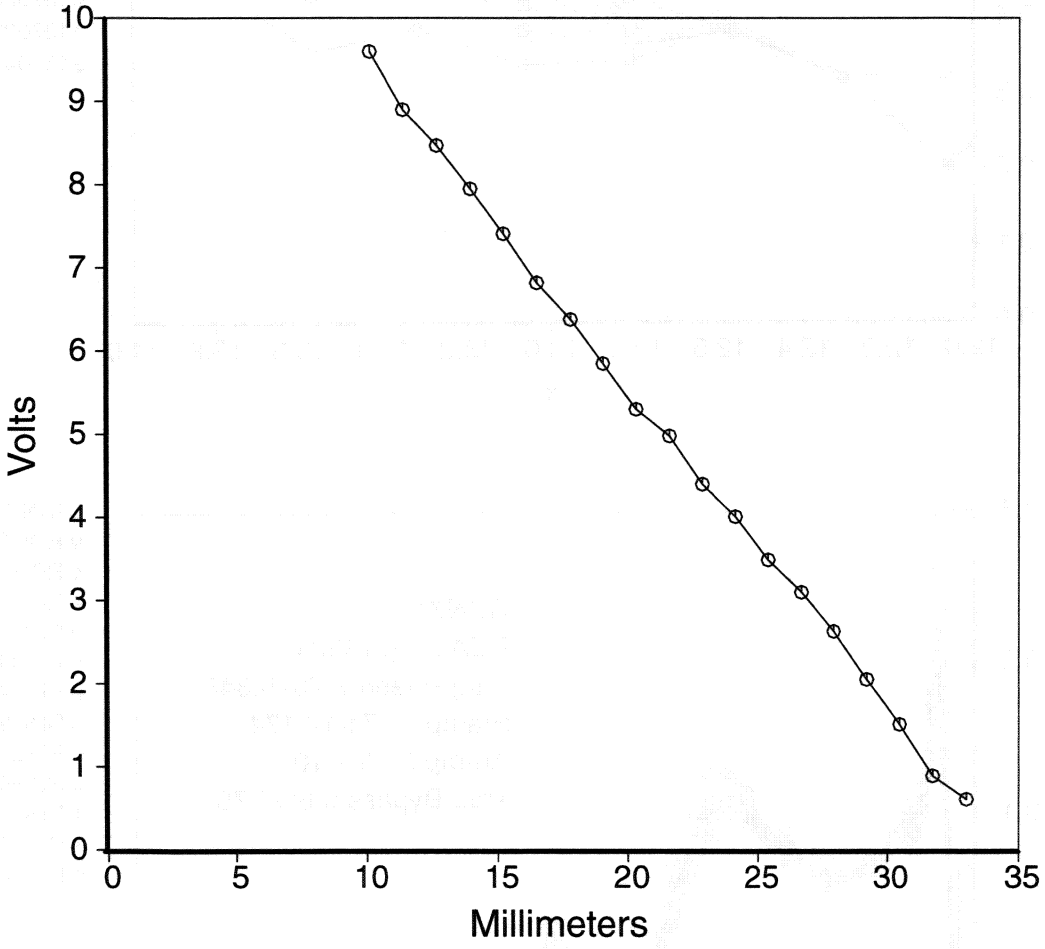

Figure 5–6. Shock Sensor Calibration Curve

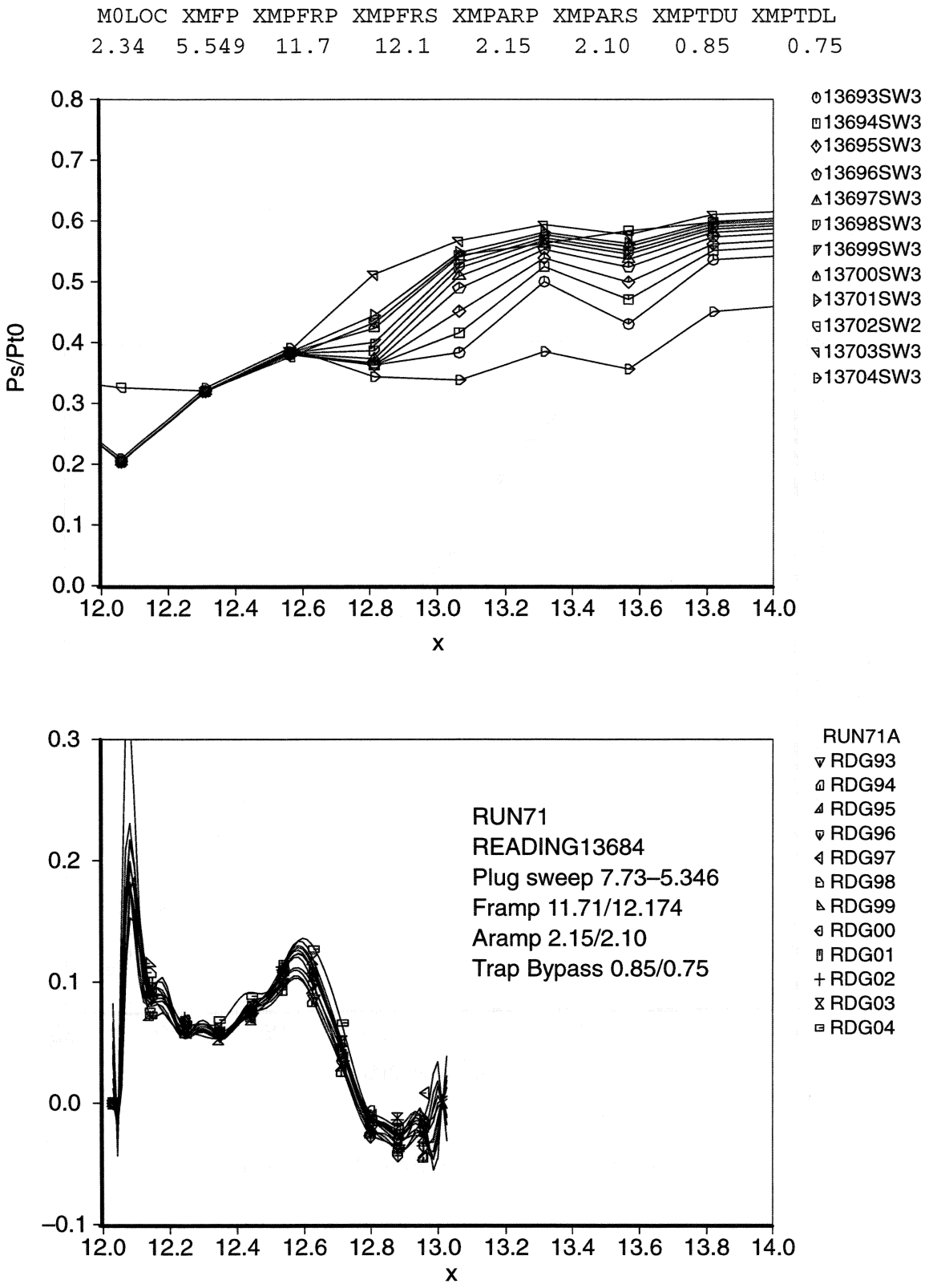

Figure 5–7. Comparison of Shock Sensor Output to Static Pressure Profile

6. CFD ANALYSES AND COMPARISONS

CFD was chosen to help provide insight into the BTSSI performance, such as the subsonic diffuser performance, as well as the details of the flow field, including 3D, dynamic and viscous effects. This section details the 3D and 2D steady state computational analyses performed on the BTSSI.

6.1. 3D VISCOUS PARC ANALYSIS

The PARC analysis of the 10" BTSSI model has been an ongoing effort to obtain 3D viscous solutions of the model geometry as part of the pre–test support. The overall objective of the current BTSSI wind tunnel test is to substantiate the inlet's supersonic diffuser performance levels predicted by CFD, and demonstrate a high level of normal shock stability. When using current analytical tools in inlet design, experimental validation of the design is still necessary to determine the overall inlet performance with aerodynamic and mechanical features and interactions simulated at the same time.

The scope of the test program was dictated by the reality of very limited funding. As such, the design of the wind tunnel model was compromised to allow use of the existing subsonic diffuser, engine face instrumentation and flow control system. The engine face recovery predicted for the wind tunnel model prior to the availability of the 3D CFD results was about 92% (just under what is predicted by the mass averaged CFD results).

Due to the fact that the subsonic diffuser was an old design with a large centerbody at the end of the subsonic ramp, there has been concern about the performance of the subsonic diffuser. The PARC results provide information on how the flow field in the subsonic diffuser affects the inlet recovery. The work reported here details the experiences and results from the 3D viscous analyses of the 10" BTSSI model at Mach 2.35. Results are presented for several normal shock locations with different amounts of plenum bleed for the baseline aft ramp leading edge and for one normal shock position for the alternate #1 leading edge.

6.1.1. Discussion

The geometry for the analyses was obtained from the CATIA model definition and passed to the Boeing developed geometry program AGPS using an IGES file transfer. AGPS then trimmed surfaces where needed and generated a network of points on each surface for input to the grid generator, GRIDGEN.[4] Due to symmetry, only one–fourth of the inlet was analyzed (one–half of one side). A multiple block grid was then constructed with GRIDGEN which contained 11 blocks. When problems with the solution were noticed along a grid singularity line, an overlapping block was added along this line to eliminate the singularity from the computational domain. This additional grid block produced a well behaved flow field. The final grid contained 1.45 million grid points in 12 grid blocks. The grid had 81 points between the ramps and the cowl, 37 points from the centerline to the sidewall, and 282 points from the upstream boundary to the inlet exit (256 to the engine face).

Fig. 6–1 shows three views of the computational grid. Fig. 6–1a shows the grid along the inlet centerline (which corresponds to one side of the computational domain), while Fig. 6–1b and Fig. 6–1c show station–cuts of the grid at two locations in the subsonic diffuser. Fig. 6–1b shows a 'Cartesian' type of grid used in the mostly rectangular region of the diffuser and Fig. 6–1c shows a 'polar' type of grid used in the round region of the diffuser. For these two grid regions to communicate properly in the PARC analysis, they must overlap each other in order to interpo-

late information back–and–forth. This overlap is shown in Fig. 6–1a. Also shown in Fig. 6–1a and 6–1c is the grid block added along the singularity line in the polar subsonic diffuser grid. One other region that utilized overlapping blocks was the slot region block which overlapped the aperture and plenum blocks. The remaining block connections had point–to–point matching.

The 3D PARC flow solver (Ref. 5) was used in the viscous mode with the Baldwin–Lomax algebraic turbulence model. The plenum slot shear layer was computed as laminar due to the lack of a working shear layer turbulence model. The plenum was also laminar due to problems with the turbulence model dealing with the numerous corners in the plenum. The original version of the code was rather slow when run on the NASA Lewis Cray Y–MP. Improvements to the I/O of the code (i.e. less I/O) by Boeing Propulsion Research and keeping all temporary files in central memory resulted in a large (up to a factor of 6) increase in throughput on the Y–MP.

The wind tunnel model had boundary layer bleed in order to improve the recovery of the inlet by reducing separation that may occur inside the inlet. The PARC analysis included boundary layer bleed that attempted to match the bleed patterns for the model which were designed using a method of characteristics code and a boundary layer with bleed code. However, since the computed bleed regions must follow grid lines (which were basically vertical and horizontal), the angled (to the grid lines) sidewall model bleed zones were simulated using a stair–step pattern in the PARC computations as shown in Fig. 6–2 The thick solid lines represent the actual bleed locations of the 10" model for the two most upstream sidewall bleed locations. This figure depicts how the grid bleed regions were set–up to match the model bleed. The model bleed zones at the throat are nearly rectangular so that the grid bleed zones followed the model zones quite well. The boundary layer bleed in the computations was based on a specified mass flux at the surface and did not adjust for the local conditions as would happen in the wind tunnel.

The inlet was first computed as a flow–through case (i.e. no back pressure at the inlet exit) which resulted in supersonic flow through the subsonic diffuser. A converging–diverging nozzle was placed at the inlet exit to create a normal shock. Positioning of the normal shock occurred by varying the contraction ratio of the converging–diverging nozzle at the end of the inlet and the amount of bleed through the plenum slot. Mass removal from the plenum was accomplished with a mass flux boundary condition on the sidewall of the plenum at the approximate location of the wind tunnel model plenum exit.

6.1.2. Findings

When the normal shock was introduced and began moving upstream in the subsonic diffuser, large amounts of separation occurred at the normal shock which caused the normal shock to breakdown into a series of shocks. These shocks proved difficult to move upstream to the aperture. By adding boundary layer bleed in the subsonic diffuser and introducing the shock farther upstream, a well defined normal shock developed that was pushed into the aperture region.

When the normal shock entered the aperture region, a large amount of separation began occurring in the cowl–sidewall corner due to an observed vortex near the corner. One possible origin for the vortex was the leading edge of the side plate where a vortex was being created due to a pressure differential between the outside (higher pressure) and inside of the sideplate. A vortex would form as the flow separated while going around the sharp leading edge. To reduce this vortex, and hence the separation, two leading edge extensions were added to the leading edge geometry by extending the no–slip boundary conditions on the sideplate and nacelle into the exterior flow field. The extensions were one grid cell thick and protruded roughly the same dis-

tance away from the original leading edge along the entire length of the sideplate. Fig. 6–3 shows a comparison of the flow field ahead of the cowl lip for the three leading edges. One can see that the extensions isolate the interior and exterior shock systems and thereby reduce the curvature of the ramp shock in the region of the sideplate.

Fig. 6–4 shows a comparison of flow field cross–sections in the aperture for the three sideplate leading edge geometries. The figure shows that the leading edge extensions have little effect on the corner vortex located in the upper–right corner of each cross–section. It was found that additional bleed in the sidewall–cowl corner near the cowl lip was the most effective way to reduce the corner vortex. These are labeled as 'corner vortex bleed zones' in Fig. 6–2 Fig. 6–5 shows a comparison of flow field cross–sections in the aperture with and without boundary layer bleed in the cowl–sidewall corner. One can see that this reduced the size of the corner vortex much more that the leading edge extensions shown in Fig. 6–4

During the computations it was found that high bleed rates on the sidewall effect the shape of the shear layer in the plenum slot. With high bleed rates along the sidewall, the slot shear layer was pulled out of the plenum into the aperture as shown in Fig. 6–6 This would cause low energy flow from the plenum to enter the subsonic diffuser and produce flow separation along the aft ramp with the result of lower total pressure recovery. The conclusion from this is that inlet performance can be reduced by too much sidewall boundary layer bleed. This is a finding that would be difficult to determine in a wind tunnel test.

It was further found that the added bleed on the cowl and sidewall near the cowl lip did not eliminate separation in the corner at the normal shock. To significantly reduce this separation, the cowl and sidewall throat bleed zones had higher bleed rates in the corner than elsewhere in the zones. The bleed rates in the corner were higher by 50% on the cowl and 70% on the sidewall than away from the corner and resulted in little boundary layer separation in the corner.

During the initial runs, it was noticed that the Mach contours in the plenum were jagged and the flow was very unsteady. It was felt that the numerical dissipation in the plenum was being reduced by PARC because the code was determining the plenum region to be a boundary layer and, therefore, was turning off the dissipation. This is desired, and actually done, in the boundary layers to ensure that the numerical dissipation does not become larger than the physical viscosity. However, when the numerical dissipation is turned off in the plenum, the flow becomes erratic due to lack of any dissipation since there are not large velocity gradients (the velocities are near zero) to produce physical dissipation. Compounding this is the lack of turbulent viscosity as mentioned previously. Since present finite difference methods, like PARC, require some form of dissipation, numerical dissipation was increased in the plenum block only by switching to the Euler (invscid) type of numerical dissipation (i.e. PARC inputs 'ifltr' was changed form 2 to 1 and 'splend' was changed from 0.0 to 1.0.). This resulted in a more stable flow in the plenum without smearing out the features of the flow.

6.1.3. Results

By varying the contraction ratio of the converging–diverging nozzle at the end of the inlet and the amount of bleed through the plenum slot, the normal shock was eventually positioned in the aperture. Fig. 6–7 shows three waterline cuts of the flow field with the normal shock at the critical location with the plenum bleed at 1.8% of the captured flow. The shock position near the centerline was not steady in the computations and the position shown in the figure is the most upstream location. The normal shock was oscillating between this position and 25% of the throat

height downstream. The shock position towards the sidewall remained in a more constant location.

In Fig. 6–7, one can see a low Mach number region upstream of the centerbody. An examination of the velocity distribution shows separation occurring in this region which resulted in the computed engine face recovery varying at each PARC iteration. The average recovery for the condition in Fig. 6–7 was found to be 92.5% for mass flux weighted averaging and 91.0% for area weighted averaging. The model rake based average recovery was 88.0%. The following table gives the boundary layer bleed for the critical position for the PARC analysis compared to the design values.

Table 6–1. Boundary Layer Bleed Requirements as A/Ac

method	Sidewall			Cowl	Total
	forward	mid	throat	throat	
PARC	0.0022	0.0074	0.0111	0.0186	0.0393
design	0.0022	0.0058	0.0100	0.0093	0.0273

The cowl throat bleed had a 50% higher bleed rate over the outer 1/3 of the bleed region. Not included in the PARC values are the corner vortex bleed zones near the cowl lip. These bleed rates were 0.00078 for the sidewall and 0.0019 for the cowl.

Fig. 6–8 shows a comparison between the PARC computation and experiment of surface pressure along the inlet centerline for the baseline and alternate #1 aft ramp leading edges. The experimental reading from bleed pattern 7 was chosen because it had the most similar normal shock position compared to the PARC computations. The figure shows good agreement except over the cowl bleed zone where PARC predicts a lower pressure due to the uniform mass flow bleed boundary condition used in the calculations. Looking at the normal shock positions, it can be seen that the experimental location is slightly downstream of the PARC location. This difference probably contributes to the difference in pressures along the aft ramp where the PARC values are higher. The figure also shows that the alternate #1 leading edge produces a different pressure distribution downstream of the the shock probably due to a slightly different shock location. The pressures for the PARC alternate #1 case were obtained from averaging four solutions due to normal shock movement in the calculations.

Fig. 6–9 shows a comparison of off–centerline surface pressure distributions between experiment and PARC for the baseline leading edge. The figure shows that up to the normal shock there is excellent agreement. Downstream of the shock the agreement is fair with the PARC results showing oscillations due, in part, to boundary layer bleed in the subsonic diffuser.

A calculation was obtained with the baseline leading edge with a subcritical shock position by reducing the boundary layer bleed in the subsonic diffuser while increasing the amount of plenum bleed. Fig. 6–10a shows a centerline cut of the flow field with the normal shock in a subcritical location with the plenum bleed at 3.0% of the captured flow. At this bleed rate and shock position, the normal shock remained steady at the position shown in the figure. In order to main-

tain attached flow in the throat at the cowl–sidewall corner, the bleed flow in the outer 1/3 of the cowl throat bleed was increased from 0.0070 to 0.0187 A/Ac.

An additional solution was obtained by further reducing the subsonic boundary layer bleed while increasing the plenum bleed to 6.5%. Fig. 6–10b shows the computed results for the 6.5% bleed case. Comparing Fig. 6–7 and Fig. 6–10 shows that the normal shock moves slightly upstream as the amount of plenum bleed increases. Total bleed on the cowl was increased to 0.0317 A/Ac. There was some movement in the normal shock but it remained in the slot region.

As mentioned earlier, PARC results were obtained with the alternate #1 leading edge geometry and the results are shown in Fig. 6–11 One can see that the flow field is very similar to the baseline flow field shown in Fig. 6–7 This case had 2.0% bleed through the plenum. Like the baseline geometry, it was found that the normal shock position never reached a steady position with Fig. 6–11 showing a representative position.

Each of these flow fields required between 10,000 and 15,000 PARC iterations before it could be determined where the normal shock would remain. During these calculations, only those blocks affected by the normal shock movements (i.e. the internal flow blocks) were computed. When running on the NASA Lewis Cray Y–MP, these conditions required between 60 and 90 CPU hours which were typically obtained in one to two weeks. This usage, however, does not take into account computing the initial flow–through solution or computations required to push the normal shock into the aperture region. These solutions together would take about 100–200 CPU hours depending on how good of a guess was made on the contraction ratio of the exit CD nozzle. Of course, since this was the first attempt at a 3D viscous supersonic inlet calculation, much less CPU time would by required to get the shock in the aperture on a second attempt.

6.1.4. Future Work

The current work could be improved by improving the boundary layer bleed model, incorporating a compressor face boundary condition, and using a turbulence model better suited to the slot shear layer, separation occurring in the subsonic diffuser, and the corner vortex. The boundary layer bleed model could be improved so that local flow conditions and wall porosity are taken into account when determining the wall mass flux. This would enable a more realistic analysis by simulating such phenomena as the increase in mass flux when a normal shock passes over a bleed zone. This capability currently exists in NPARC[6] as does the compressor face boundary condition which would result in less CPU requirements due to less grid points being computed. The algebraic turbulence model used in the calculations is not well suited for some of the flow conditions encountered since it was constructed for flat plate boundary layers without separation. Higher–order models should simulate these conditions more realistically at the cost of more computer requirements. The current experiment should give guidance as to the importance of the the type of turbulence modelling.

6.1.5. Conclusion

The work reported here detailed several important findings about 3D viscous PARC analyses of the 10" BTSSI. The ability of CFD to provide details of an inlet flow field not easily obtained from a wind tunnel was demonstrated with the effect of sidewall bleed distorting the slot shear layer which could result in lower performance. Also, it was shown how leading edge extensions straighten out the flow field but do not reduce the cowl–sidewall corner vortex. It was found that cowl and sidewall bleed are effective at reducing the corner vortex. The calculations showed

that separation occurs along the aft ramp ahead of the centerbody. It was demonstrated that 3D viscous analyses of a bifurcated TSSI type of inlet can be performed with the normal shock in various positions in the inlet with different amounts of slot bleed.

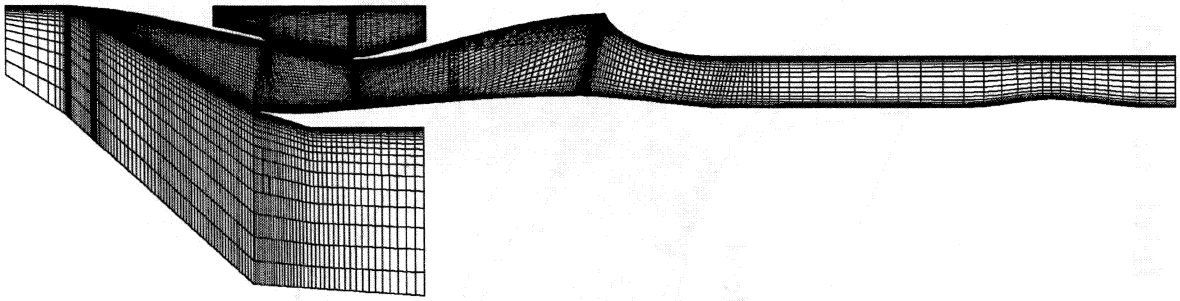

(a) Grid along centerline.

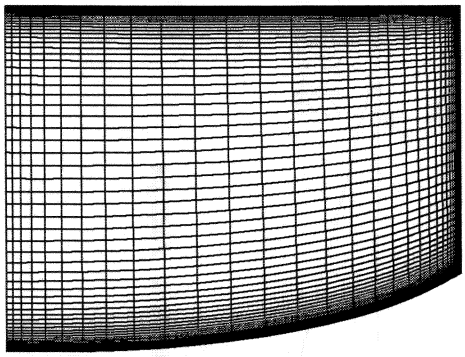

(b) Cartesion grid in subsonic diffuser.

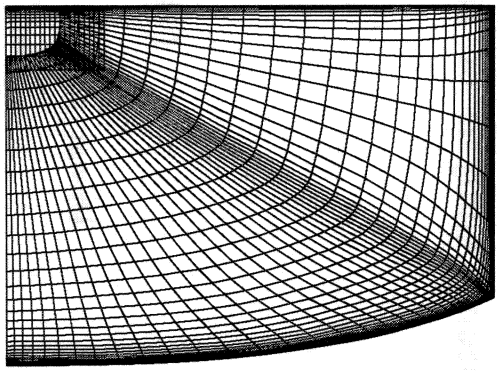

(c) Polar grid in subsonic diffuser.

Figure 6–1. BTSSI Computational Grid for PARC Calculations.

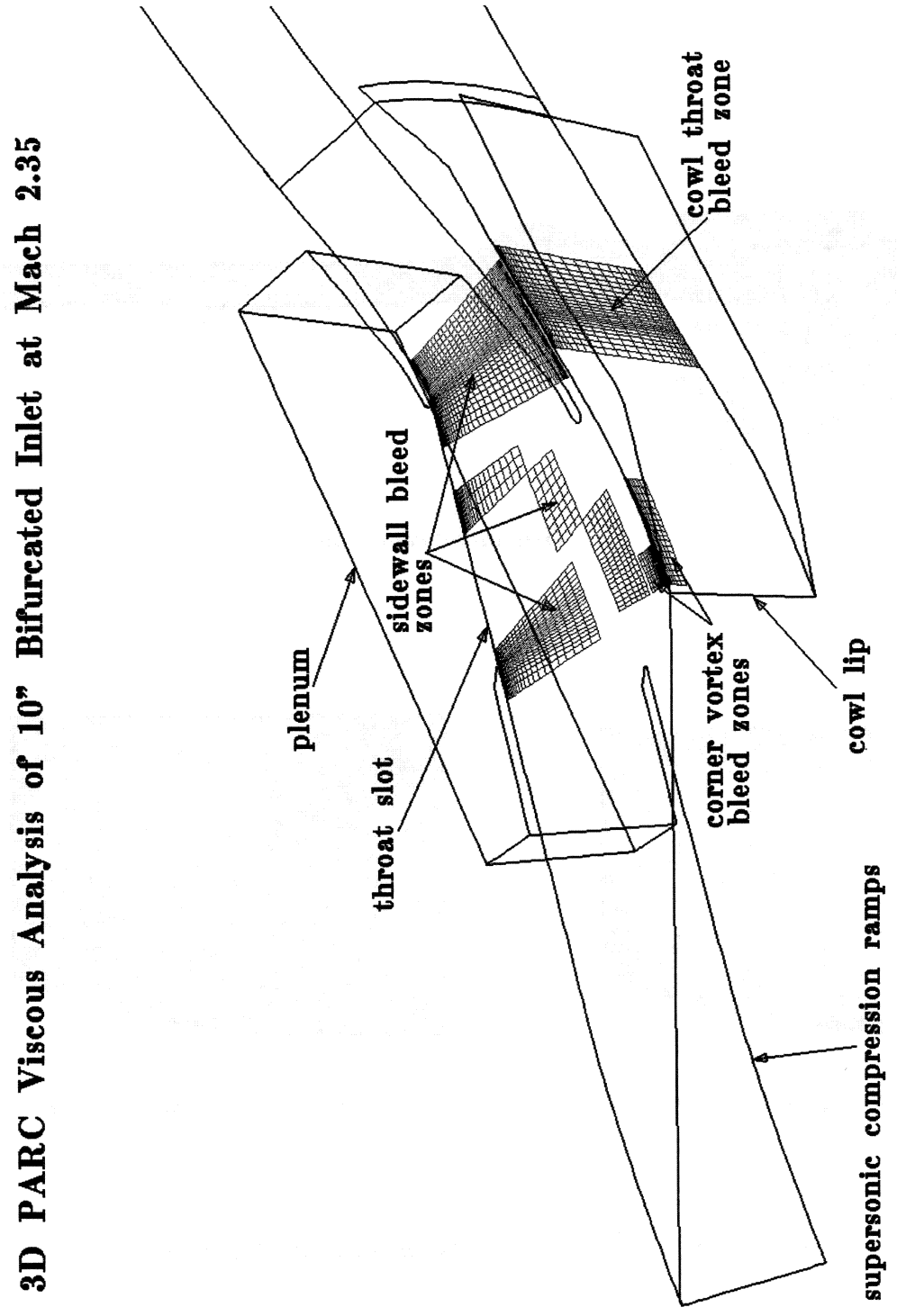

Figure 6–2. Bleed Zones for PARC Calculations.

Figure 6–3. PARC Computed Leading Edge Effect.

Figure 6–4. PARC Computed Leading Edge Effects in the Aperture.

Figure 6–5. PARC Computed Corner Bleed Effects in the Aperture.

Figure 6–6. PARC Computed Slot Shear Layer Behavior.

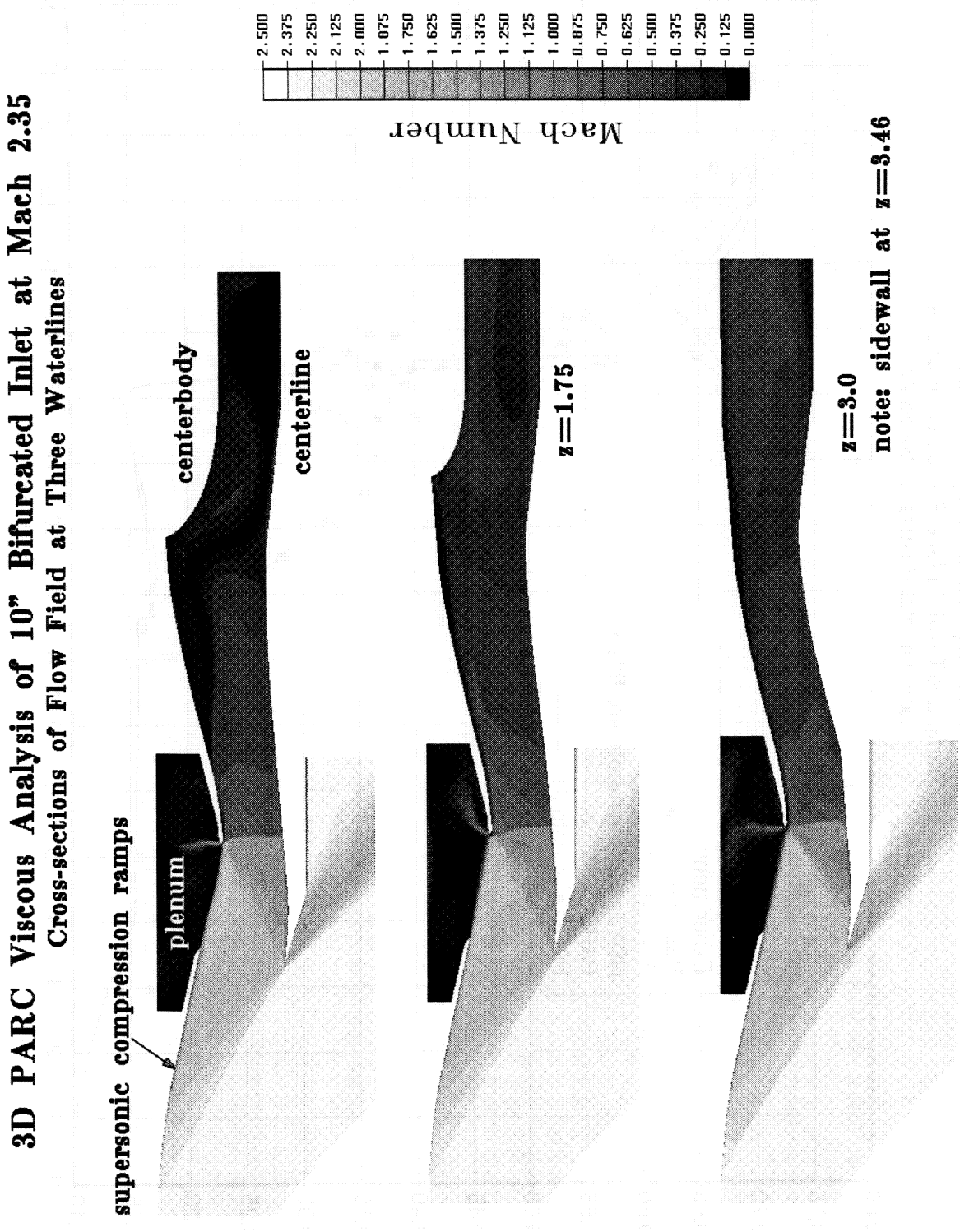

Figure 6–7. Mach Contours with Normal Shock at Critical Location.

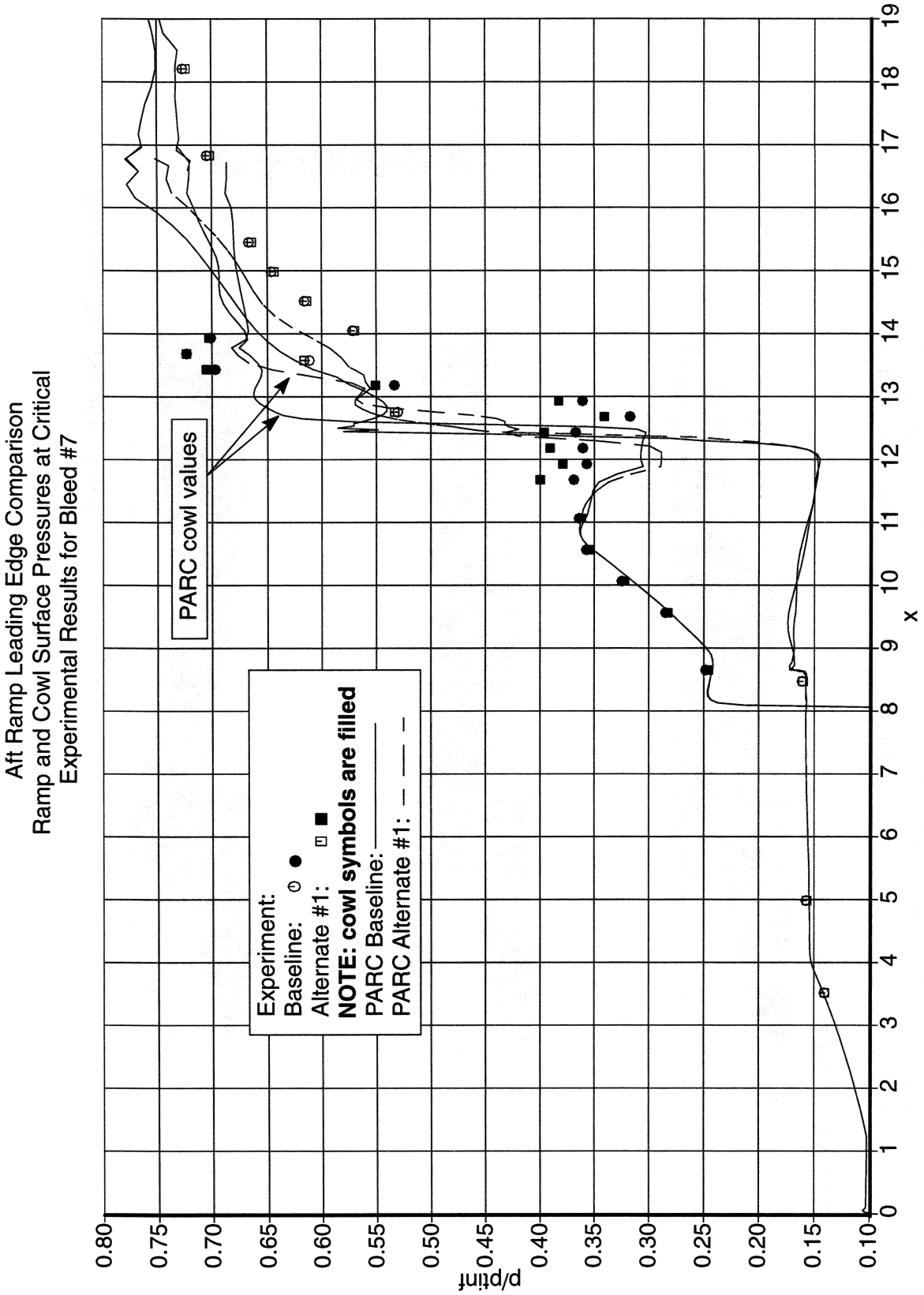

Figure 6–8. PARC and Experimental Surface Pressure Comparison.

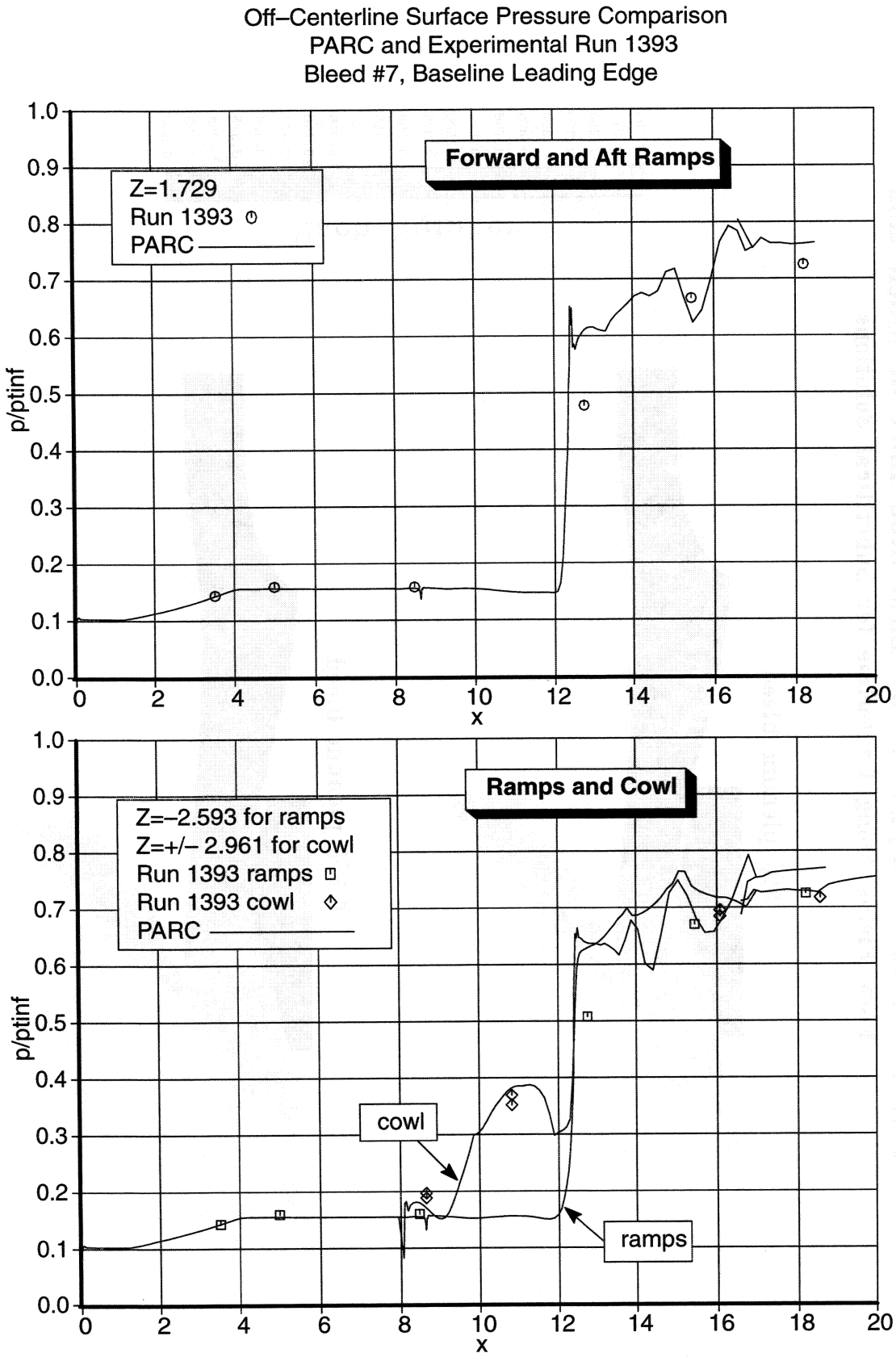

Figure 6–9. PARC and Experimental Surface Pressure Comparison.

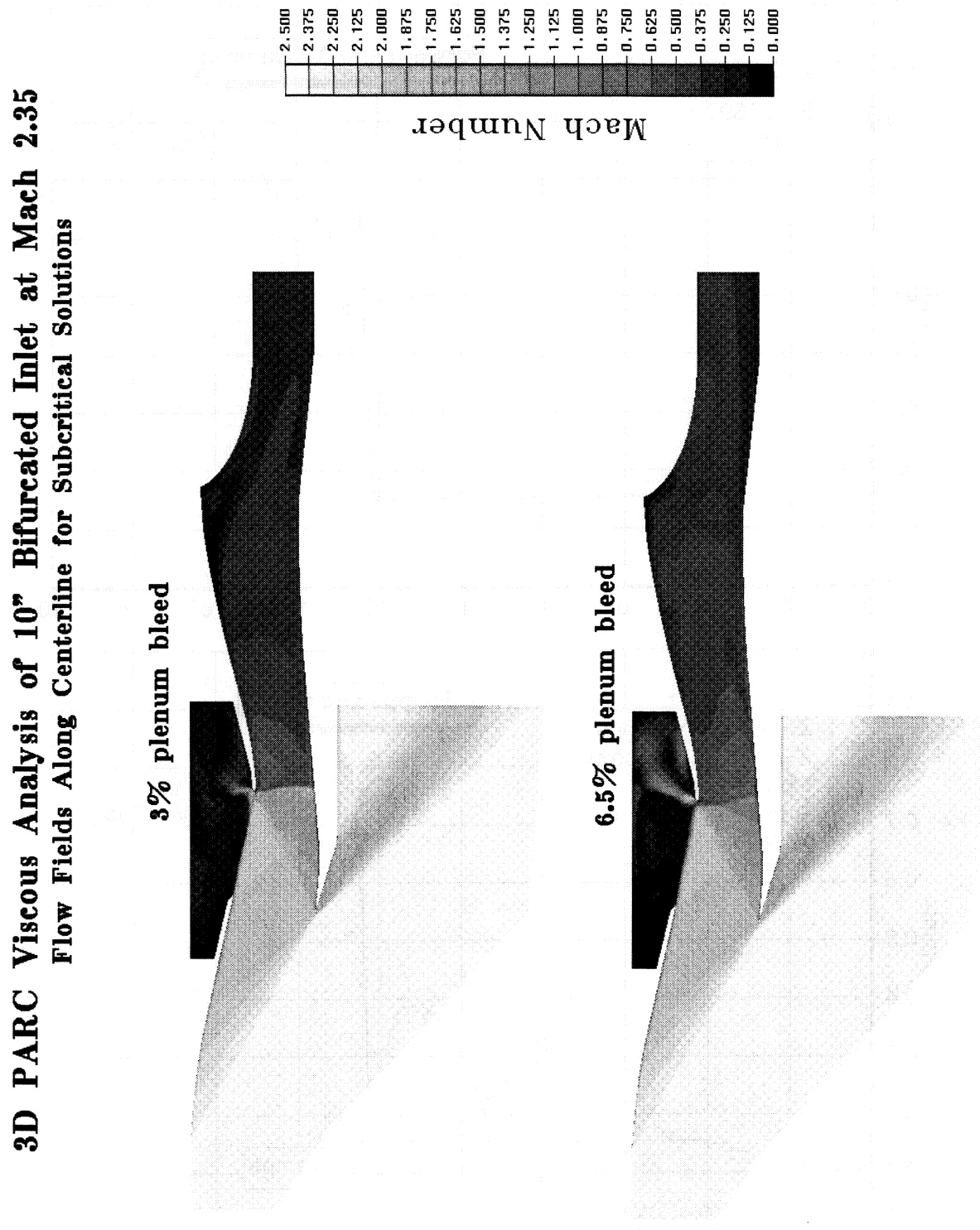

Figure 6–10. Mach Contours with Normal Shock at Subcritical Location.

Figure 6–11. Mach Contours for Alternate #1 Leading Edge.

6.2. 2D NAVIER–STOKES ANALYSIS

Prior to the test a 2D CFD analysis was begun with the objective of providing information on the dynamic behavior of the model in the tunnel. The main dynamic parameter looked at was the pressure differential across the forward ramp which was used by the control system to control the normal shock. As the test progressed, the 2D NPARC analysis was used to understand why the plenum bypass did not provide the normal shock stability predicted prior to testing.

6.2.1. NPARC Performance Predictions

The inlet was analyzed with the two–dimensional version of the NPARC Navier–Stokes code.[5,6] The code was extended to include the bleed and compressor face boundary conditions developed by Boeing.[7,8] The analysis was run fully viscous, but with slip–wall boundary conditions to minimize the grid requirement at the wall. This approach takes into account the free shear layers that exist in the inlet flow, but does not take into account the boundary layers (and possible boundary layer separation). In Section 6.2.2. the predicted pressures along the cowl wall are used in a boundary layer analysis to evaluate the potential for boundary layer separation.

Fig. 6–12 shows a schematic of the geometry that was analyzed. The supersonic diffuser lines are for the baseline configuration with the ramps at the Mach 2.35 position. Leading edge configuration No. 3. was used for the aft ramp. The two–dimensional to round transition region and the cold pipe were modeled by adjusting the cowl wall side of the duct to yield the same effective flow area as in the test configuration. This geometry was gridded with 9 grid blocks and a total of 20,056 grid points.

The cases were run at zero angle of attack and yaw, with freestream Mach number = 2.35, for a range of cold pipe exit conditions, and for four shock trap bypass flow rates as shown in Table 6–2. The freestream stagnation pressure and temperature agreed upon before testing were 14.58 lbf/in^2 and 547°R, respectively.

Table 6–2. Flow Conditions

M_{exit}	Engine Face Corrected Flow [lbm/s]	Supercritical Shock Trap Bypass Flow
0.450–0.360	10.79–9.00	3.9%
0.450–0.370	10.79–9.21	3.0%
0.450–0.390	10.79–9.63	2.1%
0.460–0.390	10.97–9.63	1.2%

Fig. 6–13 shows the predicted values for the total pressure recovery at the engine face, PTEFAV, the inlet mass flow, MRWTOT, (i.e., the sum of the mass flow through the bleed plenums, the shock trap plenums and the cold pipe normalized by the capture mass flow) and forward ramp pressure difference across the forward ramp trailing edge, DELPRT. These results are shown for shock trap plenum bleed rates of 1.2%, 2.1%, 3.0%, and 3.9%. Note that increasing the bleed rate through the shock trap plenum results in improved recovery with unstart occurring at a lower corrected flow.

Figs. 6–14, 6–15, and 6–16 compare predicted and experimental values with a nominal shock trap bypass flow rates of 2%, 3%, and 4%, respectively The most obvious difference between analysis and experiment is that NPARC predicts a higher recovery. One reason for the difference is the 2D assumptions in modeling the 3D subsonic diffuser. Another cause is likely due to the lack of the sidewall–cowl corner in the analysis. The other difference between the two results is the prediction of the forward ramp pressure differential where NPARC predicts a more negative value. The exact reason for this is difficult to understand, but it is probably related to NPARC predicting increasing recoveries with more bypass flow. The few spikes in the NPARC curves are due to convergence problems when the inlet unstarts.

6.2.2. Boundary Layer Analysis

The results discussed in Section 6.2.1. show that the predicted recovery at the critical point improves with increased bypass flow. The experimental recovery values do not exhibit a similar trend. The NPARC predicted Mach contours with 2% supercritical bypass flow are shown for supercritical and critical flow conditions in Figs. 6–17 and 6–18, respectively. Figs. 6–19 and 6–20 show similar results at 3% supercritical bypass flow. Comparison of the supercritical and the critical Mach contours shows that at critical flow conditions the shear layer across the shock trap plenum generates an oblique shock that will interact with the boundary layer on the cowl wall. The cowl boundary layer may separate due to the adverse pressure gradient generated by the oblique shock wave. To investigate this possibility the boundary layer characteristics on the cowl wall were analyzed using Boeing's boundary layer code, P139.[9]

The pressures predicted with NPARC along the cowl wall were specified as a boundary condition to the boundary layer analysis. The boundary layer results with 2% and 3% bypass bleed flow are shown in Figs. 6–21 and 6–22, respectively. Each figure contains plots of the static pressure, displacement thickness, shape factor (i.e., displacement thickness divided by the momentum thickness), and skin friction coefficient along the cowl wall.

Boundary layers will typically separate when the shape factor exceeds 1.8. As shown in Fig. 6–21 the boundary layer at the critical condition is very near to separation at x = 11.5 in. with 2% bypass flow. The corner flow between the cowl wall and the sideplate is even more likely to separate. Fig. 6–22 shows that at the critical condition the shape factor exceeds 1.8 at x = 11.5 in. with 3% bypass flow, indicating that the boundary layer is likely to separate.

6.2.3. Conclusion

The following conclusions are drawn from the results of the 2D Navier–Stokes Analysis:

- At the critical condition the shear−layer can generate an oblique shock. This shock can be strong enough to cause the boundary−layer on the cowl wall to separate. The corner flow between the cowl and the sideplates is even more likely to separate.
- Boundary layer separation on the cowl wall may explain why the experimental recovery values did not improve with increased bypass flow.
- The inlet could be redesigned to avoid separation caused by the oblique shear layer shock. The current inlet model would need to have the cowl bleed extended forward or have the forward ramp trailing edge moved aft.

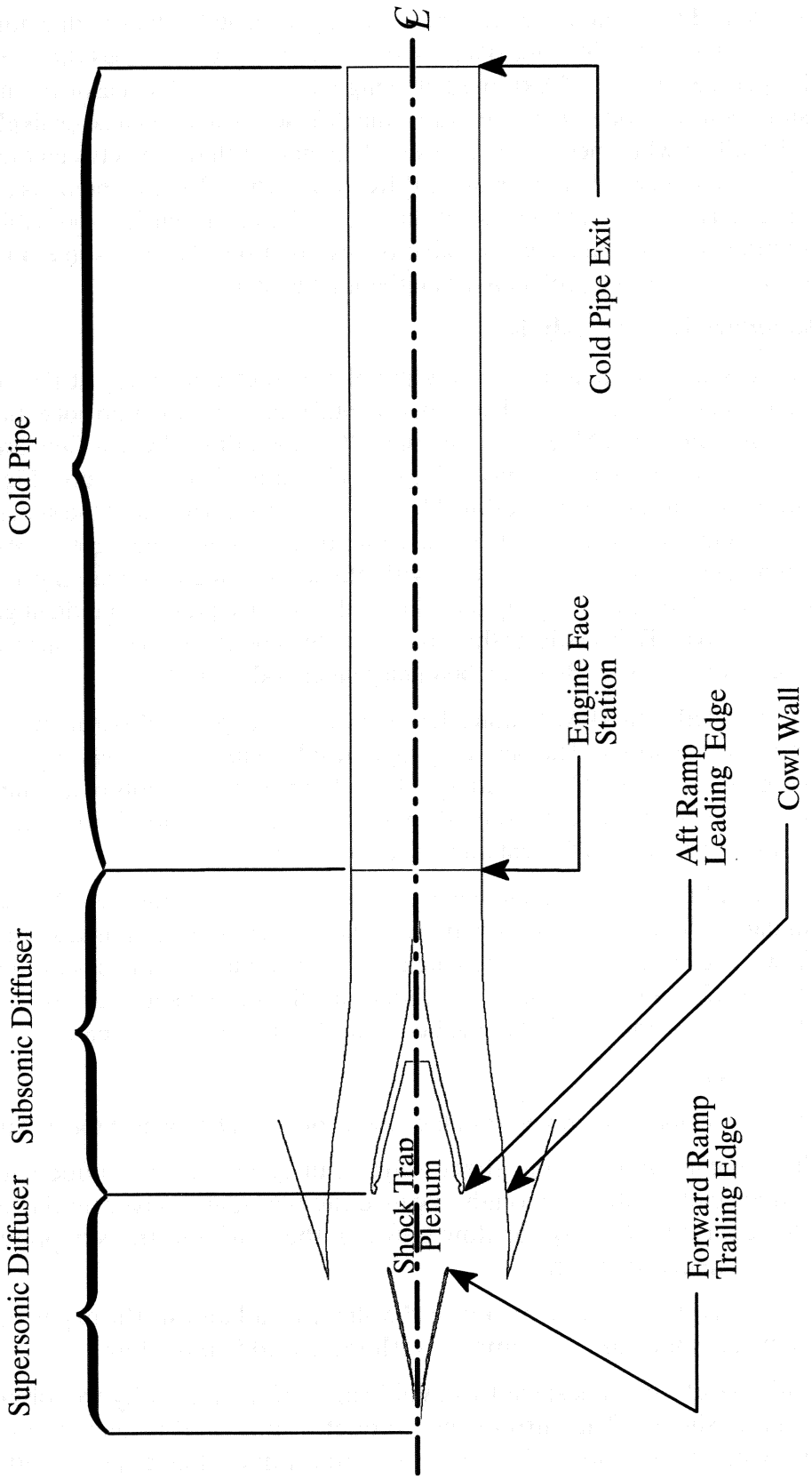

Figure 6–12. Inlet Schematic (Top View)

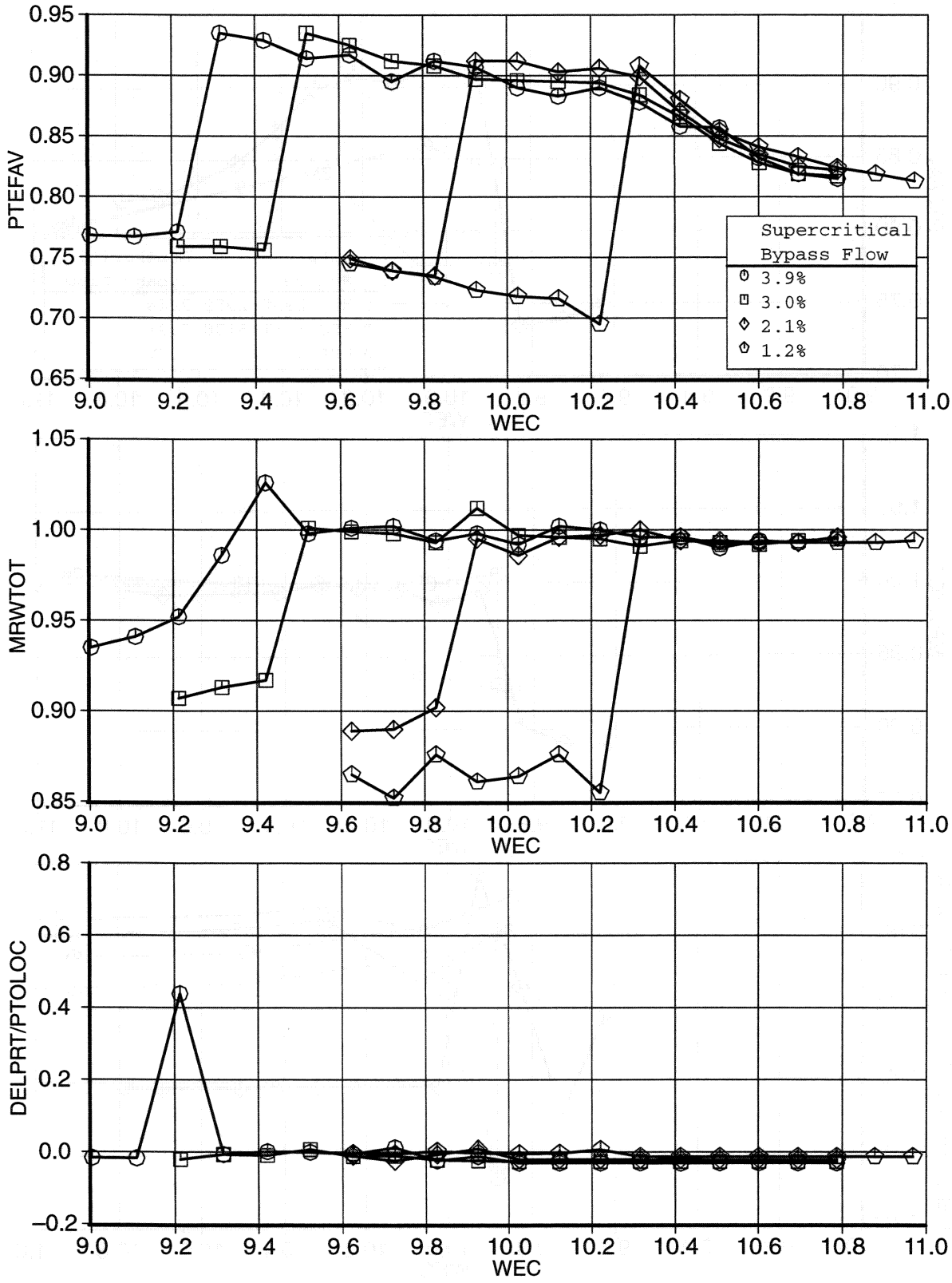

Figure 6–13. Predicted Recovery, Mass Flow and Forward Ramp Pressure Difference

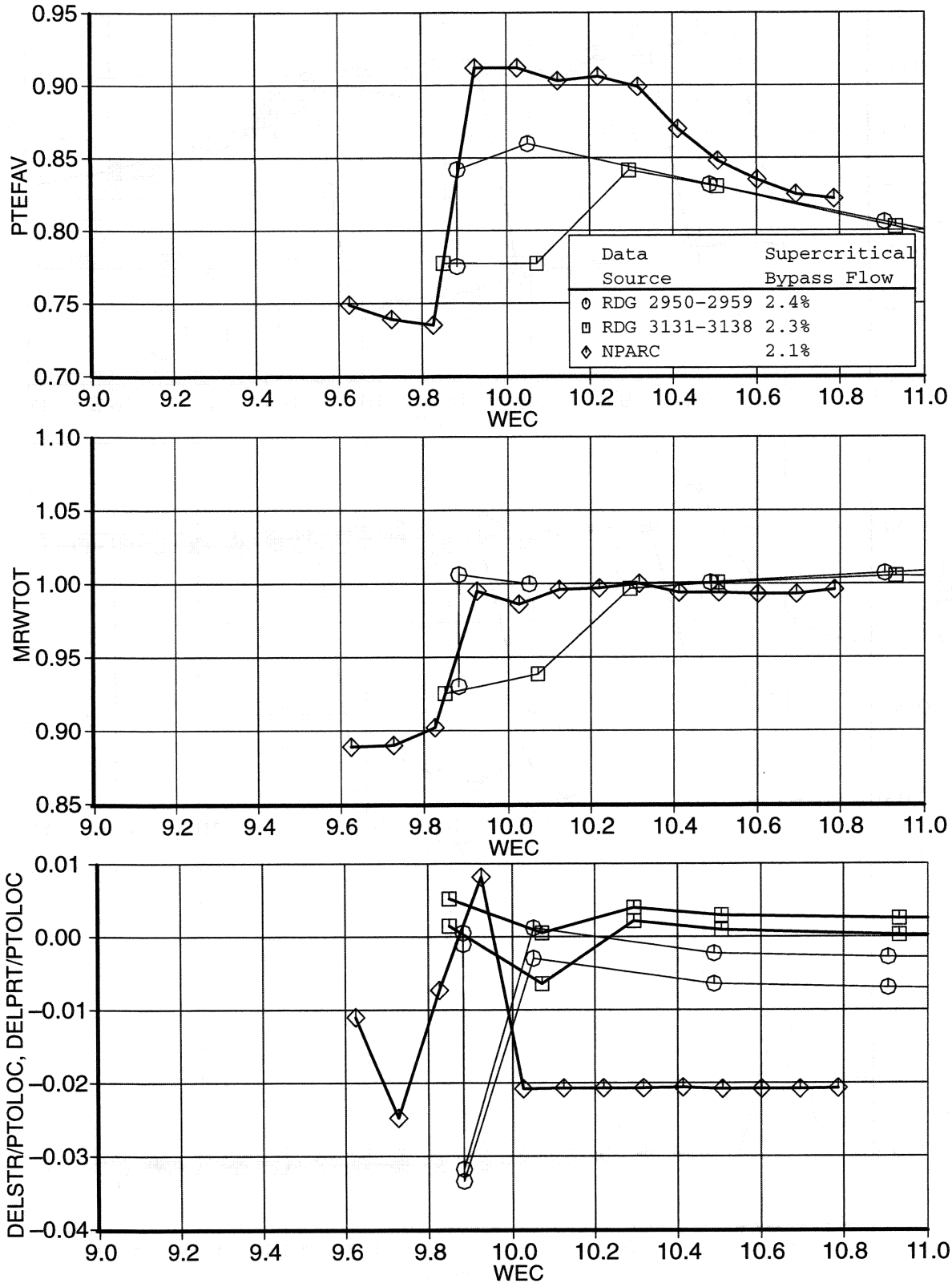

Figure 6–14. Predicted vs Experimental Recovery, Mass Flow and Forward Ramp Pressure Difference with 2% Supercritical Bypass Flow

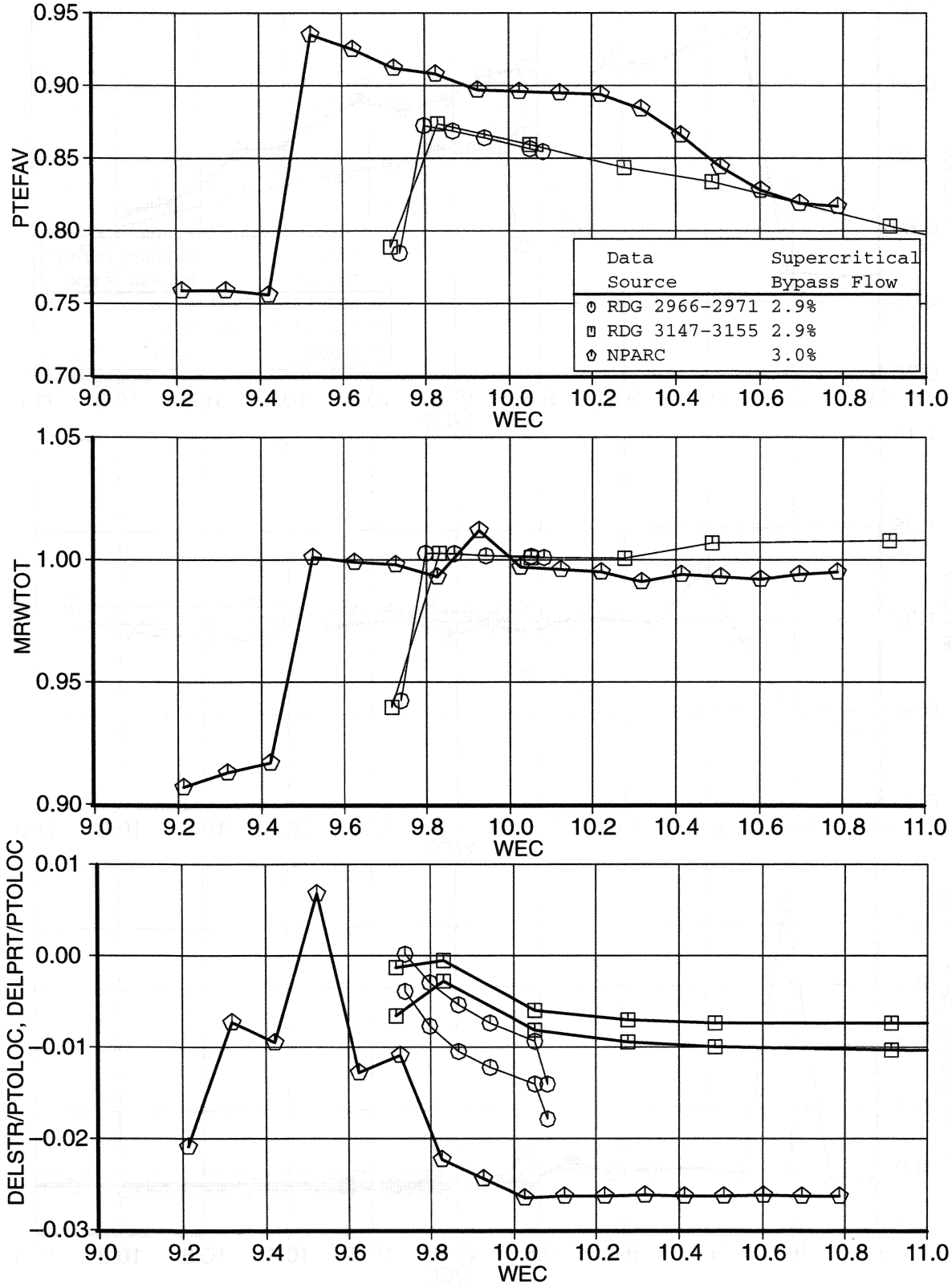

Figure 6–15. Predicted vs Experimental Recovery, Mass Flow and Forward Ramp Pressure Difference with 3% Supercritical Bypass Flow.

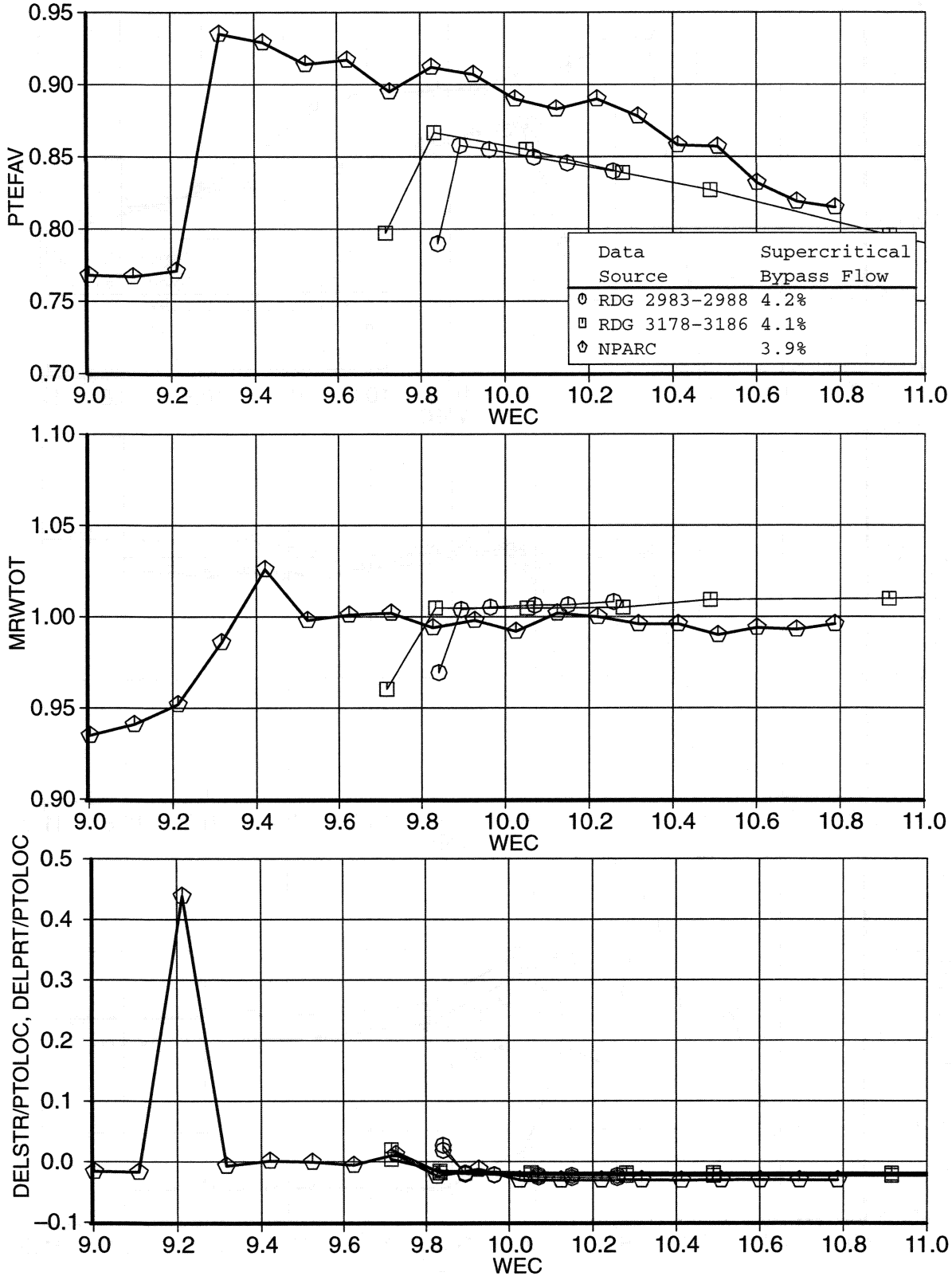

Figure 6–16. Predicted vs Experimental Recovery, Mass Flow and Forward Ramp Pressure Difference with 4% Supercritical Bypass Flow.

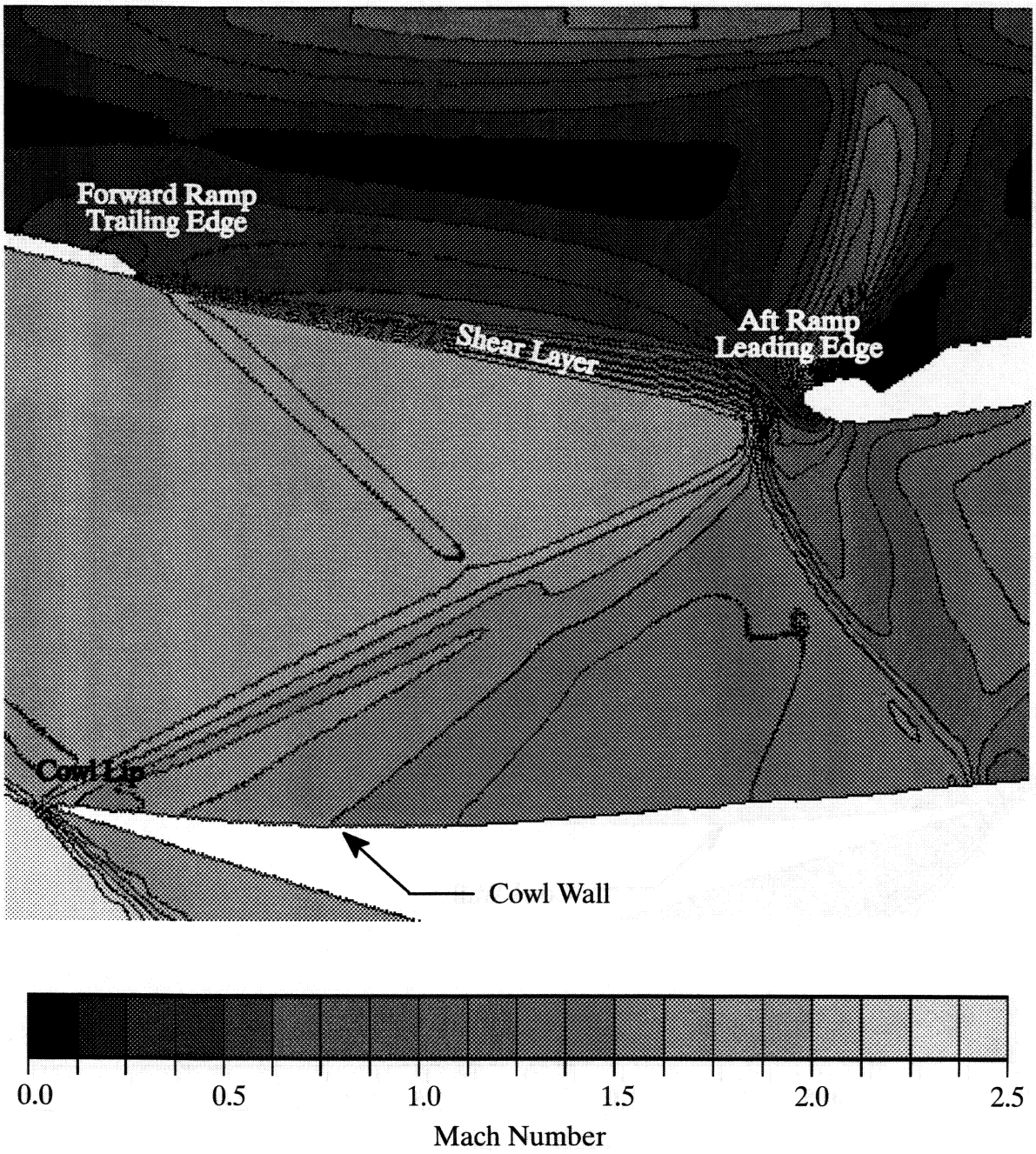

Figure 6–17. Mach Contours at Supercritical Condition with 2% Supercritical Bypass Flow.

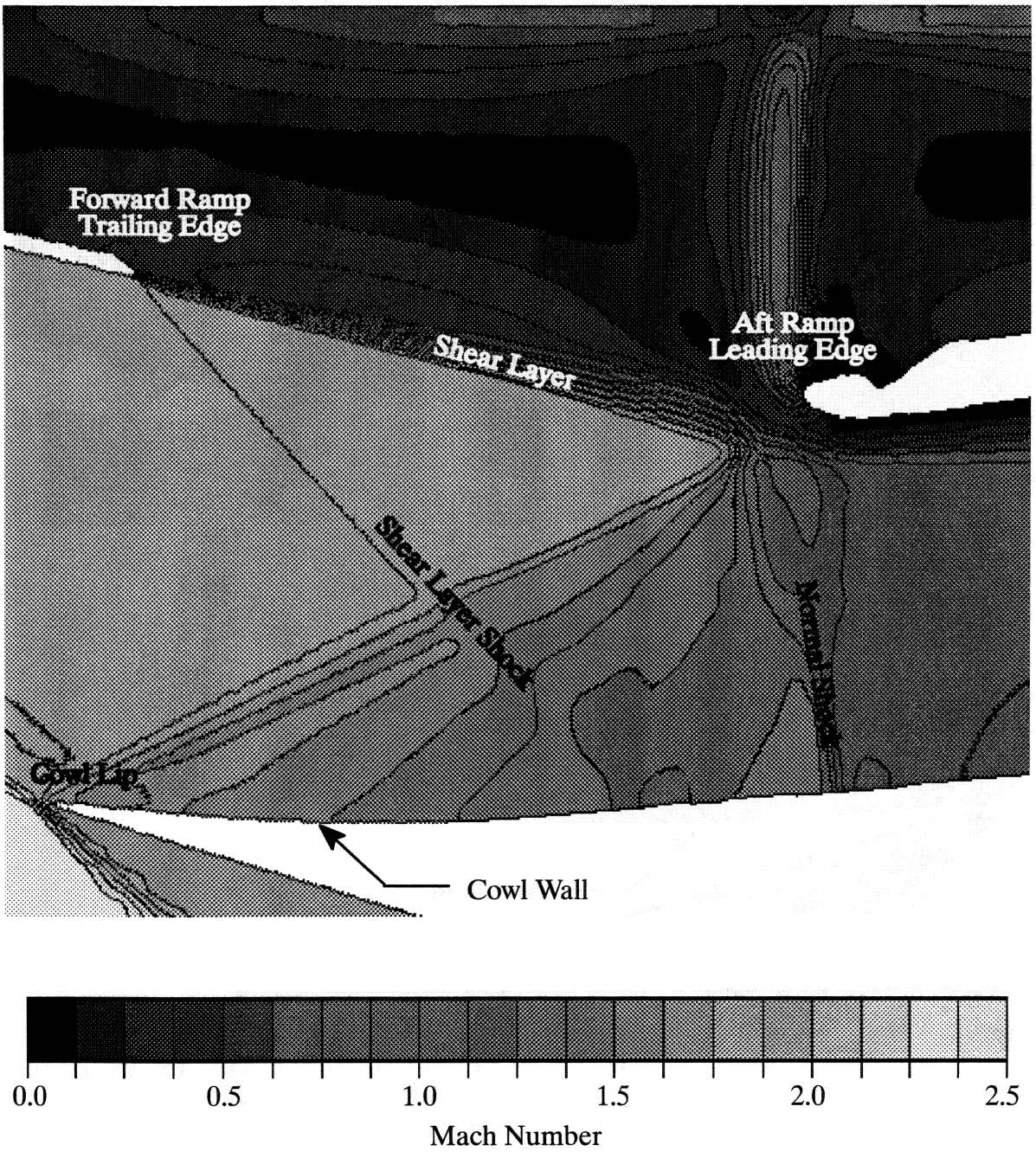

Figure 6–18. Mach Contours at Critical Condition with 2% Supercritical Bypass Flow.

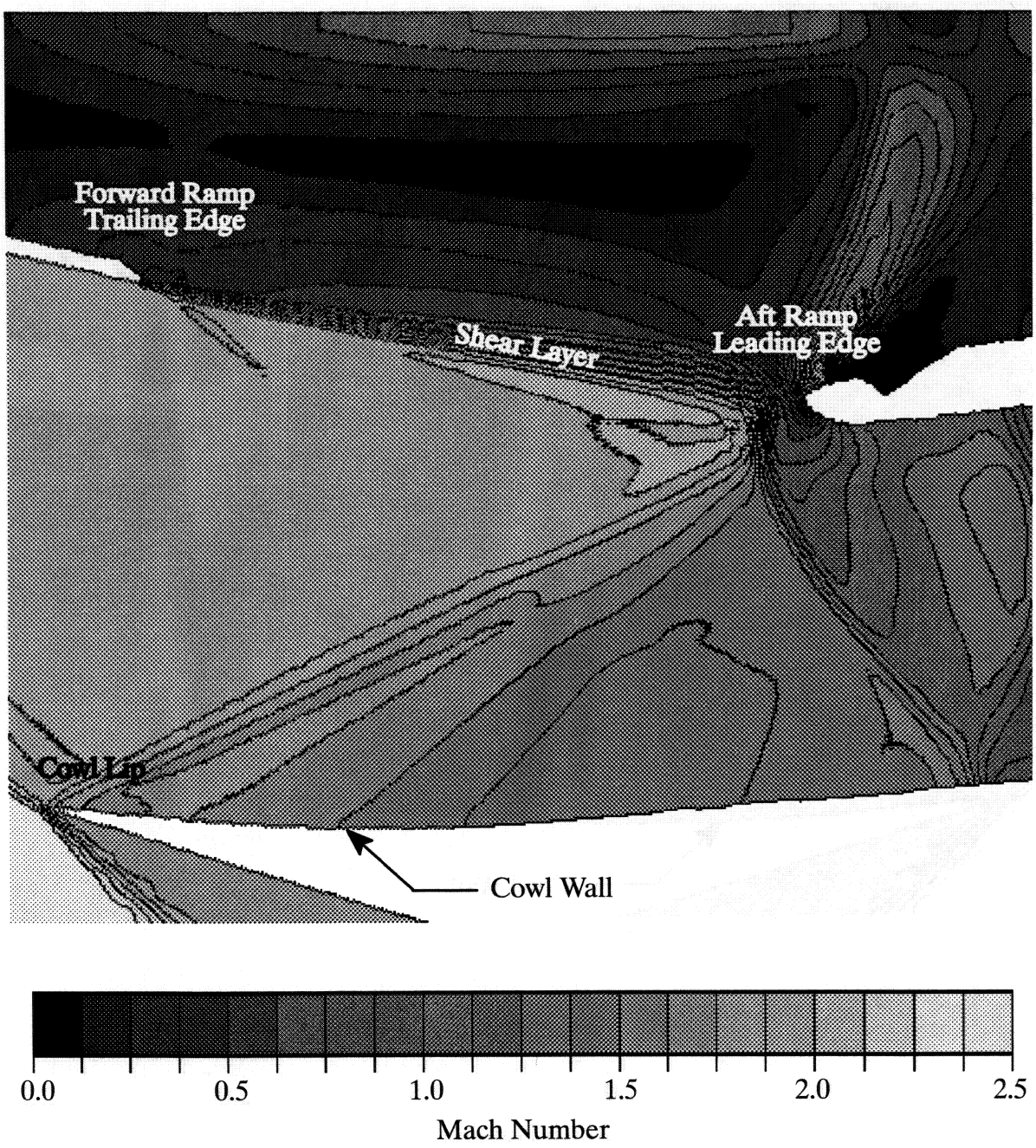

Figure 6–19. Mach Contours at Supercritical Condition with 3% Supercritical Bypass Flow.

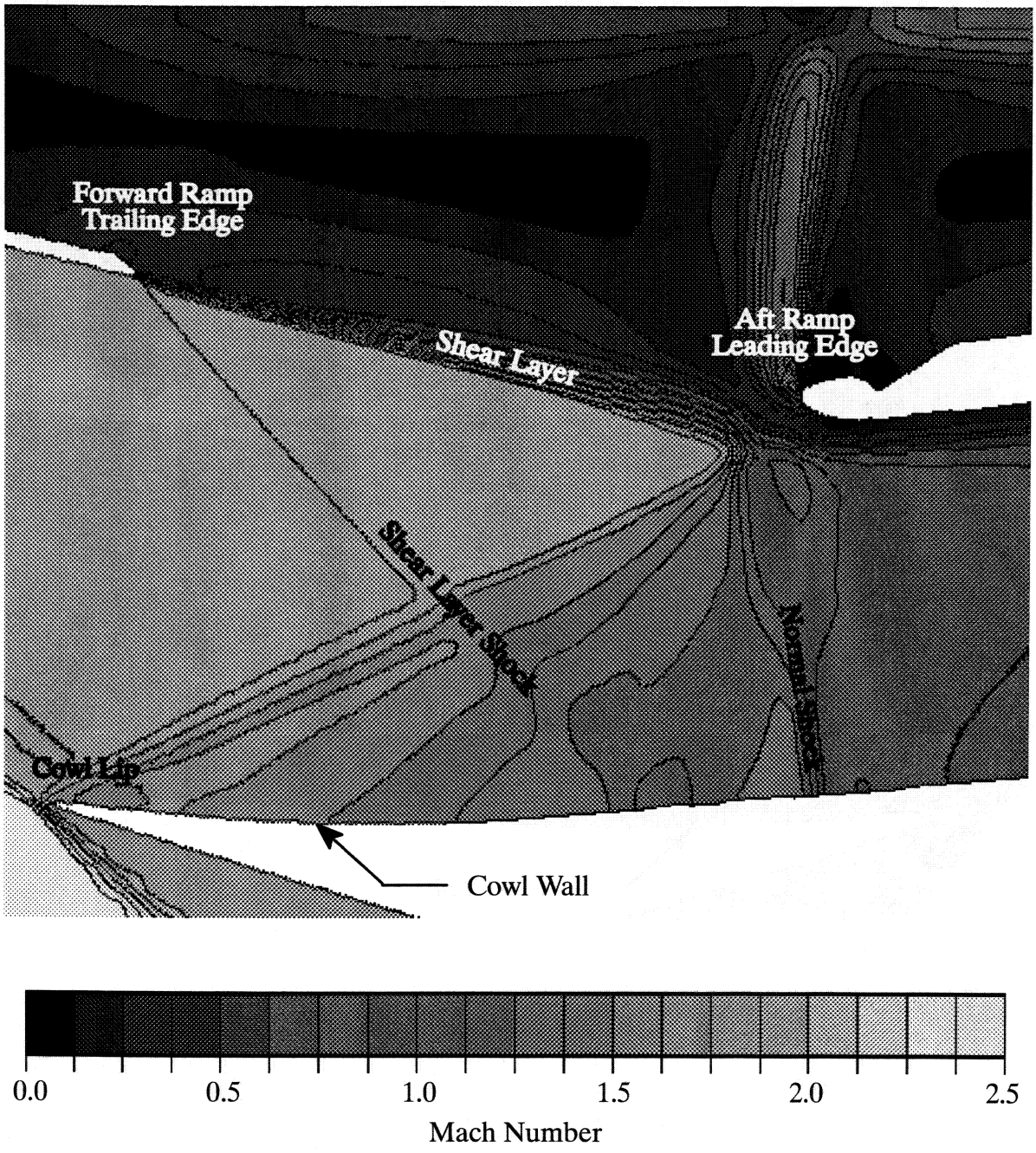

Figure 6–20. Mach Contours at Critical Condition with 3% Supercritical Bypass Flow.

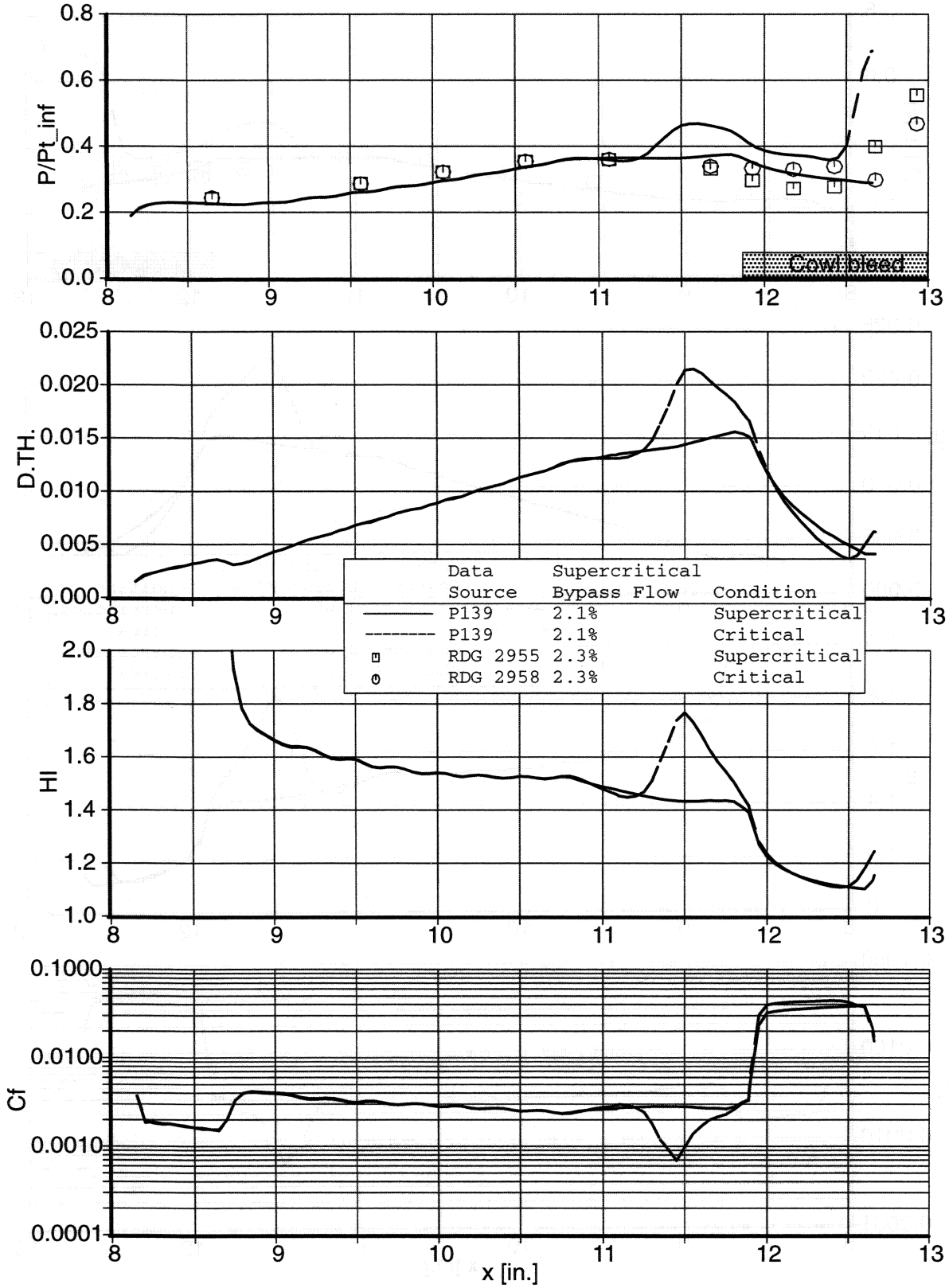

Figure 6–21. Critical vs. Supercritical Cowl Boundary Layer Characteristics with 2% Supercritical Bypass Flow.

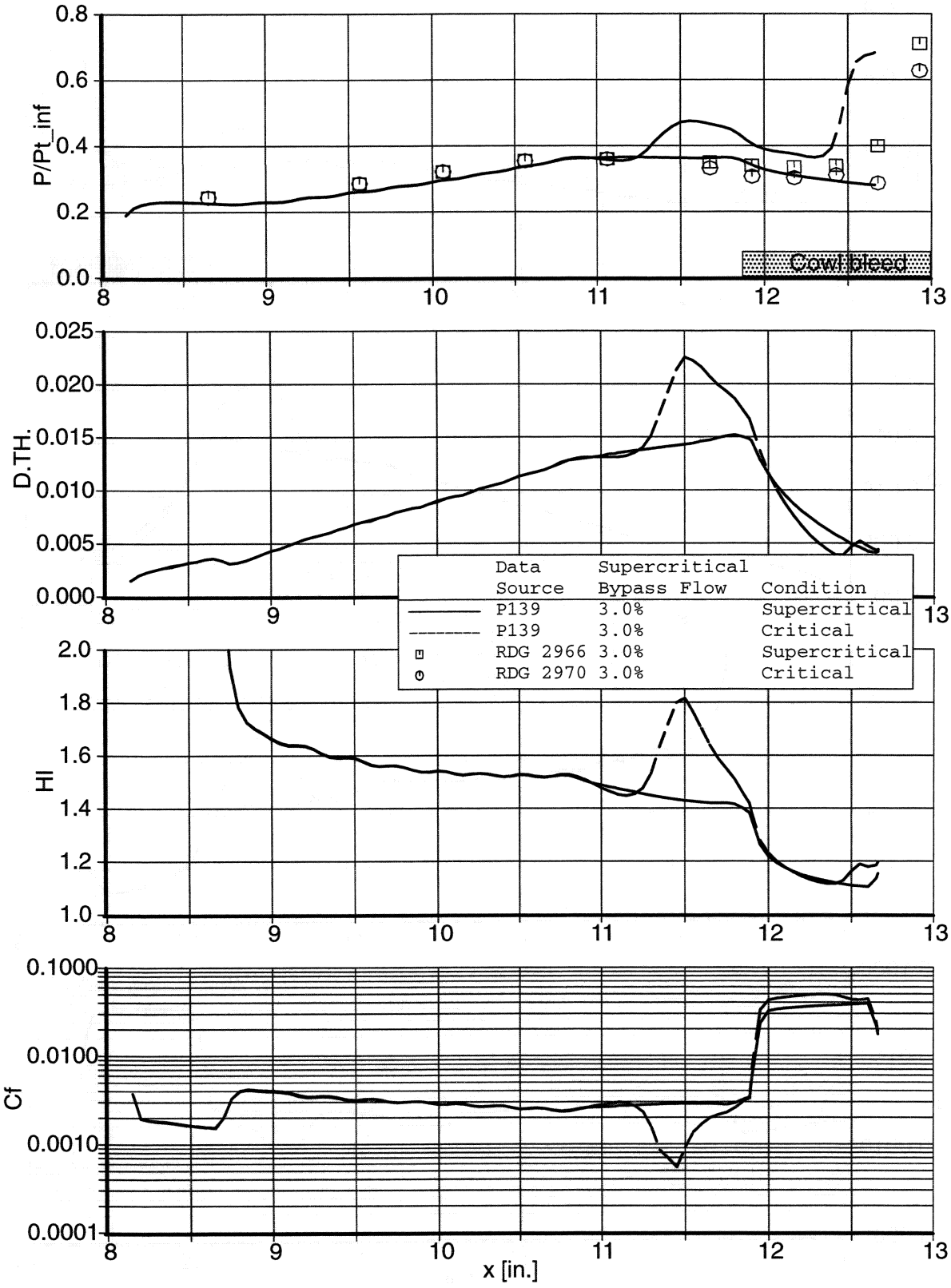

Figure 6–22. Critical vs. Supercritical Cowl Boundary Layer Characteristics with 3% Supercritical Bypass Flow.

7. CONCLUDING REMARKS

Although the stability benefits propounded for the BTSSI inlet were not confirmed, the inlet proved to have the following potentially attractive features: it is virtually buzz free; unstart is much less violent than that of a conventional mixed compression inlet; and thus the external effects of unstart are much less significant than that of a conventional mixed compression inlet.

The model tested includes new as well as existing old hardware. A new supersonic section was built to represent the configuration evaluated analytically in prior Propulsion Airframe Integration Technology contract tasks. The subsonic section was salvaged from hardware built, but never tested, during the 1970's.

Three different vortex generator patterns were studied in order to determine their effect on subsonic diffuser performance. Due to the poor subsonic diffuser, achieving an acceptable level of distortion was not possible with any of the vortex generator configurations. The lowest level of distortion was over 18% whereas a level on the order of 10% is considered acceptable. The measured total pressure losses in the subsonic diffuser were between 4% and 6%. Clearly, the inlet performance could be improved with a better subsonic diffuser.

During the course of the testing an unusual "semi–started" mode of operation was encountered. The inlet was able to spill up to 30% of the captured airstream without fully expelling the normal shock. In this mode the total pressure recovery dropped approximately 6% without increasing distortion.

Dynamic instrumentation at the cowl lip station indicates the semi–start mode may in fact be a series of unstart/re–start cycles with frequency ranging from 0.2 to 20 Hz. The frequency of the unstart event could be controlled. It is unclear how this mode would effect an engine, however, since the effect depends on performance of the subsonic diffuser. It is reasonable to assume some effect would be realized. Engine face total pressure measurements show an influence due to the unstart/re–start cycle, but at a reduced level of impact than occurs at the cowl lip. Further investigation of this phenomenon is required before it is fully understood.

Fully started inlet stability did not improve as the shock trap plenum doors were opened. This result was unexpected since prior testing of the concept, with a smaller scale single duct design, allowed extension of fully started inlet operation to regions of significantly reduced supply flow without reducing recovery. Computational fluid dynamic analyses suggest that the boundary layers on the cowl or in the corners between the cowl and sidewalls may have separated, inducing a premature inlet unstart that limited the effectiveness of the shock trap plenum doors.

CFD predictions using the PARC code compare reasonably well with experimentally measured surface static pressures and throat station and engine face recoveries. The PARC calculations use a constant mass flux across a smooth surface to model the bleed without taking into account roughness effects produced by the bleed. Thus the theoretical model requires less bleed to achieve a given recovery level.

A parametric study was conducted to optimize the geometry of the aft ramp leading edge. The shape of the aft ramp leading edge appears to be less important than its location.

The following remarks are grouped in three categories: control law related, control implementation related, and inlet configuration related.

Control Law: The ramp control scheme was found to be acceptable in that it was relatively straightforward to implement a control law which would maintain the ramps in a configuration appropriate to the prevailing inlet angle of sideslip and Mach number.

The bypass door loop never achieved satisfactory operation for a variety of reasons outlined in the commentary on inlet configuration, below.

Control Implementation: Signal noise was found to be a severe limiting factor in all control loops evaluated. This suggests a number of areas in which future effort should be concentrated.

1. Definition of noise models for inclusion in simulations so that solutions to the problem can be evaluated analytically.
2. Development of techniques for predicting aerodynamic noise in a proposed sensor location.
3. Development of quiet aerodynamic probe configurations.
4. Evaluation of advanced filter schemes in the controls application.

Pressure transducer accuracy was observed to be problem in the ramp control loop and is expected to be one in the bypass door loop. Incorporation of precision pressure transducers in the wind tunnel configuration controller is recommended as early as possible. The design of the new bifurcated inlet currently in progress addresses this.

Rapid analysis of control system results was impeded by lack of supporting software. Specifically we had no means of writing a file of controller data which could easily be correlated to facility steady state data. Nor did we have a means of automatically checking transducer calibrations at the beginning of each run. Lack of these capabilities lead to delays in identifying problems and limited our ability to understand problems we could identify. The controller software configuration developed for the upcoming axisymmetric inlet test addresses these issues.

Because the control system never achieved the maturity to justify full mission simulations the wind tunnel's inability to continuously vary Mach number, conveniently achieve low Mach numbers, or represent an underwing flow field did not directly affect the test. However, operation in the facility made the facility restrictions apparent. With these restrictions techniques other than wind tunnel test alone will be required to achieve the confidence in control system operation necessary for product launch. The possible techniques include much more elaborate bench test simulations than contemplated to date and flight test of a controlled HSR propulsion system over the inlet operating envelope.

Inlet Configuration: Although the stability benefits propounded for the BTSSI inlet were not confirmed the inlet proved to have a number of potentially attractive features:

1. It is virtually buzz free.
2. Its unstart is much less violent than that of a conventional mixed compression inlet.
3. The external effects of its unstart are much less significant than that of a conventional mixed compression inlet.

The inlet design should be revised such that the throat bypass door can influence normal shock position prior to unstart, and such that shear line control (ramp delta p) can be effected with a control independent of that controlling normal shock position.

The bifurcated inlet's lack of angle of attack tolerance (as opposed to sideslip) should be carefully considered in the inlet downselect process since the fundamental premise that the under wing installation protects the inlet from angle of attack variations may not be true for the small variations allowable particularly in the lower portion of the outboard installation.

REFERENCES

1. NASA 10" 2D Inlet Model, Drawing No. CF73994.
2. "Propulsion Airframe Integration Technology Task 1; Subtask 1.7.9, Interface Control Document 10 Inch Bifurcated Two Stage Supersonic Inlet Model Control System," The Boeing Co., D6–56974 Rev A, Oct. 17, 1994.
3. "Engine Inlet Optical Shock Sensor Configuration and Analysis," NASA CR –195385, Nov. 1995.
4. Steinbrenner, J.P, Chawner, J.R., Fouts, C.L., and Nguyen, M.D., "GRIDGEN 3D Multiple Block Grid Generation System", AF–WAL–TR–90–0001, January, 1990.
5. Cooper, G. K., and Sirbaugh, J. R., "The PARC Code: Theory and Usage," Sverdrup Technology, Inc., Arnold Air Force Base, TN, AEDC–TR–89–15, Dec. 1989.
6. "NPARC Version 1.2 User Notes," The NPARC Alliance (Arnold Engineering Development Center, Arnold Air Force Base, TN and NASA Lewis Research Center, Cleveland, OH), Jun. 1994.
7. Mayer, D. W. and Paynter, G. C., "Boundary Conditions for Unsteady Supersonic Inlet Analyses," ISABE 93–7104, In *Papers from the 11th International Symposium on Air Breathing Engines*, Tokyo, Japan, International Society for Air Breathing Engines, Vol. 2, Sep. 20–24, 1993, pp. 1062–1070. See also *AIAA Journal*, Vol. 32, Jun. 1994, pp. 1200–1206.
8. Mayer, D. W. and Paynter, G. C., "Prediction of Supersonic Inlet Unstart Caused by Freestream Disturbances," AIAA 94–0580, Jan. 1994. See also *AIAA Journal*, Vol. 33, Feb. 1995, pp. 266–275.
9. Reyhner, T. A., "A Computer Program for Finite–Difference Calculation of Compressible Turbulent Boundary Layers," The Boeing Company, Seattle, WA, D6–23236, Jun. 1970.

NOMENCLATURE

ALPHA	Angle of attack [degrees]
BETA	Angle of yaw [degrees]
Betam	Inlet sideslip angle
Cf	Skin friction coefficient
DELPRT	Static pressure in the shock trap plenum minus the static pressure at the forward ramp trailing edge on the port side
DELSTR	Static pressure in the shock trap plenum minus the static pressure at the forward ramp trailing edge on the starboard side
DIST	Distortion
D.TH.	Boundary layer displacement thickness
HI	Incompressible shape factor
L	Cowl lip height, 4.48"
Machlocf	Inlet local Mach number
MOLOC	Local freestream Mach number (i.e., just ahead of the inlet)
MRWTOT	inlet mass flow (i.e., the sum of the mass flow through the bleed plenums, the shock trap plenums and the cold pipe normalized by the capture mass flow)
P	Static pressure
PAIT	Propulsion Airframe Integration Technology
PDFR2F	ramp differential pressure port side
P/Ptinf	Static pressure to Freestream total pressure ratio
PSCLREF	cowl pressure ratio reference value
PSCL9RM	cowl pressure ratio pscl9/ptof
Ps/Pt0	Static pressure to Freestream total pressure ratio
Pt_inf	Freestream stagnation pressure
Ptinf	Freestream stagnation pressure
Pt/Ptinf	Total pressure to Freestream total pressure ratio
ptof	tunnel total pressure
PTOLOC	Local freestream stagnation pressure (i.e., just ahead of the inlet)
PTTHAV	Average stagnation pressure recovery at the throat station
PTEFAV	Average stagnation pressure recovery at the engine face station
RDG	Reading number
ulsbdtg	bypass door command out of regulator module

unusbdr	bypass door base schedule
usfrg	starboard forward ramp command out of regulator module
usfrr	starboard forward ramp base actuator schedule
x	axial coordinate [in.]
XMPARP	Port aft ramp position
XMPARS	Starboard aft ramp position
XMPFRP	Port forward ramp position
XMPFRS	Starboard forward ramp position
XMPTDL	Lower shock trap plenum door position
XMPTDU	Upper shock trap plenum door position
WCPWO	Mass flow ratio through the cold pipe
WEC	Corrected mass flow ratio
B	Angle of yaw [degrees]

The following is nomenclature used to define measured data, individual sensor location is given by the appropriate reference figure:

Symbol	**Name**	**Ref. Fig.**
O_{NSS}	Optical normal shock sensor	2–15, 2–16
O_{PTD}	Throat slot bypass door optical position sensor	2–23
P_{BCP}	Cold pipe base static pressure	2–27
P_{SAR}	Aft ramp static pressure	2–19, 2–20
P_{SBD}	Subsonic diffuser bypass static pressure	2–12, 2–13
P_{SCE}	Cowl boundary layer bleed exit cover static pressure	2–25, 2–26
P_{SCL}	Cowl lip static pressure	2–8, 2–9
P_{SCP}	Cowl boundary layer bleed plenum static pressure	2–8, 2–9
P_{SCS}	Cowl spacer static pressure	2–10, 2–11
P_{SD}	Subsonic diffuser bypass door static pressure	2–14
P_{SEF}	Engine face static pressure	2–7
P_{SFR}	Forward ramp static pressure	2–17, 2–18
P_{SFS}	Cold pipe duct static pressure	2–27
P_{SSE}	Sidewall boundary layer bleed exit static pressure	2–25, 2–26
P_{SSP}	Sidewall boundary layer bleed plenum static pressure	2–15, 2–16

Symbol	Name	Ref. Fig.
P_{SSR}	Spinner/Wedge static pressure	2–21, 2–22
P_{SSW}	Sidewall static pressure	2–15, 2–16
P_{STE}	Throat slot bypass exit static pressure	2–25, 2–26
P_{STP}	Throat slot plenum static pressure	2–15, 2–16 2–23, 2–24
P_{TBC}	Cowl boundary layer rake total pressure	2–9
P_{TBS}	Sidewall boundary layer rake total pressure	2–15
P_{TCE}	Cowl boundary layer bleed exit total pressure	2–25, 2–26
P_{TDL}	Bypass door total pressure	2–14
P_{TEF}	Engine face total pressure	2–7
P_{TFS}	Cold pipe duct total pressure	2–27
P_{TSE}	Sidewall boundary layer bleed exit total pressure	2–25, 2–26
P_{TTC}	Cowl throat rake total pressure	2–8
P_{TTE}	Throat slot bypass exit total pressure	2–25, 2–26
P_{TTP}	Throat slot plenum total pressure	2–23, 2–24
RP_{DCL}	Cowl Lip dynamic static pressure	2–8, 2–9
RP_{DFR}	Forward ramp / throat slot plenum delta dynamic static pressure	2–15, 2–16 2–17, 2–18
RP_{DNS}	Pneumatic normal shock sensor dynamic static pressure	2–8, 2–9
RP_{DSEF}	Engine face dynamic static pressure	2–7
RP_{DTEF}	Engine face dynamic total pressure	2–7
RP_{DTP}	Throat slot plenum dynamic static pressure	2–15, 2–16
RP_{SCL}	Cowl Lip dynamic static pressure	2–8, 2–9
RP_{TBC}	Cowl boundary layer rake dynamic total pressure	2–9
RP_{TTC}	Cowl throat rake dynamic total pressure	2–8
T_{TPS}	Pneumatic normal shock sensor total temperature	2–8, 2–9
XM_{PAR}	Aft ramp position sensor	2−19, 2−20
XM_{FP}	Engine airflow control plug position sensor	2–27
XM_{PFR}	Forward ramp position sensor	2–17, 2–18
XM_{PTD}	Throat slot bypass door position sensor	2–23, 2–24

APPENDIX A

A.1. NORMAL SHOCK POSITION FOR LEADING EDGE STUDY

Conclusions were made in Section 3.2. that were based on relative shock locations for the PARC calculations and experimental readings. This appendix is to show the detailed data on which those conclusions were based.

Figure A–1 shows sidewall surface pressure distribution comparisons between experimental results and PARC calculations for the baseline, alternate #1, and alternate #2 aft ramp leading edges. All the experimental results were for bleed pattern #7. As can be seen in the figure, all the experimental readings have a normal shock (the pressure rise between x=12 and x=14) that is downstream of the PARC results. This results in lower pressures in the subsonic diffuser as discussed in Section 3.2..

Figure A–2 shows sidewall surface pressure distribution comparisons between experimental results and PARC calculations for the alternate #1 and alternate #3 aft ramp leading edges. The experimental results were for bleed pattern #8. The figure shows that for the experimental readings the normal shock is slightly downstream of the PARC calculations. The experimental shock location for these readings is further upstream than shown in Figure A–1 which should produce pressures in the subsonic diffuser that are closer to the PARC calculations. Reviewing Figures 3–32 and 3–35 shows that this is the case.

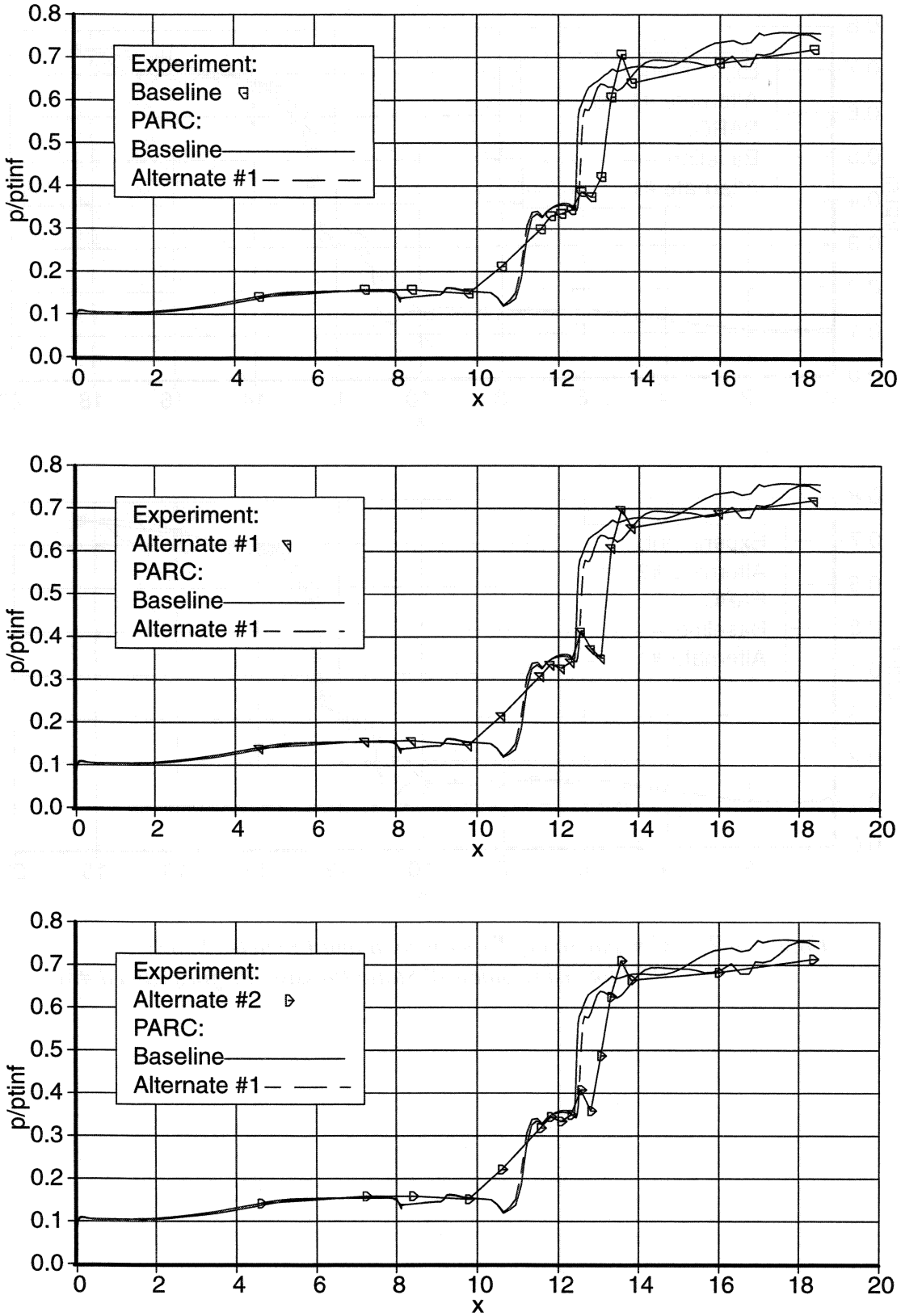

Figure A–1. Comparison of Experimental and Predicted Shock Position using Sidewall Static Pressure Profiles (Bleed #7)

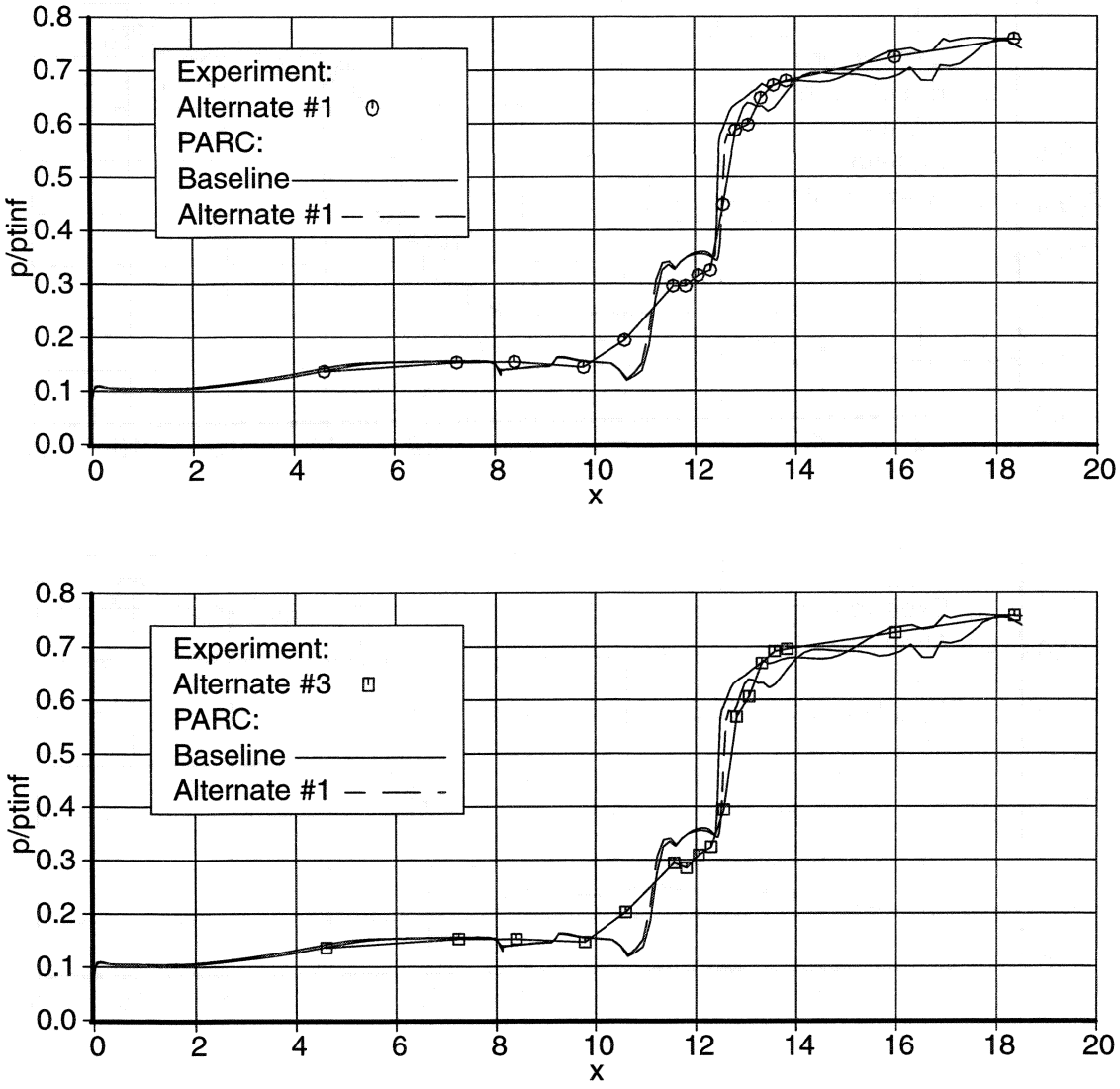

Figure A–2. Comparison of Experimental and Predicted Shock Position using Sidewall Static Pressure Profiles (Bleed #8).

REPORT DOCUMENTATION PAGE

Form Approved
OMB No. 0704-0188

1. AGENCY USE ONLY (*Leave blank*)	2. REPORT DATE	3. REPORT TYPE AND DATES COVERED
	July 2003	Final Contractor Report

4. TITLE AND SUBTITLE

Supersonic Test of the 10-Inch Bifurcated Two-Stage Supersonic Inlet (BTSSI)

5. FUNDING NUMBERS

WBS–22–714–01–38
NAS3–25963

6. AUTHOR(S)

C.M. Carlin, I. Frisch, J.J. Kolden, J.L. Koncsek, K.J. Marrs, D.W. Mayer, S.L. McMahon, K.H. Milligan, and D.M. Sommerfield

7. PERFORMING ORGANIZATION NAME(S) AND ADDRESS(ES)

The Boeing Company
P.O. Box 3707
Seattle, Washington 98124

8. PERFORMING ORGANIZATION REPORT NUMBER

E–13902

9. SPONSORING/MONITORING AGENCY NAME(S) AND ADDRESS(ES)

National Aeronautics and Space Administration
Washington, DC 20546–0001

10. SPONSORING/MONITORING AGENCY REPORT NUMBER

NASA CR—2003-212313

11. SUPPLEMENTARY NOTES

Project Manager, John Saunders, Turbomachinery and Propulsion Systems Division, NASA Glenn Research Center, organization code 5850, 216–433–6278.

12a. DISTRIBUTION/AVAILABILITY STATEMENT

Unclassified - Unlimited
Subject Categories: 02 and 07 Distribution: Nonstandard

Available electronically at http://gltrs.grc.nasa.gov

This publication is available from the NASA Center for AeroSpace Information, 301–621–0390.

12b. DISTRIBUTION CODE

13. ABSTRACT ***(Maximum 200 words)***

Experimental results from testing of a novel supersonic inlet model in NASA Glenn Research Center's 10- by 10-foot supersonic wind tunnel are presented. The patented inlet concept, called Two-Stage Supersonic Inlet (TSSI), incorporates a large cavity, or throat slot, in the supersonic diffuser intended to enhance the stability of the normal shock. The present embodiment of the concept is a bifurcated (twin-duct) design. During the course of testing an unusual "semi-started" mode of operation was encountered. The inlet was able to spill up to 30 percent of the captured airstream without fully expelling the normal shock. In this mode, the total pressure recovery dropped approximately 6 percent without increasing steady-state distortion. Dynamic instrumentation at the cowl lip station indicates the semi-start mode may be a series of unstart/restart cycles with frequency ranging from 0.2 to 20 Hz. Engine face total pressure measurements indicate a modest impact due to this event. However, since the current test article does not have a representative subsonic diffuser (and is in fact separated), it is unclear how this mode of operation would effect an engine. Further investigation of this phenomenon is required before it is fully understood. Prior testing of the TSSI concept allowed extension of fully started inlet operation to regions of significantly reduced supply flow without reducing recovery. The test article was a smaller scale than the present test and was a single duct design. In the present test, the expanded range of stable operation with high recovery was not realized.

14. SUBJECT TERMS

High Speed Civil Transport (HSCT); Supersonic; Inlet; Diffuser; Propulsion; Flow stability; Experiment; CFD; Analysis

15. NUMBER OF PAGES

210

16. PRICE CODE

17. SECURITY CLASSIFICATION OF REPORT	18. SECURITY CLASSIFICATION OF THIS PAGE	19. SECURITY CLASSIFICATION OF ABSTRACT	20. LIMITATION OF ABSTRACT
Unclassified	Unclassified	Unclassified	